TU TECHNISCHE
UNIVERSITÄT
WIEN
Vienna University of Technology

Dissertation

Screening and Characterization of Potential Light-Metal High Entropy Alloys by Magnetron Sputtering

Ausgeführt zum Zwecke der Erlangung des akademischen Grades eines

Doktors der technischen Wissenschaften

unter der Leitung von

Ao.Univ.Prof. Dipl.-Ing. Dr.techn. Christoph Eisenmenger-Sittner

E138

Institut für Festkörperphysik

eingereicht an der Technischen Universität Wien

Fakultät für Physik

von

Dipl.-Ing. Johannes Kirschner BSc

Mat.Nr.: 01027482

Wien, am 24.4.2022

Ich nehme zur Kenntnis, dass ich zur Drucklegung meiner Arbeit unter der Bezeichnung

Dissertation

nur mit Bewilligung der Prüfungskommission berechtigt bin.

Diese Arbeit wurde begutachtet von

Erstbegutachter
Prof. Dr.
Jozef Keckes
Lehrstuhl für Materialphysik
Montanuniversität Leoben
Jahnstraße 12, 8700 Leoben
Österreich

Zweitbegutachter
Ass. Prof. Dr.
Helmut Riedl-Tragenreif
Angewandte Oberflächentechnik
Technische Universität Wien
Getreidemarkt 9, 1060 Wien
Österreich

———————————————   ———————————————

Eidesstattliche Erklärung

Ich erkläre an Eides statt, dass die vorliegende Arbeit nach den anerkannten Grundsätzen für wissenschaftliche Abhandlungen von mir selbstständig erstellt wurde. Alle verwendeten Hilfsmittel, insbesondere die zugrunde gelegte Literatur, sind in dieser Arbeit genannt und aufgelistet. Die aus den Quellen wörtlich entnommenen Stellen, sind als solche kenntlich gemacht. Das Thema dieser Arbeit wurde von mir bisher weder im In- noch Ausland einer Beurteilerin/einem Beurteiler zur Begutachtung in irgendeiner Form als Prüfungsarbeit vorgelegt. Diese Arbeit stimmt mit der von den Begutachtern beurteilten Arbeit überein.

Wien, 24. April 2022   ———————————————
                                        Unterschrift des Studenten

Kurzfassung

Die Entwicklung und Erforschung neuartiger Legierungssysteme ist einer der Grundbausteine für technologischen Fortschritt. Durch neue Konzepte können Eigenschaften von Materialien optimiert werden, welche Anwendungen in allen technischen Bereichen finden. Insbesondere die Kombination von mehreren Komponenten in signifikanten Anteilen (> 5 at%) in einem System entwickelte sich in den letzten 15 Jahren zu einem hochmodernen Zweig der Metallurgie. Diese sogenannten Multi-Principal Element Legierungen (MPEAs) oder Hochentropielegierungen (HEAs) konnten bereits vielversprechende Ergebnisse hinsichtlich der absoluten mechanischen Belastbarkeit zeigen. Die Weiterentwicklung dieses Legierungsansatzes in die Richtung von Leichtmetallen und einer damit möglichen Gewichtsersparnis ist insbesondere im Hinblick auf die Realisierung von nachhaltigen Transportkonzepten und potentieller CO_2 Ersparnisse essentiell.

Das Ziel dieser Arbeit war die experimentelle Herstellung von Legierungsbibliotheken mehrkomponentiger Leichtmetall-Systeme (Dichtebereich ≈ 6 g/cm^3). Durch günstige Wahl der Materialien soll eine Ausbildung intermetallischer Phasen unterdrückt und eine einfache Kristallstruktur gefördert werden. Diese Legierungen zeichnen sich vor allem durch erhöhte Festigkeit und Duktilität aus und sind somit relevant für viele technologische Anwendungen. Grundlage zur Erforschung dieser HEAs ist die systematische Herstellung von Legierungsbibliotheken. Hierzu wurden verschiedene Leichtmetalle mittels magnetfeldunterstützter Kathodenzerstäubung (Magnetron Sputtering) in unterschiedlichen Zusammensetzungen auf einem Substrat aufgebracht. Um dies durchführen zu können, wurde eine Sputteranlage designt und gebaut, welche Beschichtungen von mehreren Quellen erlaubte. Die Verwendung von zwei seperaten 2 Zoll Targets ermöglichte eine systematische Herstellung von Proben bestehend aus bis zu 5 verschiedenen Elementen. Deren Anteil konnte kontrolliert variiert werden und unter Verwendung von Reintargets beziehungsweise Mehrkomponenten Targets leicht abgeändert werden.

Eine speziell für die geometrische Anordnung des verwendeten experimentellen Aufbaus programmierte Software unterstützte die Vorhersage der Schichtzusammensetzung, um so kontrolliert Zusammensetzungen auf dem Substrat herzustellen. Nach Angabe einiger Prozessparameter wie Substrat-Quellen Abstand oder angelegter Leistung wurde die Schichtzusammensetzung berechnet und konnte so a priori entsprechend dem gewünschten Zusammensetzungsbereich optimiert werden.

Zu den Elementen, welche zur Kombination in den Multikomponentenlegierungen verwendet wurden, zählten Mg, Al, Si, Ti, Cr, Cu und Zn. Diese Elemente wurden nach Gesichtspunkten

der technologischen Relevanz, nach Zugehörigkeit zu den Gruppen im Periodensystem und nach in der Literatur postulierten Kriterien und Modellen ausgewählt.

Die Schichten wurden nach dem Herstellungsprozess in einem selbstkonstruierten Wärmebehandlungsofen nachbehandelt, um das Erreichen eines Gleichgewichtszustandes zu ermöglichen. Die produzierten Proben wurden anschließend mit gängigen Analyseverfahren (REM, EDS, AFM, XRD, FIB, TEM, Vickers Härtemessungen) charakterisiert und auf potentiell interessante konzentrationsinduzierte Eigenschaften untersucht.

Die Untersuchungen konnten Zusammenhänge der Zusammensetzung verschiedener Elemente aus verschiedenen Materialklassen (Übergangsmetalle, Leichtmetalle, Halbleiter) mit mechanischen Eigenschaften und kristallographischer Ordnung aufzeigen. Insbesondere die Erforschung von einphasigen Bereichen stand im Mittelpunkt der Arbeit. Es konnten mehrere Bereiche mit überwiegend einphasigen Strukturen gefunden werden. Diese wurden von komplexen intermetallischen Prototypen und einfachen metallischen Gittern dominiert. Insbesondere die FCC Struktur der terminalen Festkörperlösung von Cu wurde bis zu einem Anteil von ≈ 35 at% der Legierungselemente Al-Mg-Zn aufrecht erhalten. Dies entspricht je nach angewandter Definition einer Hochentropie- oder Medium-Entropielegierung mit einer mittleren Dichte von ≈ 6.5 g/cm^3.

Des Weiteren wird ein einfaches Simulationswerkzeug vorgestellt, mit dem die energetisch günstigste Anordnung der Atome unter Einbeziehung der binären Bildungsenthalpien berechnet werden kann. Diese Simulationen wurden mit den experimentell gewonnenen Daten verglichen und zeigten eine gute Übereinstimmung für eine Vielzahl von Elementkombinationen. Diese Übereinstimmung zwischen dem Experiment und den aus den Daten dieses einfachen Simulationswerkzeugs gewonnenen Ergebnissen zeigt das Potenzial, schnell eine große Anzahl von Elementkombinationen zu scannen. Aufgrund des stark vereinfachten Ansatzes können jedoch keine detaillierten Aussagen über bevorzugte Kristallsysteme oder mechanische Eigenschaften gemacht werden.

Die Ergebnisse aus den experimentellen Untersuchungen dienten als Grundlage für hoch entwickelte Simulationen mittels Cluster Expansion und Dichtefunktionaltheorie, welche in Kollaboration mit der TU Hamburg erarbeitet wurden. Ausgewählte, durch die experimentellen Arbeiten identifizierte, Zusammensetzungen wurden mit diesen Methoden nachgerechnet. Hierbei wurden die experimentell gefundenen Kristallstrukturen als Inputgröße verwendet und auf ihre energetische Günstigkeit getestet. Diese theoretischen Betrachtungen konnten die im Experiment gefundenen Zusammenhänge bestätigen. Zudem ermöglichen die von der TU Hamburg entwickelten Modellrechnungen die theoretische Bestimmung mechanischer Eigenschaften wie beispielsweise des E-Modules. Dies ist in der Entwicklung und für das Design von technologisch genutzten neuartigen Legierungssystemen und Konzepten von entscheidender Bedeutung.

Die gewonnenen Ergebnisse der engen Zusammenarbeit von Theorie und Experiment in dieser Arbeit soll es zukünftig ermöglichen, ein gültiges Modell zur Vorhersage von HEAs zu entwickeln. Zudem können die gefundenen Zusammenhänge für zukünftige Untersuchungen sowohl

experimenteller als auch computergestützter Natur als Datenbank herangezogen werden und bei der Erschließung von komplexen Legierungssystemen als wichtiger Input dienen.

Abstract

The development and research of novel alloy systems are one of the basic building blocks for technological progress. Through new concepts, properties of materials can be optimized, which find applications in a variety of technical fields. In particular, the combination of multiple components in significant proportions (> 5 at%) in a single system has evolved into a cutting-edge branch of metallurgy over the last 15 years. These so-called multi-principal element alloys (MPEAs) or high entropy alloys (HEAs) have already shown promising results in terms of absolute strength. The further development of this alloying approach in the field of light metals and a resulting potential weight reduction is essential, especially with regard to the realization of sustainable transport concepts associated with potential CO_2 savings.

The aim of this thesis was the experimental production of alloy libraries of multicomponent light metal systems (density regime ≈ 6 g/cm^3). Due to a favourable choice of the applied materials, the formation of intermetallic phases can be suppressed and a simple crystal structure can be promoted. These alloys show increased mechanical strength and ductility and are therefore relevant for numerous technological applications. The basis for the investigation of these HEAs is the systematic production of alloy libraries. For this purpose, various light metals in different compositions were combined on a substrate using magnetic field-assisted sputtering (magnetron sputtering). In order to do this, a sputtering system was designed and built that allows depositing coatings from multiple sources. The usage of two separate 2 inch targets enabled a systematic production of samples containing up to 5 different elements. The composition could be varied in a controlled manner and easily modified using pure or multi-component targets.

A software specially programmed for the geometric arrangement of the used experimental setup supported the prediction of the layer composition to achieve a controlled manner of sample production. After specifying various process parameters such as substrate-source distance or applied power, the layer composition was calculated and could thus be optimized a priori according to the desired composition range.

The elements used for multi-component alloys included Mg, Al, Si, Ti, Cr, Cu and Zn. These elements were selected on the basis of technological relevance, membership of the groups in the periodic table and criteria and models postulated in the literature.

After the manufacturing process, the layers were post-annealed in a self-constructed temper-furnace to allow the equilibrium state to be reached. The produced samples were subsequently characterized by common analysis methods (SEM, EDX, AFM, XRD, FIB, TEM, Vickers hardness measurements) and investigated for potentially interesting concentration-induced

properties.

The investigations demonstrated correlations of the composition of various elements from different material classes (transition metals, light metals, semiconductors) with mechanical properties and crystallographic order. In particular, the exploration of single-phase regions was the focus of the work. Several domains with predominantly single-phase structures were found. These were dominated by complex intermetallic prototypes and simple metallic lattices. In particular, the FCC structure of the terminal solid solution of Cu was maintained up to ≈ 35 at% of the alloying elements Al-Mg-Zn. This corresponds to a high entropy or medium entropy alloy with an average density of ≈ 6.5 g/cm^3, depending on the definition applied.

Furthermore, a simple simulation tool is presented, which calculates the most energetically favorable arrangement of atoms by incorporating the binary enthalpies of formation. These simulations were compared with the experimentally obtained data and showed good agreement for a variety of element combinations. This agreement between the experiment and the results obtained from the data of this simple simulation tool shows the potential to quickly scan a large number of elemental combinations. However, due to the highly simplified approach, no detailed statements can be made about preferred crystal systems or mechanical properties.

The results from the experimental investigations served as the basis for sophisticated simulations using cluster expansion and density functional theory, which were developed in collaboration with the TU Hamburg. Selected compositions identified by the experimental work were recalculated using these methods. The experimentally identified crystal structures were used as input variables and tested for their energetic favourability. These theoretical considerations were able to confirm the correlations observed in the experiment. In addition, the model calculations developed by the TU Hamburg enable the theoretical determination of mechanical properties such as the elastic modulus. This is of crucial importance in the development and design of technologically relevant novel alloy systems and concepts.

The results obtained from the close cooperation of theory and experiment in this work should make it possible to create a valid model for the prediction of HEAs in the future. In addition, the correlations found can be used as a database for further investigations of both, an experimental and computer-assisted nature and can act as an important input in the development of complex alloy systems.

Acknowledgements

One of the most important aspects of such a thesis is covered in this section: The acknowledgments.

First of all, I would like to thank you, the reader, for taking the time to read this work. The only purpose of a scientific thesis is to present someone's work and to share it with people who are interested in critically questioning it, gaining ideas or comparing their results. You carry out this so important task and therefore you transform this work into what it should be.

I would like to thank Prof. Christoph Eisenmenger-Sittner, who welcomed me into his thin films research group and made it possible for me to work on this exciting project. In addition to the daily willingness to share his expertise in all aspects of sputtering and material synthesis, he was also the good soul of the working group and made sure that we were not only colleagues but a sworn community.

I would also like to thank DI Clemens Simson, the project manager of the "PL2N_A" project. Not only was he responsible for making the project possible, he was also the contact person for all questions concerning metallurgy. His expertise and easy-going character made the work on this project not only productive but also an enjoyable experience.

As already mentioned in the abstract, a large number of the results presented in this work were compared with the Institute of Advanced Ceramics at the TU Hamburg. The close collaboration with Gregor Vonbun-Feldbauer and Wernfried Mayr-Schmölzer including numerous discussions, joint writing of articles and reports or constructive project meetings were important for this work on a professional as well as a personal level.

Prof. Johannes Bernardi, Jakob Gruber, Martin Binder, Angelika Grossmann, Sabine Schwarz and Karin Whitmore and the entire USTEM Electron Microscopy Service Facility deserve my gratitude for introducing me to the exciting world of electron microscopy, for helping me with

sample analysis, or for carrying it out and for making their equipment accessible. The analysis of the samples using USTEM instruments represents a big part of this work.

Furthermore, I would like to thank DI Werner Artner, representative of the X-Ray Center of the Vienna University of Technology, who introduced me to the use of X-ray equipment and the subsequent analysis and who was always a source of motivation and good humour during long days of measurement and analysis.

As with any experimental work, the production of prototypes and the adjustment of many technical parts were necessary. These were carried out in the workshop of the institute for solid state physics. My gratitude goes to Andreas Lahner, Jürgen Gindl, Friedrich Faszt and Josef "Pepi" Sicherl, who sometimes made the impossible possible, and every now and then, turned a blind eye to missing dimensions.

A big influence on the last few years and on the possibility to gain experience was done by students I supervised, thanks a lot Georg, Robert, Mario, Silvia G., Florian, Niko, Silvia T., Jakob, Immanuel, Laurens, Simon, Clemens, Noah, Florian, Katja und Frederik and of course for always bringing a good mood into the office, despite extreme heat, pandemics or whatever else hit us during the last few years, my officemates Daniel and Manuel.
In particular, David Böhm, Lukas Belhadj, Lukas Thajer, Stefan Pribitzer, Miriam Giparakis, Jan Fiedler and Robin Kurinjimala, as long-time group members of the "functional materials" group, were substantially involved in the creation of this work through technical discussions, "motivating" afternoons and support in all aspects.

In contrast to all persons so far, the following people were more of emotional and personal support during the last years. I would like to thank my parents Margarita and Johann Kirschner, who supported me throughout my studies, who were happy with me in good times and shared the burden in difficult times. Without them, this work would never have come about for so many reasons. A big thanks also goes to my twin sister Elisabeth. As a sister, temporary roommate and permanent contact person in all matters, she was an important part of this work and has been a constant companion in my life since 9 months before my birth. I would like to thank my better half Simona Strazdaite for being there for me every day, slowing me down when I took things too seriously and pushing... no, nevermind. You always knew what I needed, no matter if it was a hug when I was angry on a computer, sugar when I was getting grumpy after long working days or a comment which I suppose was considered to be funny by you when things didn't work out. Without you, this work and the last years would not have been possible.

Last but not least, I would like to point out that while writing these lines I realized how many people had an influence on me, directly or indirectly. It is impossible to mention all people by name, but I remembered you all and this is for those who feel addressed:

Thank you!

Contents

Contents

1. Introduction

The design and research of novel materials with low weight are especially important in areas where weight reduction plays a major role [1]. These include the aerospace and automotive industries and the entire energy sector, which are interested in new alloys ideally without cost increase [2]. Studies have indicated that a weight reduction of 10 % in vehicles can lead to a fuel consumption decrease of 7 % and thus result in a lower CO_2 load [3]. Substitution of steel in the structural design of automobiles can reduce body weight by up to 50 % [4], resulting in an overall weight decrease of 20 % to 30 % [5]. To date, lightweight materials are limited by their restricted properties or high manufacturing costs [1] and great efforts are being made to develop low-cost materials with improved mechanical properties [5].
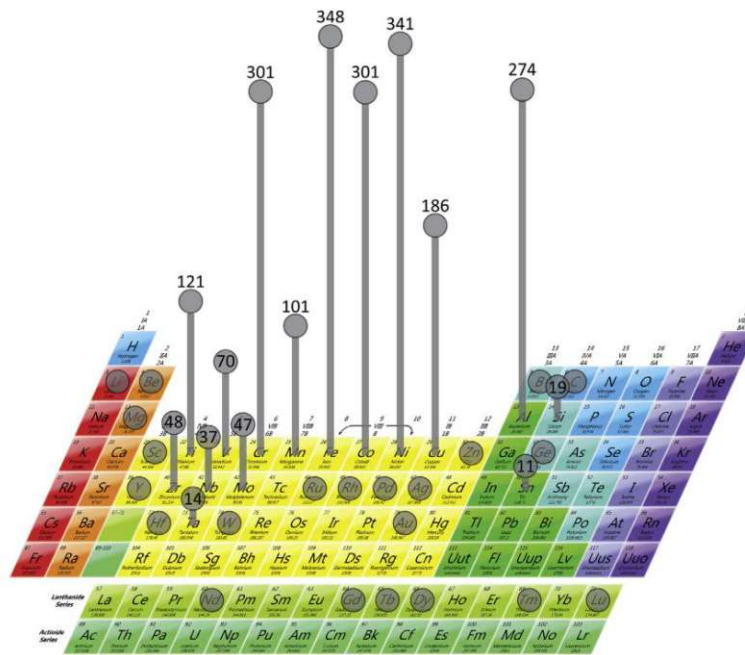
Figure 1.1.: Overview of the frequency of occurrences of various elements used in MPEAs [6]. A clear preference for using refractory metals can be observed.

A promising approach to producing light and at the same time, mechanically strong alloys are the so-called multiprincipal element alloys (MPEAs) or high entropy alloys (HEAs). In these, multiple elements (usually around five) in significant proportions of 5 at% to 35 at% of each alloying element are combined [7–9]. Closely related to the term high entropy alloys is the term solid solution. In a solid solution, the system exhibits a random arrangement of its constituents [10]. This maximum randomness coincides with the maximization of config-
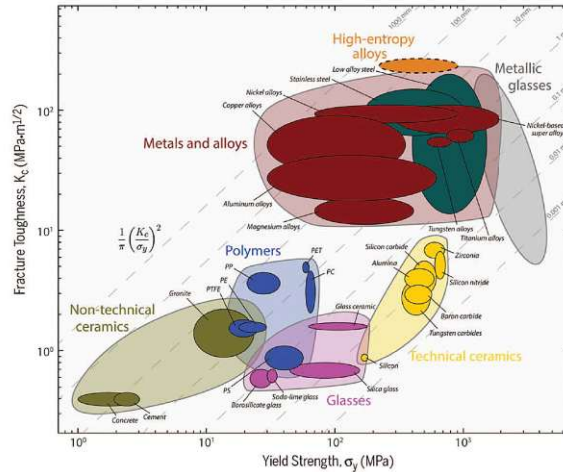
Figure 1.2.: The mechanical properties of fracture toughness and yield strength of different classes of materials [15].

urational entropy. Especially the solid solution character of this material class is associated with interesting properties such as increased mechanical toughness, hardness, or compressive yield strength [7, 8, 11]. The first HEAs were developed for high-temperature refractory applications to replace superalloys and therefore have relatively high densities in the range of 10 g/cm^{-3} [5, 12–14]. The elements which were most frequently used to produce complex MPEAs can be taken from Fig. 1.1.

Studies on HEAs showed that the new alloying approach leads to interesting mechanical properties and outperforms conventional alloys, for example, in terms of toughness and strength [15]. A comparison with various other technologically relevant material classes is shown in Fig. 1.2. The increasing interest in this class of alloys is also reflected in the number of published papers indicated in Fig. 1.3.
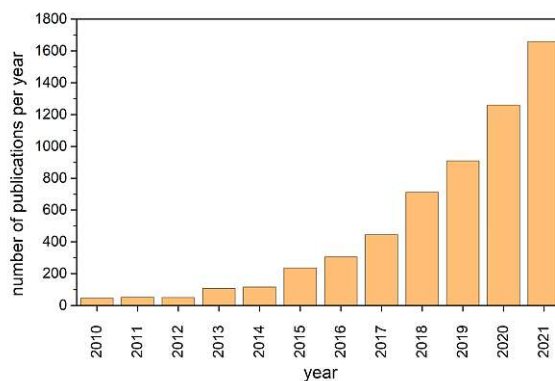
Figure 1.3.: The number of publications on the subject of HEAs from 2010 to 2021 reflects the increasing interest in this type of alloys. The data for this graph was retrieved by a keyword search for "high entropy alloys" in the material science section on *Scopus.com* [16].

In addition to the described potentials of this new alloy development, the combination of many different components brings systematic challenges. While phase diagrams and thus structural and crystallographic properties are available and accessible for binary and partially ternary compounds, they are difficult to obtain for alloys of more than 3 elements. In these cases, theoretical modeling as well as postulated semi-empirical correlations and criteria must be employed, including for instance, parameters as the valence electron concentration and the atomic size difference [11, 17–19, 19–22]. In some cases these 'rules' and parameter sets were able to show good agreement when compared with experimentally detected HEAs, but often reach their limitations. Especially in the context of light metals, no generally valid model has been found to date. One approach for the prediction of equilibrium states of multicomponent alloys is semi-empirical calculations of phase diagrams (CALPHAD). In this approach, the Gibbs free energy of multicomponent systems is calculated using reported data sets of the binary and ternary subsystems [23, 24]. However, only more sophisticated computational approaches are expected to provide a solution. Among those applied are density functional theory DFT [25, 26], which however is not directly applicable for ab-initio alloy prediction and design due to the immense number of degrees of freedom and associated exploding computation times. In order to develop model calculations and rapid computer-assisted procedures that can predict potential alloys, databases and derived training data for simulations are necessary.

In this work and the related project, a combined approach between experimental alloy production and theoretical simulations was chosen. Databases linking compositions and material properties in multidimensional alloy systems are valuable sources of information for complex relationships and correlations. In addition, they serve as an important basis for the testing and further development of existing models and new approaches in state-of-the-art materials development.

2. Theory

In this section, the theory of the alloy concept on which this work is based, is explained in detail. First, the difference between MPEAs and conventional classical alloys is discussed, followed by an overview of previous research results from literature.

2.1. Alloys

Since the beginning of the use of metals as tools and weapons, people have tried to optimize materials by the way they are processed or by their composition [27]. The historical term "Bronze Age" already implies that combining different metals was a long-established and proven concept of materials research for thousands of years [28]. In metallurgy, mixtures of different metals play a dominant role, and the "art" of alloying is one of the cornerstones of metals research and industry and is constantly growing in importance [28]. Traditionally, alloys are created according to the "base element" concept. In this approach, the main element is usually mixed with small amounts of other materials to change the properties of the alloy [29].

Initial work on the investigation of the dissolution behavior of metals and the formation of solid solutions by Hume-Rothery led to rules which are still considered and used to date in the development of alloys. The following criteria, generally referred to as Hume-Rothery rules, were established for the formation of substitutional solid solutions: [30–32]

- The atomic radii of the solvent and the solute must not be more than 15 % apart:

$$\delta r = \frac{r_{solute} - r_{solvent}}{r_{solvent}} \cdot 100\% \leq 15\% \tag{2.1}$$

  A stricter restriction applies to complete solubility, where the difference must not be more than 8 %. [33, p. 67]

- To promote solubility, the crystal structures of the two elements must be similar or the same.

- For complete solubility, solvent and solute must have the same valency [34, p. 139 - 140]. For metals, it applies that one metal is more likely to dissolve another metal with a higher valency [34, p. 139 - 140] [35].

- The electronegativity of the atomic species involved should be similar [36, p. 398]. This may suppress the formation of intermetallic phases.
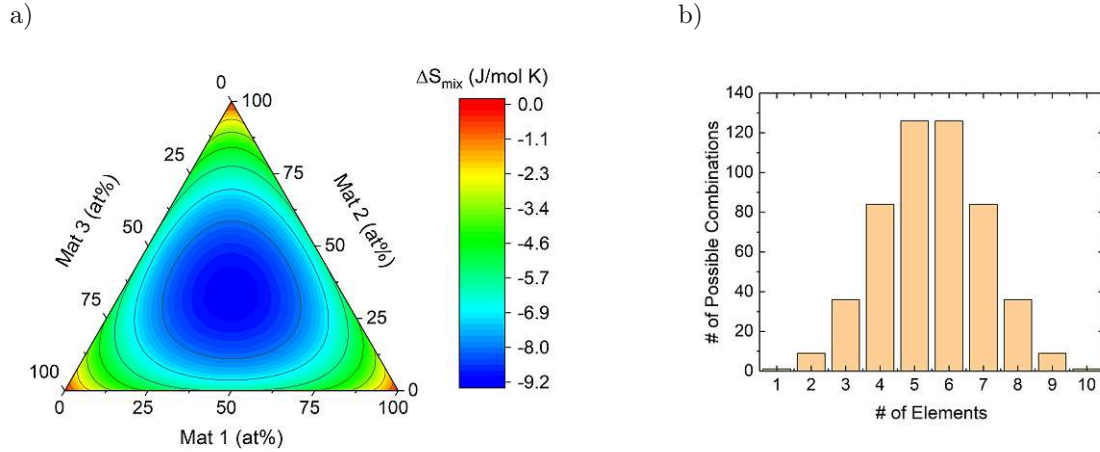
a)

b)

Figure 2.1.: a) The configurational entropy ΔS_{mix} for a ternary system shows an increase when moving away from the corners (pure materials). The maximum of ΔS_{mix} is given for an equimolar composition.   b) Number of possible combinations at concentrations $\Delta c_i = x \cdot 10 \{x \in \mathbb{N}_{>0} : x < n\}$ depending on the number of components n. The restriction that each element had to be represented by at least 10 at% led to the symmetrical form of the distribution.

A different method is used in the development of high entropy alloys (HEAs) or multi principal element alloys (MPEAs). In contrast to the alloying approach mentioned above, many (3 and more) metals are mixed in approximately equal quantities. In terms of phase diagrams, this corresponds to a shift from the corners of the phase diagram towards the center (blue area in Figure 2.1 a)). This modification in the conceptual approach results in a huge phase space being available. Based on a Δc of 10 at%, there are, for example, already 126 possible combinations considering a system of 5 elements. This is shown conceptually in Figure 2.1 b).

2.1.1. Theory of High Entropy Alloys

After several preliminary studies and introductions of novel alloying concepts focusing on the expansion of the number of components [28, 37], the first results of investigations on MPEAs were published in 2004 [38]. These focused on the exploration of the central region of multicomponent phase spaces. This region exhibits the biggest configurational entropy as can be seen from Figure 2.1 a). Shortly after, high entropy alloys were mentioned by name and became the subject of excessive research [7, 39–42]. The first papers defined HEAs as alloys containing 5 or more principal elements in equimolar proportions [7]. This definition was followed by extensions, e.g., the proportion of each individual principal element was extended from 5 at% to 35 at% or the addition of minor elements was included [8, 42]. A second accepted definition directly considers the entropy. Alloys with a configuration entropy $> 1.61\,R$ (R denotes the universal gas constant) are classified as HEAs. The entropy can be estimated using the Boltzmann equation [29, 43]:

$$\Delta S_{mix} = -R \sum_{i=1}^{n} c_i \ln c_i. \tag{2.2}$$

Here, R denotes the universal gas constant and c_i the atomic fractions of the elements involved. A problem with this definition is the non-trivial entity of the entropy. Firstly, the configurational entropy is only a part of the total mixing entropy of a system. However, it is used because it is dominant over other contributions such as vibrations, magnetic dipole and electronic randomness. [7]. Entropy is temperature dependent and can therefore vary greatly depending on the equilibrium temperature considered. To remove this ambiguity, it was assumed that alloys can be considered as liquid solution states, with thermal energies sufficient to ensure the occupation of random lattice positions by different elements [8]. However, this approximation was shown to have limited arguability, as even binary metallic liquids were shown to be non-ideal solutions with random atomic ordering [44].

In general, 4 main effects are dominant when considering HEAs due to the use of a large number of different elements [8]:

2.1.1.1. High Entropy Effect

The probably most prominent and therefore also name-giving effect is the high entropy effect which is suspected to promote the formation of solid solutions and to increase strength and ductility due to solution hardening by simplifying microstructures [33, p. 53].

To determine the entropy of a system the configuration entropy S_{mix} is mainly used, since it dominates over other entropy terms (e.g. vibrational, electronic or magnetic entropy) [29, 43, 45].

Which phases form in a system and remain stable is determined by the change of the Gibb's free energy. This thermodynamic quantity is given by

$$\Delta G_{mix/IM} = \Delta H_{mix/IM} - T\Delta S_{mix/IM}, \tag{2.3}$$

with ΔG for the change of the Gibb's free energy, ΔH the enthalpy, ΔS the entropy of the system, and T representing the temperature. The subscript $_{mix/IM}$ indicates if a mixing configuration (comparable to a solid solution (SS) state) or intermetallic phases are considered. Several approaches for predicting phase formation and development of HEAs have been established and studied. Initially, the formation of SS phases in HEAs was explained purely by the mixing entropy of the system and its elements [7]. The mixing entropy (also called configurational entropy) depending on the number of different elements is calculated according to eq. (2.2). In a simple approach, S_{mix} is compared in HEAs with the fusion entropy of pure metals [6, 7, 29] or the formation enthalpy of intermetallic phases [6, 7, 23].

However, investigations by Otto *et al.* showed that the approach with the exclusive consideration of the configurational entropy cannot sufficiently explain the formation of SS or IM phases [46]. This was shown by successively replacing Co, Cr, Fe or Ni with Ti, Mo, V and Cu

in the single-phase solid solution system CoCrFeMnNi. In a first approximation, the configurational entropy should remain unchanged by this exchange and thus, no change in the phase formation should occur. It has been shown that this assumption could not be confirmed, and thus, in addition to the configuration entropy, further factors contribute significantly to the formation of HEAs. The exclusive dependence between the formation of a single phase SS and the configurational entropy has then been contradicted by a large number of studies, see Figure 2.4 a). Here it can be seen that for small values as well as for large values of ΔS_{mix} single-phase SS, multiphase and amorphous systems were found [47]. This implies that the value of ΔS_{mix} is not the sole parameter to predict the formation of a SS HEA. In particular, if light metals are part of the alloy, the high entropy effect might not be the driving factor as studies on, e.g., AlLiMgSnZn, showed [48]. However, for systems in which the effect of ΔH and the atomic size difference δr (compare eq. (2.4)) is negligible, ΔS_{mix} can dominate the formation of (single) phases [49]. Various research groups found that eq. (2.2) represents a high-temperature approximation, therefore, it is not directly usable for calculations at low temperatures [19, 21, 50].

In addition, the atomic sizes of the different elements affect the stability of disordered solid solution phases [29]. The different atomic radii induce distortions of the lattices and enter into the free energy of the system by additional strain energy. Atomic sizes have been shown to be leading factors in the formation of structures of intermetallic phases [51–54]. By combining elements of different dimensions, more efficient packing can be established, which can be seen, for instance, in the formation of special ordered structures. Examples of this are the $MgCu_2$, $MgZn_2$ and $MgNi_2$ Laves phases [29]. Furthermore, interstitial spaces can be filled by occupation with mainly small elements (e.g., C, N) [29]. Various atomic sizes can, therefore, decisively influence the formation and stability of intermediate phases [29].

2.1.1.2. Lattice Distortion

In addition to the thermodynamic effects caused by the combination of different elements (including effects of the atomic size difference), the varying atomic radii of the components affect the alloy in a more atomistic way. A solid solution can be seen as a superordinate matrix occupied by a multitude of subsystems and elements. The lattice of this matrix is distorted mainly by the different sizes of the atoms, but also by differences in the binding energies and crystal structures of the constituents [8, 29, 55, 56]. By combining large proportions of significantly different atoms, these distortions increase and are more pronounced than in conventional alloys [6, 29].

The lattice distortion is commonly estimated by the atomic size factor [11, 17, 57]:

$$\delta r = \sqrt{\sum_i c_i (1 - r_i/\bar{r})^2} \cdot 100\%. \tag{2.4}$$

Here, r_i denotes the atomic radii of the atoms present in the system, the average atomic radius

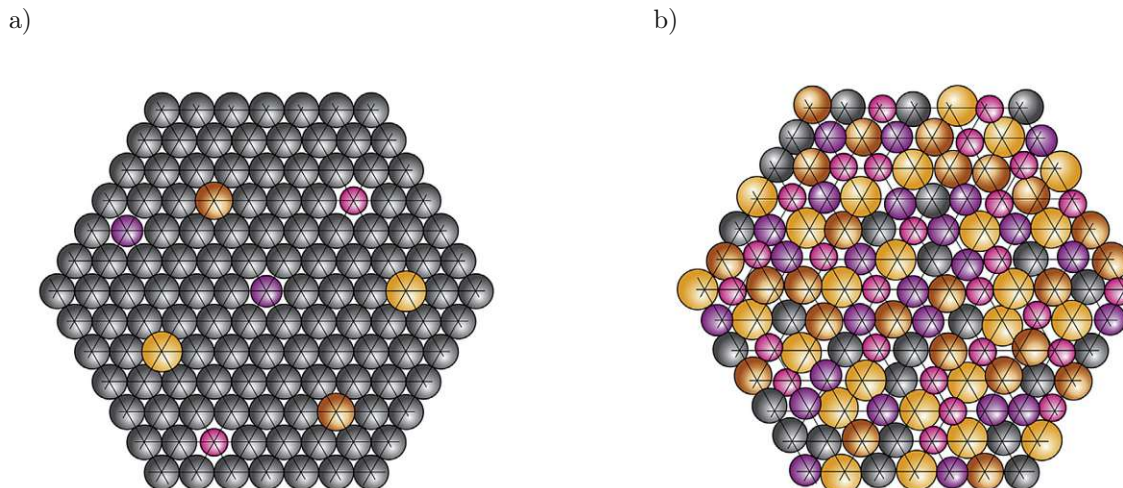a)   b)

Figure 2.2.: Atomic size effect on a) a dilute solution in which the atomic position is given
by the surrounding main material atoms and b) a mixture without dominant
species. Here, due to the deviation of the atomic positions, a contribution to an
excess configurational entropy is made [6].

$\bar{r}$ is calculated according to the expression $\bar{r} = \sum c_i r_i$, c_i again denotes the concentrations of the elements. The effect of the occupation of a variety of different elements on the atomic arrangement can be seen in Fig. 2.2. Lattice distortions, in addition to reducing electrical and thermal conduction due to larger scattering of free electrons and phonons [58], can also significantly increase hardness. For instance, hardness values three times higher than expected by a rule of mixing were found in MoNbTaW and MoNbTaVW alloys [59].

In addition, the uncertainty of the occupation of the individual lattice sites increases the excess entropy and will effect the value of the entropy (compare Fig. 2.3).

2.1.1.3. Sluggish Diffusion

Atomic diffusion determines the formation of phases. To reach an equilibrium state cooperative diffusion of elements is necessary [6, 8]. This contrasts with a limited number of vacancies [33, p. 59]. In HEAs, diffusion might be hindered, principally caused by lattice distortions and fluctuations in the bonding environment due to the presence of various elements [7, 42, 60]. This leads to higher recrystallization temperatures and activation energies, which can lead to the easier formation of amorphous structures [8]. This was demonstrated, among others, by Tsai *et al.* by measuring the diffusion coefficients in the Co-Cr-Fe-Mn-Ni HEA. It was shown that the degree of sluggish diffusion depends on the number of elements involved and increases with their number. [56] Recent studies on HEAs showed that sluggish diffusion occurs primarily in BCC structures and plays a minor role in FCC systems [10].

Sluggish diffusion has a great influence on the following processes and properties, which can be used advantageously: [61–68]

- easiness to get supersaturated states and fine precipitates

- increased recrystallization temperature

- slower grain growth

- reduced particle coarsening rate

- increased creep resistance

However, due to the difficulties in measuring diffusion in alloys and the intrinsic complexity of MPEAs and HEAs, the presence of sluggish diffusion is under critical debate, especially because there is a lack of dedicated studies on this topic [6, 69].

2.1.1.4. Cocktail Effect

The term "cocktail effect" is commonly used in the context of bulk metallic glasses, superelastic and superplastic metals [70] and HEAs [6]. This term refers to the occurrence of unexpected synergies in multimetal "cocktails" [28]. The cocktail effect is intended to illustrate that combining unconventional combinations of elements and microstructures can lead to unanticipated and nonlinear results [6].

Here, the properties are defined by the elements themselves, which can be determined by the mixture rule, but also by the interactions with each other [33, p. 63]. The cocktail effect is especially important in connection with HEAs, since a large number of major elements interact and thus influence the material properties [33, p. 63]. In order to predict properties of alloys in the design process and to choose the right elements and compositions, the effects of the cocktail effect must be considered [71].

2.1.2. Parameters for the Formation of High Entropy Alloys

A parameter relevant for the determination of HEAs has been found to be [42]:

$$\Delta H_{mix} = \sum_{i<j} 4H_{ij}c_i c_j. \tag{2.5}$$

In eq. (2.5), the enthalpy of the mixture is calculated by means of the binary enthalpies H_{ij} of the elements i and j. In Figure 2.4 b), it can be seen that the formation of single-phase SS is preferred for small values of δr and low mixing enthalpies. In brief, single-phase SS occur for values of δr in the range of $0\% < \delta r < 5\%$ and slightly negative to small positive values of ΔH_{mix} ($-15\ kJ/mol < \Delta H_{mix} < 5\ kJ/mol$) [11, 47, 57]. Theoretically, the mixing entropy depends not only on the chemical composition but also on the atomic size and packing density [11, 18, 19, 22]. To include these parameters in the calculation of the mixing entropy, Mansoori *et al.* [72] found a new expression for the overall
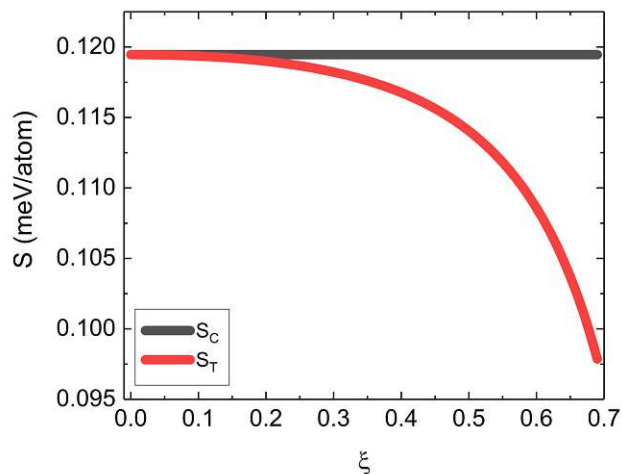
Figure 2.3.: Deviation of the configurational entropy when taking into account different atomic radii and variable packing densities for an equimolar AlCuMgZn system.

configurational entropy of mixing S_T.

$$S_T(c_i, r_i, \xi) = S_C(c_i) + S_E(c_i, r_i, \xi) \tag{2.6}$$

describes the modified configurational entropy for a sphere in a hard sphere system. Here, $S_C = -R \sum_{i=1}^{n} c_i \ln c_i$ is the configurational entropy of an ideal solution. This is equivalent to the expression in eq. (2.2). R describes the universal gas constant. The second term in eq. (2.6) S_E is defined as excessive entropy [18, 19, 72] and depends on the relative chemical composition c_i, the atomic radii r_i and the atomic packing fraction ξ. This excess entropy term has an influence on the composition at which a maximum of the configurational entropy occurs and potentially shifts it off the equimolar composition [47]. A detailed description of the calculation of S_T can be found in section A.5. The influence of different packing densities ξ on the configurational entropy can be seen in Figure 2.3 for the system AlCuMgZn.

Another quantity that is crucial in the formation of crystallographic phases is the valence electron concentration (VEC). According to the Hume-Rothery rule, the VEC can substantially influence the crystallinity of the SS in the absence of a strong atomic size effect [20]. For a system consisting of i components, the VEC results from [20]:

$$VEC = \sum_i c_i \, VEC_i \tag{2.7}$$

where VEC_i represents the VEC of the individual elements. It should be noted that the VEC differs from the average number of itinerant electrons per atom (e/a) as it includes the total number of electrons in the valence band, also the d-electrons [11, 73]. It was shown that HEAs with VEC > 8 exhibit FCC structures and BCC with a VEC < 6.87 [11, 20, 74].

A more sophisticated criterium for the theoretical prediction of potential single phase HEAs
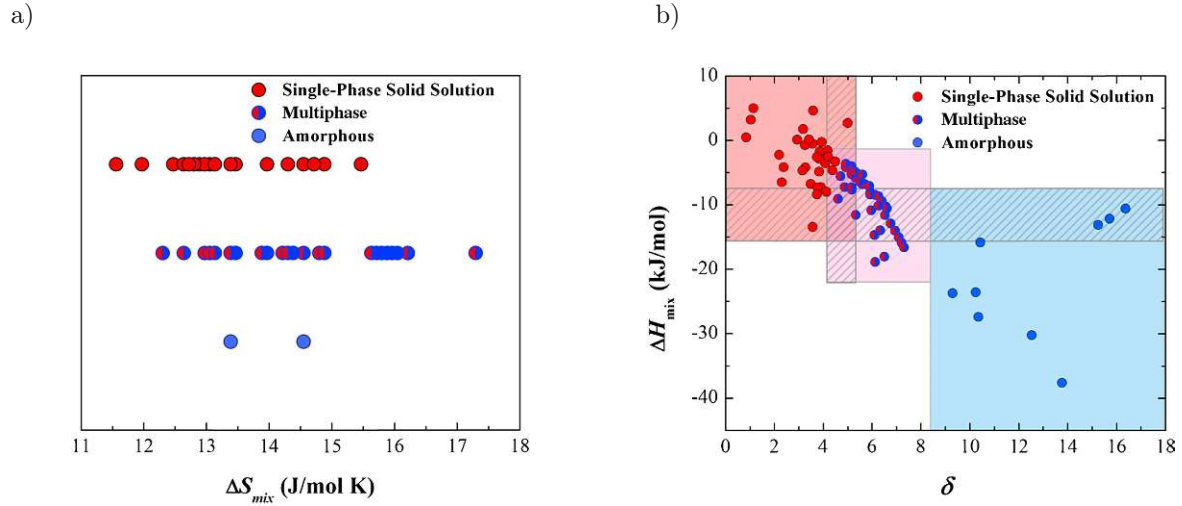
Figure 2.4.: Analysis of the dependency of a) ΔS_{mix} and b) correlation of δH_{mix} and δ_r on the formed phases [47].

has been developed by Senkov *et al.* [6]. A critical parameter κ_1^{crit} was defined, which compares the enthalpy ratios of all binary intermetallic and SS phases contained in a system with the energies of a theoretically perfect SS at a defined temperature [6]:

$$\kappa_1 = \frac{\Delta H_{total}^{IM}}{\Delta H_{total}^{Mix}} < -\frac{T\Delta S^{Mix}}{\Delta H_{total}^{Mix}}(1-\kappa_2) + 1 \equiv \kappa_1^{crit}(T) \tag{2.8}$$

In this equation, a linear dependence between ΔS_{IM} and ΔS_{Mix} ($\Delta S_{IM} = \kappa_2 \cdot \Delta S_{Mix}$) is assumed [75]. This parameter can be estimated by the site occupation and ranges from $0 \leq \kappa_2 \leq 1$ and increases as the order decreases [10, 75] It is often approximated by 0.6 [75]. The validity of this criterion was verified using experimentally found single solid solution and intermetallic phases. However, discrepancies were also observed, which put a critical view on the general validity of this prediction method. Simson *et al.* [76] modified the criterion found by Senkov *et al.* by requiring that the parameter κ_1 be $< \kappa_1^{crit}$ for any binary combination. Therefore, from equation (2.8), with the new constraints, it follows:

$$\kappa_1 = \frac{\Delta H_{ij}^{IM}}{\Delta H_{ij}^{Mix}} < -\frac{T\Delta S_{total}^{Mix}}{\Delta H_{total}^{Mix}}(1-\kappa_2) + 1 \equiv \kappa_1^{crit}(T) \quad \forall ij. \tag{2.9}$$

Troparevsky *et al.* [77] proposed a simple approach to make predictions for possible single phase systems by considering the binary enthalpies of formation comparable to the previously described criteria. A similar approach was adapted for the simulation approach presented in chapter 4.

Despite a large number of rules, criteria and parameters, there is still no generally applicable model for the reliable prediction of single phase HEAs. Therefore, experimental, theoretical

and combined studies are necessary to find regularities and to develop more reliable methods.

3. Experimental

A variety of fabrication methods of complex HEAs, especially in the field of low weight HEAs, has been presented in the literature. Besides the most commonly used approach of arc-melting [78, p. 176], casting, induction melting or mechanical alloying is often applied [79]. In addition, PVD techniques, especially the magnetron sputtering method, have been established for the fabrication and investigation of complex multicomponent systems. This method is particularly useful due to its simplicity of handling and universal applicability in combining different elements [78, p. 176].

In addition to the preparation of HEAs, the study of their properties and characterization represents a key role in the material-development. One of the most widely used analytical techniques is conventional XRD to determine the crystal structure. Furthermore, electron microscopy techniques such as scanning electron microscopy (SEM) and transmission electron microscopy (TEM) are among the standard methods for characterizing the microstructure of HEAs. Local chemical analysis by energy-dispersive X-ray spectroscopy (EDX) is essential in most studies due to the complex phases and microstructures involved. [80, p. 116]

In this section the methods of sample preparation and characterization used in this work are briefly discussed. In addition, the experimental components applied for the production and treatment of the investigated samples are presented.

3.1. Sputtering

Sputtering is a physical vapour deposition (PVD) technique in which coating particles are transferred from the solid starting material into the gas phase by means of physical interactions [81–83]. Since the first publication, which focused on thin film deposition using sputtering in 1852 [84, 85], this technique has evolved into an important tool for material design and synthesis in research and industrial applications [86]. In the following, primarily the principles of direct current (DC) sputtering are explained, but the basics can be applied to other variants.

Sputtering is a vacuum-based coating process, i.e., the process takes place in a high vacuum [87]. This is decisive for the purity of the produced samples. Unlike many other deposition methods, which are often based on thermal evaporation, sputtering is based on the momentum transfer of ions of a working gas onto the target material, which is the coating material at the same time. Therefore, the working gas is introduced into the high vacuum at the beginning of the process. This is usually argon to minimize chemical reactions with the
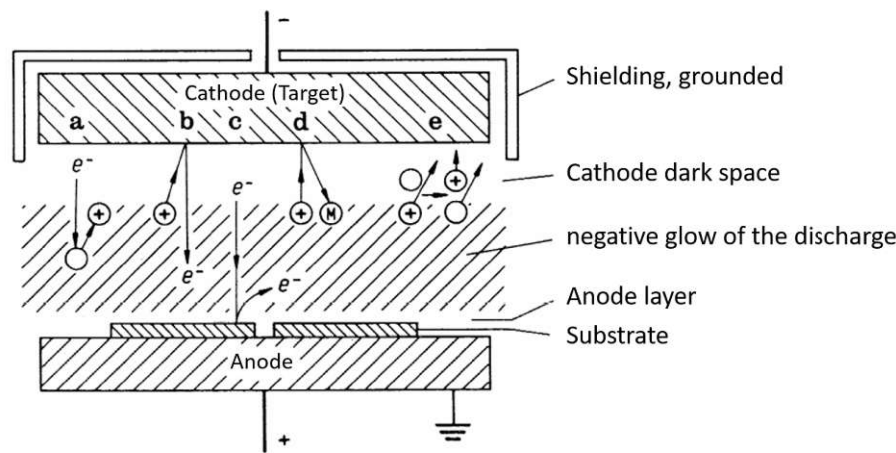
Figure 3.1.: Schematic representation of all phenomena occurring during the sputtering process (modified from [83, p. 95]):

    a   ionization

    b   electron emission from the target

    c   electron emission from the anode

    d   neutral particle emission from the target

    e   recharge

target and the substrate [88]. The partial pressure of the working gas during the deposition can go up to a few hundred mPa [89–91]. In order to start the process, a voltage of several hundred volts is applied between the target (which acts as cathode) and the anode, resulting in an acceleration of electrons in the direction of the latter [87]. This maintains an abnormal glow discharge, in which atoms of the working gas are ionized by collisions with electrons, which are accelerated towards the cathode (target) due to their now positive charge. On impact with the target, the momentum is reversed by collision cascades and atoms from the target are released. These atoms are subsequently emitted in all directions following a specific emission characteristic. A part condenses on the substrate and forms the desired layer. All important factors involved in sputter coating are schematically shown in Fig. 3.1.

3.1.1. Magnetron Sputtering

A modified form of DC sputtering is the so-called DC-magnetron sputtering. The difference to conventional sputtering lies in magnets mounted beneath the target. These magnets generate a magnetic field $\vec{B}$ transverse to the applied electric field $\vec{E}$. On a particle having the charge q, the Lorentz force

$$\vec{F} = q(\vec{E} + \vec{v} \times \vec{B}) \tag{3.1}$$

acts [83]. Charged particles are deflected perpendicular to the $\vec{E}$ and $\vec{B}$ fields, i.e., they are forced onto a cycloidal path [86, 92]. Since the electron mass is about three orders of magnitude smaller than the ion mass, this effect is particularly prevalent for electrons. After
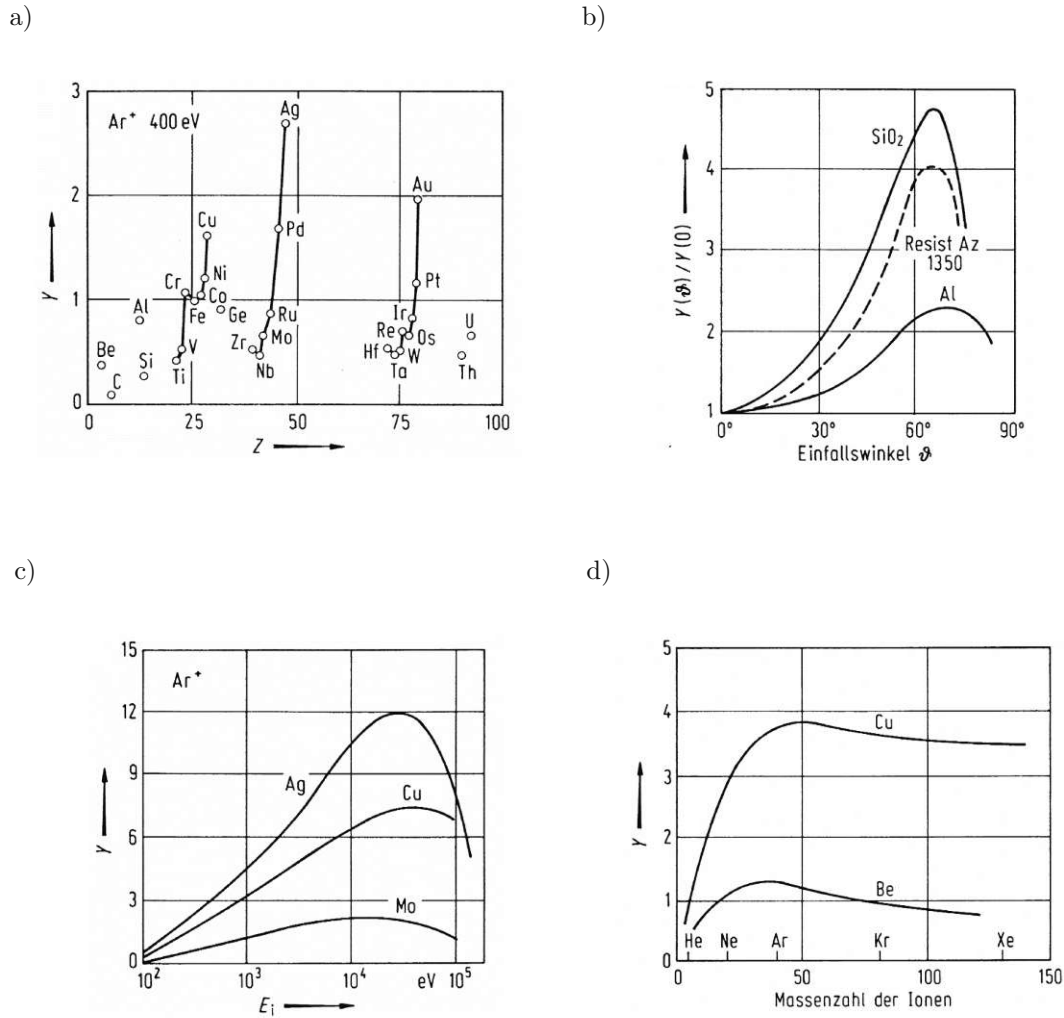
a)

b)

c)

d)

Figure 3.2.: Dependency of the sputtering yield on different parameters: a) target material, b) ion incidence angle, c) ion energy and d) ion mass [83, p. 97].

a collision of an electron with a working gas atom, a new circular orbit is started until the electron reaches the anode and is incorporated in the anode material. This "electron trap" caused by the magnets increases the duration of the electrons' stay close to the target, which leads to an increased probability of impact ionization. By these measures the working gas pressure can be reduced and the sputtering rate can be increased [93, p. 21]. This has effects on the purity as well as on the structure of the produced layer.

How easily and subsequently how many particles of the target are on average generated per incoming ion is given by the sputter yield Y [86, 88]. A detailed explanation and calculation can be found in the appendix (A.1). The sputter yield depends not only on the type of the target material and the impacting ions, but also on the ion mass, ion energy and the impact angle (see Fig. 3.2). The individual dependencies are briefly described qualitatively below: [88]

3.1.1.1. Target Material Dependency of Sputter Yield

How easily particles are emitted from the target naturally depends on the type of target material. In Fig. 3.2 a), the sputter yield is shown as a function of the atomic number of the target material. Here, a periodic course can be seen, which shows a repeating pattern following the constituents of the transition metals. This trend is inversely proportional to the sublimation enthalpy of the individual elements. [83, p. 96, p. 99]

3.1.1.2. Ion Incidence Angle Dependency of Sputter Yield

The dependence of the sputter yield on the angle of incidence of the working gas ions is shown in Fig. 3.2 b). The yield increases with increasing incident angle measured with respect to the target surface normal. This increase can be easily explained since the sputtering process is based on momentum reversal and the angle required for direction change and subsequent emission from the target becomes smaller with increasing incident angle. At larger angles ($> 70°$) the sputtering yield decreases abruptly, which is due to the reflection of the working gas ions without emitting target material. [83, p. 96]

3.1.1.3. Ion Energy Dependency of Sputter Yield

In Fig. 3.2 c), the dependence of the sputter yield on the energy of the incoming ions is shown for some target materials. An increase of the sputter yield with increasing ion energy can be observed. However, the yield decreases again at very high energies. This can be explained by the implantation of the impacting ions at high kinetic energies. In Fig. 4.1 a), calculated sputtering yields of selected materials at perpendicular incidence are shown as a function of ion energy following the approach of Matsunami *et al.* [94]. Besides the influence of the target material, the variation with increasing ion energy can be seen as well.

3.1.1.4. Ion Mass Dependency of Sputter Yield

The mass of the impacting ions (e.g., Ar) influences the sputter yield. Analogous to the consideration of the classical elastic collision, for a given ion energy in the order of a few 100 eV, a maximum of the yield results at a mass ratio of $M_{ion}/M_{target} \approx 1$. At higher ion energies, this optimal ratio shifts toward larger values. The variation of the sputtering yield for different ions is shown in Fig. 3.2 d). [83, p. 96]

3.1.1.5. Angular Distribution of Sputtered Particles

The particles emitted by momentum transfer have a non-homogeneous emission characteristic. In order to be able to predict the spatial distribution of the deposition particles, especially when using more complex geometries or multiple sources, the analysis of the emission is essential. The particles are preferably emitted perpendicular to the surface plane. In a simple

approximation, this emission characteristic is given by a cosine law [82] [83, p. 77]:

$$dm = \frac{m \; \cos \phi}{\pi} \; d\omega. \tag{3.2}$$

Here, dm describes the mass flux and ϕ the emission angle measured from the surface normal. The expression $d\omega$ describes the covered solid angle and can be substituted by a surface element A according to

$$d\omega = \frac{dA}{r^2} \cos \theta. \tag{3.3}$$

This depends on the angle of incidence θ on a small area at the distance r (compare Fig. 3.3). The rate distribution R is defined as the change in particles and associated mass increase per area element and can be calculated by substituting eq. (3.3) into eq. (3.2) to the form:

$$R = \frac{dm}{dA} = \frac{m}{\pi \; r^2} \cos \theta \cos \phi. \tag{3.4}$$

Using these relations, the number of incoming particles can be calculated for any arrangement of targets (emitters) and substrates (recipients).

In the special case of a small target and an extended plane substrate, eq. 3.4 can be simplified (compare the sketch in Fig. 3.3). By applying the relation

$$r^2 = \frac{a^2}{\cos^2 \phi} \tag{3.5}$$

follows, by substituting into eq. (3.4)

$$R = \frac{m}{\pi \; a^2 / \cos^2 \phi} \cos \phi \; \cos \theta = \frac{m}{\pi \; a^2} \cos^4 \phi. \tag{3.6}$$

In the last step, it was exploited that $\phi = \theta$ is valid. From eq. (3.6) it can be seen that the rate distribution and thus the coating rate follows a cosine law to the 4th power. The distribution of the emitted particles on the substrate as a function of the emission angle is shown in Fig. 3.3 b).
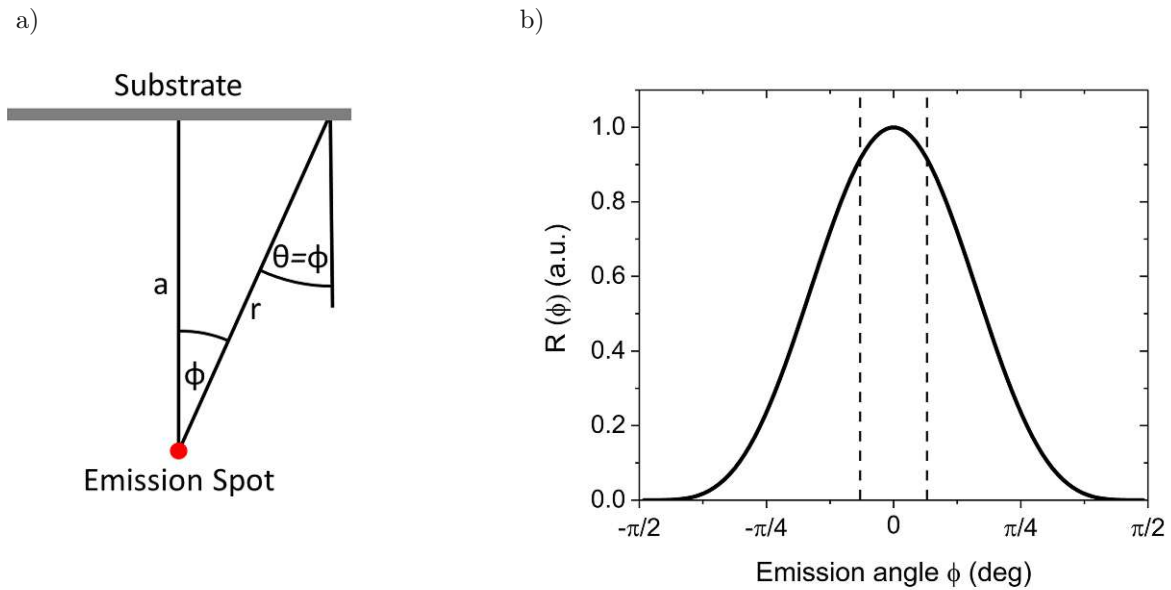
a)

Substrate

b)

Figure 3.3.: a) Sketch for calculation of a rate distribution on a planar substrate and b) distribution of the calculated mass flux. The two vertical lines show the region covered in the experiments.

3.2. Experimental Setup

In order to cover a wide compositional space, a deposition system was optimized for the chosen screening approach. Furthermore, a variety of analytical measurement methods suitable for characterizing the produced alloys was used. In the subsequent sections, the main theoretical principles of the components utilized are described before the setup for sample preparation is presented. This is followed by a description of the fundamental principles of the applied analytical characterization methods.

3.2.1. Vacuum Generation

The deposition of the samples must be carried out in a vacuum, as described in section 3.1. Important parameters in vacuum and coating technologies are the mean free path length and the coverage time. The mean free path length is defined as the length in which a moving particle can travel on average without collisions. This length is dependent on the size of the moving and colliding particles (d) and the number of particles in the unit volume (n) and assuming a model of hard spheres can be expressed by: [95, p. 54 - p. 56]

$$\lambda = \frac{1}{\sqrt{2}\pi d^2 n}.$$

(3.7)

Using the ideal gas law, the average number of particles can be substituted as a function of pressure and temperature:
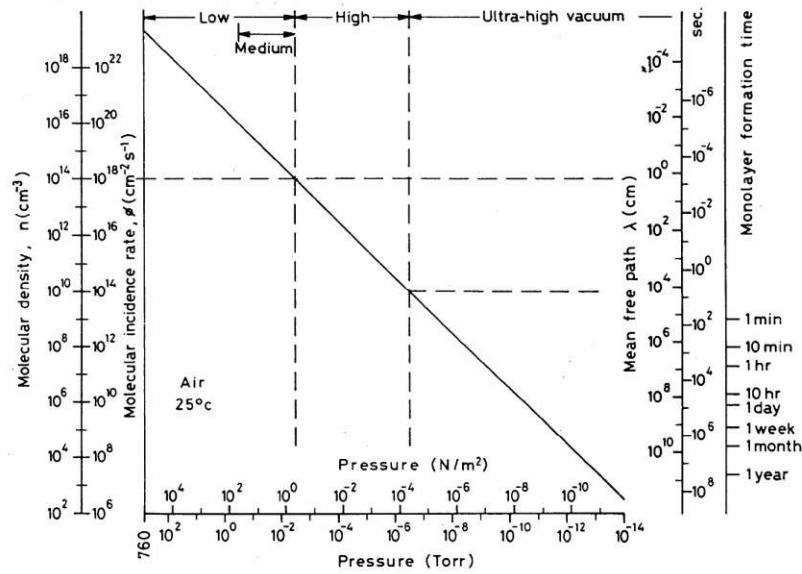
Figure 3.4.: Vacuum-specific quantities such as mean free path, monolayer formation time and molecular impact rate as a function of ambient pressure [96, p. 2].

$$\lambda = \frac{RT}{\sqrt{2}\pi d^2 N_A \, p}, \tag{3.8}$$

with T being the temperature, R the universal gas constant, N_A the Avogadro's number and p the pressure.

The degree of coverage is another important parameter that indicates the average time it takes for a monolayer to form. The higher the number of residual gas particles in a vacuum chamber, the faster a layer forms (compare Fig. 3.4). If materials with a high gas pressure accumulate on the chamber components, they can significantly affect the final pressure that can be achieved, and can also lead to contamination of the samples produced. In addition to sufficient pumping capacity, it is therefore essential to prevent the adsorption of volatile elements (e.g., Zn or Mg) as much as experimentally possible (compare section 3.3).

An overview of the different pressure regimes and characteristic vacuum parameters can be found in Table 3.1.

The ideal vacuum is defined as an "empty" volume, i.e., it has an absolute pressure of 0 Pa. However, this pressure cannot be achieved in a laboratory. Reasons for this are the following limitations [99, p. 47]:

- Outgassing of the chamber walls: Molecules adsorbed on the walls of the vacuum chamber and all objects contained within it are likely to degas. This increases as pressures become lower and the temperature rises.

- Leaks: In all seals, microscale defects (e.g. scratches) can lead to leaks.

- Processed materials: Similar to the outgassing of the chamber and chamber components,

Table 3.1.: Overview of the different pressure regimes used in vacuum technology [97] [98, p. 258] [95, p. 37]. The mean free path is calculated for Ar atoms and a temperature of 273 K, and the covering time corresponds to the time it takes to form one monolayer [96, p. 2] [95, p. 56 - p. 58].

Denomination	Pressure regime (Pa)	Mean free path (m)	Coverage time (s)
Rough vacuum	10^5 - 10^2	10^{-7} - 10^{-5}	10^{-8} - 10^{-5}
Medium vacuum	10^2 - 10^{-1}	10^{-5} - 10^{-1}	10^{-5} - 10^{-2}
High vacuum (HV)	10^{-1} - 10^{-6}	10^{-1} - 10^4	10^{-2} - 10^3
Ultra high vacuum (UHV)	10^{-6} - 10^{-9}	10^4 - 10^7	10^3 - 10^6
Extremely high vacuum (XHV)	$< 10^{-9}$	$> 10^7$	$> 10^6$

gas molecules desorb from the materials that are subsequently processed. This occurs particularly during the processing or in the event of heated materials.

- Virtual Leaks: Physically trapped gas in, for example, screw threads can only escape slowly into the chamber. Therefore, it appears as if the chamber is leaking, although the pressure-increasing gas originates from inside the chamber.

In vacuum technology, different pressure regimes are separated, which can be generated by pumps. These are (see also Tab. 3.1):

- Rough Vacuum: The rough vacuum can be achieved with simple positive displacement pumps. There are no major limiting requirements on the materials, e.g., normal steel can be used. This pressure range is characterized by viscous gas flow, in which collisions of the gas particles with each other are more likely than with the chamber wall. [97,100] The mean free path in this pressure regime is in the range of 10^{-7} m to 10^{-5} m.

- Medium Vacuum (or Process Vacuum): This regime can be obtained using positive displacement pumps, with more demanding material requirements, e.g., stainless steel must be used. This regime forms the transition region from viscous to molecular flow and is also referred to as the Knudsen flow regime [100]. At room temperature, the mean free path ranges from 10^{-5} m to 10^{-1} m.

- High Vacuum (HV): This pressure range can be achieved with elastomer seals in addition to elaborate materials such as stainless steel [97]. Special pumps suitable for the high vacuum range (e.g., turbomolecular pumps) must be used. In this range, molecular flow occurs in which there are virtually no collisions between the molecules [100,101]. The mean free path ranges from 10^{-1} m to 10^4 m.

- Ultra High Vacuum (UHV): In this region, special requirements are imposed on the material being used. In addition to UHV-suitable material (e.g., low-carbon stainless steel), metal gaskets as well as bake-out of the vacuum chamber are essential. [97] Mean free path lengths from 10^4 m to 10^7 m are typical in this pressure range.
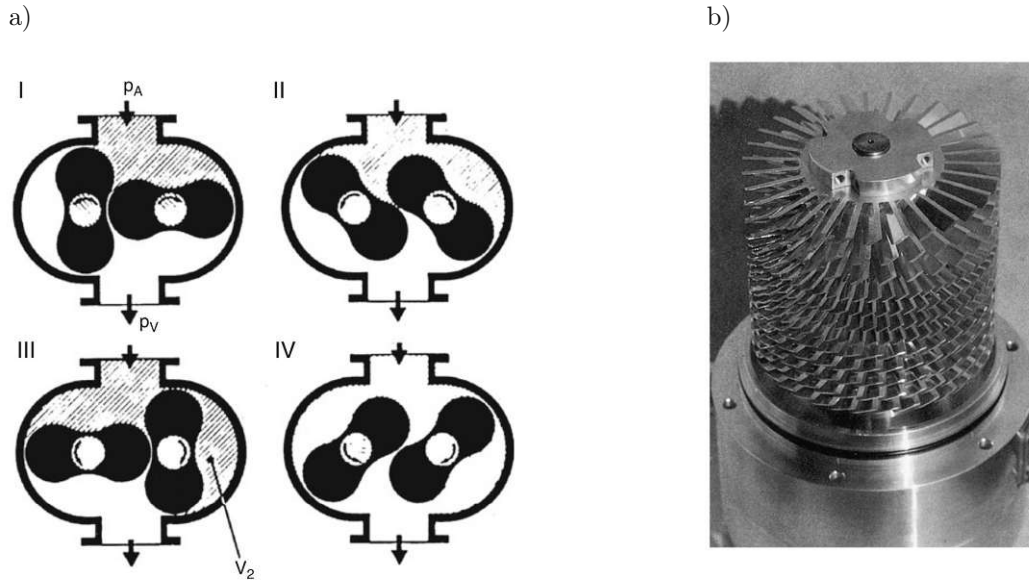
Figure 3.5.: a) Individual stages of a roots pump cycle. Steps I and II in the intake process, the volume is increased towards the recipient. In step III, the volume V_2 is confined and ejected from the pump volume in step IV. [95, p. 385] b) Image of the rotor blades system of a turbomolecular pump [102, p. 276].

- Extremely High Vacuum: In this pressure range, special materials such as vacuum-heated low-carbon stainless steel or titanium, metal gaskets, as well as special surface preparation processes and cleaning, and additional getter pumps must be used. [97] The mean free path length exceeds 10^7 m.

There are various methods and devices available depending on the selected pressure range, requirements for the final vacuum and internal process limitations:

3.2.1.1. Roots Pump

A roots pump consists of two eight-shaped pistons which rotate in opposite directions. The pistons do not touch each other during their movement and are separated by a gap of the order of 0.1 mm. The sequence of movements of one cycle is shown in Fig. 3.5. By counter-rotation in steps I and II, the volume is increased to the side of the volume to be pumped. With further rotation, a section of the pumped volume is closed off by the rotor (section III). This is subsequently ejected to the high pressure side by opening the outlet valve. Due to the geometry of the pistons, 2 such volume portions are created per full rotation, which can be pumped. The pistons have a dual design, thus 4 volumes of size V_2 can be pumped per cycle. High selected speed (e.g., 3000 rpm = 50 Hz) allows to achieve high pumping speeds, even with smaller pump designs. In addition, due to the non-contacting nature of the movements, no lubrication is required, allowing oil-free operation and thus eliminating contamination and enabling a lower final pressure. [95, p. 384 - 386]
A Pfeiffer Vacuum ACP 28 roots pump was used in this work.

3.2.1.2. Turbomolecular Pump

If pressures in the HV and UHV range are required, turbomolecular pumps can be used. The design of such a pump is shown in Fig. 3.5 b). Gas molecules enter the pump through the suction flange from the volume to be pumped and are compressed through several stages before being directed into the backing pump and discharged. In this process, backing pressures of up to 100 Pa can be generated. [95, p. 512 - 524] Due to the high rotational speeds ($\sim 24\,000$ rpm), high demands are placed on the rotor blades [99, p. 12]. These are shrunk onto the shaft, which is supported at both ends (e.g., via permanent magnet bearings) [95, p. 517 - 518]. The advantages of turbomolecular pumps are the simple assembly, the relatively maintenance-free operation and the lack of contamination with oil [99, p. 12] [98, p. 265 - 266].

A turbomolecular pump of the type *Edwards nEXT240* ensured a final pressure of $\approx 10^{-5}$ Pa in the chamber used for the depositions.

3.2.2. Pressure Measurement

Measuring the gas pressure in the vacuum chamber before and during a coating process is essential to provide reproducible results. In principle, two different measurement approaches are possible. At higher pressures ($p > 10^{-3}$ Pa), the force exerted by the pressure can be measured. At lower pressures, where this is no longer possible, the pressure is determined indirectly using pressure-dependent gas properties (e.g., heat conduction). [95, p. 655] [103, p. 81]

3.2.2.1. Membrane Vacuum Gauge

In membrane vacuum gauges, a membrane separates a low pressure reference from regions of higher pressures which have to be determined. Ideally, the reference part of the cell should hold an ideal vacuum (0 Pa). Due to the pressure difference between this reference pressure and the pressure to be measured, this membrane is deformed. The displacement can be detected, for example, by capacitive methods. This can be done up to pressures of a minimum of 1 mPa [95, p. 663 - 668]. A schematic illustration of the most important parts of a membrane vacuum gauge is depicted in Fig. 3.6.

3.2.2.2. Heat Conduction Vacuum Gauge

The pressure dependence of the heat conduction of a gas can be used to measure the pressure in the range of fine and rough vacua. The principle of measurement is based on the work of Pirani [104], which is why this type of measuring cell is often called a Pirani cell. To measure pressure, a heated wire acts as one resistor in a Wheatstone bridge [103, p. 88]. The wire is supplied with electrical energy, and is as well used to measure the dissipated power by resistance measurement. The power is dissipated both by heat conduction and, at pressures above 1 kPa, by convection. The amount of dissipated energy is determined by the number of
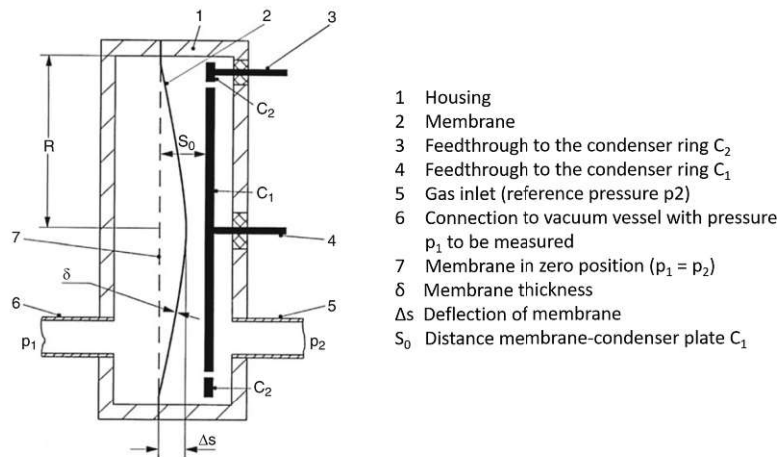
Figure 3.6.: Schematic overview of a membrane vacuum gauge [95, p. 669].

gas particles in the gauge volume. Interfering factors, such as heat conduction at the end of the wire and thermal radiation, must be taken into account in the measurement [95, p. 687 - 688]. In addition, oxidation and contamination of the measuring wire can lead to errors, so the cell must be cleaned regularly and calibrated to the gas present in the volume [95, p. 698] [105]. Heat conduction vacuum gauges usually operate at pressures as low as 0.1 Pa, special or certain types of such gauges are capable of measuring pressures down to 10^{-3} Pa [103, p. 89].

3.2.2.3. Ionization Gauges

When measuring pressures in the HV or UHV range, ionization vacuum gauges can be used. Ionization vacuum gauges measure an electrical quantity that depends on the particle number density, for example, the gas discharge current or ion current [95, p. 705]. The generation of this electrical quantity is based on electron impact ionization [103, p. 94]. In a hot cathode gauge, electrons are generated from the cathode by means of glow emission and accelerated toward the anode. Collisions with residual gas particles ionize the particles and can be measured by the ion collector as an ion current [95, p. 705]. The number of positive ions formed is proportional to the number of gas molecules [95, p. 708]. In this process, the pressure is not determined, but only the number of gas particles in the volume to be measured. Only when the temperature is kept constant the pressure can be assumed to be proportional to the particle density. [103, p. 95]

A cold cathode gauge (also called Penning gauge) uses a high voltage of around 2 kV to ignite a glow discharge between the cathode and the anode [95, p. 708]. The gas discharge current is similar to the ion current in the case of the hot cathode gauge pressure-dependent and therefore determined to measure the pressure. To extend the working range towards lower values, a $\vec{B}$ field is superimposed on the $\vec{E}$ field, which increases the probability of electrons being located between the anode and the cathode. Due to the subsequently increased ion yield, the gas discharge can be maintained at lower pressures. Typically, pressures down to

10^{-6} Pa are measured. [95, p. 726]

In this work, a membrane vacuum gauge from *mks* of the type 627F was used to determine the pressure during the coating process, which was carried out at 0.8 Pa. In addition, a Penning/Pirani combination cell (*adixen ACC 2009*) was employed to detect the entire pressure range from atmospheric to a minimum pressure in the order of 10^{-5} Pa.

The experimental equipment for sample preparation consisted of two separate units: a sputtering chamber for the production of the samples and a post-processing chamber in which the samples were subjected to a heat treatment. Both units are described below in the following section.

3.3. Sputtering Chamber

The investigation of a large compositional space required the adaptation and optimization of a sputtering system for simultaneous coating of multiple elements. Since the targets were predominantly produced by melt-based synthesis methods and thus limitations in the possibility to combine different elements could potentially arise, two separate sources were used. This allowed greater freedom in the choice of elements to be combined in a target (elements that are difficult to be incorporated into a single target by melting can be divided among the targets), as well as allowing the systematic variation of only one component. Figure 3.7 a) shows a CAD drawing of the sputtering chamber. The basis of the unit consisted of a stainless steel chamber with a total volume of about 20 liters. Using a turbomolecular pump (*Edwards nEXT240*) pumped by a roots pump *Pfeiffer ACP 28*) a base pressure in the regime of 10^{-5} Pa could be achieved. Several pressure gauges tracked the pressure prior to deposition (Penning/Pirani gauge) or were used to monitor the pressure of the working gas during the sputter process (Baratron). The base pressure for all samples described in this work was chosen below $5 \cdot 10^{-4}$ Pa. During the sputtering process, the working pressure was 0.8 Pa. The material used for the coating was provided by two magnetron sources (*AJA international*, model: *ST20-UBQD*). These were arranged perpendicular to each other (see Figure 3.8 a)). Both sources could be displaced in the lateral plane, and thus, the distance to the substrate was variable. To minimize cross-contamination from one source to the other, a dividing wall was installed between the sputtering sources (compare Fig. 3.7 b)). For all experiments a normal distance of 7 cm between substrate and target surface was chosen. The substrate was freely rotatable, and hence the orientation of the substrate surface relative to the two sources and thereby the composition could be adjusted. The power required for the sputtering process was provided by two power supplies of the type *Advanced Energy MDX 500* with a maximum output of 650 W. By varying the individually applied powers, the chemical composition of the samples could be controlled in addition to the rotation. In the center of the chamber the substrate was mounted on a copper substrate holder. The substrate holder was designed to
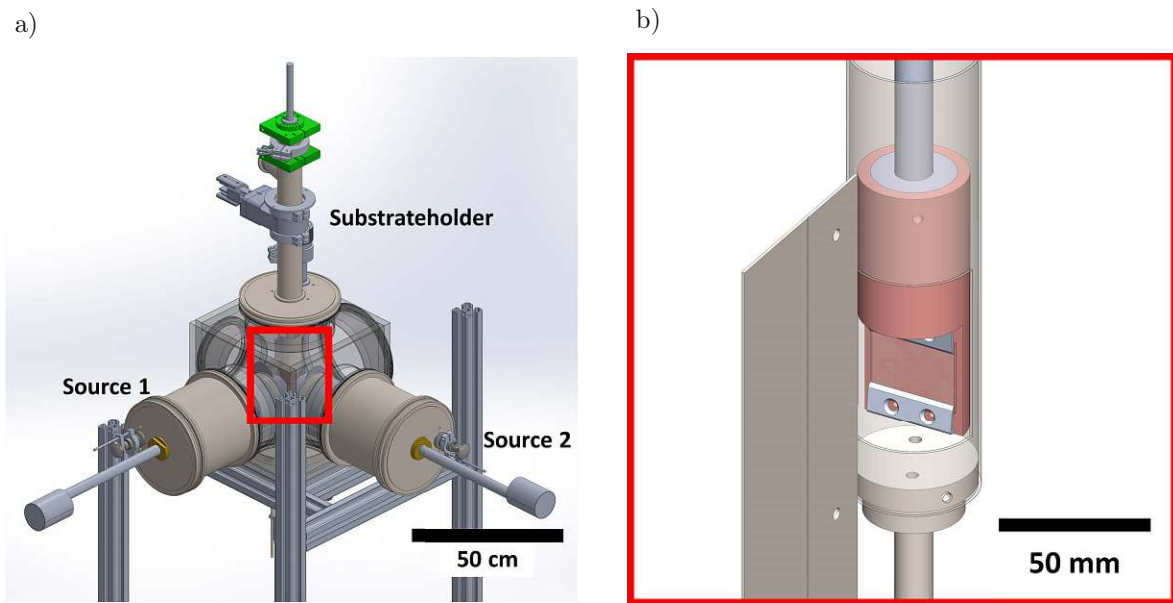
a)　　　　　　　　　　　　　　　　　　b)

Figure 3.7.: a) CAD drawing of the sputter deposition chamber. The ports for the 2 sources and the substrate holder system can be seen. b) A detailed view of the substrate holder and the rotary shutter. Furthermore, the barrier wall for the prevention of cross-contamination of the two sources is displayed.
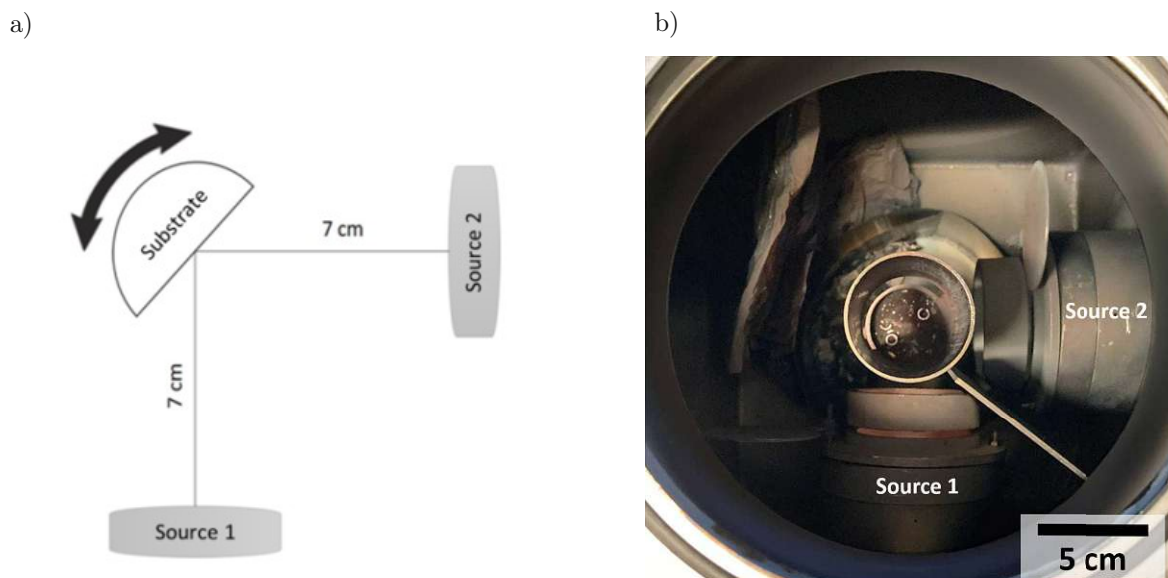
a)　　　　　　　　　　　　　　　　　　b)

Figure 3.8.: a) Schematic representation of the arrangement of the sputter sources relative to the rotatable substrate. b) Top view of the deposition chamber showing the rotary shutter, and the two sources. The substrate was mounted in the center.

a) b) c)
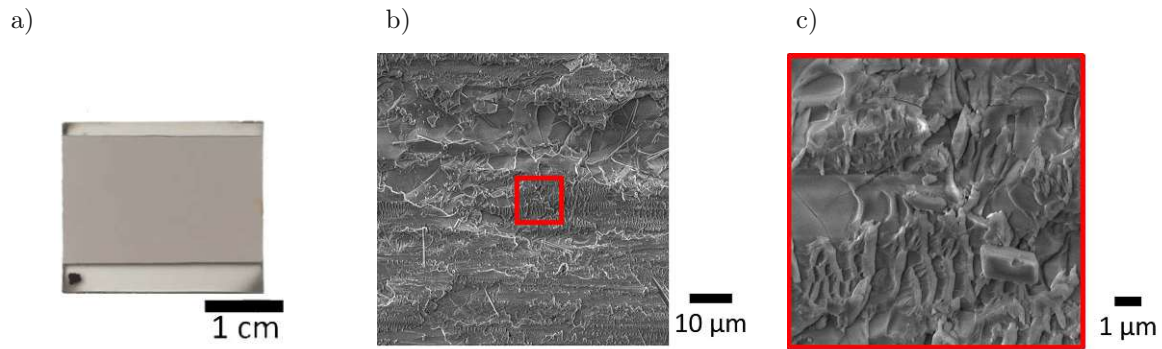
Figure 3.9.: a) Coated glass substrate. Uncoated areas are visible at the lower and upper edges, which were used to measure the layer thickness using a profilometer. Panels b) and c) show electron micrographs of the uncoated glass surface. The textures of the roughened glass substrate are clearly visible.

hold a glass substrate having dimensions of 25 mm x 25 mm and a thickness of approx. 1 mm. The substrates were prepared from glass microscopy slides with roughened and smooth areas (Roth H686.1, soda-lime-silica glass) cut out into the correct size. A picture of the substrate employed after deposition as well as electron micrographs of the rough surface texture are shown in Fig. 3.9. The roughened texture ensured increased coating adhesion and was used to characterise the properties of samples that showed the coating peeling off on the smooth areas.

Inside the copper block of the substrate holder a thermocouple (type K) and heat cartridge combination (*Heinz Stegmeier*, type *HS 10 315 W*) was installed to monitor the temperature during the deposition process using a *Eurotherm 3216* controller. The substrate surface temperature varied depending on the coating time and ranged from 80 °C to 110 °C after the coating process was completed. To ensure a precise exposure time of the substrate to the sputter sources, two barriers were positioned in between the targets and the substrate. Two separate shutters were placed directly in front of the respective source, and a tubular shutter initiated and stopped the coating process by exposing the substrate. A detailed illustration of the substrate holder system is shown in Fig. 3.7 b). In particular, the processing of elements that are problematic for vacuum applications, such as Zn and Mg, required the adaptation of the vacuum chamber [106, p. 346]. The vacuum chamber was lined with aluminum foils to prevent long-term contamination and accumulation of problematic substances. In addition, special tubular shutters were mounted on the sputter sources, which limited the flow of the coating particles to a directed coating beam. Moreover, a cylindrical shutter around the substrate and the installed separation wall between the sputter sources significantly reduced the exposure of chamber parts and components that are difficult to replace, as well as cross-contamination. The measures described can be seen in Fig. 3.8 b) and Fig. 3.7 b) in detail.

The production of the samples always followed the same procedure. After the base pressure of less than $5 \cdot 10^{-4}$ Pa was reached, the pump power was reduced by about 70 % by closing

the corner valve which connects the chamber to the turbomolecular pump by 4 turns. The Ar pressure was set to 0.8 Pa using a manual needle valve. Stabilizing the plasma and conditioning of the sources at a set power on both targets was done with all shutters closed and the substrate facing away from the targets. After a run-in time of about 5 minutes, the substrate was set to the correct angular position and the shutters in front of the targets were opened. With the opening of the tubular shutter, the coating process started. This was controlled using a stopwatch and carried out until the time determined by rate determinations was reached. Closing the round shutter ended the coating process and the sample could be removed through the airlock.

3.4. Annealing Chamber

Annealing the metallic materials after sputter deposition is of considerable importance. Sputtering is a highly non-equilibrium process that leads to energetically unstable or metastable phase characteristics. Since the investigated alloys should be potentially used for industrial applications, it is essential to achieve a state of equilibrium. To realize this, 2 things are necessary: Time and energy. The energy was thermally added to the sample over a period of 24 hours. The entire chamber as well as a detailed representation of the sample holder is shown in Figure 3.10. The central part of the annealing chamber was a copper sample holder which provided space for up to 4 samples. The identical combination of thermocouple and heating cartridge (*Heinz Stegmeier*, type *HS 10, 315 W*) as in the substrate holder during the sputter deposition was mounted in the Cu block of the sample holder and provided the required heat. In order to ensure a precisely defined temperature on the sample surface, the sensor was calibrated. The calibration curve for a 1 mm glass substrate is shown in appendix A.7. The chamber could be evacuated and a final pressure of about 10^{-4} Pa could be achieved. Also, atmospheric pressure with any inert gas to prevent oxidation during the annealing process could be realized.
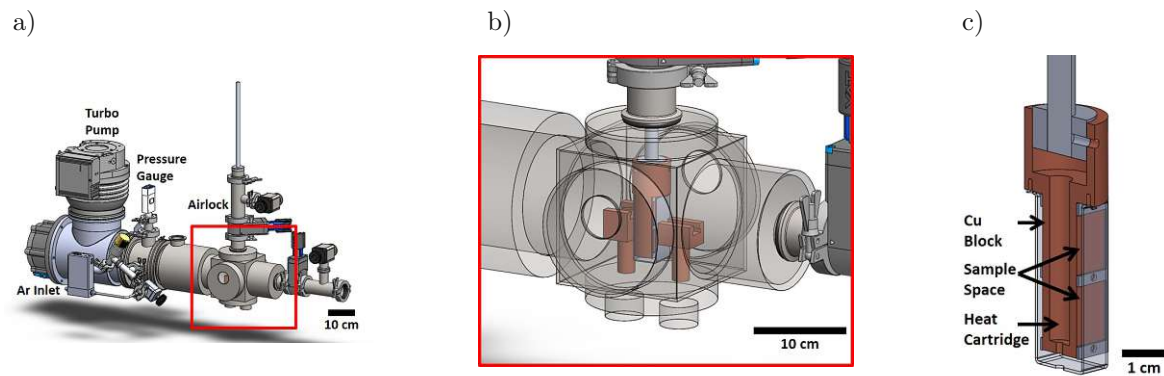
Figure 3.10.: Construction drawings of the heat treatment chamber.   a) Overview with all important parts of the annealing chamber (compare [107]).   b) Detailed view on the process chamber in which the annealing was performed and the c) sampleholder layout for the heat treatment of the prepared samples

3.5. Electron Microscopy

The main tools for the analysis and characterization of the produced alloys were based on electron microscopy.

A detailed description of the operation principle and setup of an electron microscope can be found in the dedicated literature [108–110]. In the following, the main steps and detectors for imaging and analyzing samples using electrons are briefly described: The schematic structure of an electron microscope and the essential components can be seen in Fig. 3.11. Initially, free electrons have to be generated. This can be done, for example, by emission from a filament and subsequent acceleration by means of applied voltage or field emission by applying a strong electric field [109, p. 66-70]. Subsequently, the electrons are focused by a system of magnetic lenses.

3.5.1. Scanning Electron Microscopy

A special form of electron microscopy is scanning electron microscopy, in which the electron beam is scanned over the sample. Therefore, the focused electron beam is deflected by means of a deflection coil system and directed over the sample in a raster pattern (see Fig. 3.11 a)). This allows a precisely defined area of the sample to be scanned. If the deflections are chosen smaller while the image size remains the same, any magnification can be achieved [108].

When the electron beam hits the sample surface, it interacts with the atoms of the sample by elastic and inelastic scattering. Thereby the interaction is not limited to a single event, but many occur. This leads to a gradual energy loss of the electrons, which results in a finite penetration depth of the electrons. The penetration depth depends primarily on the energy of the electrons and the sample material. Following this consideration, an interaction depth or information depth of 10 nm to 10 μm results [108]. A schematic illustration of the information

a)   b)
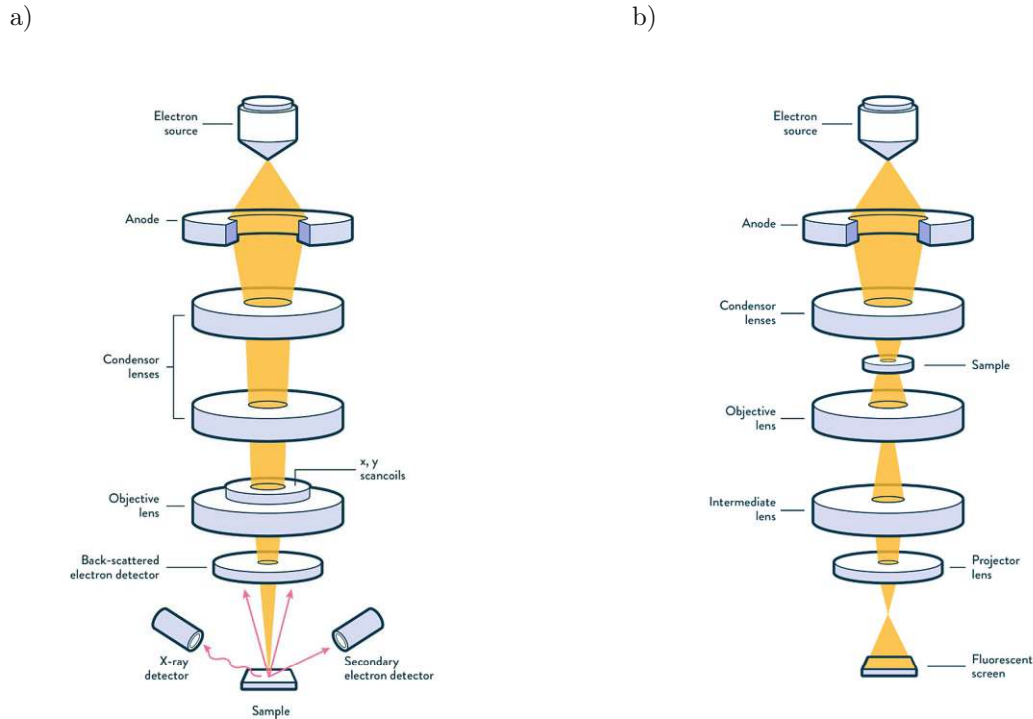
Figure 3.11.: Schematic representation of a) a scanning electron microscope (SEM) and b) a scanning transmission electron microscope (TEM) [111]

depth of different imaging methods is given in Fig. 3.12.

The analytical procedures and detection methods used for the analysis are briefly described below.

3.5.1.1. Secondary Electron Microscopy

In order to obtain information on the structure of the samples' surface and potential effects of different compositions on both texture and topography, images were taken using a secondary electron detector. Electrons must be used since the resolving power of optical microscopes is not sufficient for imaging small structures. This is imposed by the so-called Abbe limit and amounts to approx. 0.2 μm [112, p.252]. The mostly used imaging technique uses secondary electrons. These are emitted from the sample atoms after the interaction of the primary electron beam. An Everhart-Thornley detector is most commonly used for detection. The detector consists of a positively biased collector grid, which accelerates the emitted secondary electrons to a subsequent scintillator [108]. There, the signal is enhanced by means of a photomultiplier and recorded. By recording the intensity of the detected electrons and the primary beam position, spatially resolved information can thus be obtained. Secondary electrons are primarily used to visualize surface structures and topographies. However, since the secondary electron yield increases monotonically with the elementary atomic number, a material contrast can also be observed. Light atoms (i.e., low atomic number) appear darker due to the

a)   b)
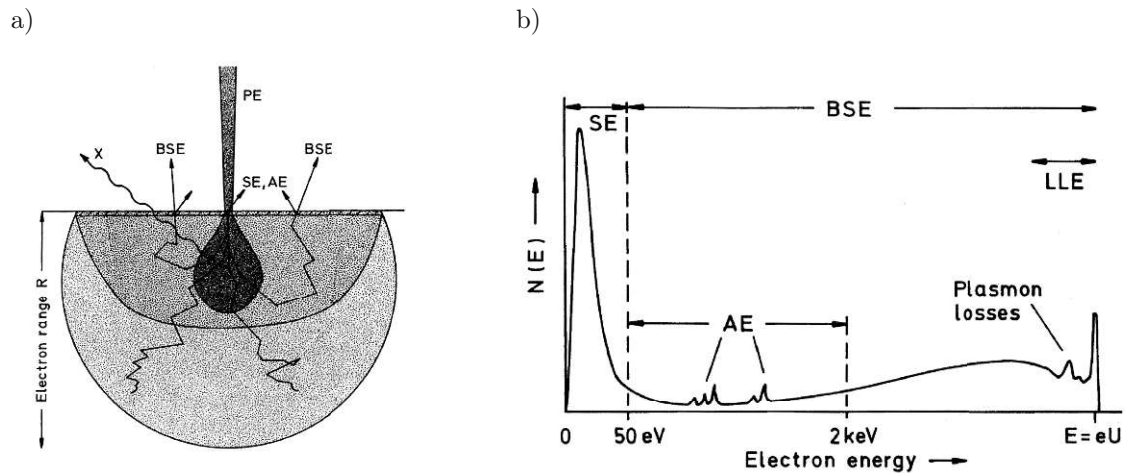
Figure 3.12.: (a) Schematic illustration of the information depth of electrons used for imaging in a scanning electron microscope and (b) energy ranges of the detected electrons (taken from [108, p. 5]).

lower secondary electron yield [108]. For investigations of material separations, however, the analysis of backscattered electrons is more suitable.

3.5.1.2. Backscattered Electron Microscopy

In order to obtain not only an impression of the topography but also information on the distribution of the individual elements present in the samples, backscattered electrons (BSE) can be detected. These are primary electrons scattered by the sample's atoms, which in contrast to secondary electrons have higher energies (compare Fig. 3.12 b)). BSE move in a straight line from the sample and must therefore be detected at a large solid angle of collection. Therefore, the detector is mounted directly under the pole shoe of the primary electron beam and the working distance is chosen small to maximize the covered take-off angle. The recorded intensity depends mainly on the mean atomic number of the region of interest; heavy elements appear lighter, light elements darker. By studying the material contrast, the mean atomic number of a region and, therefore, especially mixing and segregation can be analyzed. [113] This behaviour can be seen, for example, in the case of Al segregation, see section 6.1.3.

3.5.1.3. Energy-Dispersive Spectroscopy

Using energy-dispersive spectroscopy (EDS), surface-sensitive analysis of the chemical composition can be carried out. In most cases, the emitted X-rays are measured using energy dispersive spectrometers. These are especially suitable for simultaneous recording of the entire X-ray spectrum, which leads to fast measurement results. The underlying principle is X-ray fluorescence. First, electrons are used to 'knock out' inner shell electrons of the examined atoms. The atom is excited and offers an unoccupied space in an inner electron shell. This state is not stable and an electron of an outer shell fills it while emitting a characteristic

energy quantum in the form of X-rays. The energy of the X-ray quant can be calculated using

$$h\nu = E_2 - E_1, \tag{3.9}$$

where E_1 and E_2 are the energies of the free inner shell and the outer shell electron respectively. The energy distribution of the emitted X-rays is detected, and the relative compositions can be found by comparing the measured count rates. The intensity of the detected radiation depends on the generally known parameters such as cross sections, as well as on the number of transitions and, therefore, the number of probed atoms [113]. In addition, several material-specific parameters must be considered for correct quantification. These are primarily dependent on atomic number (Z), which affects backscattering and stopping power, X-ray absorption (A) and X-ray fluorescence (F). These ZAF corrections are taken into account in quantitative elemental microanalysis to calculate the chemical composition [108].

3.5.2. Transmission Electron Microscopy

Transmission electron microscopic (TEM) methods can be used to investigate the structure of solids in greater detail. This method differs from conventional scanning electron microscopy in that, among other things, the sample is transmitted. Since electrons must pass completely through the sample, only thin samples can be characterized. The term thin, in the context of electron transparency, depends on the sample material and the electron beam energy and ranges between ≈ 100 nm and 1 μm [114, p. 11]. Preparation techniques involve, for instance, focused ion beam cutting or precision ion polishing systems to bring the samples into the right shape and thickness. To visualize the working principle of a TEM, a schematic representation of the main components and the setup design is given in Fig. 3.11 b). The prepared samples are illuminated by a high voltage electron beam (beam voltage of 60 keV to 200 keV) [115,116]. The electron beam generated in the electron source is shaped and focused by three condenser lenses and an objective prefield lense before hitting the sample [116, p. 34]. Electrons interact when passing through the sample by elastic and inelastic collisions [112, p. 281], before they are detected on a luminescent screen or by slow-scan CCD cameras [116, p. 37]. In addition to projection images of the transilluminated sample (bright field and dark field mode), electron diffraction images can be taken to locally determine the crystallinity of the sample [117].

Since the analyses using TEM are long and complex due to the more sophisticated sample preparation and the locally very limited examination area, only selected compositions were studied. These were identified and chosen by the other analytical methods presented here.

3.6. X-Ray Diffraction

Besides the topographical and chemical properties of the samples, the crystal structure is another key parameter to be studied. X-Ray Diffraction (XRD) was used to study the crys-

tallography of the prepared samples. The theory behind X-ray diffraction is based on the interaction of X-rays with the atoms in the sample. The X-ray radiation entering under an angle δ is diffracted at the lattice planes. If the path difference of different diffracted X-rays results in an integer multiple of the X-ray wavelength, the reflected beams constructively interfere with each other. This relationship can be seen from Figure 3.13 and the Bragg equation

$$2d = m\lambda = 2a \sin(\delta). \tag{3.10}$$

Here, $2d$ is the path difference between two beams, m is an integer number, λ the wavelength of the X-rays, δ the angle of the incoming or outgoing beam, and a is the distance between the planes.

If the intensity of the detected radiation is measured as a function of the angle of incidence plus the angle of reflection, conclusions can be drawn about the lattice distances and phase determinations can be carried out. To determine the present phases, the measured diffractogram is compared to structures reported in literature employing a "search and match" approach. Subsequent Rietveld fits quantify the relative proportions of these crystal phases and give valuable insights into the atomistic order of the material.
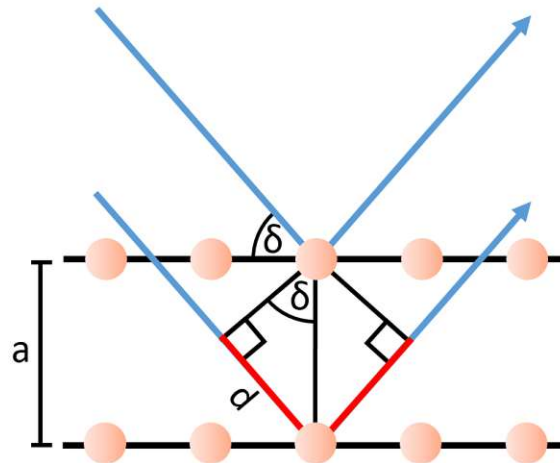
Figure 3.13.: Schematic illustration of the Bragg equation

In this work, two geometries of XRD measurements were applied. One is a classical Bragg Brentano geometry, in which the X-ray source and the detector move simultaneously.

The second geometry is used in particular to measure crystal structure in thin films. In contrast to the Bagg-Brentano geometry, a parallel mirror is used on the X-ray side together with a plate collimator (0.18° opening angle). The X-ray source is kept at a fixed small angle (e.g. 5°), resulting in a small penetration depth. The advantage of this method is, on the one hand, the surface specific sample examination, and on the other hand, the independence of the peak positions from the sample height, thus removing a possible source of error. [118]

The diffractograms in Bragg Brentano geometry were recorded with a step size of 0.014°
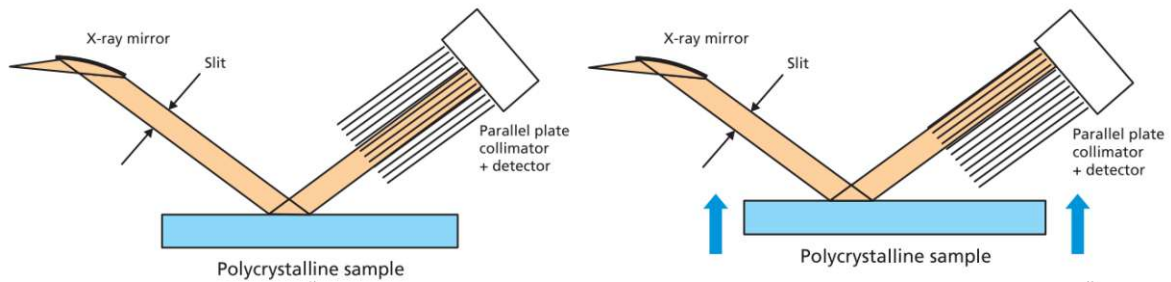
Figure 3.14.: Schematic illustration of the XRD measurements using the parallel beam geometry [118].

and a measurement time of 40 s per step using a Panalytical GalliPIX3D detector (active length = 7.1763°, 501 channels), in the parallel geometry with a step size of 0.05° and 2.7 s and a scintillator detector was used. For both cases, to limit the irradiated area and to get spatially resolved measurements, a 0.01 rad soller slit, a 2 mm mask and 1/2° divergence slit was applied to a Bragg Brentano HD mirror system and a parallel mirror system supplied by Panalytical.

3.7. Hardness Measurements

A very convenient measure for the mechanical strength of a material is its hardness [119]. Hardness is defined as the mechanical resistance of a material to a mechanical intrusion [82, 120, 121]. How a material can deform plastically depends on the mobility of the dislocations. The concepts of (indentation) hardness and strength are closely related to these mobilities, from which it follows directly that a reduction in the dynamics of dislocations results in an increase in both, and vice versa [36, p. 399]. Strength increasing methods include:

- Grain size reduction: Grain boundaries act as barriers to dislocations and are thus an important aspect in determining the material properties [122, p.144]. These barriers become stronger with increasing misorientation and thus lead to an increase in mechanical strength (and hardness). The smaller the grain size becomes, the more of such barriers there are [123]. The relationship between the average grain size and the yield strength is given by the Hall Petch relationship stating that the yield stress σ_y is proportional to the grain size by $(d_{\mathrm{grains}})^{-x}$ [124] [125, p. 347]. The exact value of the exponent x has ever since been the topic of a critical discussion, and several values have been proposed [124, 126–129]. However, qualitatively it can be seen that the yield stress increases as the grain size decreases corresponding to a grain refinement.

- Solute strengthening: Just as grain boundaries counteract dislocation mobility and thus plastic deformation, impurity atoms can have a significant influence on the mechanical properties. They distort the crystal lattice and generate stress, which acts as a barrier to dislocations and hinders their mobility through the lattice misfit effect. [122, p. 207]

[130] [36, p. 399]

- Strain hardening: The method of strain hardening (also known as cold working) describes the post-treatment of a material at relatively low temperatures (e.g. room temperature) [122, p. 175]. This causes dislocations to be entangled with each other, limiting their mobility.

- Annealing: Annealing describes the heating of the material above the recrystallisation temperature and subsequent cooling. Mostly this method is used to increase ductility. The annealing process involves 3 phases: recovery [122, p. 189], recrystallization [122, p. 179] and grain growth [122, p. 199].

To measure the hardness of solids, different experimental approaches are applied [82, 83, 120]:

- Scratch Hardness

- Indentation Hardness

- Rebound Hardness

To characterize the material's indentation hardness of the samples produced in this thesis the Vickers hardness test was used.

3.7.1. Vickers Hardness

The Vickers method is one of the indentation hardness measurement methods. To test a workpiece for hardness, an equal-sided diamond pyramid with an aperture angle of $136°$ is pressed into the sample [82, 131]. A precisely defined force is applied to the tip. After the indentation process and dwelling "in" the sample, the test tip is retracted (see Figure 3.15). The imprint left behind can then be viewed and measured under the microscope. Knowing the applied test force $F[N]$ and the average length of the two diagonals $d[mm]$, the hardness can be calculated using the equation

$$HV = \frac{0.102 \cdot 2 \cdot F \sin\frac{136°}{2}}{d^2} \approx 0.1891 \frac{F}{d^2} \quad \left[\frac{N}{mm^2}\right]. \tag{3.11}$$

The pre-factor of 0.102 is given by the conversion from Netwon to Kiloponds. For an easier comparison with other indentation hardness values in literature, the Vickers hardness values were converted to GPa.
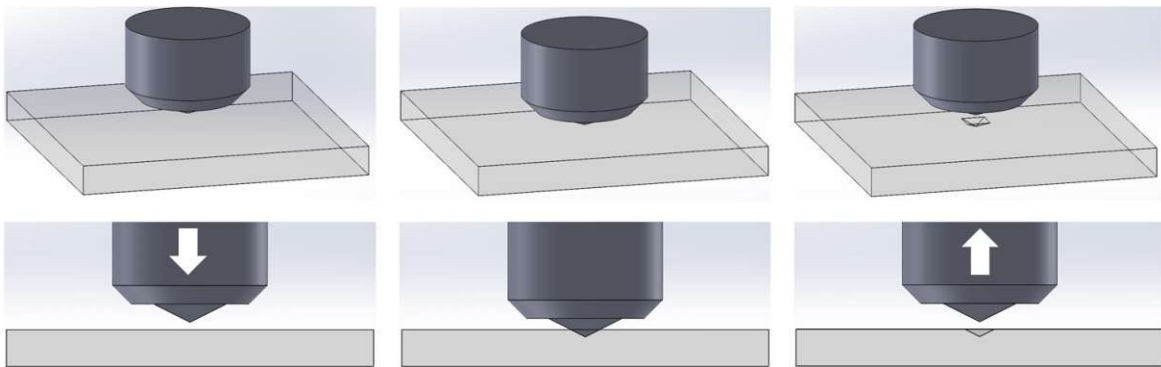
Figure 3.15.: Schematic illustration of the Vickers hardness measurement: Approach of the pyramidic shaped tip, indentation and retraction of the tip. The residual imprint in the material can be measured and the indentation hardness determined.

Despite the simple principle, hardness measurements are not trivial and are subject to a variety of sources of error that can lead to falsified results [82, 120, 132, 133]:

- Control of indentation force: Accurate control of the indentation force is essential to determine hardness. The force must be accurately dosed and be able to reach the set final value. The smaller the applied indentation force, the bigger the absolute error can be.

- The selected penetration speed of the test probe can lead to variable measurement results. The slower the tip is driven into the material, the lower the hardness values appear.

- An elongated dwell time of the probe tip at maximum load leads to further penetration of the diamond tip up to the equilibrium position. If the dwell time is too short, tip retraction may occur before the final position is reached, making the specimen appear harder than it is. Similarly, elastic recovery can also result in smaller impressions.

- When calculating the measurement indentation, the force is assumed to act perpendicularly to the sample's surface. If a non-perpendicular component exists, the impression may appear larger under the microscope.

- Surface roughness is an important factor in the generation and evaluation of indentations. If the roughness is too high, the imprints can be distorted, resulting in erroneous results.

- The size of the final indents can be selected by the applied test load. When selecting the correct indentation size, care must be taken to ensure that the indentation is large enough to be easily resolved by the optical measuring device and to measure a sufficiently large area. Particularly in the case of thin layers, the indentation force and the associated

a)

b)
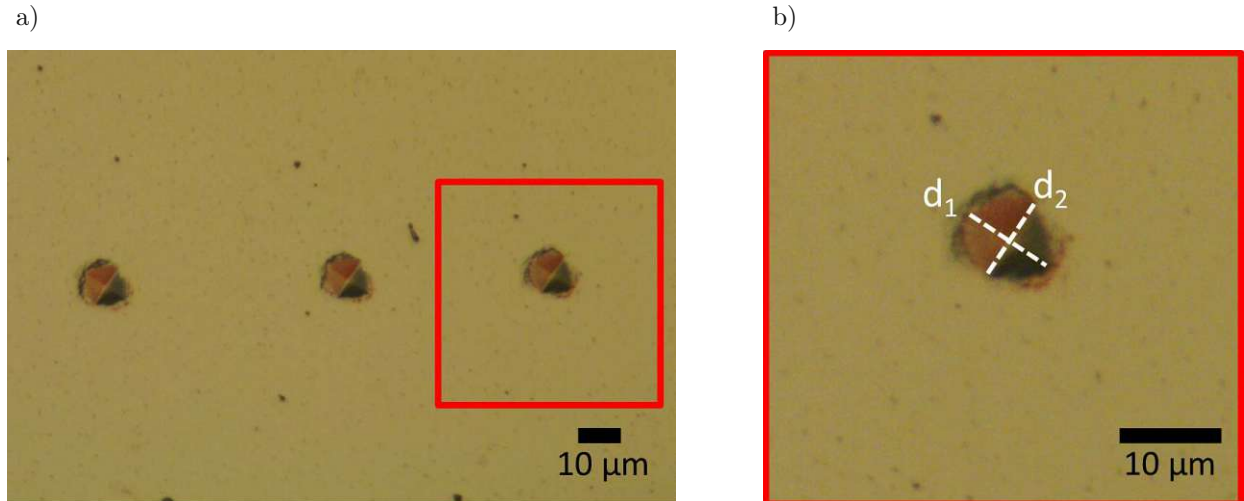
Figure 3.16.: (a) Optical microscope image of the hardness indentations created with an applied force of 10 Pond (= 0.098 N). b) Detailed image of a hardness indent with indicated diagonals which were used to determine the indentation depth.

indentation depth should be selected as low as possible in order to minimize substrate effects.

For the measurements of the Vickers hardness of the produced samples an *Anton Paar MD 4000 V* microindenter and an optical microscope (Reichert Jung 'Polyvar MET') were used.

3.8. Film Thickness Measurements

A profilometer was used to measure the thickness of the prepared samples. This measuring method involves dragging a hard tip with uniform speed across the layer-substrate transition. The deflection of the lever on which the measuring tip is mounted is measured by an inductive gauge and converted into an electrical signal [134]. This can be read out via a computer. By levelling the sample and substrate surface, a step profile and thus the thickness of the layer can be determined. The sample must have sufficient hardness to avoid damage by the measurement procedure and the forces acting on the sample surface.

In this work, a profilometer of the type *Taylor Hobson - Surtronic 3+* was used with which layer thicknesses of 50 nm to several 100 μm can be resolved.

4. Simulation

Computer-based models were developed to support the experimental work and to make predictions regarding potentially interesting elemental combinations. These are briefly described below, the underlying theory is explained, and comparisons with experimental results are made.

4.1. Substrate Composition Simulation

The prediction of the compositions of the prepared samples and, consequently, the choice of the process parameters (applied power, geometry) is essential in large-scale screening experiments. Therefore, a specifically programmed simulation was developed and acted as an effective tool to enable the efficient production of the alloy libraries. With its help, layer compositions could be estimated and predicted based on the process parameters of the applied voltage and the angle of the substrate relative to the two sources.

The simulations for the prediction of the chemical composition on the substrate are based on the emission characteristic, which was presented in section 3.1.1.5 in combination with the calculated sputter yield (section A.1). The energy dependence of the sputter yields for the elements used in this work is shown in Fig 4.1 a). As a starting point, the experimental geometry (see Fig. 3.7) was implemented in a Python code. The substrate and the two targets (sources) are described by multidimensional arrays, which are divided into discrete array points with a relative distance of 1 mm to each other. Each array point represents a spot on the target and substrate. The angle of the substrate (relative to the sources) and the distance to both sources can be varied. The lateral emission intensity was approximated by a skewed Gaussian distribution in order to take the inhomogeneous emission characteristics of the magnetron sputtering process caused by the magnets positioned behind the targets into account. The radial position of the emission maximum was determined by measuring the geometry of the magnetron system and the eroded target (compare Fig. 4.1 b)). A radius of the erosion trench of 14.5 mm for the 2 inch target was found. By point-wise calculation of the angle of the direct trajectory between the target point and the substrate point it was possible to calculate the directional distribution given in equation 3.4. Combining this with the material- and energy-dependent sputter yield, an intensity profile could be obtained for each point. By taking all target-substrate points into account and subsequently summing them up, it was then possible to calculate the relative proportion of particles deposited on the substrate and the resulting chemical composition on the substrate.

a)

b)
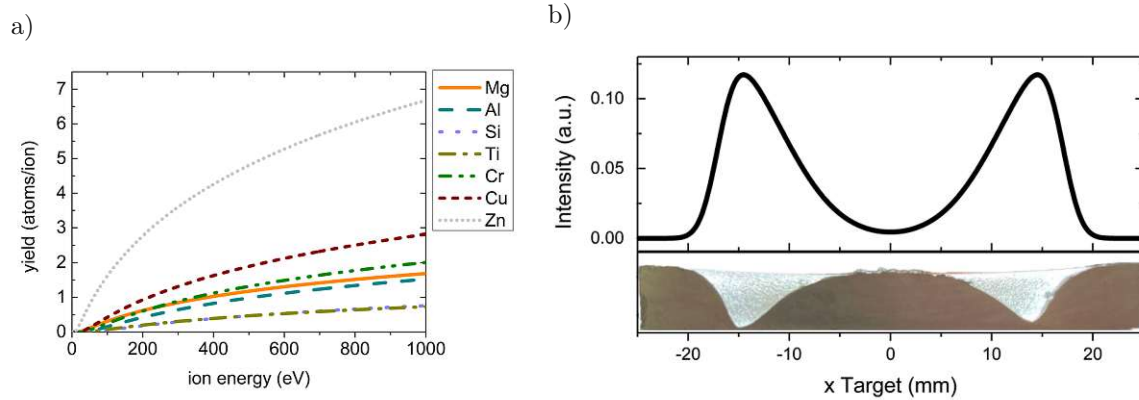
Figure 4.1.: a) Calculated sputter yield of selected pure elements. b) The top panel shows
the fitted emission intensity profile obtained by analysing an eroded target (lower
panel).

In Figure 4.2 and Figure 4.3 calculated and measured distributions of Al-Cu and Al-Zn target
combinations are shown. The calculated proportions of Cu and Al (respectively Zn) are in
good accordance with the measurements. Also, the progression of the concentration difference
over the lateral position of the substrate was reproduced well. In addition, Fig. 4.3 shows
the comparison of the simulations and the experimental chemical analysis at different angle
settings of the substrate relative to the two sources. For this purpose, one source was equipped
with an Al target, the other with a Zn target. The angles were set at 15°, 45° and 75° relative
to both targets while the power for the Zn target was chosen to be 50 W and for Al 100 W.
Due to the higher sputtering yield of Zn compared to Al, the setting with a relative angle of
15° towards Al was used to prepare a second sample using a power of 33 W applied to the
Zn target and a power of 150 W to the Al target. The parameters for all samples can be also
obtained from Tab. 4.1).

The comparison shows good agreement between the simulated chemical compositions and
the measured ones. Discrepancies are probably primarily due to inhomogeneous radiation
characteristics of the individual elements [135] and the directional dependence modified by
the varying depth of the erosion trench, which was not considered in the simulations.

a)

b)
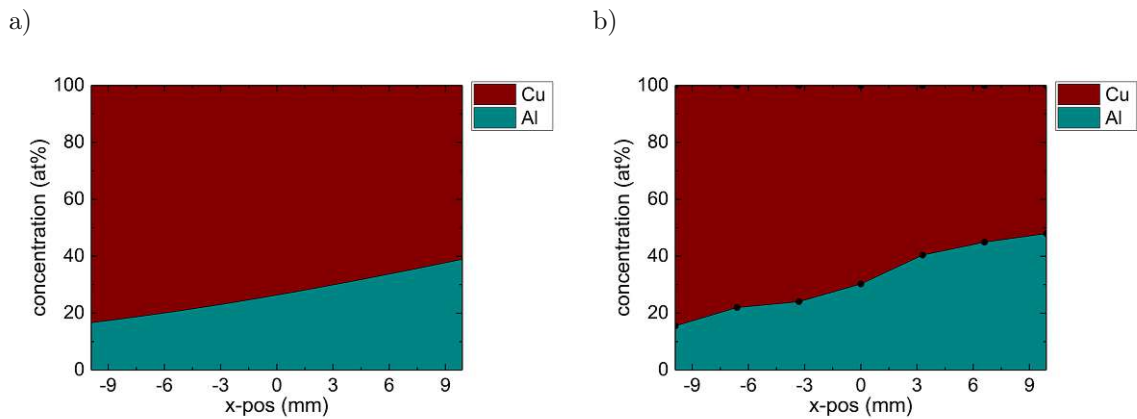
Figure 4.2.: Comparison of the a) simulated and b) measured composition of a sample produced by an Al and a Cu target with an exposure angle of 45°. The measured compositions are in good agreement with the simulations.

a)

b)
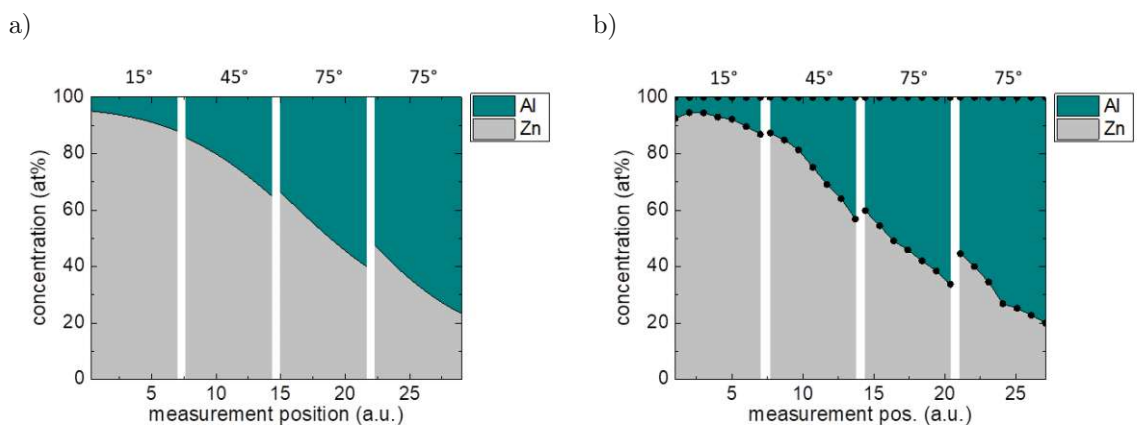
Figure 4.3.: Comparison between a) a simulated and b) an experimentally produced AlZn sample for various geometries and applied powers (see Tab. 4.1).

Table 4.1.: Parameters used to simulate the AlZn samples shown in Fig. 4.3 at various geometries and applied powers.

d_1 (mm)	material 1	angle 1 (deg)	power 1 (W)	voltage 1 (V)	current 1 (mA)
70	Zn	15	50	380	130
70	Zn	45	50	380	130
70	Zn	75	50	380	130
70	Zn	75	33	330	100

d_2 (mm)	material 2	angle 2 (deg)	power 2 (W)	voltage 2 (V)	current 2 (mA)
70	Al	75	100	350	280
70	Al	45	100	350	280
70	Al	15	100	350	280
70	Al	15	150	310	480

4.1.1. Extension to Composite Targets

The previous considerations referred to the usage of pure elemental targets as material sources. Since composite targets were used in this work to produce multi-component systems with up to 5 different metals, they had to be incorporated into the simulation. The combination of several elements primarily changes the sputter yield of the target. To account for these effects, the individual sputtering yields of the elements involved were calculated at a given voltage (i.e., ion energy) and weighted according to their fraction c_i in the compound. Following this approach, the average yield Y_m could be calculated according to:

$$Y_m = \sum_i c_i Y_i \tag{4.1}$$

Even though the total sputtering yield of alloys is generally lower than the sum of the weighted individual yields [83,136,137], this approximation was used for the calculation. The underlying reason for the nontrivial behavior of the sputtering yields of alloys is the surface enrichment of the harder-to-sputter component [82,83,138]. The concentration changes within a thickness of a few nm in favor of the component that is more difficult to sputter, which generally has a higher binding energy. As a result the mean sputtering yield tends to lower values [83,139,140]. In Figure 4.4 a), the comparison between simulated and measured chemical composition of a binary AlCu and MgZn target is shown. Both experiments were performed at a relative orientation of 45°. The predictions allowed the angle settings and applied powers to be calculated a priori and thus to be set optimally, helping to establish an effective screening method.

a)   b)
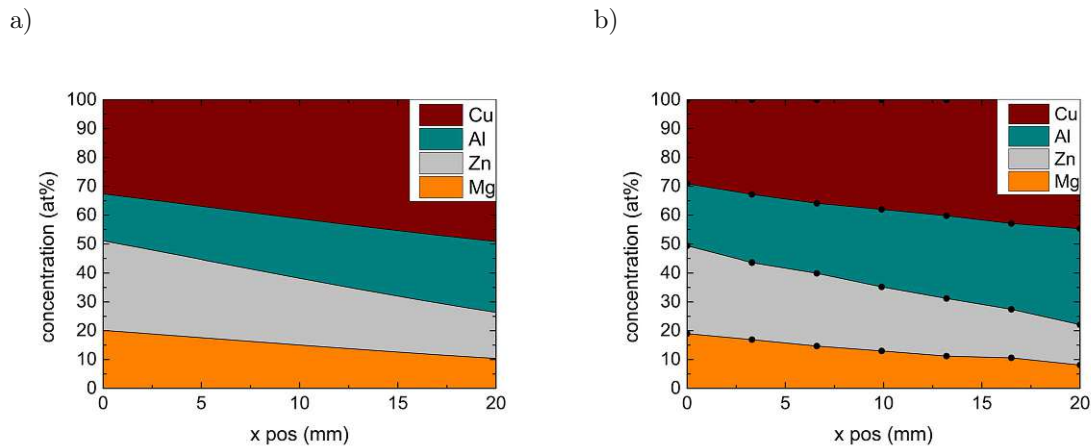
Figure 4.4.: Comparison between a) a simulated and b) an experimentally produced AlCuMgZn sample.

4.2. Simulation of Atomic Distribution

The prediction of the predominant crystallographic phases and the distribution of the constituents is essential for the development and design of alloys and complex metal systems. However, to date, it is difficult or impossible to effectively predict the structure of these phases in a multi-component alloy, and it becomes progressively more difficult with an increasing number of constituents. Nevertheless, a simple approximation, based on the formation enthalpies, was developed to estimate the atomic order and to give a hint on the phase formation.

The input parameters required for the calculation consisted of the concentration of the individual elements (chosen or obtained from the EDX measurements of existing samples) and the binary formation enthalpies of the element combinations involved. These are listed in Table A.3 for all considered materials. A Monte-Carlo algorithm was applied to simulate the formation of different domains depending on the composition of the chosen system. In order to take the non-equilibrium properties of the underlying sputtering process into account, at the beginning of the simulation a 100 x 100 pixel array was randomly filled with the elements involved in the coating. This assumption is supported theoretically and can be explained by the fast cooling rate during condensation from the vapor as well as by the experimentally observed amorphous X-ray diffractograms of non-heat-treated samples (see Fig. 5.5). When thermal energy is supplied, the system can relax into a state of equilibrium given by a minimal total inner energy. A schematic representation of the approach for energy minimisation is given in Fig. 4.5. To computationally find the equilibrium state of the system, an element from the randomly generated array was selected, and it was evaluated if an exchange with a neighbouring element results in a reduction of the energy. To take 'long range' effects into account, 3 rows and 3 columns of neighbouring atoms (black squares in Fig. 4.5 b)) were examined for the energy reduction upon a possible position change of the central atom and

the neighbouring atom. This was executed for all four directions. The sum of the enthalpies of those neighbours was calculated according to the equation

$$\sum_{j=1}^{N} c_j \Delta H_{i,j}. \tag{4.2}$$

Here, the index i describes the randomly selected atom and j all atoms defined as neighbors (black square). ΔH_{ij} describes the binary enthalpies of formation of the interaction-partners. In addition, the entropy of the subsystem is determined according to

$$\Delta S_{config} = \sum_{j=1}^{N} c_j \ln c_j \tag{4.3}$$

representing the disorder in the environment of the chosen atom. The combination of the two expressions leads to

$$\Delta E = \sum_{j=1}^{N} c_j \Delta H_{i,j} - T \Delta S_{config} \tag{4.4}$$

with T being the temperature at which the thermal post-treatment occurred. The direction in which this expression is minimized is selected here as the preferred one and an atom swap of the initially selected atom and the neighbouring one is carried out. To reach a final equilibrium state, this step was repeated at least 10^6 times.
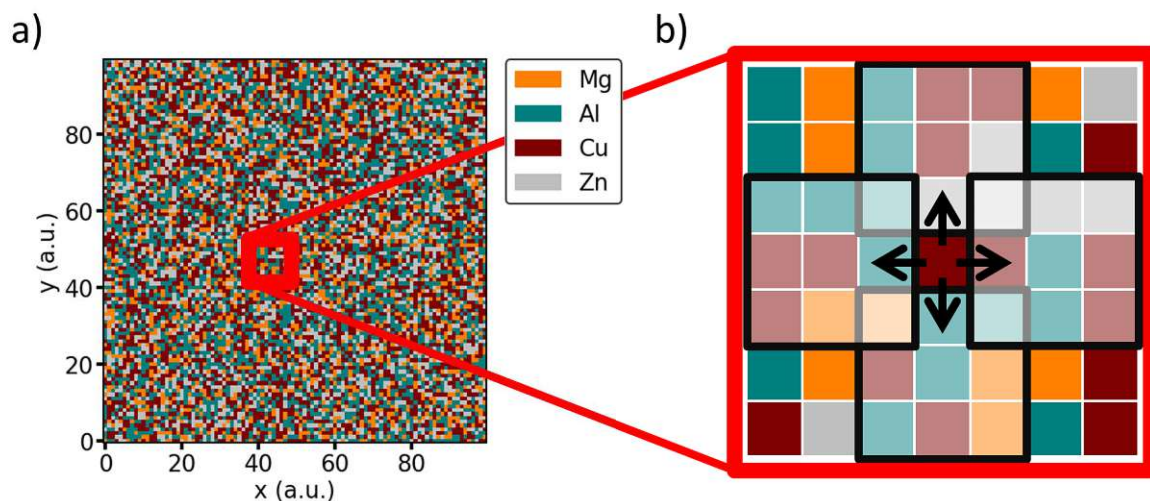
Figure 4.5.: a) Randomly distributed arrangement of atoms at the beginning of the simulation. The red square marks an area around a randomly selected atom. This area is shown enlarged in b). The indicated black squares represent the neighbouring atoms considered in each direction, which were taken into account for the minimum energy calculation.

4.2.1. Binary Systems

To test the validity of the simulation approach, initially binary systems were considered. Different combinations were used as input for the computer program, and a final state was calculated using the methods described above. Phase diagrams from the literature were then taken to estimate the plausibility of the simulation results. Such calculations of the binary systems are relatively simple, and the results are intuitively predictable. Nevertheless, these simple considerations are important to verify the functionality of the simulation.

The considered binary systems included combinations of elements used in this work. Some of these, along with corresponding phase diagrams, are shown in Fig. 4.6 - Fig. 4.9.

Firstly, systems for which a mixed state based on the phase diagram is suspected are considered, and binary enthalpies are examined. Exemplary Al-Mg and Cu-Zn systems are shown in Fig. 4.6 and Fig. 4.7, respectively. Intermetallic mixed states form in these systems, which is suggested in their corresponding phase diagrams. Comparison of the enthalpy values in section A.3 in Table A.2 reinforces this observation as both binary systems exhibit highly negative values. These intermetallic mixtures were reproduced by the simulations, which demonstrated a complete intermixing of the involved elements.
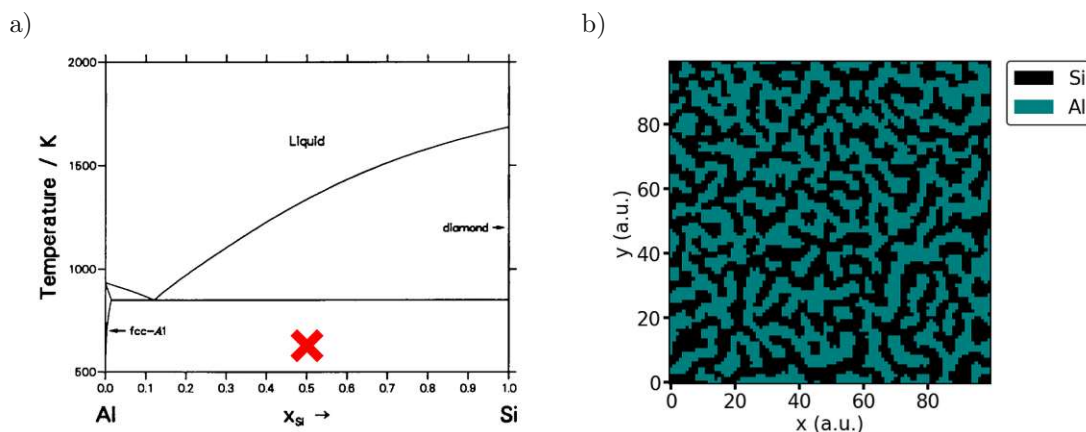
a) b)
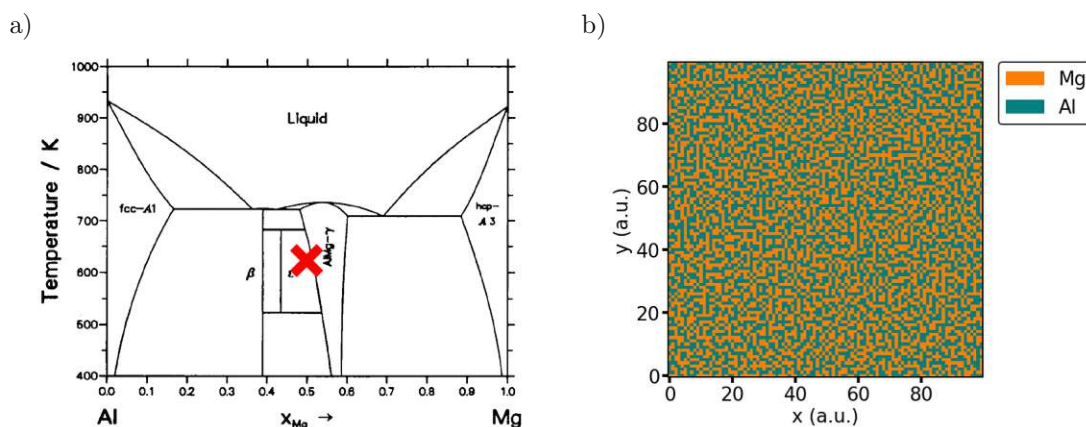
Figure 4.6.: a) Phase diagram of the binary Al-Mg [141] system and b) the simulated distribution of the components at a temperature of 350 °C (= 623.15 K) and a 50 at% : 50 at% composition of the components. The red cross in panel a) indicates the conditions (composition and temperature) chosen for the simulation.

In contrast, from the phase diagrams in Fig 4.8 and Fig. 4.9 of the combinations Al-Si and Cr-Mg, an immiscible state can be expected. The positive enthalpy values in Tab. A.2 confirm this presumption. The simulations result in a separation of the elements for these mixtures indicated by the formation of distinct islands of the individual elements, which can be seen in Fig. 4.8 b) and Fig. 4.9 b). The influence of entropy, which according to eq. (4.4) could counteract the separation by lowering the Gibbs free energy, does not seem to be large enough in these systems at the chosen temperature to promote an intermixing of the components.

In addition to the comparison to phase diagrams obtained from literature, binary systems of different elements were also prepared experimentally and studied. These are presented in

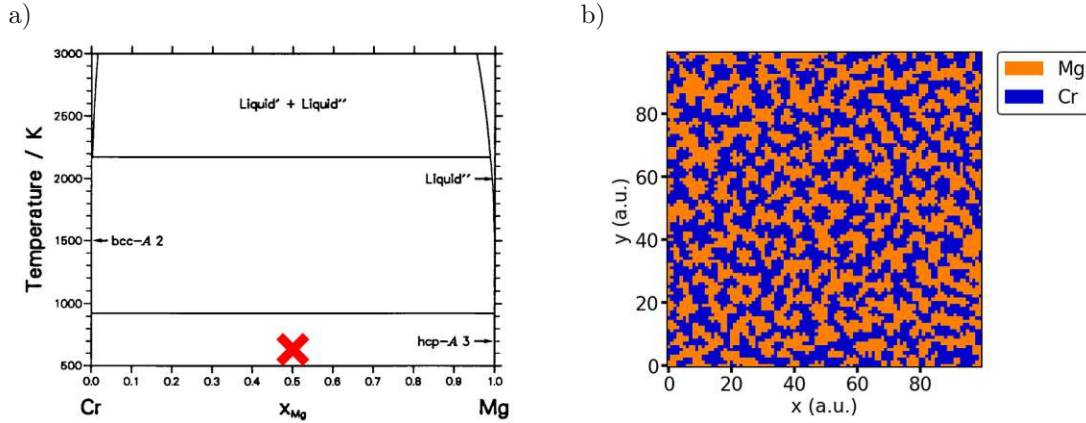a)   b)
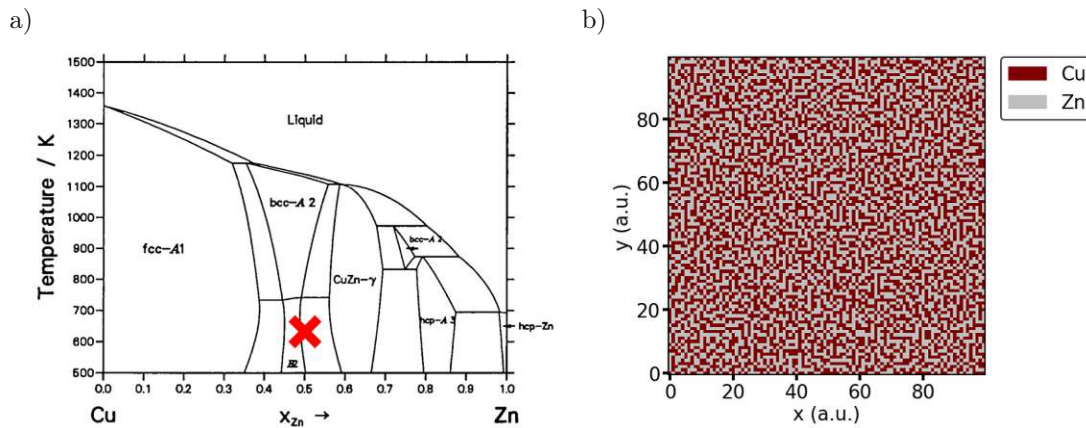
Figure 4.7.: a) Phase diagram of the binary Cu-Zn system [141] and b) the simulated distribution of the components at a temperature of 350 °C (= 623.15 K) and a 50 at% : 50 at% composition of the components. The red cross in panel a) indicates the conditions (composition and temperature) chosen for the simulation.

detail in the chapters 6.1.2 and 6.1.1 for AlCu and AlZn.

The advantage of comparing simulation and experiment using binary systems is given by the straightforward comparability. For the binary systems, the theoretical simulative and experimental results showed excellent agreement. However, given the goal of this work the extension to systems with a higher number of different elements is essential.

4.2.2. Comparison to Ternary Systems

After the successful simulations of the binary systems, the system was extended to three elements. A ternary AlMgZn system was chosen as it has been studied excessively both in literature [142–145] and throughout our previous work [146]. A detailed discussion of the experimental studies is given in section 6.1.3. Figure 6.13 shows the atomic distributions for three different compositions. Here, the Al fraction was varied while keeping the relative Mg and Zn fractions constant. With increasing Al content, the simulations show an increasing separation between Al and MgZn rich domains. These separations were also observed in the electron micrographs of the experimentally prepared ternary AlMgZn samples (compare Fig. 6.13 and Fig. 6.10 a)) [146].

4.2.3. Limitations

The simulation described in the previous section was intended as a simple aid for selecting potentially interesting material combinations and for comparison with experimentally produced samples to estimate the validity of the approach. The introduced method considers only the enthalpy of formation and the local change of configurational entropy for the computation of the system's equilibrium state. This simple approach has some limitations, which will be discussed in the following:

a)

b)

Figure 4.8.: a) Phase diagram of the binary Al-Si system [141] and b) the simulated distribution of the components at a temperature of 350 °C (= 623.15 K) and a 50 at% : 50 at% composition of the components. The red cross in panel a) indicates the conditions (composition and temperature) chosen for the simulation.

- **Diffusion:** At temperatures > 0 K, atoms can move. How easily and simply atoms move depends on a number of factors. These are accounted for in the diffusion coefficient. This coefficient depends on the temperature and the type of element. Jumps of the individual specimens can be described according to the expression: [147, 148]

$$D \propto e^{-H_M/k_B T} \tag{4.5}$$

with H_M indicating the migration enthalpy, k_B the Boltzmann constant and T the temperature. It is evident that the diffusion constant (and thus the diffusion) increases with the increase of the temperature and the decrease of the potential barrier (which depends on the type of the considered atom and the matrix in which it moves). These dependencies were not taken into account in the calculations. As a result, in the simulations, each atom can move in the same way, regardless of which atom it is or in which environment it moves. This represents limitations concerning the validity of the scale. In addition, possible inhomogeneities with respect to the atoms considered are not taken into account. Since the calculations are only intended to provide qualitative information and the exact consideration of the material- and system-dependent influential factors is difficult or only possible by approximation, these have been omitted.

- **Choice of enthalpy:** The energy minimization of the system resulted from calculations of the binary formation enthalpies. These were obtained from the "Aflowlib" database [149] and the work of Troparevsky *et al.* [77].

  For the calculation, the energetically most favorable compounds were used, i.e., the smallest (partly most negative) values. The choice of the pairwise enthalpies is one of the major limitations, since these can differ widely [48].

a)

b)

Figure 4.9.: a) Phase diagram of the binary Cr-Mg system [141] and b) the simulated distribution of the components at a temperature of 350 °C (= 623.15 K) and a 50 at% : 50 at% composition of the components. The red cross in panel a) indicates the conditions (composition and temperature) chosen for the simulation.

The enthalpies for various phases (and thus different stoichiometries) can vary significantly. As an example, different values for enthalpies are listed in Table 4.2.

Table 4.2.: Overview of the formation enthalpies for various intermetallic AlCu compounds [149] and the corresponding space groups.

compound	space group	H_{form} (meV/atom)
Al_4Cu_9	$P\overline{4}3m$	-213
$AlCu_2$	$I4/mmm$	-200
Al_2Cu	$Fm\overline{3}m$	-179
Al_3Cu_4	$I4/mmm$	-162
Al_3Cu_2	$P\overline{3}m1$	-159

Moreover, even when the stoichiometry and structures are fixed, large differences in the reported values are found in the literature. As an example, the binary enthalpies of formation of the compound $Mg_{17}Al_{12}$ phase are: in the range from -38 meV/atom to -36 meV/atom in the aflowlib database [149], -24 meV/atom in the OQMD database [150–152], -38 meV/atom in [153], -20 meV/atom in Material Project [48, 154], and -33 meV/atom in [77]. The variance of these values already shows the potential uncertainties in the estimation of the energetic minimum.

- **Informative value for crystallography:** The comparison to binary phase diagrams showed that despite the simplified approach, the calculated distributions of the elements could reproduce any mixing/de-mixing behavior well. However, while the atomic distribution can give an indication of a formed phase system, it cannot accurately reflect the exact crystallography. Therefore, the calculation can be seen as an indication for the formation of certain crystal systems (an accumulation of elements can of course lead to

a preferential phase), but should not be overestimated. Nevertheless, for systems with a large number of overlapping IM phases, the calculated distributions can be a powerful tool for a better identification of crystal phases.

5. Influence of Process Parameters on Sample Characteristics

Several studies have already shown that the analysis of samples measures not only the specimen's intrinsic characteristics but is also influenced by the parameters prevailing during production or the subsequent treatment [155, 156]. Characteristics and properties can be significantly influenced by the method of synthesis and post-processing. In order to ensure that a stable or at least metastable thermodynamic equilibrium state has been achieved to keep the samples comparable to other manufacturing methods, a thermal treatment after the deposition has been applied. Since sputtering, in particular, represents a non-equilibrium process, a critical consideration in this respect is especially important. Crucial parameters in this context are:

- the deposition temperature

- the deposition rate

- the annealing temperature

- the annealing time

In this work special focus was put on the crystallographic phases, thus the knowledge of the influence of the process parameters on the atomistic structure is essential. To ensure consistency of the analytical results within one series, overlapping areas having the same chemical composition on different samples were produced. This inevitably led to different deposition rates and relative angles to the source, and, due to the resulting changed production time, also different substrate temperatures during the coating. However, for a more detailed investigation, a variety of samples were produced using varying process parameters to study their effects in detail.

In addition to crystallography, the samples were examined with regard to their surface structure and hardness. These properties can also be significantly influenced by the process chosen for production. These were verified by overlapping areas in the individual sample series as well as by the investigation of specially prepared samples. For instance, in order to investigate the influence of varying processing parameters on the hardness, a series of pure Cu coatings under various settings was prepared. The investigations focused on the influence of the sample thickness, the varying geometry during the deposition process and effects of the thermal post-treatment.

5.1. Influence of the Thermal Post-Treatment

Thermal post-treatment is an essential part of the material production for almost all synthesis methods. Due to the manufacturing process, a sample can be in a non-equilibrium state. For most applications, this is not sufficient to allow statements about general trends of the material characteristics. Due to the enormous cooling rates of 10^2 K/s - 10^7 K/s (also see appendix A.2) sputtering can be seen as an absolute non-equilibrium process that imposes additional demands on post-treatment. The choice of the 'right' annealing temperature or duration is the subject of critical discussions as both alter the properties of the materials [157, p. 53 - 55]. The addition of thermal energy allows atoms to rearrange, form new structures and leads to changes in the crystallography [158–160]. This can result in the observed transition from crystallographic disorder and amorphous structures to crystallographic order. Such a transition can be seen in Fig. 5.1.
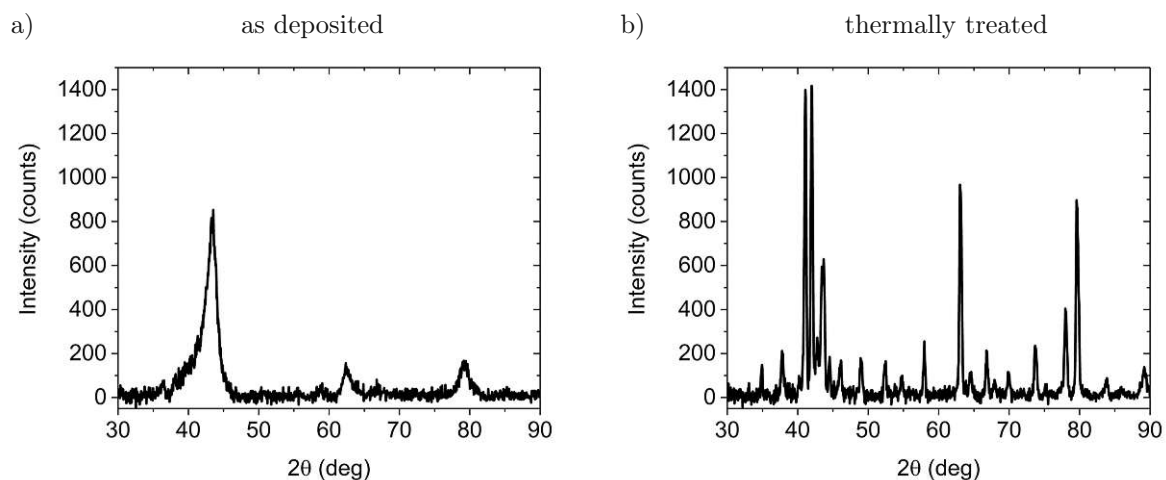
Figure 5.1.: The influence of thermal post-treatment is shown on the example of a) an as deposited and b) an AlCuMgZn sample thermally post-treated at 350 °C for 24 h.

In addition to the effects on the microscopic structure of the specimens, the thermal post-treatment subsequently influences the mechanical properties. For example, the thermal post-treatment can lead to an increase in ductility with a simultaneous decrease in hardness. [157, p. 54] [36, p. 399]

One method to ensure that the samples were at least transferred into a metastable state was to thermally post-treat selected samples at higher temperatures and for longer periods and track the occurring changes. Figure 5.2 shows samples after different annealing times and annealing temperatures in the experimentally accessible range. It was shown that there are no significant changes at temperatures T > 350 °C and durations above 24 hours. Moreover, the comparison of the "simpler" systems with classical phase diagrams available in literature shows that the equilibrium states are reached.

In Fig. 5.4, the influence of the thermal treatment on the mechanical property of the inden-

a)

b)
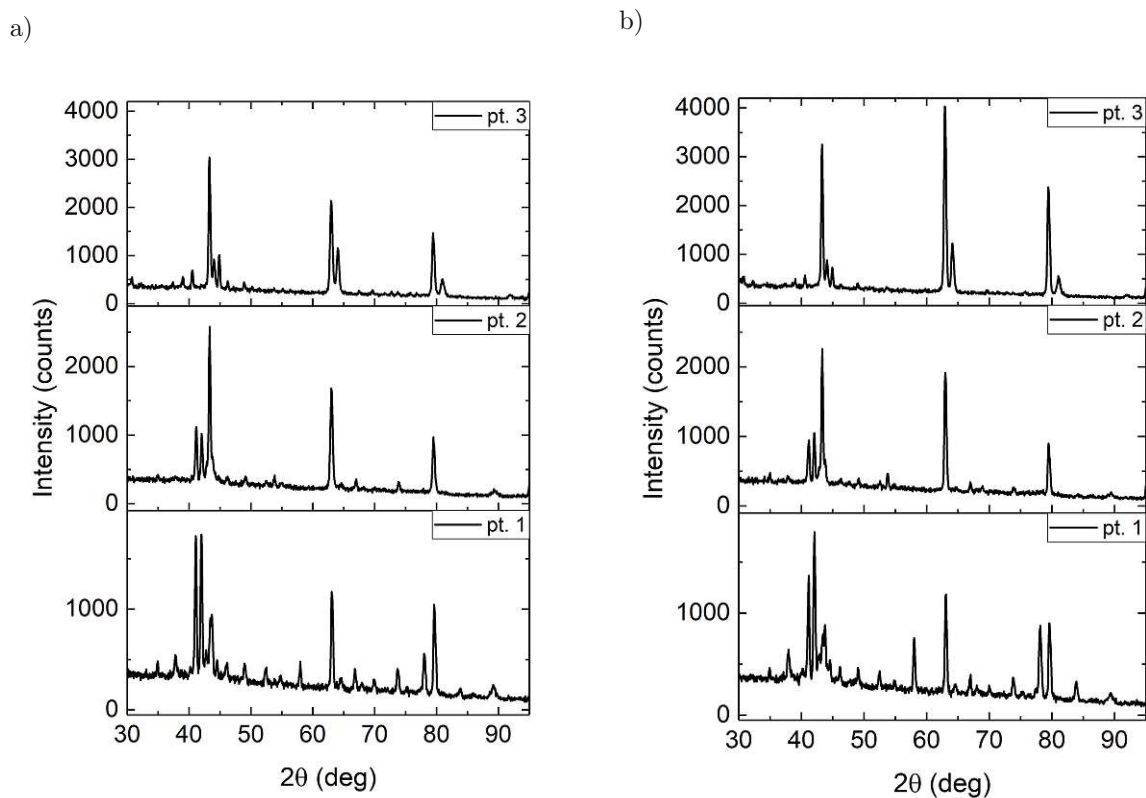
Figure 5.2.: XRD measurements for a) a sample annealed for 24 hours at a temperature of 350 °C and b) a sample annealed for 48 hours at 430 °C. The chemical composition for both samples is:
pt. 1 Al: 21.5 at.%, Cu: 29.1 at.%, Mg: 19.0 at.%, Zn: 30.4 at.%
pt. 2 Al: 26.8 at.%, Cu: 38.0 at.%, Mg: 13.0 at.%, Zn: 22.2 at.%
pt. 3 Al: 33.2 at.%, Cu: 44.7 at.%, Mg: 8.1 at.%, Zn: 14.0 at.%

tation hardness of pure Cu samples can be seen. While the final hardness of the unannealed samples was approx. 2 GPa, the thermal post-treatment reduced this by 50 % to 1 GPa. This can be explained by a reduction of the number of dislocation obstacles by recrystallization due to the promoted mobility caused by the elevated temperature [36, p. 399].

5.2. Influence of the Sample Thickness

While the principle of indentation hardness measurements seems relatively simple, accurate testing of a material, especially when dealing with thin films, is challenging. One challenge involved in measuring the hardness of thin films is the influence of the substrate on the result. This is called the substrate effect [161, 162]. Due to the limited thickness of the coating, the hardness of the substrate can falsify the measurement [163]. In literature, different statements concerning the minimum sample thickness for the penetration depth of the probe tip can be found and often the rule of thumb is used that the indentation depth shouldn't exceed 10 % of the specimen's thickness [161, 164, 165]. In order to estimate the influences of deviations in specimen thickness and potential sources of error in the hardness measurements, Cu coatings of different nominal thicknesses were prepared and subsequently examined by means of Vickers hardness tests. Cu was chosen as a relatively soft material. From Figure 5.3, the theoretical correlation between penetration depth and hardness of the coating can be seen. The softer the sample, the deeper the sample tip penetrates and possible effects of the substrate can still be observed at higher film thicknesses. Thus, by choosing a soft material, a lower limit of the layer thickness up to which the substrate effect is measurable should be estimated. For each parameter set, 2 samples were produced, one of which received thermal post-treatment. This post-treatment followed the same procedure applied to the later examined multicomponent series (24 h, $T_{surface} = 350\,°C$, heating ramp of $\Delta T/\Delta t = 10\,°C/min$, cooling ramp $\Delta T/\Delta t = -10\,°C/min$ until $\approx 100\,°C$, then it took around 2 hours to reach a final temperature of 50 °C before the sample was removed from the annealing chamber). The samples in this series were also prepared by using identical conditions (200 W, 0.8 Pa, d = 70 mm, $\alpha = 0°$). In Figure 5.4, the variation of the Vickers hardness as a function of the layer thickness is shown. Both series show a high initial value of indentation hardness which is attributed to the hardness of the glass substrate (HV 0.01/5 = 6.06±0.45 GPa for the untempered plane glass substrate, HV 0.01/5 = 7.02 ± 1.09 GPa for the uncoated tempered glass substrate). The untempered samples (Figure 5.4 a)) reach relatively stable values at thicknesses $\gtrsim$ 0.65 μm. The final Vickers hardness is about 2.3 GPa. In the case of the annealed samples (Figure 5.4 b)), a lower value of Vickers hardness of approx. 0.9 GPa is obtained even for thicker layers (d = 15 μm). This corresponds to a decrease of around 50 % compared to the as deposited sample. The initial drop in hardness also extends over a wider range of thicknesses. The thickness above which no major changes occur was determined to be approximately 5 μm. This can be explained by the deeper penetration due to the softer material.
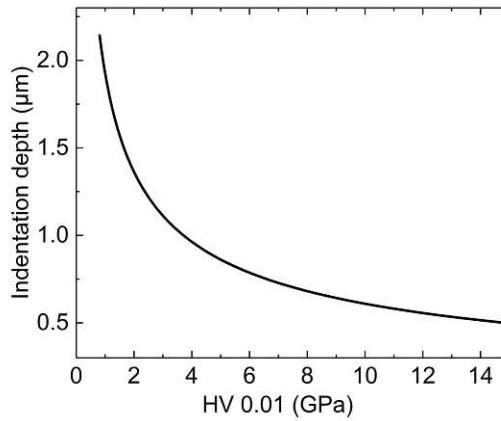
Figure 5.3.: Indentation depth of the probe tip in dependence of the hardness at an applied force of 10 pond.

a)

b)
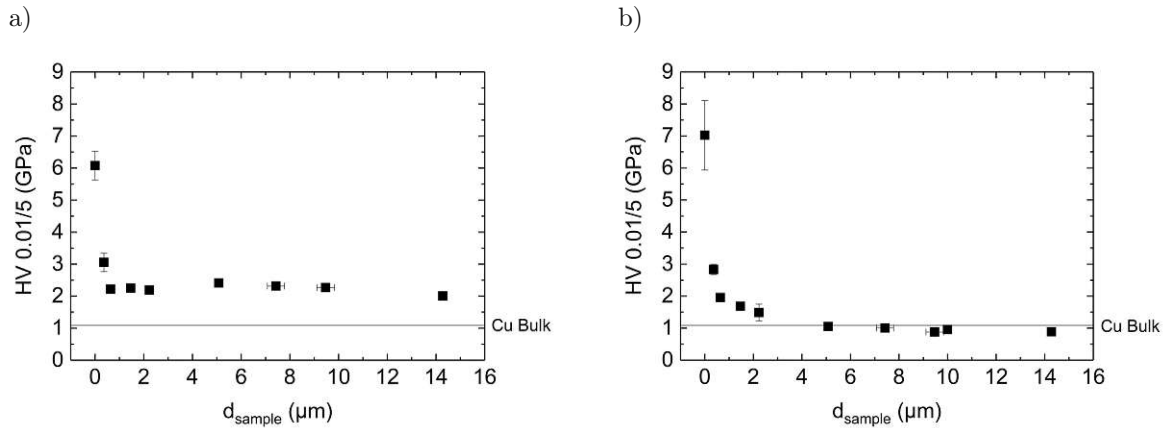
Figure 5.4.: Hardness as a function of Cu layer thickness for a) unannealed and b) annealed samples. For comparison, the Vickers hardness of a pure Cu target ('Cu Bulk') is plotted.

The samples analysed in this work had a minimum film thickness of $10\,\mu$m. Based on the results presented here, we can largely rule out any corruption of the determined hardness values due to substrate-effects.

The crystallography should naively not depend on the sample thickness. However, on closer consideration, the sample thickness may have an indirect effect on the crystal structure (temperature variation, etc.). To investigate the effects of different thicknesses on the crystallography, two layers of AlCuMgZn with thicknesses of $2\,\mu m$ and $10\,\mu m$ were studied by XRD. The results shown in Fig. 5.5 and Fig. 5.6 indicate that the different sample thicknesses have no effect on the predominant crystal structure. The slightly different relative peak heights, in turn, suggest moderately different textures. In addition, the effects of thermal post-treatment on the development of peaks in the diffractograms can be seen by comparing the as deposited (Fig. 5.5) and the thermally treated samples (Fig. 5.6).

a)

b)
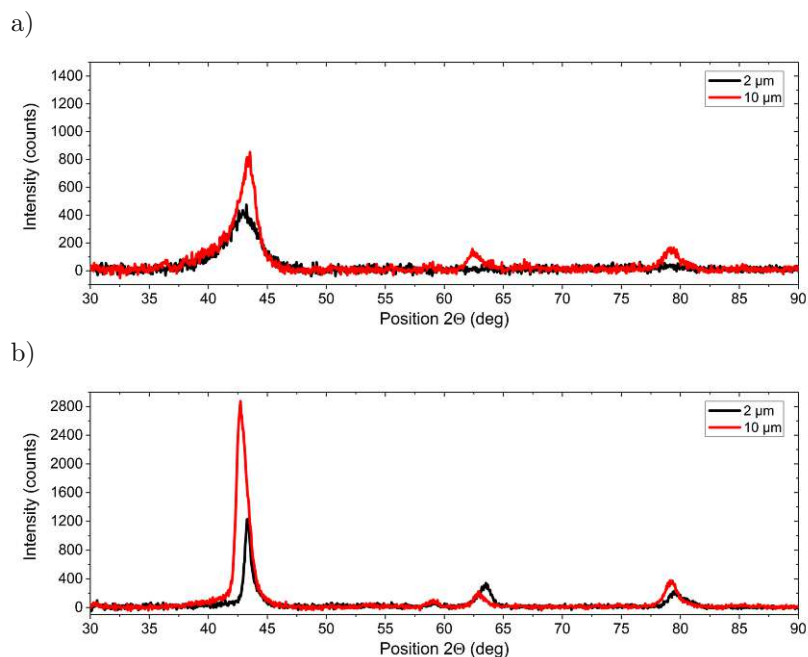
Figure 5.5.: XRD measurements of an AlCuMgZn sample before thermal post-treatment (as deposited). a) and b) show the results at different measurement positions and accordingly varying compositions.

a)

b)
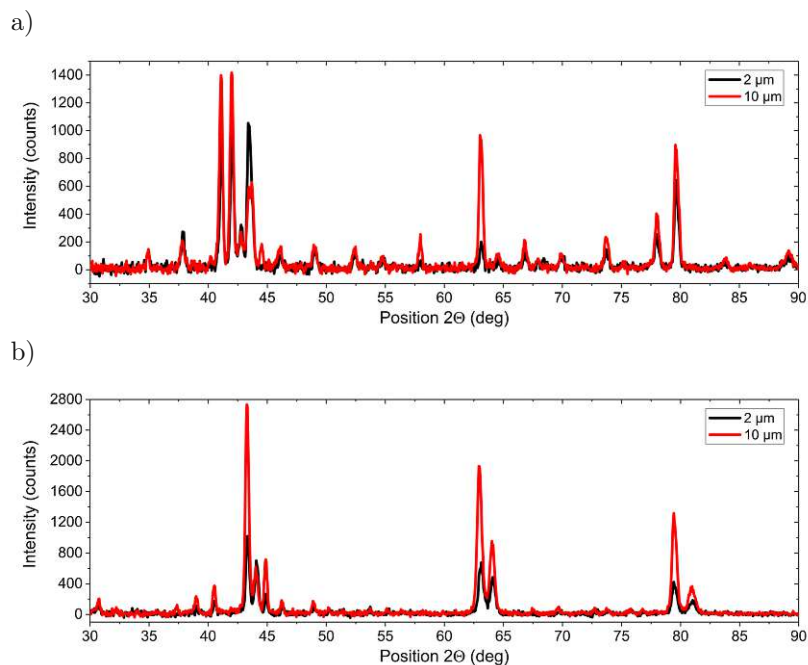
Figure 5.6.: XRD measurements of an AlCuMgZn sample after 24 hours of thermal post-treatment at 350 °C. a) and b) show the results at different measurement positions and accordingly varying compositions.

5.3. Influence of the Deposition Rate

The deposition rate is mainly determined by the applied sputter power, the distance between the target and the substrate and the relative angle of tilt between substrate and sources. Since a variation of the angle corresponds to a complex change of the entire system, only the applied power was varied for the subsequent comparisons. In a first approximation the deposition rate linearly changes with the applied power. These changes can potentially lead to variations in the growth characteristics and subsequently effect the layer structure. Since, in addition to the geometry, the power was varied to produce samples of different compositions, it is important to see to what extent the applied power and thus the changed coating rate has an influence on the sample properties.

Fig. 5.7 and Fig. 5.8 show XRD measurements for two different samples of AlMgCuZn, which only differ in the applied powers during the sputtering process, thus, the deposition rate varied. The resulting rates were determined to be 75 nm/min and 115 nm/min. A comparison of the two diffractograms shows that the measured peaks appear predominantly at the same positions. Only minor deviations can be detected, indicating that the crystal structure is identical for both samples.

Also, the effect on the hardness as a function of the applied power and, therefore, at different deposition rates is shown in Fig. 5.9 c) and d) for the as deposited and annealed state. To keep the analysis simple, pure Cu samples with a thickness of 10 μm produced with a deposition rate of 65 nm/min, 100 nm/min and 130 nm/min were analyzed. Here, no significant difference can be observed between the different deposition rates. Again, the difference in the indentation hardness between the untreated and thermally post-treated samples can be seen.

In Fig. 5.9 a) and b), SEM micrographs of the surface of the samples prepared under different deposition rates are presented. While a slight increase in grain size is evident for the as deposited condition, it is not visible for the thermally post-treated one. Thus, in the investigated range of 65 nm/min to 130 nm/min, the deposition rate does not seem to exert a significant influence on any of the properties under consideration.

The results are supported, for instance, by studies of Thornton [166] and Movchan and Demchishin [167], who did not observe any significant influence of the deposition rate on the formed structures in the low temperature range (T/T$_m$ = 0.25 - 0.3 with T$_m$ being the melting temperature of the sample material).

a)

b)
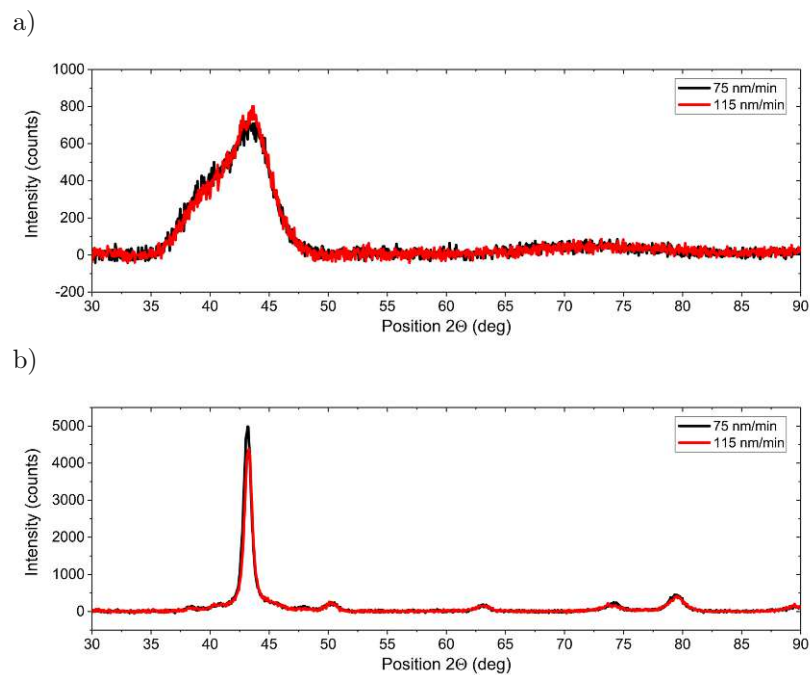
Figure 5.7.: XRD measurements of two untempered AlCuMgZn samples prepared at different deposition rates. a) and b) show different positions and accordingly different compositions.

a)

b)
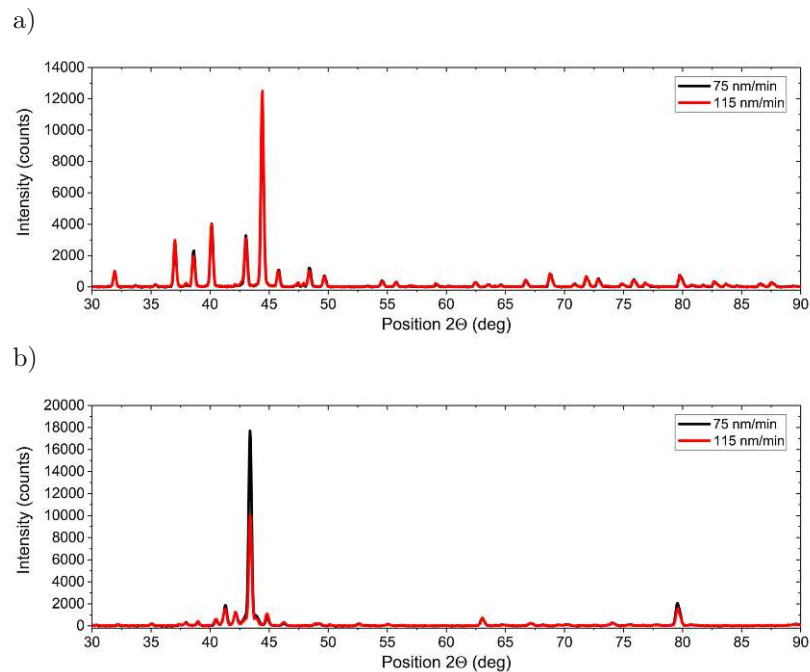
Figure 5.8.: XRD measurements of two AlCuMgZn samples prepared at different deposition rates after 24 hours of thermal post-treatment at 350 °C. a) and b) show different positions and accordingly different compositions.
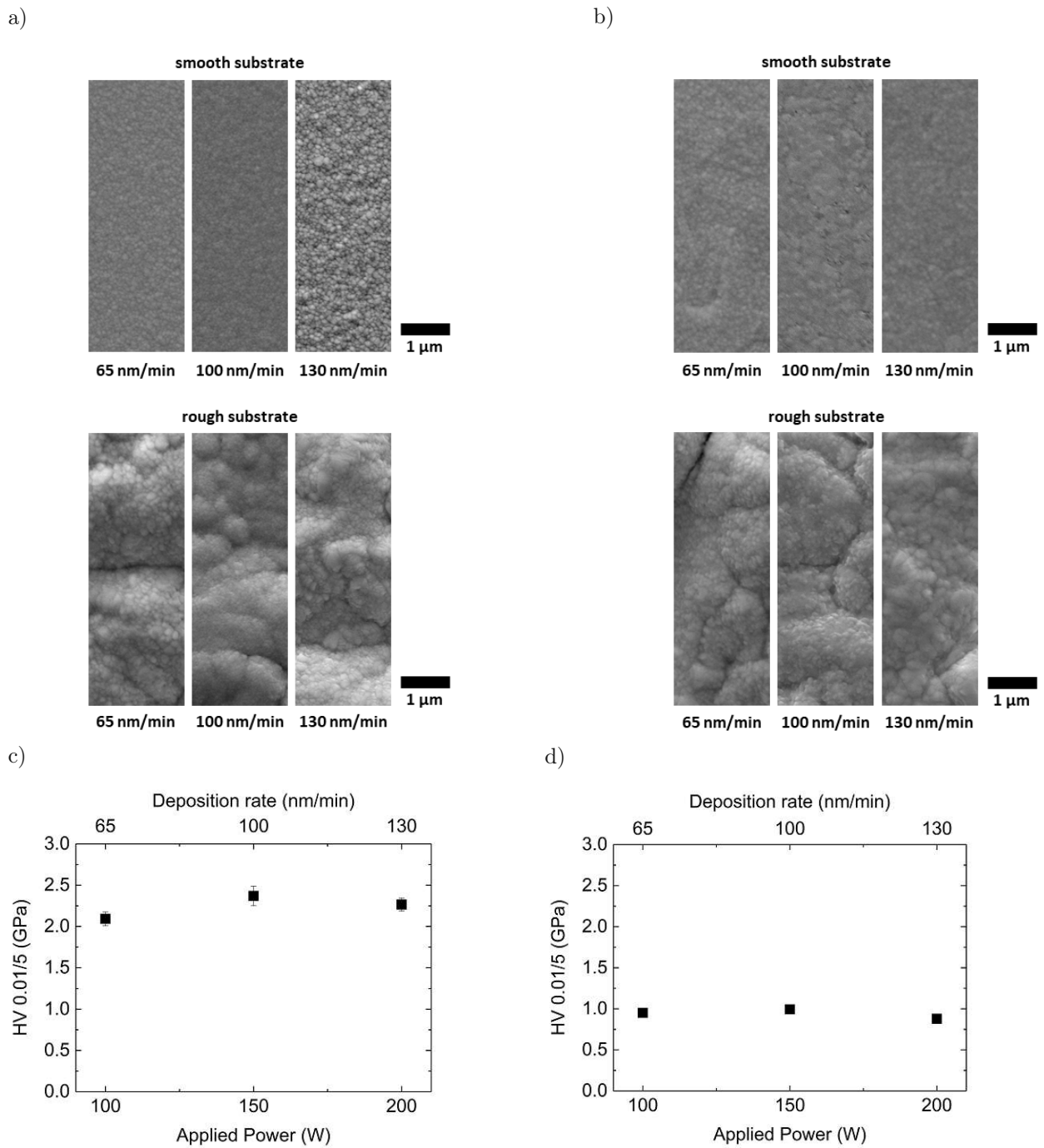
Figure 5.9.: Surface structure of the a) as deposited and b) annealed Cu samples. In each case, the upper panel shows the structure of the layer deposited on the smooth glass substrate, and the lower panel shows that on the rough substrate. Panels c) and d) show the indentation hardness of the Cu samples for different applied powers (i.e., different coating rates) for unannealed and annealed samples.

5.4. Influence of the Deposition Angle

The structure of the coatings produced by the sputtering process might be dependent on the geometrical arrangement of the substrate and the source during the coating process. Since in this work the chemical composition of the samples was varied by changing the applied power and the angle between substrate and source, the influence of the latter on, for example, the indentation hardness had to be determined. This was studied again on pure Cu films with equal thickness deposited under varying substrate-target angles. The variation of the relative angle indirectly influences not only the impingement angle of the coating particles but also the deposition rate. Based on the results of the previous section and the demonstrated lack of influence of the latter, all possible changes in the specimen properties can be attributed to the angle variation.
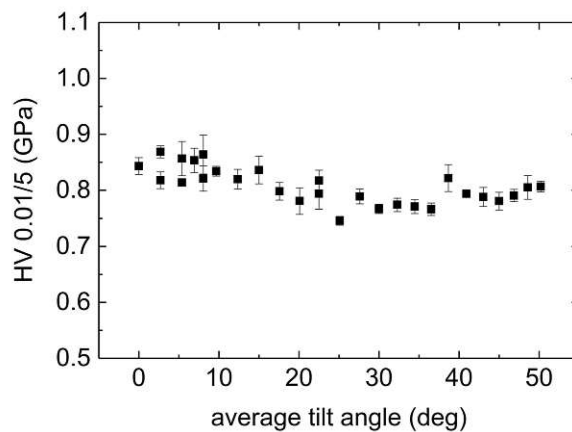
Figure 5.10.: Values of the Vickers indentation hardness as a function of the tilt angle (measured from the sample surface normal) relative to the coating source.

The influence of the angle of incidence of the coating material on the hardness can be seen in Figure 5.10. Four Cu samples of the identical thickness were produced, each with different relative orientations to the source during the coating process (see Fig. 3.8). Since the tilt of the substrate results in different distances and relative angles depending on the lateral position on the substrate, 7 measuring points were distributed over the entire width of the sample. Due to the geometry induced by the tilting, local variations in specimen thickness may occur on the substrate. However, based on the results from section 5.2, these small differences should not have a significant effect on the mechanical property of the indentation hardness.

Comparing the hardness values at increasing angles, a decrease in indentation hardness of approx. 10 % was observed. This can be explained by small changes in the structure due to varying growth directions and dynamics caused by the tilt. Fig. 5.11 shows the sample's surface for different relative exposure angles towards the sputter source. The small deviations in the indentation hardness are supported by the appearance of slightly different surface

structures composed of granular textures in the SEM images. No significant variations in hardness are apparent across a single sample. This is consistent with the investigations at different thicknesses, as the increased distance only leads to small variations in the sample thickness. Due to the relatively high initial thickness, these variations play a minor role.
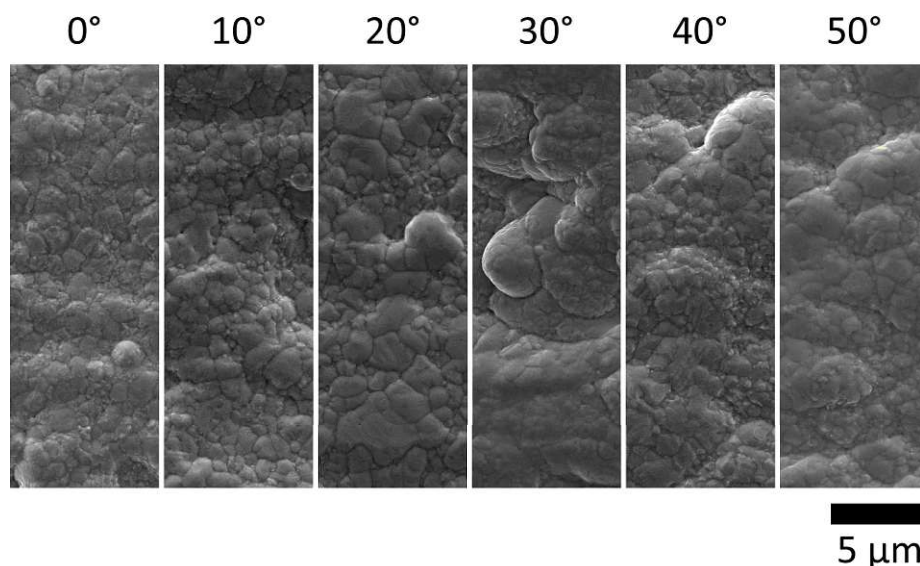
Figure 5.11.: SEM images of the surface structure of pure Cu samples (thickness of 10 μm) at different relative tilting angles between the sputter source and the measurement point on the substrate.

In summary, when comparing samples produced at different relative substrate-target angles, indentation hardness deviations of max. 10 % were observed. No significant variations in hardness could be found within a single sample, therefore the hardness trends observed on a single sample can be considered trustworthy.

5.5. Influence of the Substrate Roughness

Insufficient adhesion of coatings on substrates induced by compressive stress within the specimen is a well-known problem, especially when relatively thick coatings are employed [168–170]. Measures to increase the adhesion include the application of an adhesion promoter. For example, a Cr layer of the thickness of a few 100 Å can significantly improve the sticking properties of metallic layers to glass substrates [171]. This idea was discarded because of concerns about potential interactions with the actual sample due to diffusion. Another way to increase adhesion and relieve layer stresses, which may ultimately lead to detachment of the specimen film from the substrate, is to increase the substrate temperature during coating. Since this leads to significant variations in sample structure and texture, this method was also rejected.

The use of roughened substrates was chosen to increase the coating adhesion to the point

where no detachment of the samples occurred. The roughness of the substrate allows the coating to anchor more effectively and reduces stresses. The usage of a roughened substrate potentially has an impact on the manufactured samples. In particular, the surface structure can be affected by shadowing effects during the coating process due to the rough substrate structure. In the SEM images shown in Fig. 5.9 a) and b) and in Fig. 5.12, the surface structure of the samples, which are determined on the smooth and the rough part of the glass substrate, are displayed. At first glance, clear differences can be seen. In the case of the samples deposited on rough substrates, coarser flake-like textures are visible. However, the finer textures are the same for both substrate types. In the case of the pure Cu samples in Fig. 5.9 a) and b), fine-grained textures dominated the surface appearance. These features are as well visible superimposed on the coarse structures. Similar behaviour can be observed for a representative AlCuMgZnTi sample shown in Fig. 5.12 a) and b). The finer scaly textures are evident on both, the smooth and rough samples.

Samples exhibiting extended elemental segregation were also analyzed on smooth and rough substrates (Fig. 5.12 c) and d)). In addition to the aforementioned differences in the larger textures, the same features are evident in both images. The segregation showed comparable manifestations regardless of the substrate's texture.

An essential part of the sample characterization was the chemical composition analysis. Since the surface condition of a sample potentially distorts the compositional analysis by EDX, the relative proportions of alloying materials were determined and compared on smooth and on rough parts of the glass substrate. The results of such a series are shown in Table 5.1. It could be shown that, despite of the varying surface structure, no significant differences in the chemical composition or the results of the EDX evaluation were detectable.

Table 5.1.: Elemental analysis of an AlMgZn sample measured at 3 different measuring points on a smooth and a rough substrate.

smooth substrate				rough substrate			
	pos. 1	pos. 2	pos. 3		pos. 1	pos. 2	pos. 3
Al (at%)	17.7	36.7	42.0	Al (at%)	17.8	35.8	40.0
Mg (at%)	35.4	25.7	23.2	Mg (at%)	37.7	27.0	25.1
Zn (at%)	47.0	37.5	34.8	Zn (at%)	44.4	37.2	34.9

The indentation hardness of the identical sample composition was determined for one specimen on the smooth and on the rough substrate part. The results are shown in Fig. 5.13. In absolute terms, the indentation hardness showed minor deviations depending on the surface structure of the substrates used. However, the direct comparison also shows the same trends for both series of measurements.

The presented results showed that the physical properties of samples deposited on the rough glass substrates show trends that are mainly associated with the alloy compositions. The nature of the substrates plays a role mainly in the surface texture, which must therefore be

a)

b)

c)

d)
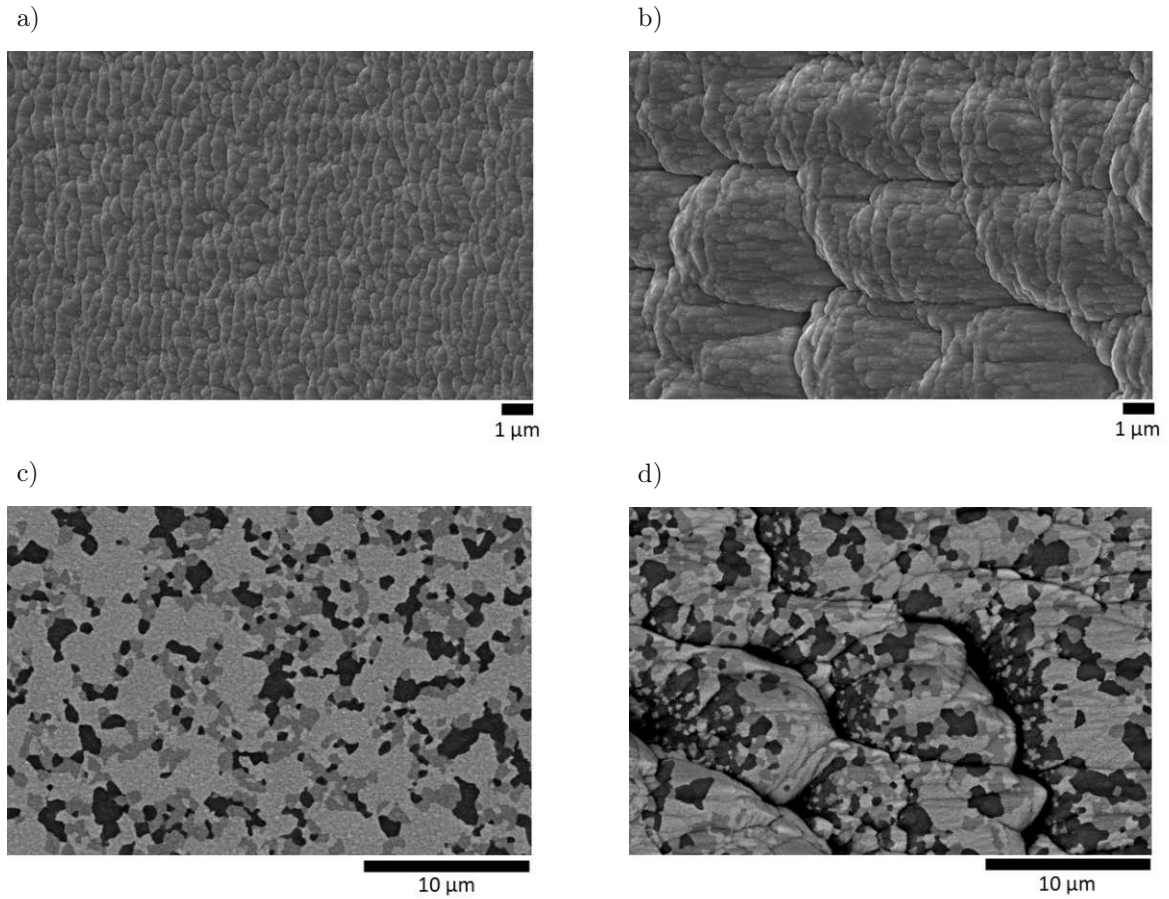
Figure 5.12.: Surface structure of an AlCuMgZnTi sample deposited on a) a smooth and b) a roughened glass substrate. The SEM images of an AlCuMgZn sample on a c) smooth and d) roughened substrates show the same segregation behaviour of dark Al-rich regions in both cases.
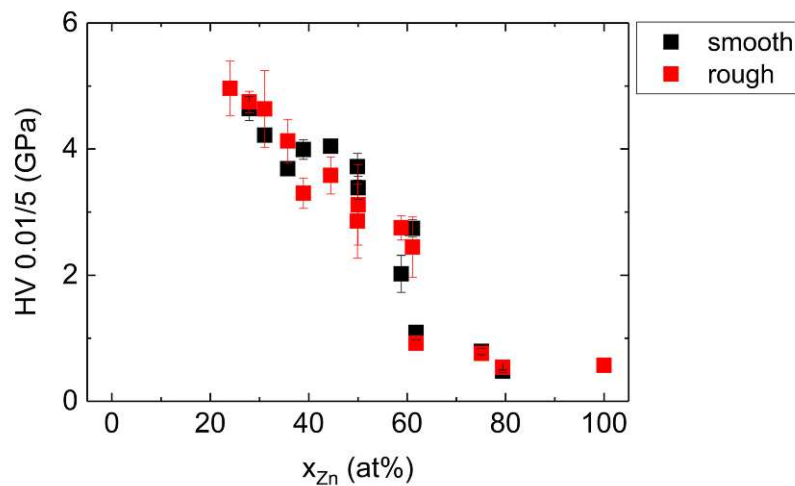
Figure 5.13.: Comparison of indentation hardness of AlCuMgZn coatings with varying Zn content applied on smooth and rough substrates.

considered with caution. Analysis of 10 μm thick films deposited on both, rough and smooth glass substrates showed two distinguishable feature types on different size scales. Features with extensions in the range of several μm are due to effects caused by the substrate surface structure. Relatively coarse flake-like features are formed due to the initial roughness and, subsequently, growth dynamics caused by shadowing. The smaller structures were observed on both the smooth and rough specimens. These appear to be characteristic for the sample and independent of the substrate texture. Even dynamic processes such as element segregation were observed equally on smooth and rough substrates. However, responses to the rough surface texture can be seen as additional information. Conclusion about the diffusion behaviour of different alloys could be drawn by comparing the ability to compensate texture irregularities. The hardness values showed comparable behaviors. Due to the simpler evaluation and the higher probability of valid hardness impressions, the indentation hardness was determined on smooth areas of the specimens whenever possible.

5.6. Conclusion

Since the effects of the relative proportions of alloying elements are to be studied, the influences of other parameters on the atomic, mechanical and structural properties must be estimated. Here, the angle of the substrate to the coating sources showed no significant difference in the mechanical properties under consideration. Similarly, the crystallography and indentation hardness did not exhibit any deviations in samples produced with different deposition rates. However, it could be shown that the variations of the process parameters deposition rate and deposition angle might influence some of the sample properties, but cannot be solely responsible for significant alterations. Therefore, it seems legitimate to attribute massive variations in hardness and crystallography to different compositions. Care must be taken

when analysing the (surface-)structures, as these depend on both the texture of the substrate and the coating angle.

As expected, thermal post-treatment showed large effects on both crystallographic and mechanical properties. Due to the high cooling rates that occur during sputter deposition, thermal post-treatment is essential. By post-treatment at 350 °C for 24 hours, an equilibrium state could be reached. XRD measurements and the formation of crystal structures showed clearly that this was the case. In addition, hardness measurements showed values similar to those reported in the literature for classically manufactured materials.

Furthermore, it was demonstrated that the substrate effect should have no influence on the layer hardness measurements for a sample thickness of 10 μm. Likewise, at varying coating angles, an approximately constant indentation hardness value showed that hardness changes of more than 10 % could not be explained by process-related deviations.

Nevertheless, in order to minimize the errors due to the process parameters, an effort was made to generate and compare overlapping compositions of specimens prepared with different parameters. The aim was to provide an additional test for the validity of the obtained data.

6. Systems

The following chapter describes the multi-metal systems investigated in this thesis. As a starting point, technologically relevant materials for alloys were selected. Subsequently, the number of elements was successively extended in order to move towards the formation of high entropy alloys.

The core of these investigations were Al-Cu-Mg-Zn based alloys. To initially reduce complexity, subsystems with binary and ternary compositions were extracted and characterized individually before various trajectories in the 4-dimensional composition space were studied. Based on these results, more exotic elements of other groups were added to the investigated subsystems. Finally, complex alloys with five different elements were synthesized.

Some element specific properties of the atoms of the starting quaternary alloying system are given in Table 6.1. Among the important factors influencing bonding and promoting parameters for the formation of high entropy alloys are the atomic radii, electronegativity and valence electron concentration (VEC).

6.1. Al-Cu-Mg-Zn based Alloys

Al-based alloys are especially technically relevant, in particular, due to their low weight. They quickly became popular after the development of the Hall Heroult process and are, among other things, used in airframes. [174, p. 60]. Furthermore, other low weight alloys, including materials like Mg, have been developed. In order to eliminate drawbacks, such as limited properties in terms of hardness and strength or high manufacturing cost, that occur when using low weight alloys [175, 176], a variety of Al-based alloys have been developed and researched. Al-Cu-Mg and Al-Cu-Zn-Mg are the main systems for this industrial branch [174, p. 60] and will therefore be examined in detail.

Table 6.1.: Element specific properties of Al, Mg, Zn and Cu [11, 172, 173].

	Mg	Al	Cu	Zn
atomic mass (u)	24.3	27	63.5	65.4
atomic radius (pm)	150	125	135	135
electronegativity	1.31	1.61	1.9	1.65
density (g/cm^3)	1.73	2.7	8.92	7.14
VEC	2	3	11	12
T$_{melt}$ (°C)	639	660	1083	420
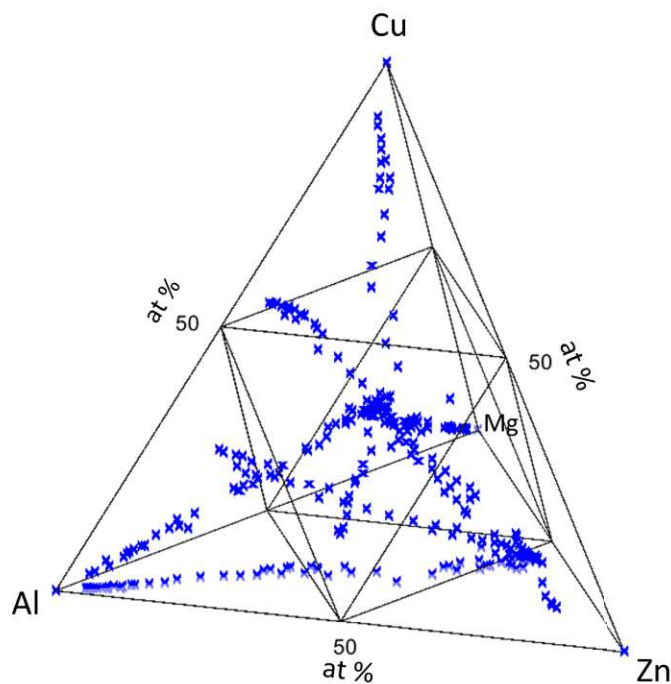
Figure 6.1.: 4-dimensional composition space of an Al-Cu-Mg-Zn system. The blue crosses correspond to investigated relative concentrations of the individual components. For better clarity, the binary trajectories (Al-Zn and Al-Cu) are not plotted.

The experimental strategy to screen the complex multi-component system with a maximum of four elements can be visualized using a tetrahedron (see Fig. 6.1). The tetrahedron vertices herein correspond to the pure elements, the sidelines to the binary compositions enclosed by the vertices, the planes the ternary compositions, and the inner part of the structure the quaternary composition space. Fig. 6.1 also shows the compositional trajectories studied in the Al-Cu-Mg-Zn system (for clarity, the binary AlZn and AlCu trajectories have been omitted). Each of the plotted dots represents a measurement point, for which the surface structure, crystallography, mechanical properties and morphology were investigated. This allowed the fast and effective screening in this complex compositional space.

Firstly, 'simple' binary systems were investigated to validate the applicability of the analytical approach proposed in this thesis. These systems have already been studied extensively in the literature. Thus, a comparison to the samples produced in this work could have been made. Al and Cu, as well as Al and Zn mixtures, were used as model systems, which will be discussed in the following sections.

6.1.1. Al-Zn

The AlZn system has been the subject of a large number of studies [177]. This class of alloys shows an increased interest for industrial applications due to its high corrosion resistance and tribological properties [178–183]. Zn and Al interact relatively weakly with each other,
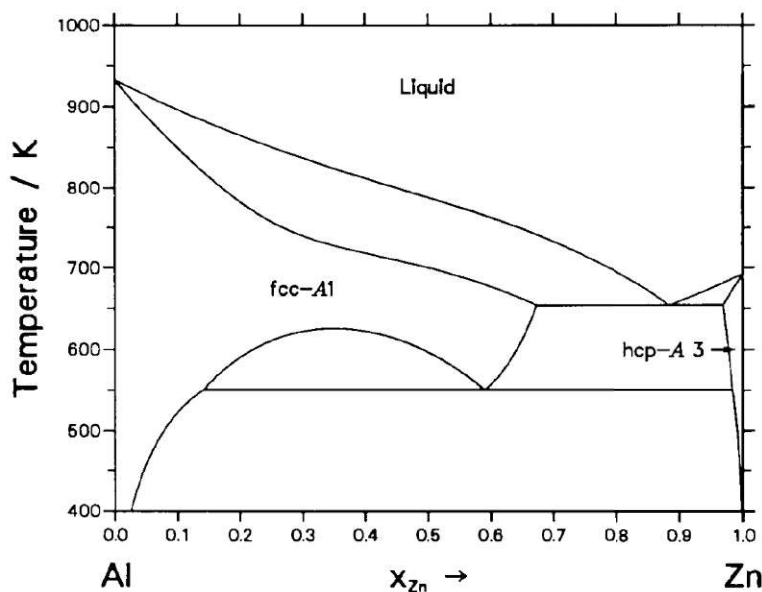
Figure 6.2.: Binary AlZn phase diagram reproduced from ref. [141].

preventing the formation of intermetallic AlZn phases [184]. Both elements have different anisotropy and atomic radii, which affect the microstructure. Because of this, varied interfacial energy modifying morphologies and directions of dentric growth are formed [179, 183–185]. Studies showed that the Zn content influenced and promoted dendritic growth [185–188]. The formation of grains and structures in the alloys leads to the variation of mechanical properties, for example, the increase of hardness. This increase was explained by the formation of precipitates acting as obstacles to dislocation movement [123]. In addition, the refinement of the microstructure is known to have positive effects on plasticity [178].

Figure 6.2 shows the phase diagram of the binary Al-Zn system. It can be seen that the AlZn system does not show pronounced mixed phases. The solubility of Zn in Al at the eutectic temperature of 277 °C amounts to 16.5 at%. Above this temperature, the solvus curve is on the Zn rich side of the FCC miscibility gap. The maximum solubility here is about 67 at%. In contrast, the maximum solubility of Al in Zn is approximately 2.8 at%. [189]

The computational methods described in chapter 4.2 were used to calculate the material distribution for different relative compositions of Al and Zn (Figure 6.3). Panels a) to c) show the initial random arrangement of Al and Zn atoms which corresponds to the as deposited state of the sputtered films. These are subjected to heat treatment at a temperature of 350 °C in the calculations. Clearly separated regions of Al and Zn developed over the entire concentration range are shown in panels d) to f). This finding suggests that the computational approach can well reproduce the expected crystallographic state derived from the phase diagram for the binary AlZn system. To compare the theoretical results with experimentally prepared samples, specimens with the concentrations shown in Fig. 6.4 c) were synthesized.

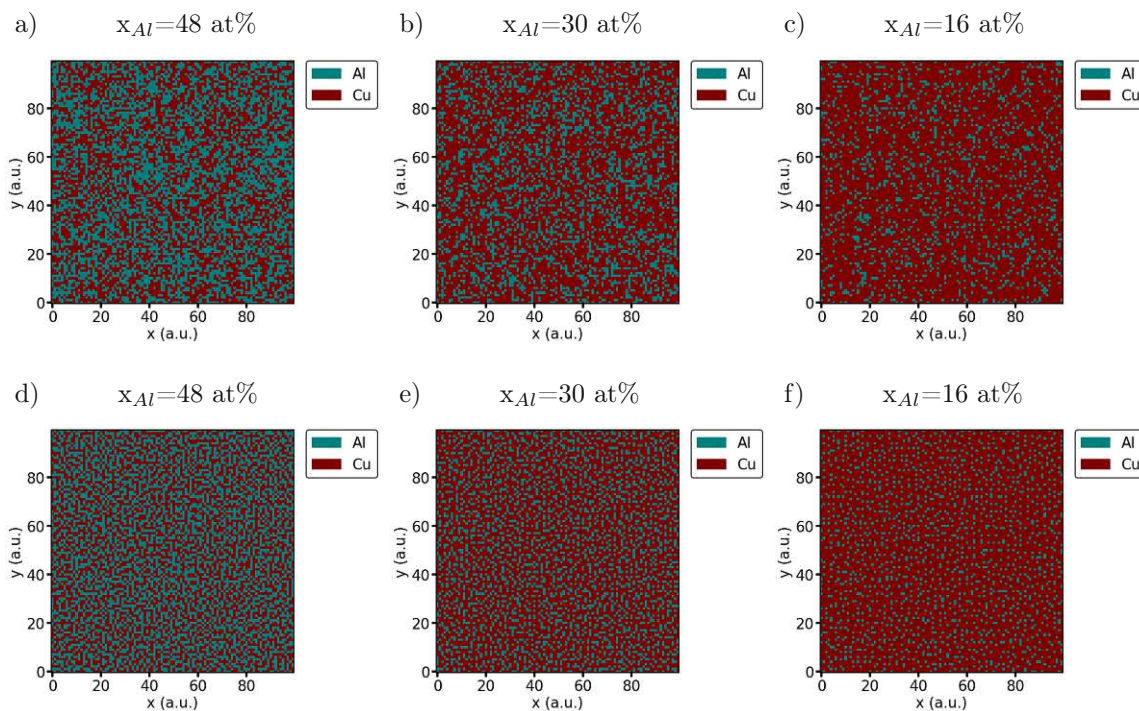Fig. 6.4 a) and b) show SEM images of the samples at different compositions. In panel a)
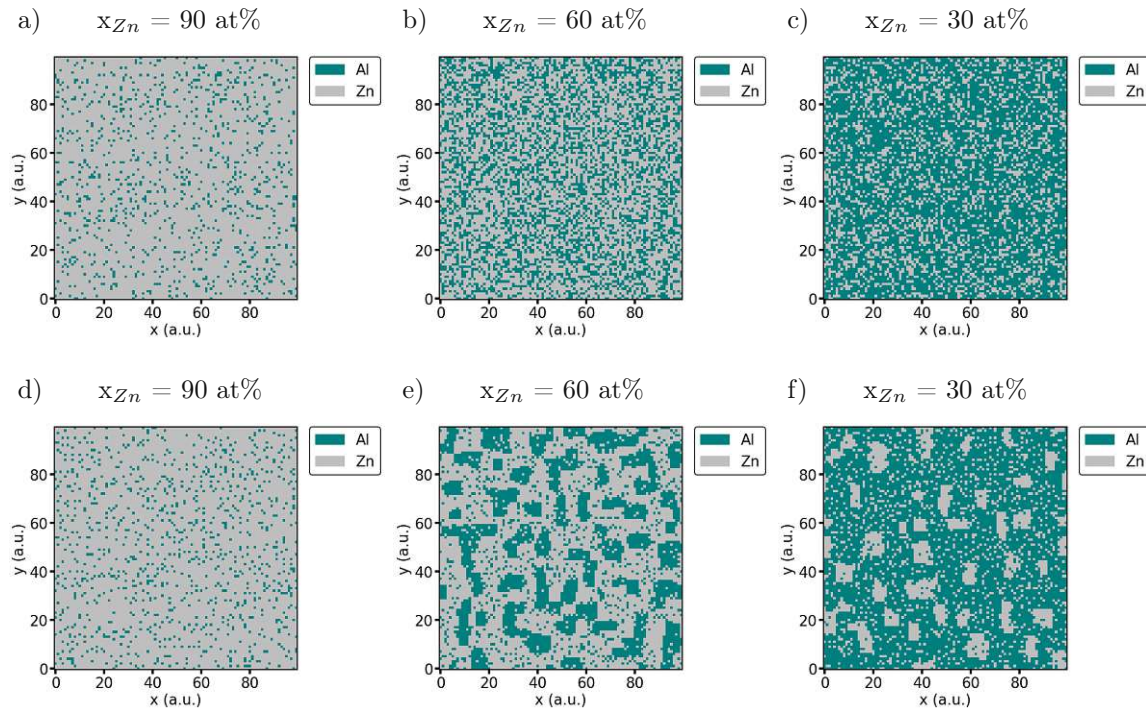
Figure 6.3.: a) - c) show the (random) initial state of the simulated AlZn array for different compositions. In d) to f) the respective final states after thermal annealing are shown. The development of pure Al and Zn precipitates can be observed.

backscattered electron micrographs of the cross-sections of the samples exhibit fine grains for all regarded compositions. The image contrast suggests a separation of the light element Al (dark areas) and the heavy Zn (light areas). This is in accordance with the overall increase of the dark areas with increasing Al content. In Fig. 6.4 b), the surface of the samples can be seen at the corresponding locations and compositions. The structure is dominated by granular structures over the whole compositional space considered. The size of the individual features is enhanced with increasing Al content and the texture becomes coarser. The overall dentric structures are consistent with the behavior of AlZn alloys described in the literature [185–188]. XRD measurements and subsequent quantitative phase determination and analysis revealed a binary phase system at all compositions (Fig. 6.5). The samples crystallized into a hexagonal Zn and a cubic Al lattice without any indication of crystallographic mixed phases. The formation of these phases, which are supposed to be present in the equilibrium state according to the phase diagram, confirms that the thermal post-treatment was sufficient to transform the system into an equilibrium state. The simulations performed with the simple calculation tool could reproduce the experimentally observed trends. The segregation of Al and Zn, which was clearly shown in the simulations, was verified by the XRD measurements.

All the presented results are consistent with previously published reports and the phases suggested by the binary phase diagram. The very good agreement of the experimental and theoretical results with those established in the literature showed once again the applicability
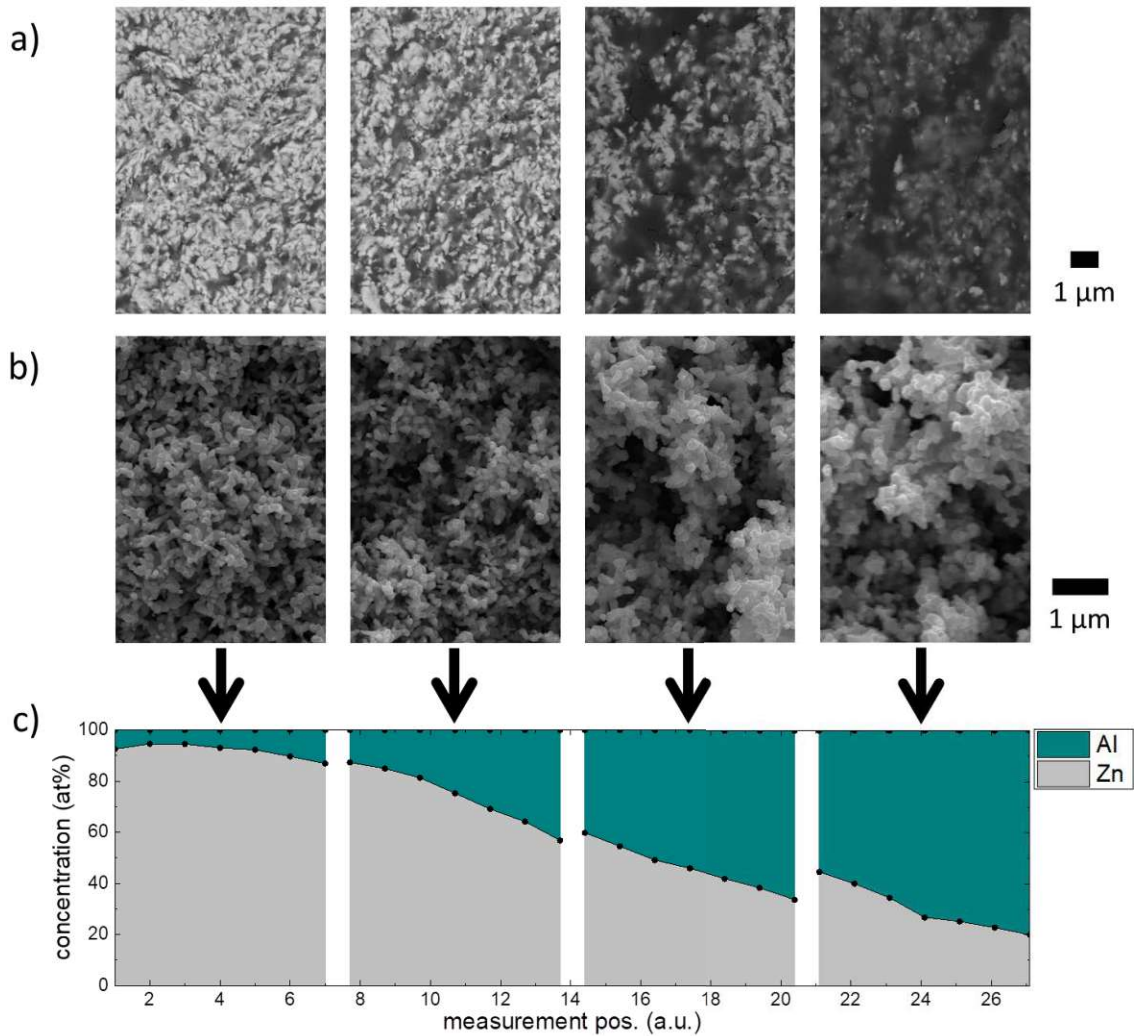
Figure 6.4.: a) Backscattered electron images of metallographic cross-sections of the sample at different Al-Zn compositions. b) shows the surface structure of selected AlZn samples and c) the chemical analysis exhibiting the relative Al and Zn content.

of the proposed methods.
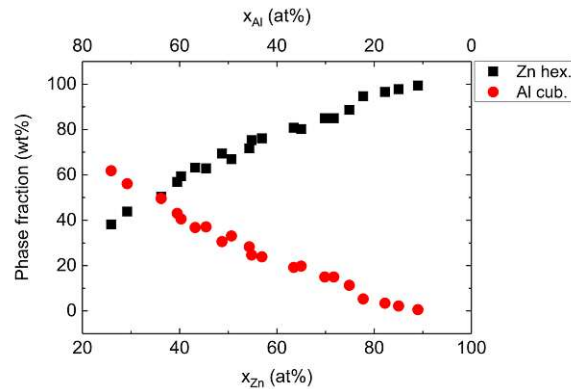
Figure 6.5.: Rietveld quantification results show the presence of two separated Al and Zn phases over the whole compositional space under consideration.

6.1.2. Al-Cu

The second binary system studied experimentally consisted of the elements Al and Cu. These elements are widely used in alloys for applications in the fields of aerospace and the automotive industry due to the good strength to weight ratio [176]. The corresponding phase diagram is shown in Figure 6.7 a). A relatively simple alloying behaviour for Cu concentrations < 33 at% and equilibrium temperatures < 800 K can be observed. Here the system segregates into a tetragonal Al_2Cu phase (shown as ϑ in the diagram) [190] and a pure Al phase. The pure Al phase crystallizes in an FCC lattice and the solubility of Cu in Al amounts to approximately 2.5 at% [191]. At higher Cu contents, a variety of intermetallic AlCu phases form. In the range of around 50 at% of both elements, monoclinic and orthorhombic crystal structures were reported. Between 30 at% and 40 at% Al the so-called γ-brass with differently assigned structures (cubic, monoclinic, rhombohedral) occurs. At Cu concentrations > 70 at%, the BCC β-brasses form at elevated temperatures, which transition similar to the γ-brasses into a pure FCC Cu lattice at Cu concentrations > 80 at%. [191, 192]

Al and Cu compositions were simulated using the approach described in chapter 4.2 to predict phase formation. Selected simulated samples are shown in Fig. 6.6. These indicate the transition from a random arrangement of Al and Cu atoms corresponding to the as deposited state in panel a) to c) to the equilibrium state in panel d) - f). The comparison suggests the formation of periodic patterns at an equal composition of Al and Cu, which correspond to the complete mixing of Al and Cu. This can be interpreted as the formation of an intermetallic phase. As the Cu enrichment increases, the Al domains become smaller and the embedding of individual Al atoms in a Cu matrix becomes apparent (see Fig. 6.6 e) and f)). This can be understood as the formation of a pure Cu phase containing Al at Cu lattice sites. In comparison with the binary phase diagram, this corresponds to the formation of the terminal solid solution of Cu.

An AlCu sample, covering a composition range from 50 at% to about 83 at% Cu, was prepared to compare phase diagrams based on classical material synthesis to the simulations. The

Figure 6.6.: a) - c) show the (random) initial state of the simulated AlCu array for different compositions. In d) to f) the respective final states after thermal annealing are shown. The development of AlCu mixtures with increasing Cu concentration is demonstrated.

sample was thermally post-treated at 350 °C ($\approx$ 623 K) and several measurement points were analysed afterwards for their crystallography using XRD. The results of the Rietveld analysis are shown in Figure 6.7 b). Here, for the equal Al-Cu fractions, the crystal system is characterized by intermetallic AlCu phases. A monoclinic and an orthorhombic lattice were detected using a "search and match" approach. These prototypes consist of large complex unit cells. In the range of 50 at% - 80 at% Cu content, an Al_4Cu_9 cubic phase is additionally present, with a maximum quantitative presence at about 65 at% Cu concentration. At higher Cu contents (Cu > 65 at%) this phase is successively replaced by a pure FCC Cu lattice, which fully dominates the crystallography above a concentration of x_{Cu} > 80 at%. The comparison with the classical phase diagram shows that the experimentally identified phases are identical to the predicted phases. The concentration ranges in which mixed phases and crystallographic phase transitions are predicted could be observed in the analysis of the experimental data. This result shows that the pursued approach can be considered as an approximation to classical material synthesis. Furthermore, the comparison with the results of the simulations shows that even this simple computational approach predicts qualitatively the results. The calculations predicted correctly an increase of the AlCu mixture with decreasing relative Cu content.

The surface structure at different Al to Cu ratios can be seen in Fig. 6.8 a). Here clear differences are apparent depending on the composition. While coarse textures with deep fissures are visible at high Cu concentrations, these become finer and denser at more balanced

a)

b)
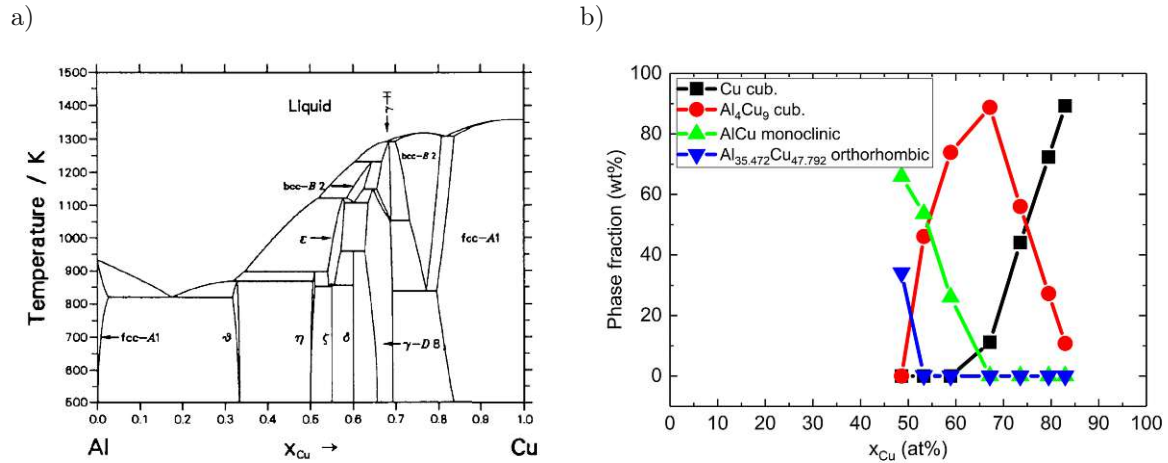
Figure 6.7.: a) Binary Al-Cu phase diagram [141]. b) The quantitative analysis of the XRD measurements showed a transition from a pure cubic Cu lattice to a binary AlCu mixed system (monoclinic and orthorhombic).

compositions. The secondary surface texture is composed of fine grains on the lamellar or flaky features. This fine-grained structure was already found in pure Cu samples during the investigations in Chapter 5.3, while the fissures were not present. This finding suggests that the coarse columns are generated by the substrate's tilting towards the sources during the deposition process.
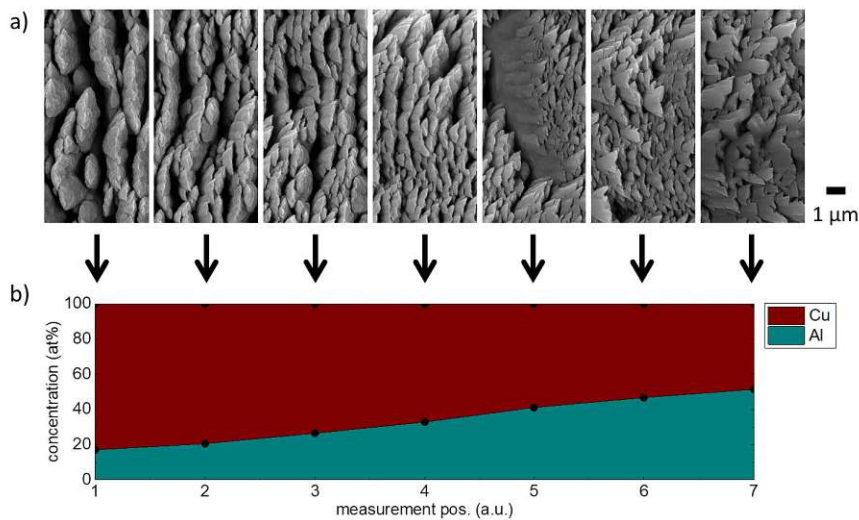
Figure 6.8.: a) Surface texture of AlCu samples at different sample compositions showing transition from larger to finer flaky textures. b) Relative Al and Cu content of the samples determine from EDX analysis.

6.1.3. Al-MgZn

An Al-MgZn element combination was chosen as the starting model for ternary alloys. This system has already been described in detail in terms of structure and mechanical properties due to its technical relevance [142–145]. Particularly when used in airframes for aviation, alloys containing these elements provide enough mechanical strength, and at the same time, are low weight. [174, p. 60].

The alloy consists of two light metals (Al, Mg) and a transition metal (Zn). For this material combination, it is especially interesting to investigate how a relatively strong binary system (Mg and Zn) reacts to an oversupply of a third component, in this case to Al. The binary MgZn phase diagram is depicted in Fig. 6.9 a). The Al-MgZn trajectory was studied by combining a pure Al target and a binary MgZn target and is depicted in Fig. 6.9 b).

a)

b)

c)
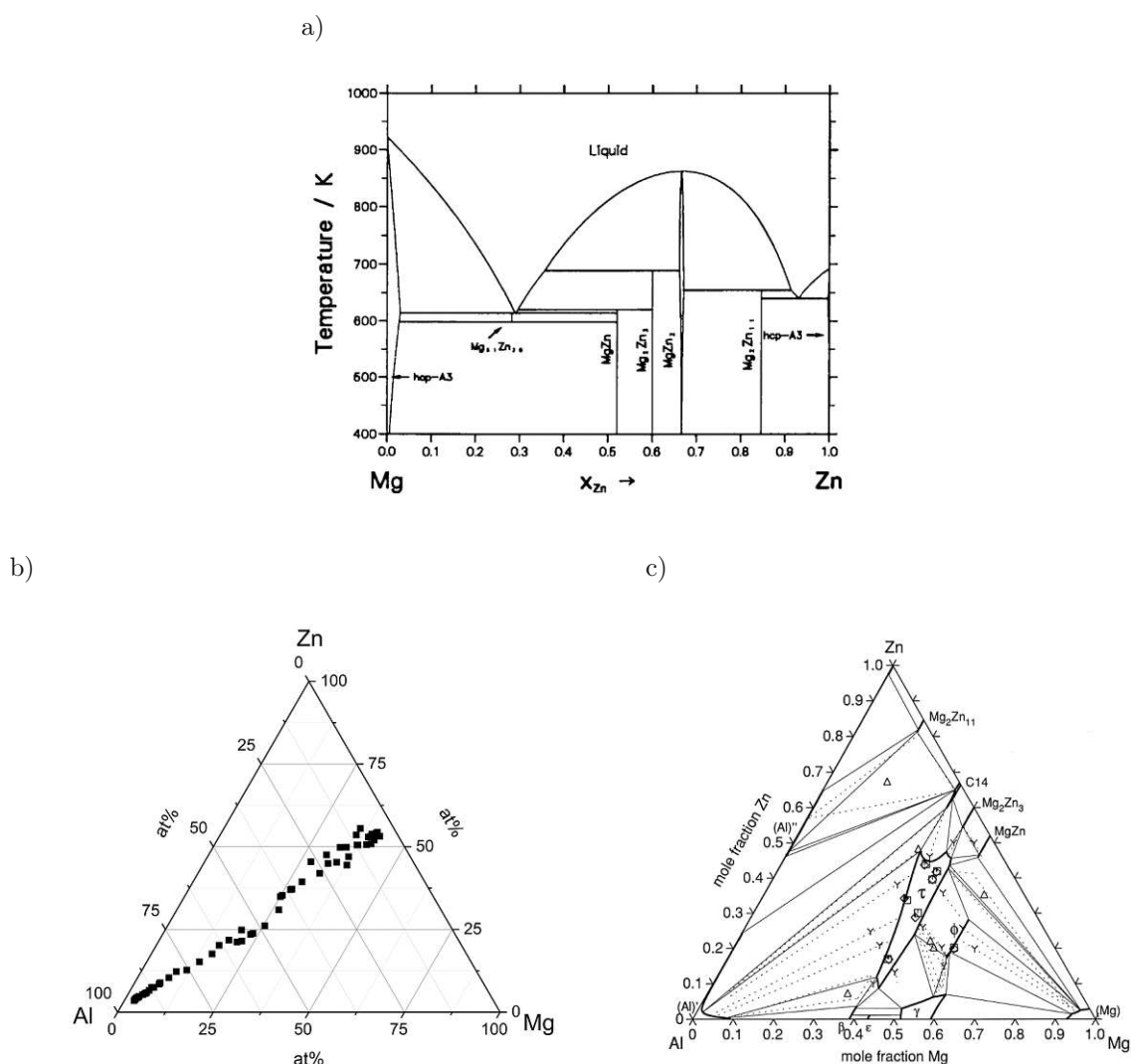
Figure 6.9.: a) Binary Mg-Zn phase diagram shows a variety of intermetallic compounds [141]. Panel b) shows measured compositions of the ternary Al-Mg-Zn system and c) the ternary phase diagram at an equilibrium temperature of 608 K [142].
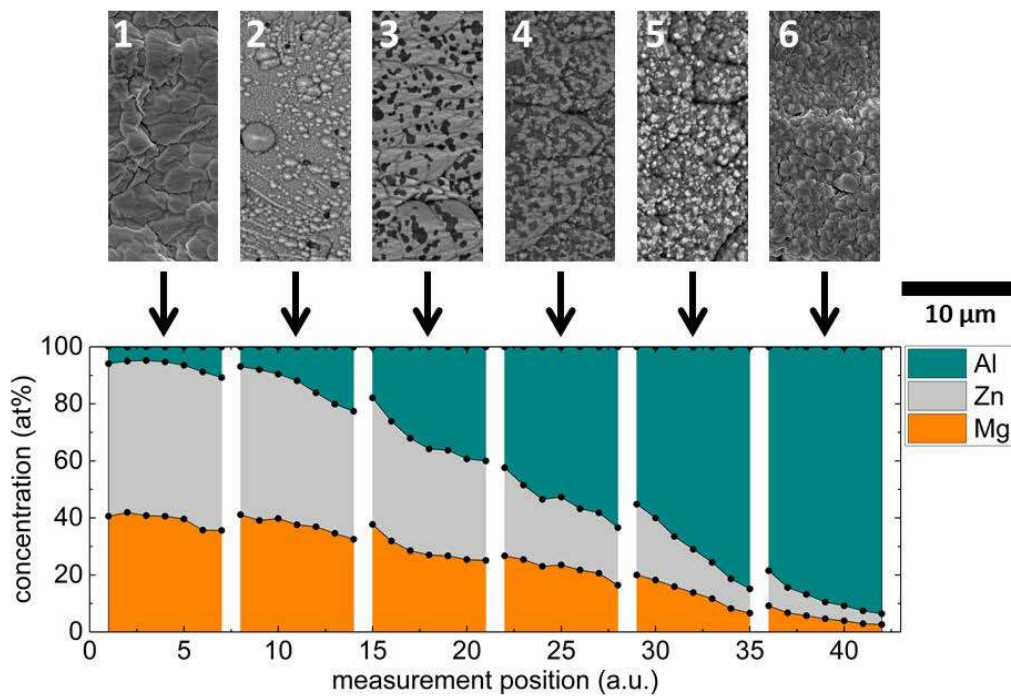
Figure 6.10.: Top Panel: Electron microscopic images of the sample's surface. The increase of dark precipitates (starting in image 3) is apparent with increasing Al concentration. Bottom panel: Chemical composition of the synthesised samples.

The chemical composition of the samples and the measuring points used for the characterization are shown in Figure 6.9 a) and Figure 6.10 a). The top panel of Figure 6.10 a) shows SEM images of the sample's surface. Here, dark precipitates are visible that occupy larger areas with increasing Al concentration. EDX mappings confirmed that these are Al-rich areas (Figure 6.11 a)). This finding will be further reinforced by the XRD results presented in the following paragraph. These Al-rich areas are not only visible on the sample's surface but also extend across the entire thickness of the layer, which can be seen in the FIB cross-section depicted in Fig. 6.11 b). The dark precipitates appeared only after thermal treatment, applied to bring the samples to an equilibrium state (see Fig. 6.12).

In order to make predictions of possible phase formations different relative compositions of Al and MgZn were simulated. Within the series, the Al content was increased from 5 at% to 95 at%. The Mg to Zn ratio was determined according to the target used in the subsequent experiments and corresponded to a ratio of approx. 1 : 1.3. Simulated distributions at all composition combinations showed Al-rich precipitates (compare Fig. 6.13). At low Al concentrations (0 at% - 5 at%), a periodic MgZn pattern appeared, which can be attributed to a MgZn intermetallic compound, as in the case of AlCu. At approx. 10 at% concentration, the formation of Al domains emerges and becomes progressively more pronounced with increasing Al amount until, finally, Al dominates (Fig. 6.13 b) to f)). In contrast to the Cu dominated samples in the binary AlCu series (Fig. 6.6 f)), the Mg and Zn domains are not statistically

a) b)
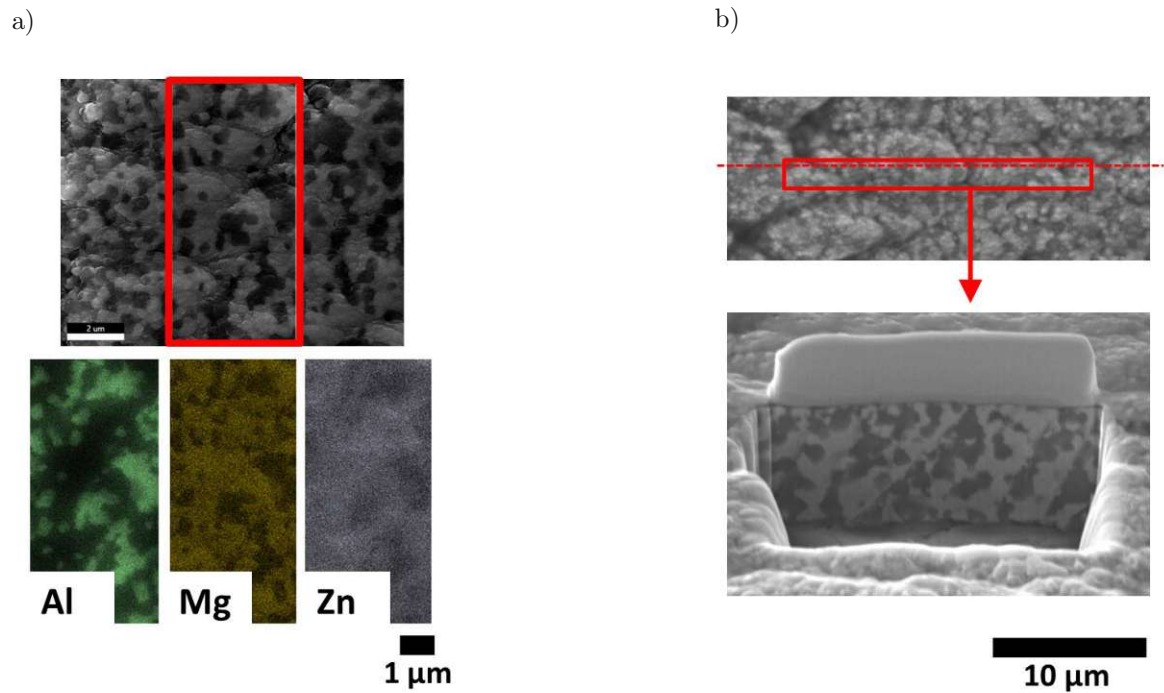
Figure 6.11.: a) EDX mappings assigned the dark spots to Al rich domains. b) The FIB cut shows the continuous segregation of the dark Al and light MgZn regions.
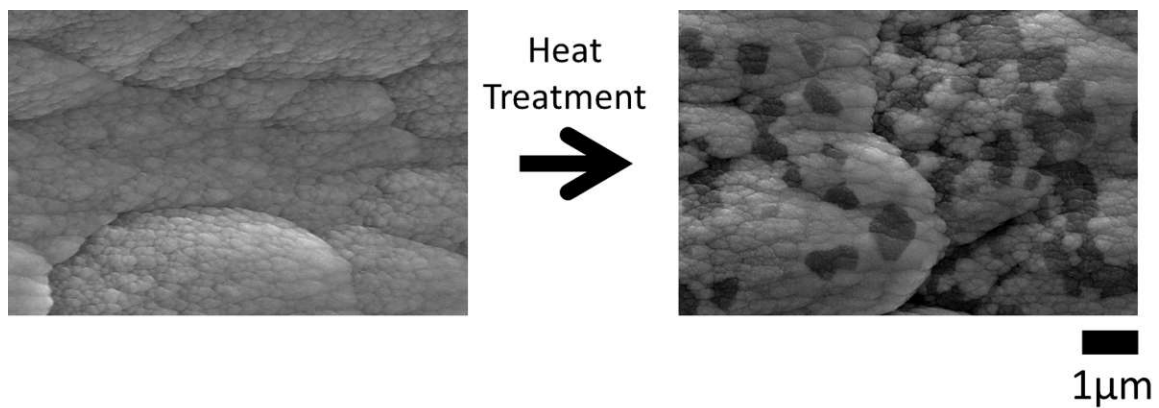
Figure 6.12.: Effect of the thermal treatment on the sample structure. The formation of dark percipitates after 24 hours at 350 °C can be clearly observed in the SEM images.
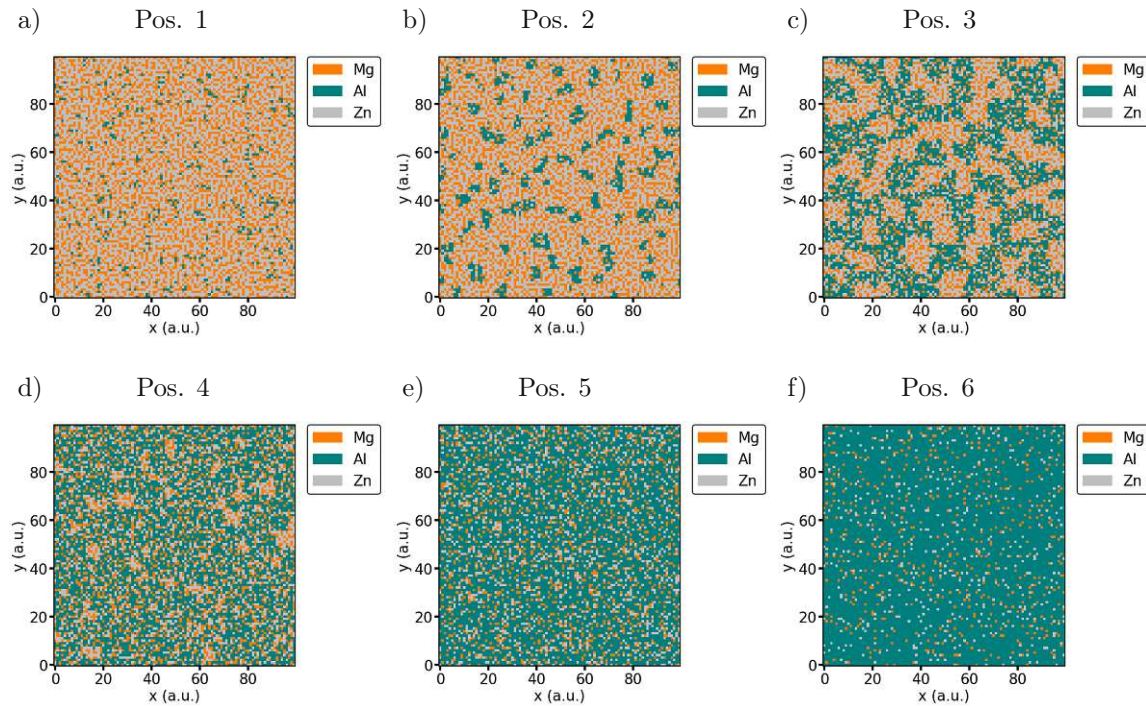
Figure 6.13.: Simulations of phase formation for different proportions of Al and MgZn. The Al content increases from a) 5 at% to f) 90 at%. Al-rich precipitates are visible over the entire concentration range. The numbers indicate the compositions noted in Fig. 6.10 a)

distributed over a wide compositional range. This finding suggests that there is no exclusive Al lattice (whose lattice sites are partially occupied by other atoms) but that there are at least two distinct phases.

The crystallography was determined by XRD along the depicted measuring points in the lower panel of Fig. 6.10. It is shown in Fig. 6.14 and Fig. 6.15 that the crystal structure is composed of 3 phases over the entire concentration range. Starting from the predominantly binary MgZn composition (dominated by the hexagonal $MgZn_2$ C14 Laves phase), the cubic Al phase is already established at approx. 7 at% Al concentration. This amount of phase steadily grows with increasing Al concentration. In the Al range of 43 at% - 48 at%, a third phase, a ternary AlMgZn phase following the Bergman phase prototype was identified, which disappeared again outside this narrow concentration range. A comparison with literature values confirms the experimentally observed findings [142]. From the ternary phase diagram in Figure 6.9 b), it can be seen that a two-phase equilibrium is predominant over a wide concentration range. In addition, a small area with the coexistence of a three-phase equilibrium is evident (in the Al range of 35 at% to 40 at%).

In order to draw conclusions on how different phases affect the mechanical properties of the alloys, the Vickers hardness was determined at measuring points distributed over the entire concentration range under consideration. The results of these measurements are shown in Fig. 6.15 b) and show a direct correlation between the phases found and the hardness of the

a)

b)

c)
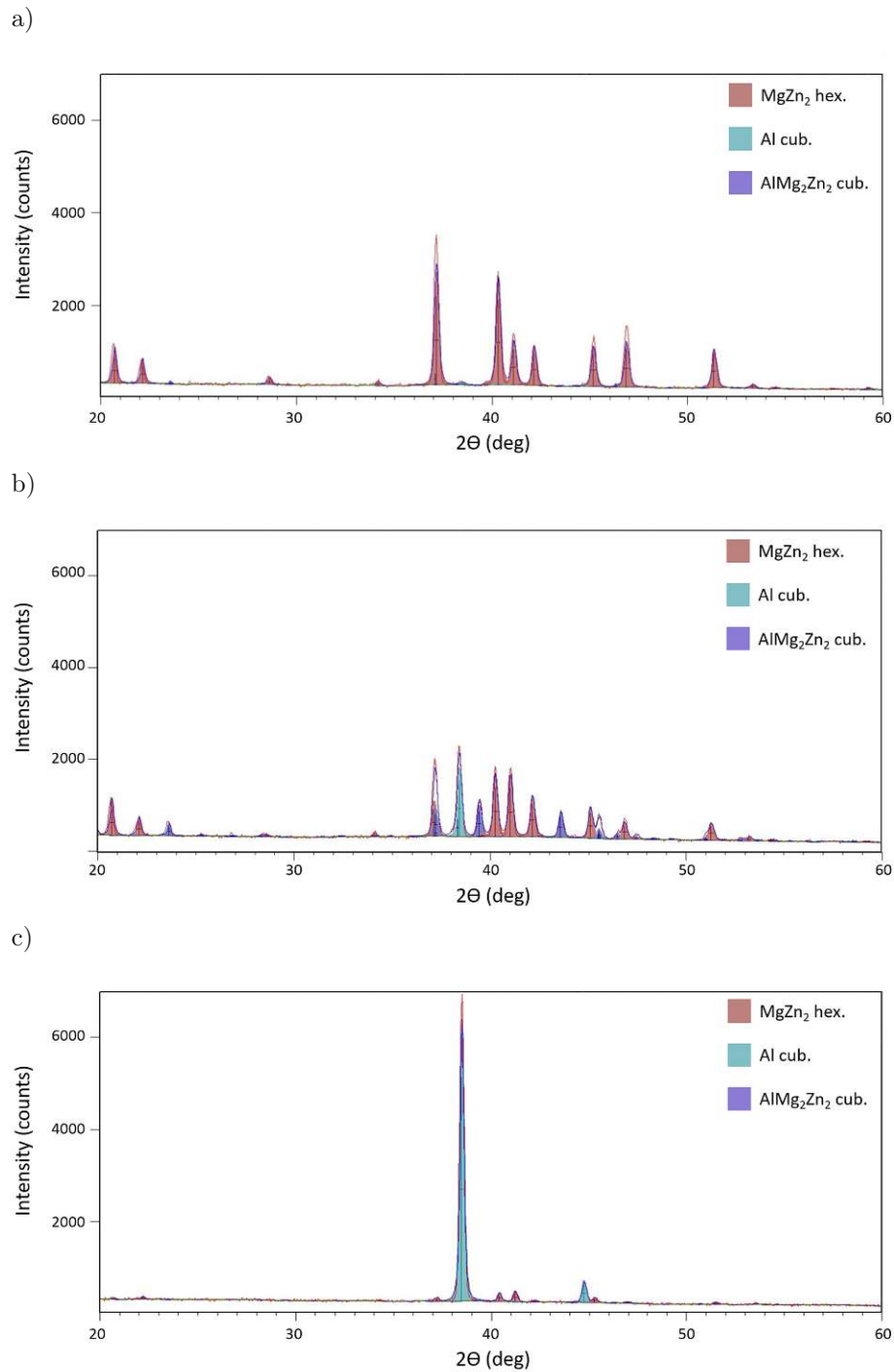
Figure 6.14.: XRD measurements of Al-MgZn samples with different Al concentrations a) $x_{Al} = 18$ at%, b) $x_{Al} = 42$ at%, and c) $x_{Al} = 94$ at%. The appearance and intensity changes of the various detected phases can be seen.

a)   b)
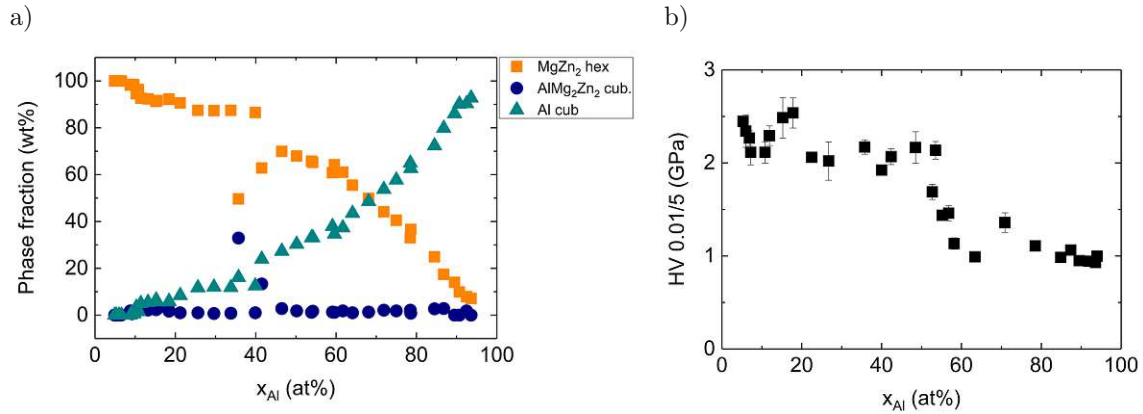
Figure 6.15.: a) Results of XRD phase analysis as a function of Al concentration. b) The measured indentation hardness shows a decrease with increasing Al content.

alloy. The hardness decreases with increasing Al concentration and dominance of the cubic Al phase. Given the low hardness of pure Al (HV $0.01/5 \approx 0.55$ GPa (compare also Table 6.5)) the decrease of the indentation hardness with more volume occupied by Al can be expected.

Summary

The samples with a ternary composition showed segregation behaviour dictated by the Mg-Zn interaction. This separation was visible through darker Al-rich areas in the SEM images. These results were confirmed by the analysis of the XRD measurements, where a transition of the $MgZn_2$ to a pure cubic Al phase was found. No significant mixing or formation of a ternary solid solution systems occurred over the entire concentration range. Only in a narrow concentration range a mixed phase assigned to the AlMgZn Bergman phase was identified. The analysis of the mechanical properties showed a steady decrease in the indentation hardness with increasing Al concentration. This can be explained by the coexistence of a harder MgZn phase and a softer Al phase. The direct comparison to the pure MgZn and Al samples showed that the hardness was higher in the ternary samples despite the identical crystallographic phases. This finding can be explained by the hardening effect when the number of defects is increased, in this case by the occupation of lattice sites by 'impurity' atoms. The computations of the bonding preferences in the ternary Al-Mg-Zn system showed excellent agreement with the analysis carried out by electron microscope and the crystal structure determinations by XRD. The segregation of Al and the formation of Al enriched domains could be reproduced by the simulations.

6.1.4. Al$_2$Cu-MgZn$_2$

Parts of the following section were executed in the course of a Master Thesis carried out within the project PL2NA [193].

Similarly to the ternary system, the strategy followed for the quaternary AlCuMgZn system was to combine two relatively "strong" phases in order to investigate the effects and influence

of an oversupply of alternative elements on the crystal structure. As can be extracted from the binary phase diagrams in Fig. 6.7 a) and 6.9 a), stable phases are the tetragonal Al_2Cu C16 phase and the hexagonal $MgZn_2$ C14 Laves phase for Al-Cu and Mg-Zn. The effects of Cu on the formation of intermetallic phases with Al-Zn and Mg-Zn have already been studied in the literature [194, 195]. Some phases found include: the cubic Al_4Cu_9, the body centered tetragonal Al_2Cu, the BCC Cu_5Zn_8 and the $(Cu,Zn)_2Mg$ Laves phase.

By varying the applied sputtering power and angle relative to the individual sources, samples with the chemical compositions shown in Fig. 6.16 b) were produced. To analyse the surface structure of those samples, images were made using electron microscopy techniques which are shown in Fig. 6.16 a). Clearly visible dark regions are present in the central area. Additional EDX measurements revealed that these regions are Al rich. The same trend has been observed in the previously described Al-MgZn system. The surface texture shows minor changes with varying chemical compositions. At closer inspection, a refinement of the surface features can be observed at more balanced compositions (measurement pos. 15 - 22).

Table 6.2.: Composition of the simulations depicted in Fig. 6.17.

	Mg (at%)	Al (at%)	Cu (at%)	Zn (at%)
a)	37	7	2	54
b)	25	26	7	42
c)	19	39	11	31
d)	17	44	15	24
e)	12	52	22	14
f)	6	60	26	8

The material distribution in experimentally analysed samples was calculated by means of computer simulations in this series as well. Some of the final states are shown in Fig. 6.17. Clearly separated regions dominated by MgZn and AlCu are visible over the entire concentration range. A mixture of the two subsystems cannot be found. Due to the chemical composition and the non-mixing character of the system, the MgZn domains are Zn rich while the AlCu domains show an Al excess. The Al rich domains found in SEM micrographs at Al contents of 25 at% to 50 at% could not be identified in the simulation results. This can be attributed to the strong binding between Al and Cu and a correspondingly high negative enthalpy of mixing. This leads to the binding of Cu in the Al areas, a possible Al-Cu separation in these domains can thus be underestimated.

The quantification of the fits (see Fig. 6.18) of the XRD measurements is shown in Fig. 6.19 a). The $MgZn_2$ C14 Laves phase dominates on the MgZn-rich side (proportion approx. 90 wt%). This phase is predicted in the binary MgZn system (see phase diagram in Fig. 6.9 a)). In addition, a small fraction of the Mg_2Zn_{11} phase is formed. This crystallographic phase is also present and predicted by the classical binary phase diagram. As the aluminium content increases, the dominance of the $MgZn_2$ Laves phase decreases continuously. From a concen-
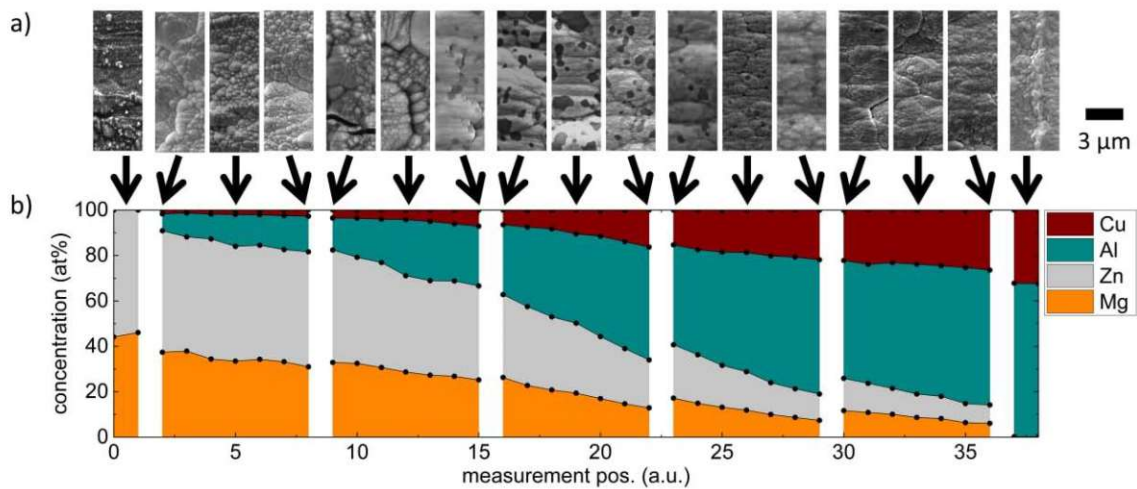
Figure 6.16.: a) The surface structure of the samples at the specified measurement positions. Dark precipitates can be observed in the central region (position 20). b) EDX measurements of the chemical composition. By varying the exposure angle as described in the text, the gradient in the $MgZn_2$ and Al_2Cu concentration could be varied in a controlled manner.
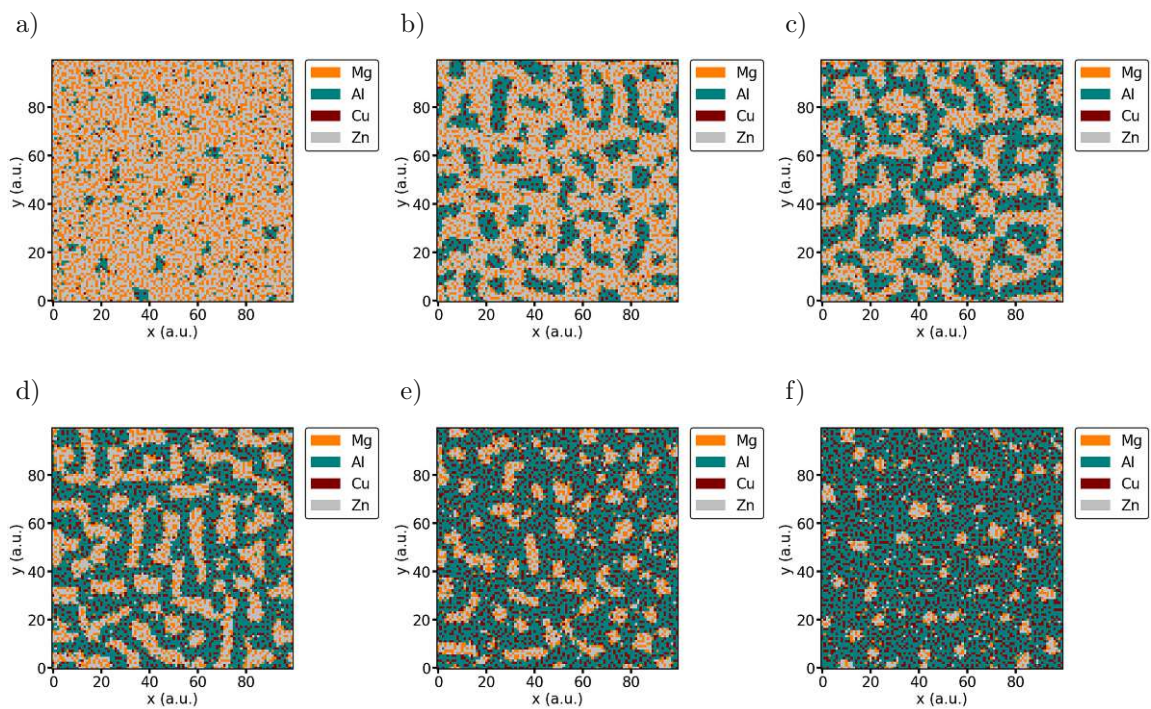
Figure 6.17.: Simulated distributions with different $MgZn_2$ and Al_2Cu contents. The MgZn content decreases continuously from a) to f). The concentrations can be found in Tab. 6.2.

a)

b)

c)
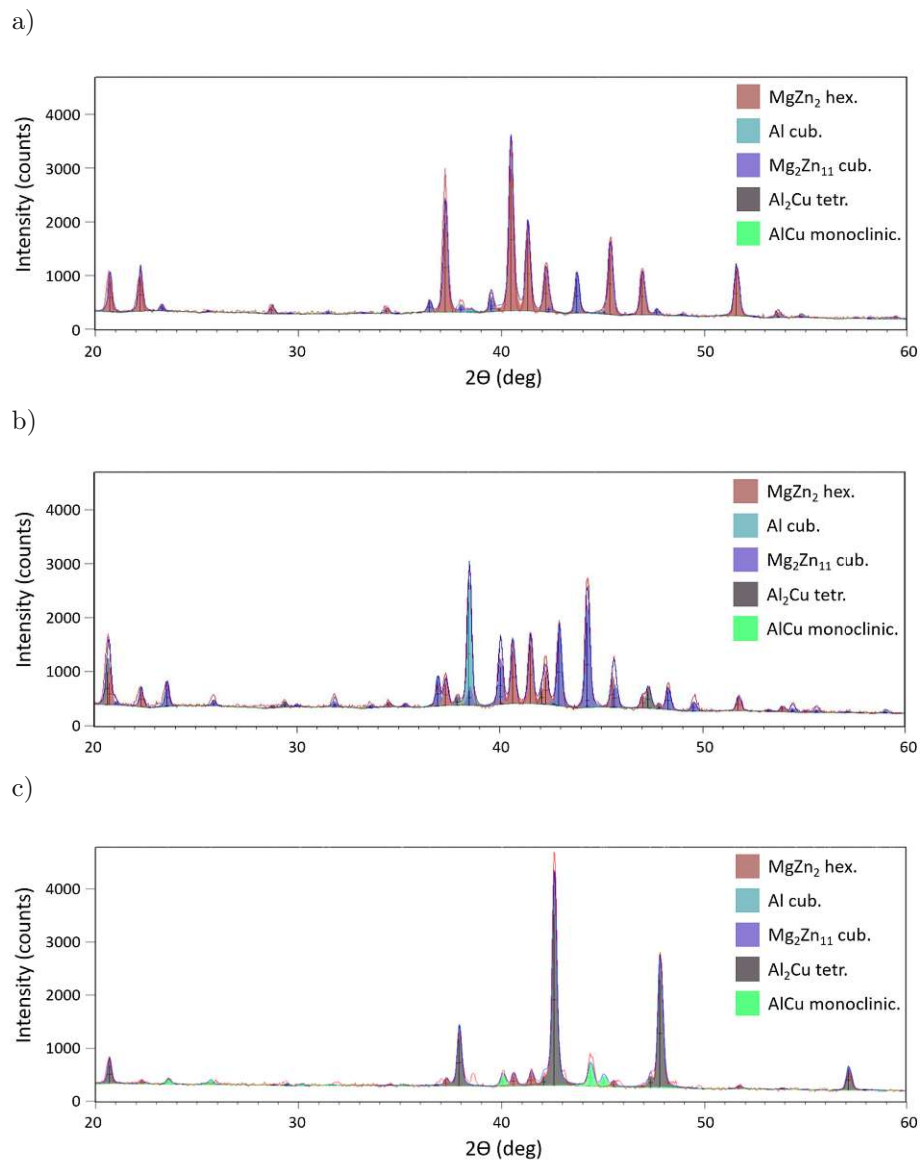
Figure 6.18.: XRD measurements for different concentrations. The relative compositions can be retrieved from Fig. 6.16 b) and correspond to a) pos. 2 b) pos. 20 and c) pos. 36. The increase of the Mg_2Zn_{11} and Al phase in the middle panel can be observed.

a)

b)
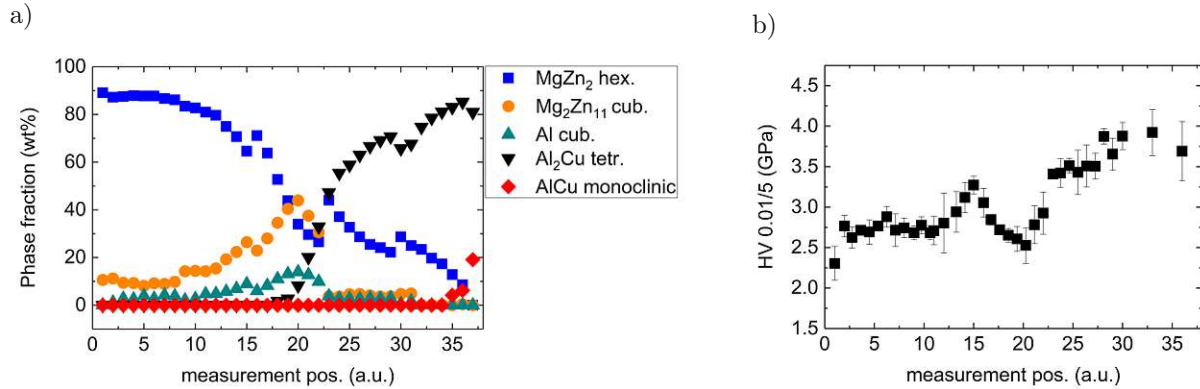
Figure 6.19.: a) Results of the XRD data evaluation. Binary crystallographic phases ($MgZn_2$ hexagonal and Al_2Cu tetragonal) form at the edges. In the central region a pure Al phase and a cubic Mg_2Zn_{11} phase were found. b) Indentation hardness values at the different measuring positions (i.e., different compositions). A significant drop in hardness was observed in the composition range in which the pure Al phase was found.

tration of approx. 26 at% Al, 25 at% Mg, 42 at% Zn, and 7 at% Cu a pure Al phase is established, which reaches its maximum at an Al content of 44 at% and then decreases again. In this range, the cubic Mg_2Zn_{11} also shows an increase followed by a decline.

In the area of the first increase of the Al and Cu fractions, shifts of the peaks of the $MgZn_2$ and the Mg_2Zn_{11} phase could be observed. These are shown in Fig. 6.20. The shifts to larger Bragg angles here correspond to a compression of the unit cell. A more detailed analysis showed that the lattice parameters of the hexagonal $MgZn_2$ were reduced from a = 5.223 Å to a = 5.193 Å, from c = 8.566 Å to c = 8.551 Å and for the cubic Mg_2Zn_{11} phase from a = 8.552 Å to 8.425 Å.

Subsequently, an Al_2Cu tetragonal phase is established in the AlCu-dominated region.

The analysis of the mechanical property of indentation hardness indicated a monotonic increase with increasing AlCu concentration from around 2.5 GPa to around 4 GPa. Only in the region of the Al precipitates and the presence of the pure Al cubic prototype, a significant decrease in hardness can be seen in the form of a dip in the recorded hardness values (Fig. 6.19 b)).

Summary:

The Al and Zn dominated AlCuMgZn system showed no evidence of promoting single phase domains. The dominant binary crystallographic phases could not be broken up by the supply of other elements and subsequent increase of entropy, thereby leading to decomposition. It was evident over a wide concentration range that the most prominent binary phases of the MgZn and the AlCu system coexisted and no significant mixing occurred. This was further confirmed by the simulation, which suggested a clear separation of the MgZn and AlCu atoms over the entire compositional space. Only in the range from x_{Al} = 25 at% to x_{Al} = 50 at% these dominant phases were discontinued. In this range, two cubic phases were established,

a)

b)
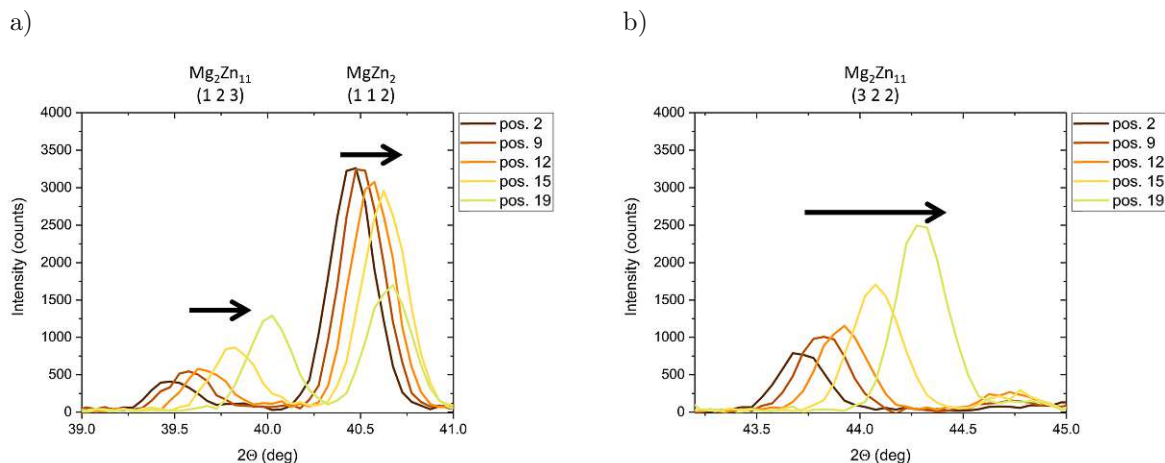
Figure 6.20.: Selected XRD reflexes for the $MgZn_2$ and Mg_2Zn_{11} phase show shifts towards higher Bragg angles with increasing content of Al and Cu. This corresponds to a compression of the unit cell.

one following the Mg_2Zn_{11} prototype and a pure Al phase. At Cu and Al concentrations of < 4 at% and < 17 at%, respectively, they are primarily incorporated into the crystal lattices of the existing phases ($MgZn_2$ and Mg_2Zn_{11}). This is suggested by the distorted structures of these. The compression of the Mg_2Zn_{11} lattice corresponds to the region of the first hardness increase. When the content of both elements Al and Cu is increased in parallel with a decline of the Mg and Zn content, and the critical Al concentration of 25 at% is reached, a pure structure was formed. Since the Cu content is still very low at 7 at%, Cu atoms remain as interstitial atoms. The reason for this separation could be the oversupply of Al, especially with respect to the favored bonding partner Cu. This crystal phase regime is characterized by a significant indentation hardness decrease due to the soft Al. Only at a concentration of 44 at% Al and 12 at% Cu a tetragonal Al_2Cu phase begins to form. The described behavior can be explained by considering the binary Al-Cu phase diagram in Fig. 6.7 a) in the concentration range of $x_{Cu} = 0$ at% - 32 at%. In direct comparison to the alloy system containing only Al, Mg and Zn, Al is bonded more, and the areas where segregation occurs on an atomic or microscopic scale are reduced. Cu therefore acts as a strong bonding partner preferentially to Al in this system. The observed XRD results were confirmed by electron microscopy measurements which revealed Al segregation at the measurement points where the Al crystal phase was detected. The simulations showed limitations in the region of the Al segregation. Apart from that, however, the calculations yielded comparable results. The distributions of the atoms in the simulated final states showed a separation of MgZn and AlCu atoms, which corresponds to the crystal structures found in the XRD measurements.

6.1.5. $AlCu_2$-$MgZn_2$

The influence of Cu as a 'bond breaker' for strong phases of the systems will be investigated in this section. By choosing an AlCu target with Cu excess and a MgZn target with Zn excess,
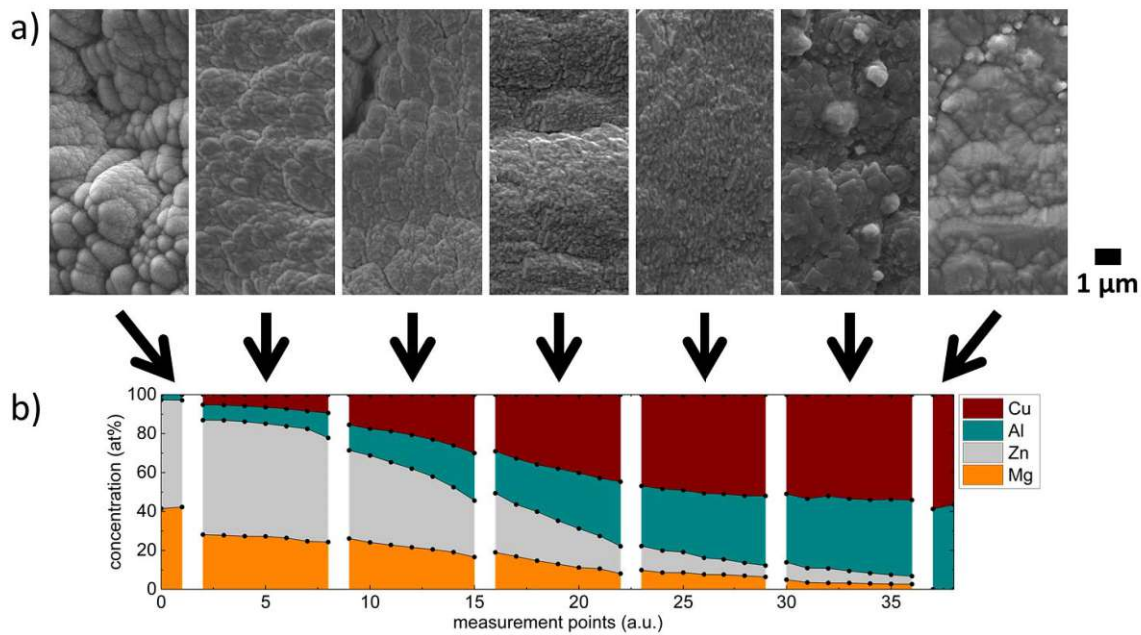
Figure 6.21.: a) Surface structure of the samples at the measurement positions indicated by arrows. b) EDX measurements of the chemical composition showing the varying MgZn and AlCu content.

samples with a reversed Al to Cu ratio could be produced. The results of the Al-MgZn and the Al_2Cu-$MgZn_2$ series showed that the elements Al, Mg and Zn have relatively strong binding preferences. In the latter system, the addition of Cu promoted a small region enforcing a cubic mixed phase (indexed as Mg_2Zn_{11}). The chemical compositions of the samples are shown in Fig. 6.21. The MgZn content decreases continuously, starting from a composition of about 40 at% Mg : 60 at% Zn and is replaced by AlCu in a ratio of about 40 at% : 60 at%.

To estimate a priori the potential atomic distribution, the experimentally prepared compositions were simulated and are shown in Fig. 6.22. Panel a) shows the binary MgZn system. Here, a random intermixing between Mg and Zn atoms is evident, suggesting the formation of one or more intermetallic phases. This result corresponds well with the binary phase diagram of Mg and Zn. For the binary AlCu system, we found a similar correlation. The intermixing indicates an intermetallic phase formation, which seems plausible by examining the AlCu phase diagram in Fig. 6.7 a). Incorporation of the AlCu into the binary MgZn composition leads not only to the formation of AlCu domains but also to the inclusion of Cu domains into the MgZn. With the increase of Al and Cu, the area of AlCu domains and the amount of Cu atoms in the MgZn domains increase. The obtained results suggest the formation of AlCu crystal structures and the transition from MgZn to MgZnCu structures. Above the critical concentration of $x_{Al} \approx 35$ at% and $x_{Cu} \approx 50$ at%, the AlCu domains coalesce into a matrix with small MgZnCu inclusions. This finding may indicate that AlCu structures are more likely to dominate above this critical composition.

The experimental investigations of the surface structure in Fig. 6.21 a) show a fine grain
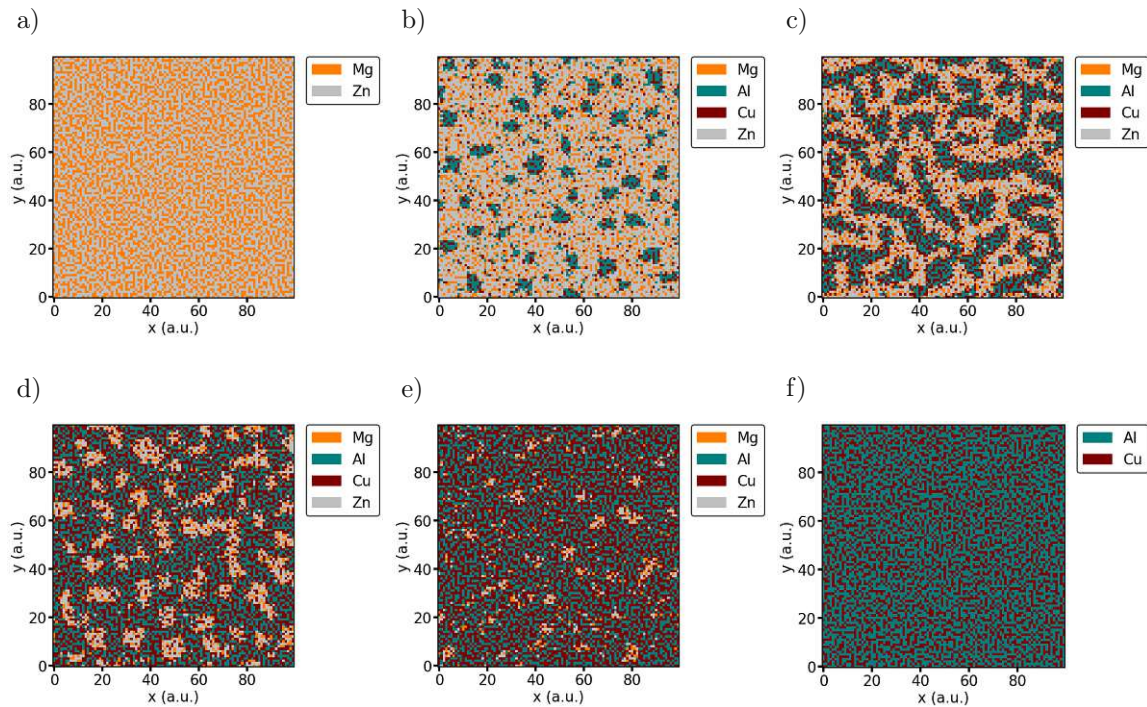
Figure 6.22.: Simulated distributions for different AlCu$_2$-MgZn$_2$ system compositions. a) and f) show the binary MgZn and AlCu systems, respectively. The MgZn content decreases continuously from b) to e).

distribution over the entire experimentally accessible range. Overall, the images of the samples do not exhibit any segregation or significant variations in texture. Only in the peripheral areas, (pure MgZn and AlCu compositions) slightly coarser features were detected.
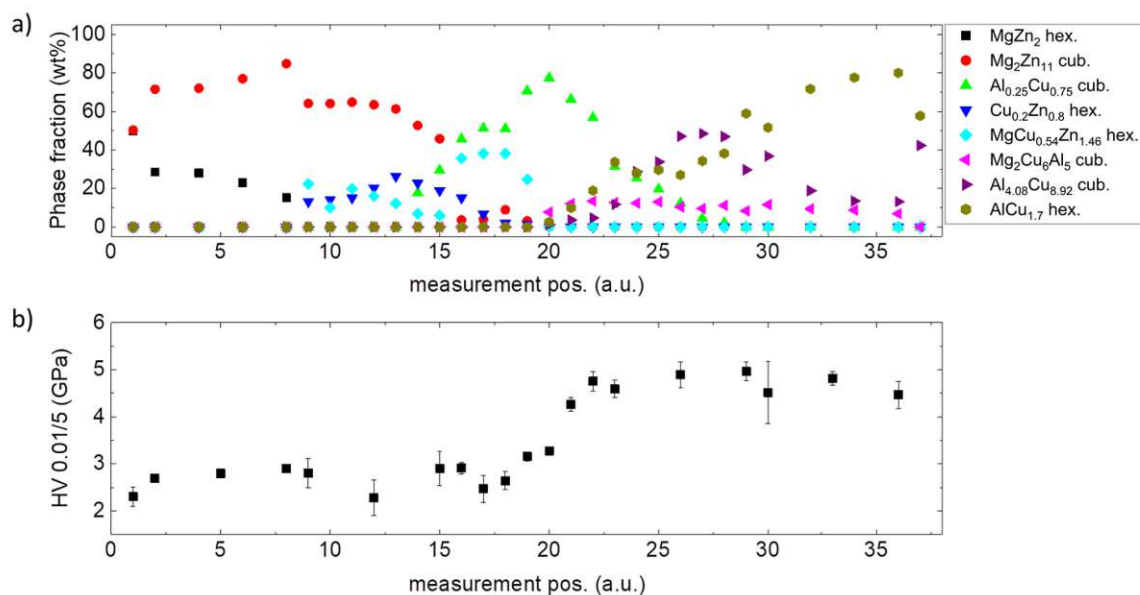
Figure 6.23.: a) Quantitative results of Rietveld analysis and b) results of indentation hardness measurements performed at different measuring positions.

The XRD measurements were performed to determine the crystallography of the samples and are shown in Fig. 6.23 a). Three distinct crystallographic regions were identified and, for clarity, will be further analyzed individually:

MgZn dominated regime:
The MgZn dominated region (proportion of MgZn > 60 at%) is characterized by a binary crystallographic phase system. The dominant phases have appeared in our previous analyses and were identified as the hexagonal $MgZn_2$ Laves phase and the cubic Mg_2Zn_{11} phase. Both are predicted according to the binary MgZn phase diagrams (compare Fig. 6.9 a)) at a Zn content between 66 at% and $\approx$ 85 at% [196]. The experimentally prepared samples contained a slightly different ratio, Mg: 40 at% and Zn: 60 at%. According to the classical phase formation description, this ratio should be characterized by the identified $MgZn_2$ and in addition a Mg_2Zn_3 phase. However, the occurrence of the latter was not confirmed by our analysis. The experimentally detected phases can be motivated by the lower formation enthalpy of the Mg_2Zn_{11} phase. Its enthalpy amounts to -67 meV/atom while that of the actually predicted Mg_2Zn_3 is 5 meV/atom [149]. The phase formation arises from an approximately random distribution, and a variety of bonding partners could suppress or disrupt the formation of the classical phases. As the proportion of the remaining alloying elements increases to a total of 40 at%, the phase states show only minor changes. Shifts of the peak positions indicate a distortion of the lattice. After a detailed evaluation of the $MgZn_2$ structure and comparison with XRD databases, we found that this phase better matches to the reported $MgCu_{0.54}Zn_{1.46}$ phase. This result shows that impurity atoms occupy lattice sites of the Laves phase. In addition, a hexagonal CuZn phase appears, which can be assigned to the hexagonal structure of ϵ-brass observed in the binary Cu-Zn phase diagram.

Intermediate regime: In the balanced MgZn and AlCu region, two crystal phases dominate the microstructure: a hexagonal $MgCu_{0.54}Zn_{1.46}$ and a cubic $Al_{0.25}Cu_{0.75}$ system. The former is a distorted version of the $MgZn_2$ Laves phase. The distortions arise due to the occupation of the lattice sites by impurity atoms. The "search and match" approach suggested that mainly Cu occupies the lattice sites, although Al could also occupy these spots. However, since an oversupply of Cu prevails, the occupation probability of Cu on Mg or Zn sites is more likely. The second detected phase ($Al_{0.25}Cu_{0.75}$) exhibits a BCC structure showing a maximum at a concentration of Mg = 11 at%, Zn = 22 at%, Al = 27 at% and Cu = 40 at%.

AlCu dominated regime: Further increase of Al and Cu above 60 at% leads to a decrease of the $Al_{0.25}Cu_{0.75}$ phase. At the same time, the fraction of cubic $Mg_2Cu_6Al_5$ and cubic Al_4Cu_9 phases increases. The latter shows a maximum at an AlCu concentration of about 80 at% and can be described as a BCC lattice [197]. Similarly, the hexagonal $AlCu_{1.7}$ phase increases.

The analysis of the mechanical property of indentation hardness shows an intriguing trend (Fig. 6.23 b)). Up to a MgZn concentration of 40 at%, there is no effect of the composition

on the indentation hardness, which stagnates at a Vickers hardness of 2.5 GPa. In the MgZn range between 40 at% and 20 at%, the indentation hardness increases significantly by around 100 % to about 4.5 GPa. It remains at this value until the pure AlCu System is formed.

Summary

The increase of the relative Cu content showed significant effects on the formed structures. The crystal phases weakened the classically predicted phases, including the "strong" phases, already discovered in other multicomponent systems. As a result, the phase landscape exhibited a high level of degeneracy. Every formed phase considered in this series, excluding the MgZn rich and AlCu rich ends, contained crystallographic phases with Cu. This finding confirms the dominance of Cu in the formation of crystallographic orders. The simple simulations were also able to indicate the crystal structures encountered in this system with Cu and Zn abundance. The separation of the AlCu and MgCuZn was confirmed in both the experimental measurements of the crystal structures and by the computational methods.

6.1.6. AlCuMgZn-Al

In this section, the influence of the light metal Al on the crystallographic structures of the multicomponent systems was investigated in detail. Previously conducted studies reported that Al significantly affects the crystallographic structure. For example, Liang *et al.* showed that the addition of Al increases the FCC fraction in the complex AlLiMgSnZn system [48].
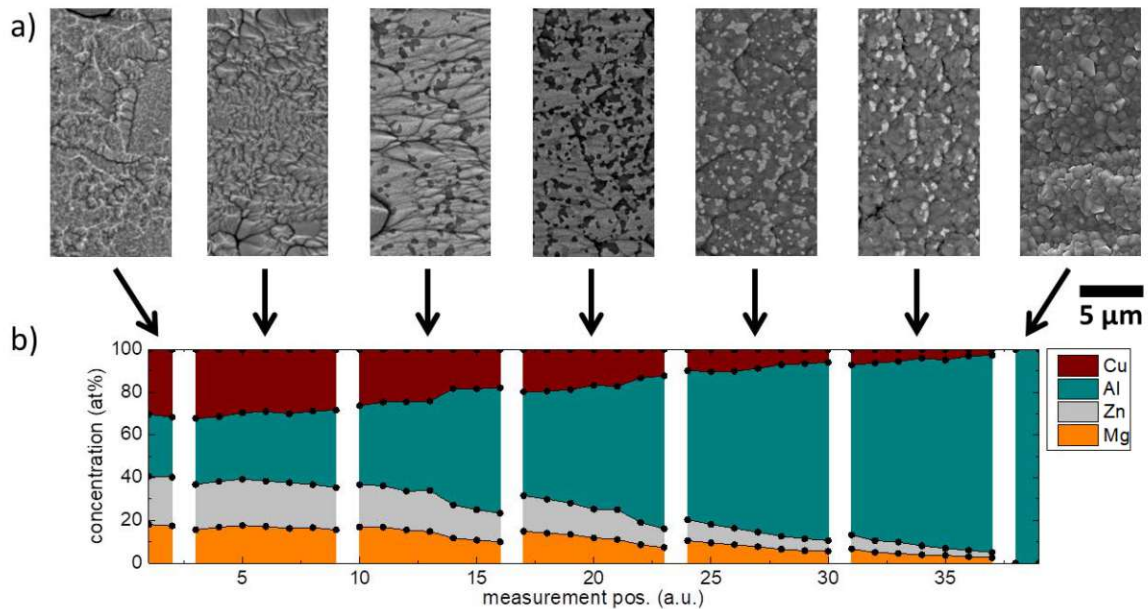
Figure 6.24.: a) Backscattered electron images of the sample surfaces at different compositions show dark Al rich precipitates. b) EDX analysis of the produced series with variable Al content.

The samples were prepared by combining a quaternary AlCuMgZn system with a pure Al target. The chemical composition of this series is shown in Fig. 6.24 b), with the aluminium

content varying from about 28 at% to 100 at%. The surface structure (Fig. 6.24 a)) shows no significant change over the whole concentration range. However, it is remarkable that above the critical Al concentration of $\approx$ 40 at%, the formation of dark domains is visible. As the Al content increases, these domains occupy larger areas. Such an increasing Al segregation, we have also identified in the ternary Al-MgZn system (section 6.1.3).

a) b) c)
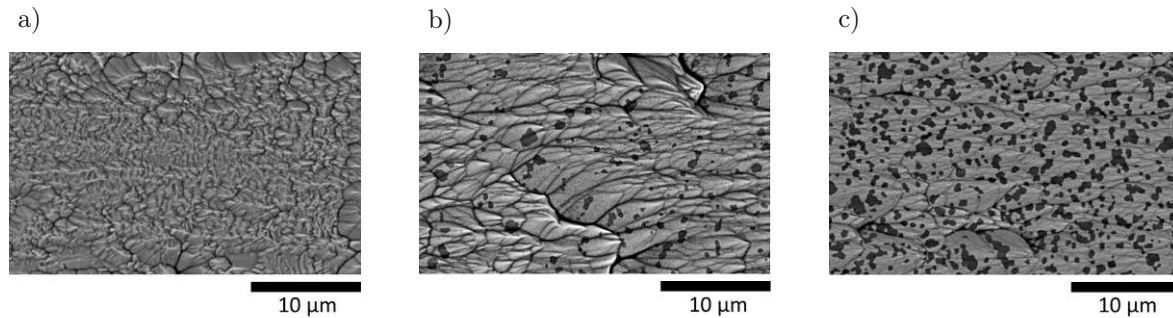
Figure 6.25.: The surface structure of two quaternary Al-Cu-Mg-Zn samples with a relative Al content: a) 32 at% and b) 37 at%. An increase of Al rich domains can be observed at higher relative Al content (>37 at%). For the comparison, panel c) depicts the ternary Al-Mg-Zn alloy with x_{Al} = 32 at%. Here, the Al rich domains are more pronounced than in sample a).

Fig. 6.25 a) shows a detailed view on the sample surface with an Al content of x_{Al} = 32 at%. Besides the smaller flake-like textures, a homogeneous layer can be seen. The comparison with the higher Al content (x_{Al} = 37 at%) in Fig. 6.25 b) demonstrates that above this concentration, the first manifestations of demixing and formation of dark domains (Al-rich phases) occur. A direct analogy with the sample without Cu content can be made (shown in panel c)). The ternary alloy (AlMgZn) shows the establishment of the Al precipitates already at an Al concentration of approx. 32 at%. The higher concentration (37 at%) at which Al-rich domains appear in the quaternary system indicates a binding effect between Cu and Al.

To get further insights into the atomic distribution of the experimentally investigated samples, we performed atomic distribution simulations (Fig. 6.26). Here, relatively distinct structures are evident, which suggest the segregation of MgZn and AlCu. However, in the electron micrographs at relatively low Al fractions (panel 1 in Fig. 6.24 a)) such segregations are imperceptible. The contrast in SEM images is mainly determined by the difference in the atomic number ratios. Thus, low or no contrast in SEM images cannot be excluded due to the similar average atomic numbers of the MgZn to AlCu domains. When the Al content increases further, the proportion of the AlCu-dominated islands expands (Fig. 6.26 c) to f)). The MgZn enriched domains become smaller and embedded in the Al dominated matrix. Cu atoms show a random arrangement in the Al matrix itself. In terms of comparison with the electron microscopy measurements, the correlation between simulated enrichment and the formation of dark domains is apparent. Due to the abundance of Al and its relatively low atomic number (Z = 13), the simulation underlines the occurrence and successive expansion
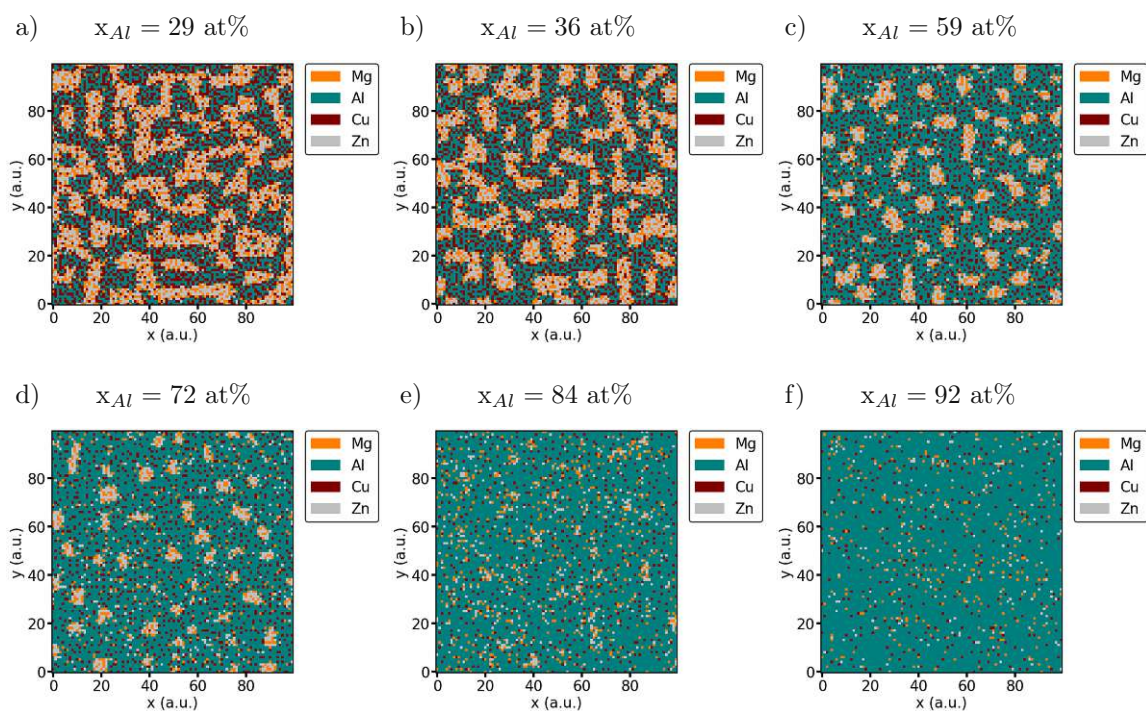
Figure 6.26.: Simulated atomic distributions for a selection of prepared AlCuMgZn-Al samples. The relative Al content increases continuously from a) $x_{Al} = 29$ at% to f) $x_{Al} = 92$ at%. A transition from relatively separated MgZn and AlCu textures to single island formation of predominantly MgZn domains in an Al dominated matrix can be seen.

of these domains. Moreover, simulations overpass the limitation of the SEM technique and identify that Al domains are rich in Cu, while Mg tends to form domains with Zn.

The crystallography results obtained from XRD analysis are shown in Fig. 6.28 a). The whole compositional space can be characterized by three different phases: a hexagonal $MgZn_2$Laves phase, a cubic $Mg_2Cu_6Al_5$ phase, and a pure cubic Al phase. The critical Al concentration at which the Al phase appears in the XRD measurements is approximately 50 at% which corresponds to the manifestation of the dark areas in the SEM images. The region with the relatively low Al contents (≈ 30 at%) is dominated by the cubic $Mg_2Cu_6Al_5$ phase together with a small fraction of the $MgZn_2$ phase. This region shows a plateau-like behavior till ≈ 50 at% Al. At higher Al concentrations, it vanishes due to replacement by the Al FCC phase. In the transition zone between the Al phase and $Mg_2Cu_6Al_5$ phase, tetragonal Al_2Cu was identified, which has already been detected in AlCu rich regions in the quaternary Al_2Cu-$MgZn_2$ system and in the binary AlCu phase diagram.

The BSE images of several samples' metallographic cross-sections are shown in Fig. 6.29. The relative compositions of these samples are given in Tab. 6.3. Contrast differences in the images reflect local enrichments of certain elements in the samples. In panels 1 - 3, two relatively clearly separated domains are visible, which seem to increase with higher Al content. EDX mappings assigned these areas to AlCu (darker region) and MgZnCu (lighter region). The direct comparison to the crystallographic results in that concentration regime (40 at% $< x_{Al} < 53$ at%) confirms this and provides a consistent picture. Panels 4 to 6 reveal three different shades of grey, which suggest the formation of another phase. Since the grey tone of the additionally formed areas is darker, the presence of a light atomic mass (low atomic number Z) element can be assumed, which was confirmed by local EDX measurements. The dark region was detected as an Al-rich domain with depletion of all other alloying elements. The panels 5 - 7 (x_{Al} from 58 at% to 68 at%) correspond to the region where the tetragonal Al_2Cu, the cubic $Mg_2Cu_6Al_5$ and the pure Al phases were detected in the XRD studies. In panel 7, a binary system can be clearly identified (Fig. 6.29). In this concentration range, XRD measurements also identified two crystallographic phases: the pure Al and the declining $Mg_2Cu_6Al_5$ phase.

Table 6.3.: Overview of the samples presented in Fig. 6.29.

Pos.	Mg (at%)	Zn (at%)	Al (at%)	Cu (at%)
1	14.8	19.2	41.8	24.2
2	14	15.9	50.6	19.4
3	13.4	14.7	53.1	18.8
4	11.8	13.5	57.9	16.8
5	11.1	13.9	57.8	17.2
6	8.6	10.4	67.7	13.3
7	10.5	9.8	69.8	9.8

The indentation hardness as a function of Al concentration is depicted in Fig. 6.28 b). It

a)

b)

c)
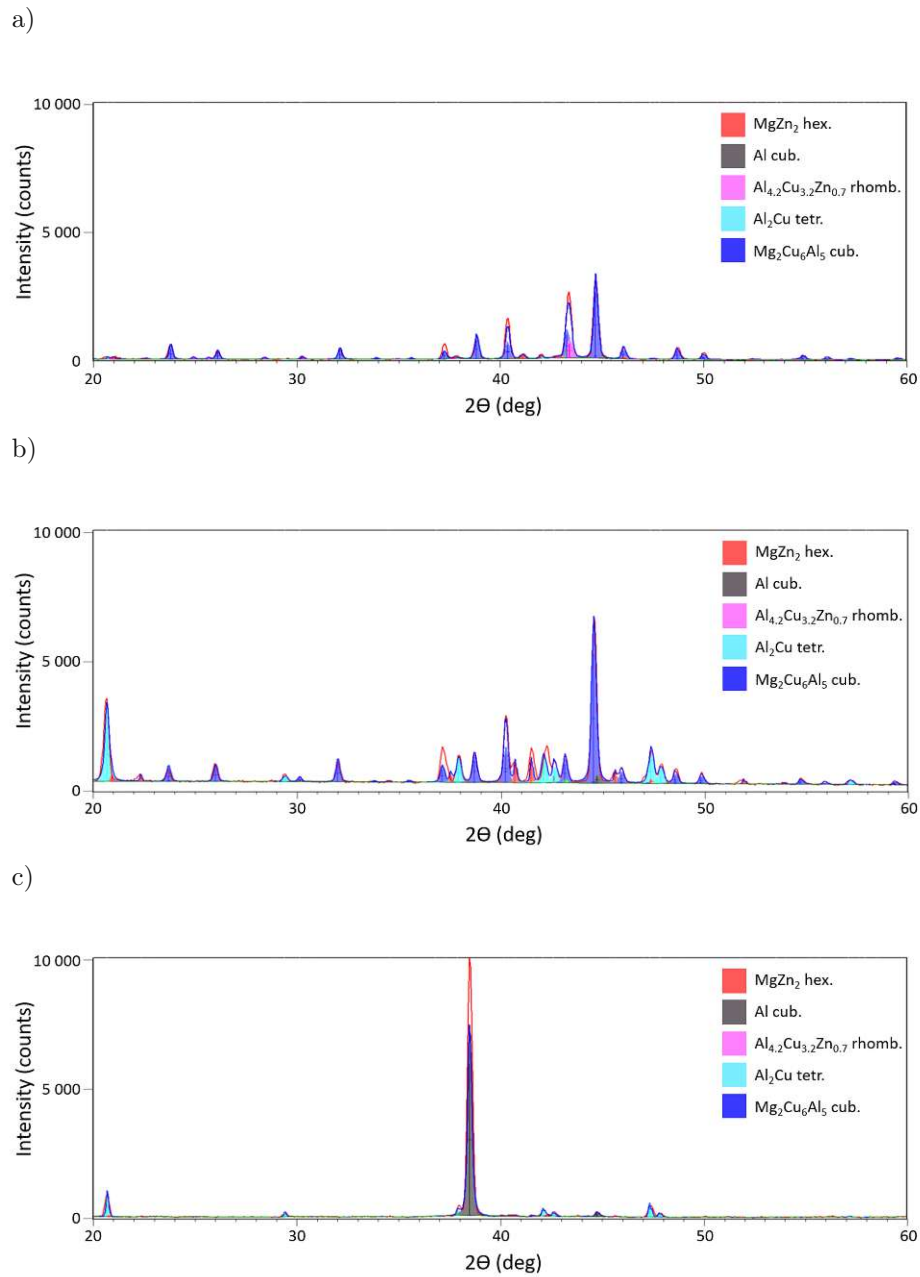
Figure 6.27.: XRD measurements of samples with different relative Al concentrations (x_{Al}): a) 31 at%, b) 51 at%, and c) 92 at%. The evolution of the detected peaks and the corresponding fits show transitions between various intermetallic phases.

a)

b)
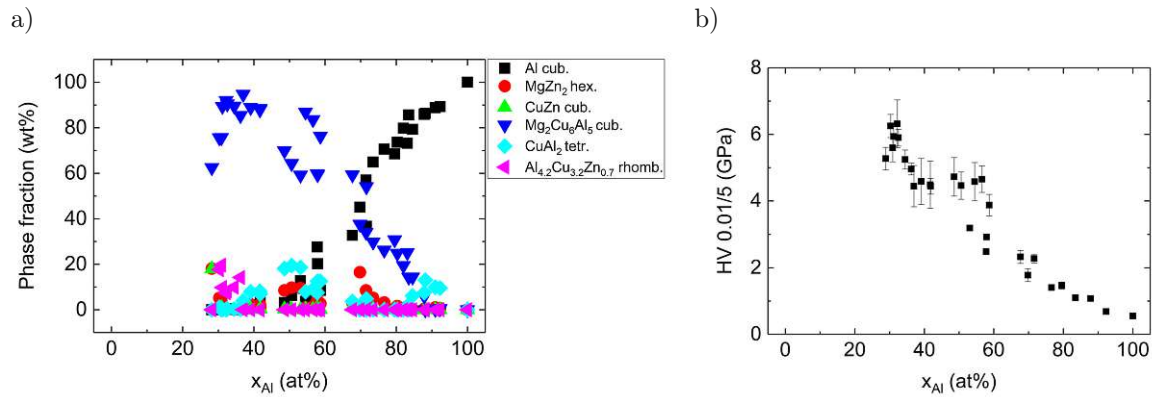
Figure 6.28.: a) Results of XRD phase analysis as a function of Al concentration. b) The measured indentation hardness shows a monotonic decrease with increasing Al content.
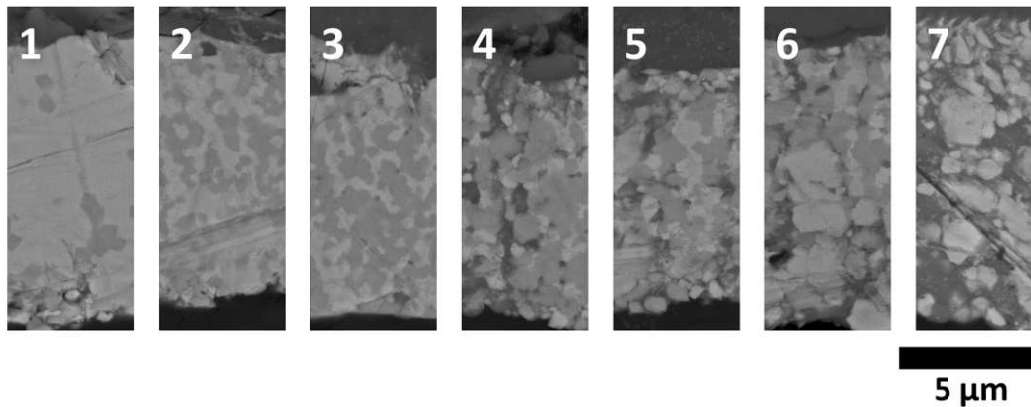
Figure 6.29.: Images of metallographic cross-sections of samples with different compositions (see Table 6.3) obtained by backscattered electron microscopy. Contrast differences indicate elemental segregation and suggest the formation of various phases.

shows a continuous decline with increasing Al concentration and a slight dip around 60 at%. The comparison with the XRD results correlates the drop in hardness to the establishment of the FCC Al phase. The softness of Al has been reported in the literature [198] and corresponds approximately to the measured value of the pure Al sample produced in this series (see Tab. 6.5). This finding shows that the crystallographic changes could also be detected in the indentation hardness in samples produced by the presented approach.

Summary:
The variation of the Al content in the quaternary AlCuMgZn alloy showed the formation of precipitates above a critical concentration of Al ($x_{Al} > 37$ at%). This was indicated by darker domains in the electron micrographs, as well as by the results of the XRD measurements. The crystal structures in the alloy were dominated by the cubic $Mg_2Cu_6Al_5$ and the cubic Al phase. The course of the indentation hardness showed a monotonic decrease, which is proportional to the increase of the pure Al crystal structure.

6.1.7. AlCuMgZn-Zn

Zinc is the heaviest element in the quaternary systems studied in this work. It can form strong bonds with Mg and Cu, resulting in a wide variety of intermetallic compounds. For example, CuZn compounds (often called brass) are of high technical relevance and are used in various relative compositions, depending on the property requirements [199–201]. To investigate the effects of Zn on the quaternary AlCuMgZn system, a pure Zn target was combined with the quaternary target ($x_{Mg} = 17$ at%, $x_{Al} = 28$ at%, $x_{Cu} = 31$ at%, $x_{Zn} = 24$ at%). The chemical analysis of the prepared samples is presented in Fig. 6.30 b), and SEM images of the surface are shown in Fig. 6.30 a). A comparison at different Zn concentrations shows significant modifications of the surface structure. While smooth surfaces and even textures are visible at balanced compositions, they become coarser grained and rougher with increasing Zn amount. Such a roughening effect at high Zn content has already been observed in the investigation of the binary AlZn system described in chapter 6.1.1. The transition in the surface structure from smooth to coarse takes place at around 40 at% relative Zn content for the quaternary system.

As with the previous systems, simulations were performed to mimic experimentally prepared samples, which are shown in Fig. 6.31. At relatively low Zn concentrations, and therefore when all elements are in a balanced distribution, two clearly separated regions are dominant, an AlCu and a MgZn region. In the latter, a minor number of Cu atoms are also present. The predicted element distributions will likely result in the crystallographic structures mainly governed by those elements. When the Zn fraction increases, the MgZn domains occupy larger areas, while the Cu fraction in those domains remains approximately constant. At relatively high Zn contents ($x_{Zn} \approx 80$ at%), Cu ultimately vanishes from the MgZn regions. The MgZn domains, however, persist up to the highest produced Zn fractions, showing a random Mg arrangement in the Zn matrix. This implies the formation of a Zn crystal structure at
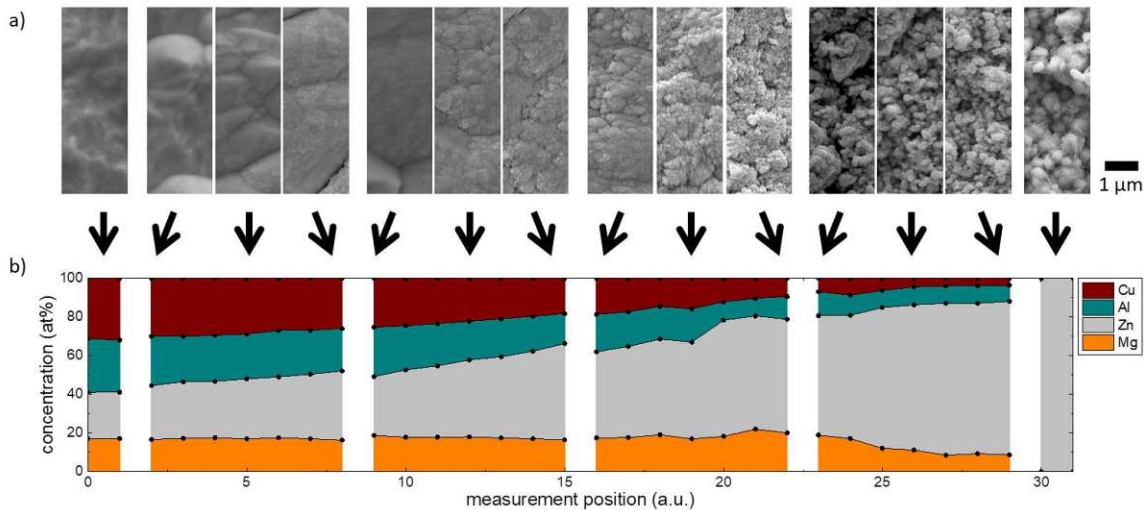
Figure 6.30.: a) SEM images of the sample surface show the changes in surface structure with increasing Zn concentration. b) Chemical analysis of the prepared samples with increasing Zn fractions.

elevated Zn concentrations. In addition, the presence of relatively well-defined regions of locally different compositions, showing agglomerations of Al and Cu atoms, suggests that this is not a single phase region and that at least a binary crystallographic prototype system will prevail.

The performed XRD measurements and the subsequent phase analysis led to the results shown in Fig. 6.33 a). In the roughly equidistributed range at a Zn content of 20 at% to 30 at%, the cubic $Mg_2Zn_{11}/Mg_2Cu_6Al_5$ phase dominates. The transition between these two prototypes could be identified from shifts of the corresponding peaks (compare Fig. 6.32). A continuous shift from larger Bragg angles to smaller ones with an increase of the Zn fraction can be observed. This can be explained by the foreign occupation of the lattice sites by Zn ($Mg_2(Cu_6Al_5)$ to Mg_2Zn_{11}). Smaller Bragg angles correspond to an increase in the unit cell size. The lattice parameter of the experimentally found crystal phase increases from a = 8.35 Å to a = 8.50 Å.

Furthermore, the cubic CuZn and the hexagonal $MgZn_2$ phases are prominent. These two decrease rapidly as a consequence of the increasing Zn content and disappear at $x_{Zn} = 40$ at%. The initial phases and their evolutions agree with the previously investigated series, which had a comparable starting composition. Also, the strong increase of the cubic $Mg_2Zn_{11}/Mg_2Cu_6Al_5$ phase was already observed in those systems. At a Zn content of 30 at%, the formation of a hexagonal Zn-dominated phase starts. The amount of the $Cu_{0.2}Zn_{0.8}$ phase increases strongly and reaches its maximum at a Zn concentration of ≈ 50 at%. At this fraction, the quantification showed over 85 wt% of this phase. At the same time, the $Mg_2Zn_{11}/Mg_2Cu_6Al_5$ phase diminishes and vanishes at $x_{Zn} = 60$ at%. At the same Zn concentration, a pure Zn lattice could be detected, whose monotonic increase was accompanied by the decrease of the hexagonal $Cu_{0.2}Zn_{0.8}$ lattice. In the pure Zn sample,
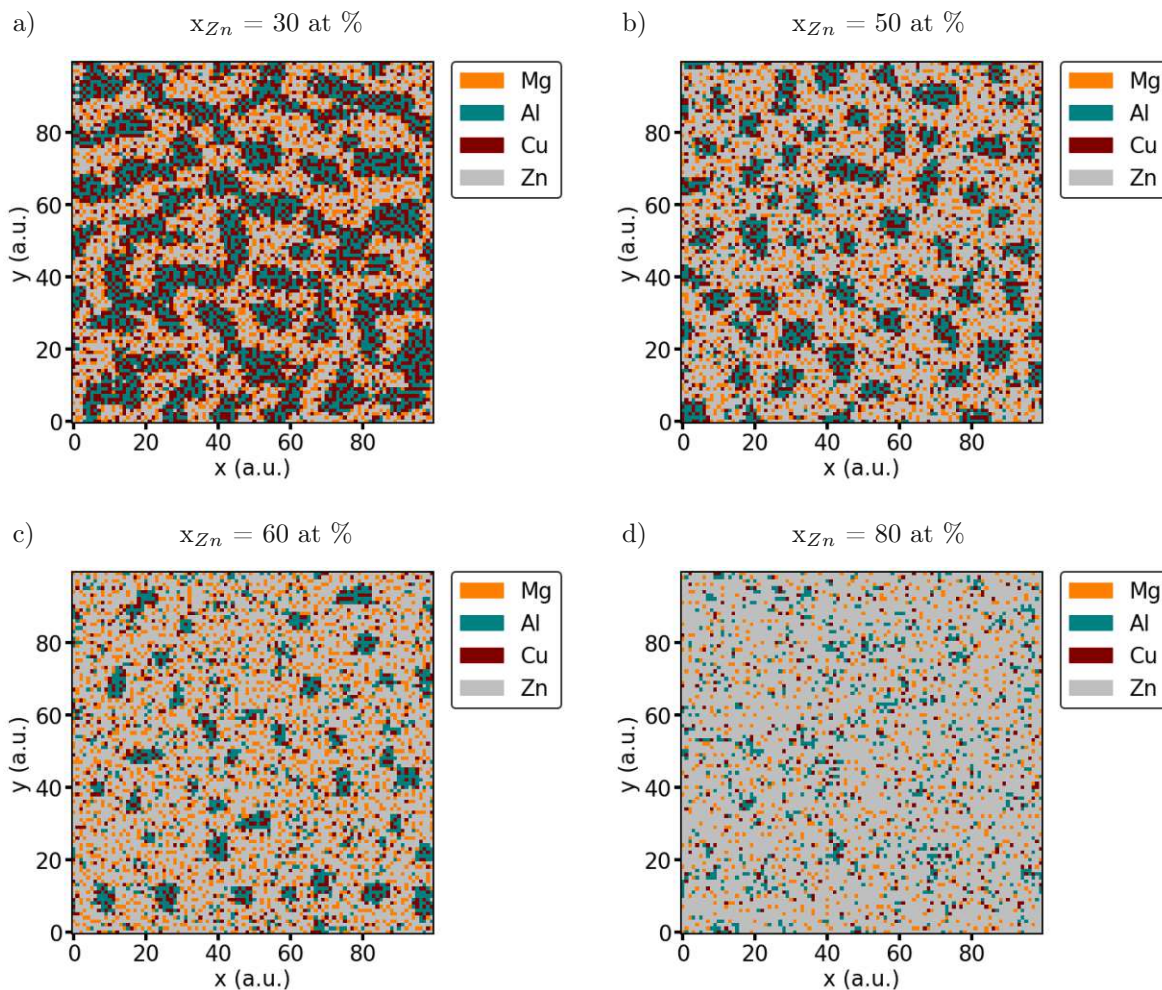
Figure 6.31.: Simulated elemental distributions of the AlCuMgZn-Zn system at varying relative Zn concentrations.
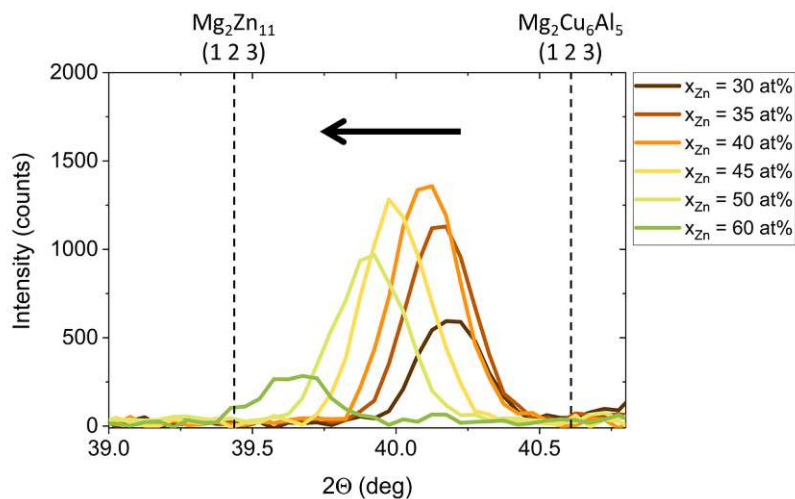
Figure 6.32.: Shift of the (1 2 3) reflex of the $Mg_2Cu_6Al_5/Mg_2Zn_{11}$ phase. The dotted lines represent the theoretical values for the corresponding peak positions ($a(Mg_2Cu_6Al_5) = 8.311$ Å, $a(Mg_2Zn_{11}) = 8.552$ Å).

a)

b)
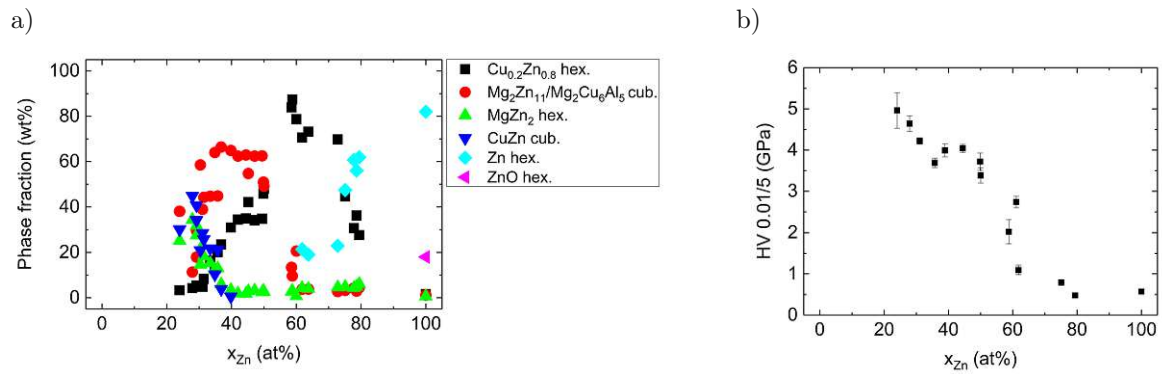
Figure 6.33.: a) Results of XRD phase analysis as a function of Zn concentration. b) The measured indentation hardness shows a monotonic decrease with increasing Zn content.

the proportion of the Zn phase is approx. 80 wt%. The remaining 20 wt% could be assigned to a ZnO phase. The oxide formation could not have been prevented during the thermal post-treatment, even when it was conducted under an Ar-protective atmosphere.

The comparison of the phase analysis with electron microscopy images reveals a correlation between the formation of the hexagonal Zn phases and the structural changes. The surface appears more granular with the establishment of the hexagonal crystal lattices. As mentioned earlier, the formation of more coarse textures has already been identified in Zn-rich alloys.

The indentation hardness as a function of Zn concentration is shown in Fig. 6.33 b). It exhibits a monotonously decreasing trend with increasing zinc concentration and a significant drop at around 60 at% Zn. In this concentration range, the XRD data revealed the formation of the pure Zn crystal system. The appearance of this crystallographic phase and the vanishing of the previously predominant $Mg_2Cu_6Al_5$ phase is reflected in the drop of indentation hardness.

Summary:

The study of the quaternary alloy system with variable Zn content showed a variety of formed intermetallic phases. At low Zn concentrations, phases of the binary MgZn and CuZn systems were most abundant. The dominance of the CuZn subsystem was most apparent at higher Zn contents. The transition from cubic CuZn to hexagonal $Cu_{0.2}Zn_{0.8}$ and subsequently to the pure Zn lattice is outlined in the Cu-Zn phase diagram as a transition from γ-brass to ϵ-brass and Zn. The other alloying elements do not exert sufficient disorder on the crystal structures to weaken them.

The mechanical property of the indentation hardness reflected the formation of intermetallic or pure metallic prototypes. Its significant decrease with the incorporation of the pure Zn phase could be detected. The simulations did provide a good agreement with the measurements for this alloy system. Mixed MgZn domains were proposed in the simulations over the whole concentration regime, while in the experiments, mainly the hexagonal Zn phase dominated. This finding can be explained by the fact that both, Mg and Zn, have a hexagonal crystal structure, and, therefore, Mg can be easily incorporated into the hexagonal Zn structure. The

AlCu interaction, shown in the calculated atomic distribution, was also revealed in the XRD results.

6.1.8. AlCuMgZn-Mg

Weight optimization evolved into a crucial aspect of alloy design. Due to its low weight, magnesium is a remarkable element for applications in which weight reduction is essential. It is regarded as one of the next generation structural materials [202]. However, at present the industrial use of conventional Mg-based alloys is very limited due to their poor mechanical strength [202].

Moreover, Mg has a relatively high vapor pressure ($p_v \approx 10^{-2}$ Pa at 350 °C) and a low melting temperature of 650 °C [203]. These characteristics cause the combination of high amounts of Mg with other elements, especially if they have high melting points, by melt synthesis or casting to be difficult [204]. Therefore, the approach of PVD technique employed in this work is particularly suitable for the study of AlCuMg$_x$Zn systems.

The chemical composition of the sequence of samples measured by EDX is shown in Fig. 6.34 b) for the surface and c) for the bulk (determined from cross-section measurements of transversely polished samples). Initially, the Mg content in the bulk and on the surface gradually increases till it reaches a concentration of $\approx$ 50 at%. Thereafter, despite a further increase of the Mg content in the samples (seen in the EDX analysis of the cross-sections), a decrease in the measured surface concentration can be observed (see measurement pos. 20 in Fig. 6.34 b)). Only at the Mg content of $\approx$ 60 at%, the surface concentration advances and equals the bulk concentration. This trend is accompanied by the formation of dark spots in backscattered electron images (Fig. 6.34 a)). Cross-sections and subsequent EDX mappings revealed the origin of this distinct feature. As shown in Fig. 6.35 and Fig. 6.36, there is significant separation of two regions around the measurement position 20, after the heat treatment. One area exhibits a dominance of pure Mg, while the remaining part of the sample displays an AlCuZn excess. A further rise in the Mg concentration leads to an increase in the volume of the pure Mg domains (red regions) and an accumulation of Mg in the remaining regions. An abrupt drop in the measured EDX response was a result of the separation of a Mg sublayer at the substrate-sample interface. Since the electron beam has a penetration depth of around 4 μm at the selected electron energy and sample composition [205–207], it did not fully probe this interface area. The combined effect of growing Mg interface thickness and the increased domain expansion towards the surface leads to a higher measured Mg population at the surface upon a further increase of the total Mg content. A tendency for the light metal to separate was also identified in previous studies on the quaternary AlCuMgZn-Al system (section 6.1.6) [146].

The results of atomic distribution simulations for certain chosen samples are presented in Fig. 6.37. At low Mg concentrations (Fig. 6.37 a) and b)), AlCu and MgZn domains are mainly visible, however, a substantial amount of Cu atoms is also embedded in the MgZn domains. These are progressively removed with an increase of the Mg content till a predominant MgZn
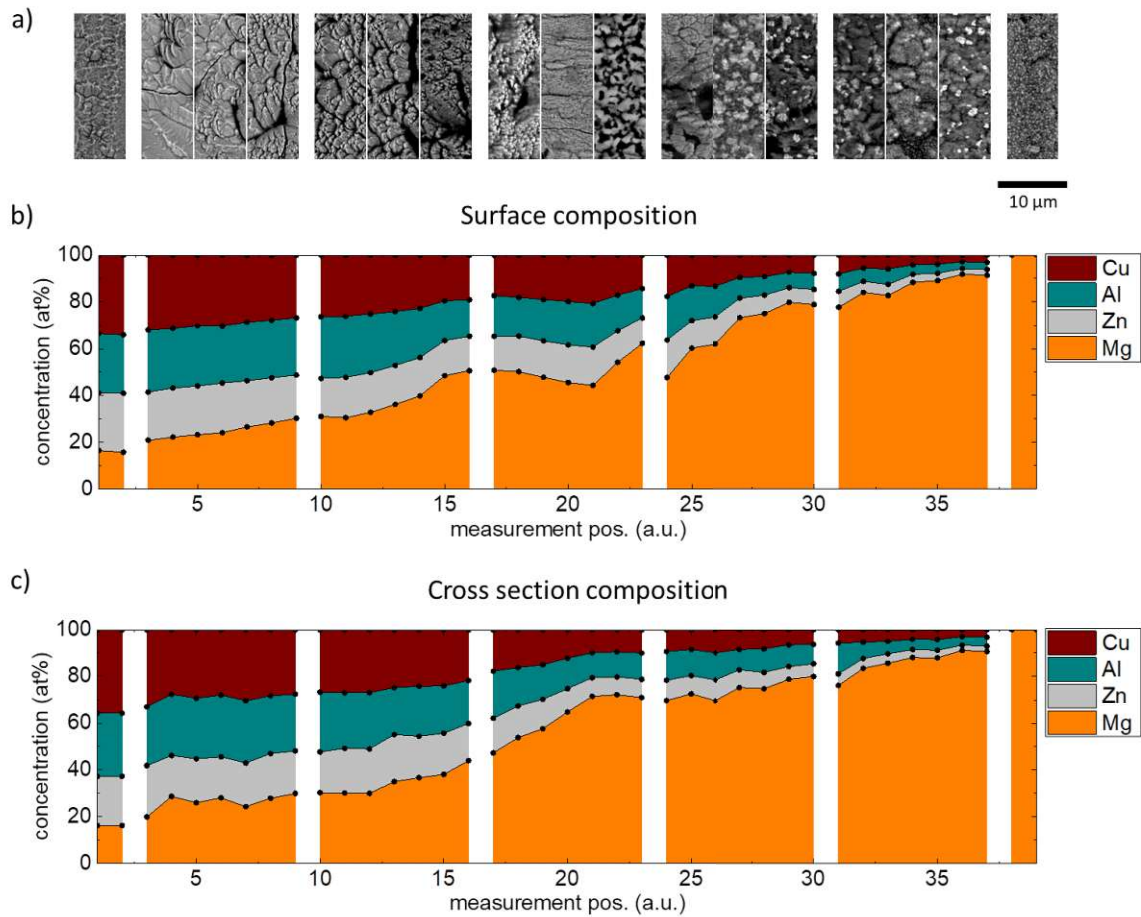
Figure 6.34.: a) BS electron images exhibit the structural changes on the surfaces of samples with different compositions. The analysis of the chemical composition measured b) on the surface and c) on the metallographic cross-section of the polished sample. The discrepancy between the surface and cross-section compositions (panel b) and c)) in the center region underlines the observed phase separation.
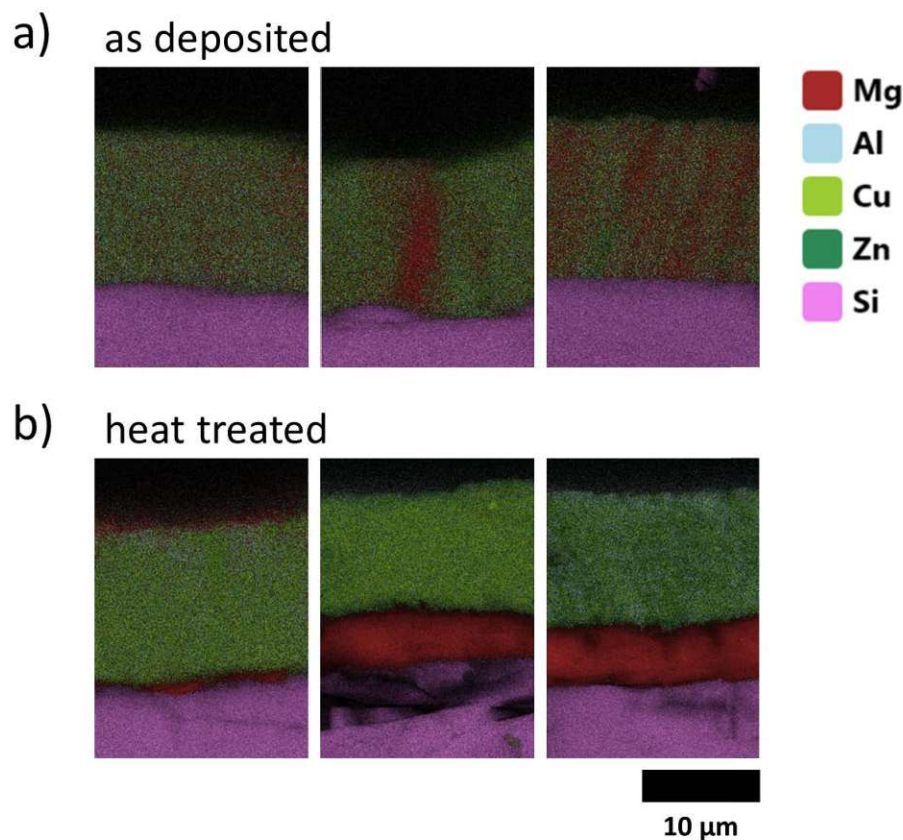
Figure 6.35.: EDX mappings of the metallographic cross-sections for a) as-deposited and b) thermally post-treated samples. The individual sections correspond to Mg concentrations (from left to right) of $x_{Mg} = 41$ at%, $x_{Mg} = 52$ at%, and $x_{Mg} = 65$ at% (pos. 17, 20, 23 in Fig. 6.34). Due to the segregation of Mg, the composition of the untempered sample has been taken. For better visibility of the substrate-sample interface, the Si layer indicating the glass substrate is marked in pink.
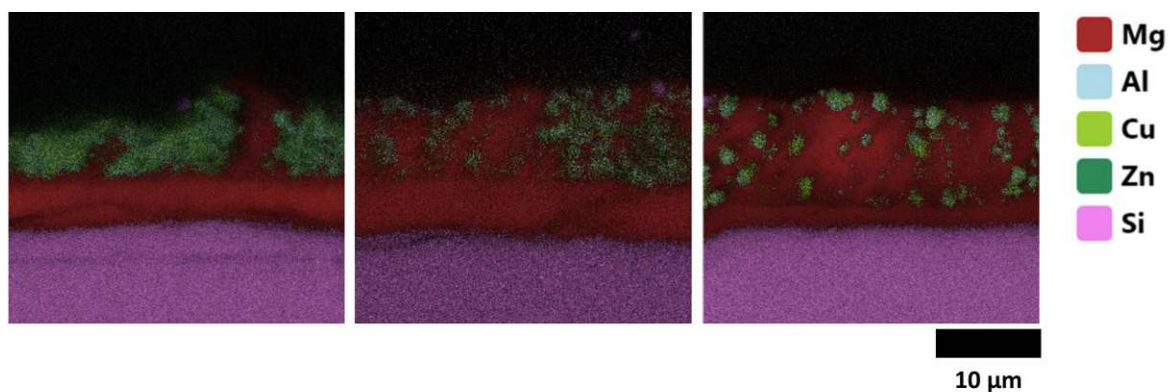
Figure 6.36.: EDX mappings of the metallographic cross-sections at higher Mg concentrations (left: 76 at%, pos 31; centre: 88 at%, pos 34; right: 91 at%, pos 37). One can see that the Mg-rich areas (in red) propagate towards the sample – 'air' interface. Si of the substrate is marked in pink.

101
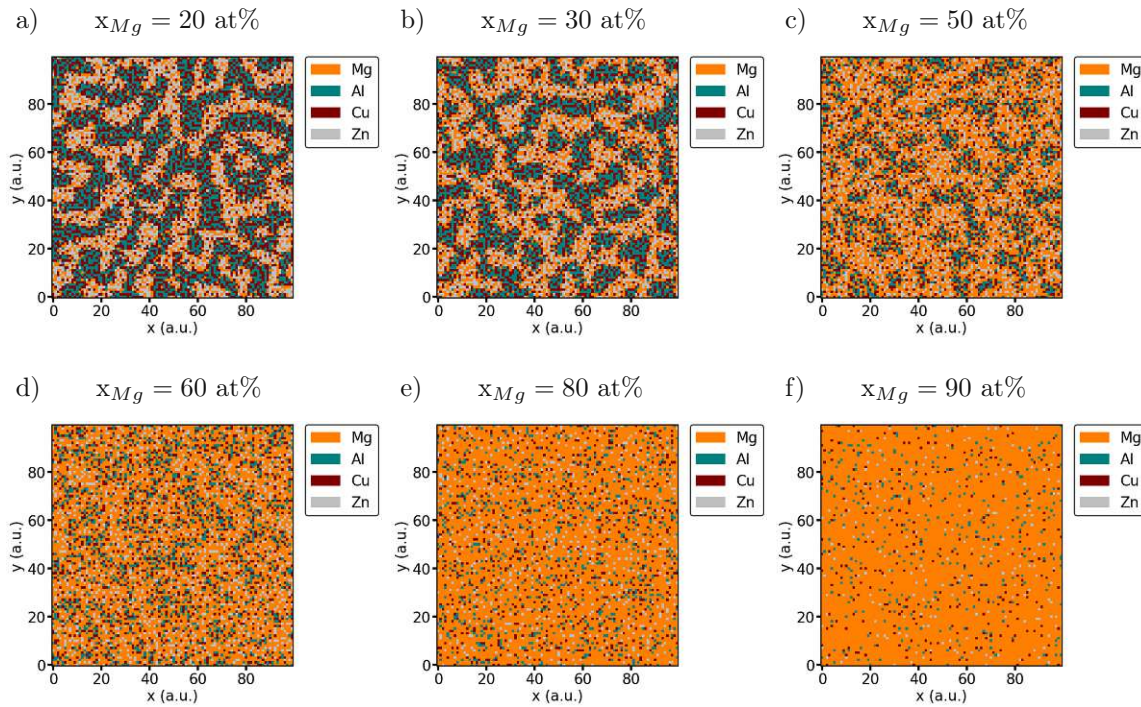
Figure 6.37.: Simulated distributions of selected experimentally prepared samples of the AlCuMgZn-Mg series. The relative Mg content increases continuously from a) $x_{Mg} = 20$ % to f) $x_{Mg} = 90$ at%.

arrangement is established. With a further increase of the Mg content (panel c)), the MgZn domains with clear Mg dominance grow, whereas the AlCu domains are still clearly defined. Finally, at a Mg content of about 60 at%, the AlCu regions start to gradually dissolve and integrate into the Mg matrix. In Fig. 6.37 e) and f) no secondary structure is visible, only a random arrangement of the Al and Zn atoms in a Mg matrix is observed.

To gain insight into the crystallography, XRD measurements were performed at the spots marked in Fig. 6.34 b). The measurements spots covered a lateral extent of 3 mm. The quantitative XRD results of a "search and match" phase identification, followed by detailed pattern analysis, are shown in Fig. 6.38 a). The examination identified 3 areas, which are discussed separately below:

Mg-poor region ($x_{Mg} < 40$ at%): In the elementally balanced region, three distinct crystallographic phases were detected. These are a cubic CuZn, a cubic $Mg_2(Cu_6Al_5)$ (Mg_2Zn_{11} prototype) and a hexagonal $MgZn_2$ phase. The latter is also known as the C14 Laves phase. As the relative Mg content increases, all Mg-containing crystal systems show an enhancement, while the CuZn phase decreases and disappears at around 20 at% Mg concentration. At this point, the $Mg_2(Cu_6Al_5)$ phase reaches its maximum before declining with further addition of Mg and completely vanishing at a Mg concentration of around 40 at%. The $MgZn_2$-Laves phase becomes progressively dominant up to its maximum phase fraction of 80 wt%. An analysis of the indentation hardness in this composition regime shows an initial stagnation

at a constant value of about 5.5 GPa. In the region dominated by the $MgZn_2$ phase, the hardness increases to a maximum value of ≈ 7 GPa. This maximum value coincides with the peak value of the presence of the crystallographic phase.

Intermediate region (40 at% $<$ x_{Mg} $<$ 70 at%): The intermediate region with a Mg concentration ranging from 40 at% to 70 at% is characterized by transitions in the crystal structure. The previously most prominent $MgZn_2$ Laves phase descends and gets consecutively replaced by a rhombohedral MgCuAl phase. This transition in the dominant crystal structure is accompanied by a change in the indentation hardness. As shown in Fig. 6.38 b), it decreases significantly from about 7 GPa to 2 GPa. Both transitions occur in the region in which EDX mappings of the cross-sections showed segregation of Mg towards the glass substrate. This segregation and the associated local change in composition into Mg-richer and Mg-poorer regions reduce the hardness. In the back-scattered electron SEM images, shown in Fig. 6.34 a), a formation of dark domains is visible in this region.

Mg-rich region (x_{Mg} $>$ 70 at%): With the increase of the Mg concentration above 70 at%, a pure hexagonal Mg phase forms, while all the previous phases ($MgZn_2$ Laves and MgCuAl rhomb.) simultaneously disappear. The direct comparison with the indentation hardness shows stagnation at low values < 2 GPa in this range and a further decrease to 0.4 GPa for the pure Mg sample. In literature, the hardness of Mg is reported to be around 0.4 GPa depending on its microstructure and fabrication method [208, 209]. The slightly higher indentation hardness already at a low content of alloying elements compared to the pure Mg sample can be explained in terms of solid solution hardening induced by the various alloying elements. The overall decrease of the indentation hardness with increasing Mg content has already been observed in other multi-component alloys (e.g., $Mg_x(MnAlZnCu)_{100-x}$) [210]. The results are consistent with the mappings of the cross-sections and the SEM images of the sample surfaces, where the increasing proportion of Mg-rich domains (dark/red areas in Fig. 6.34 a) and 6.36) is apparent.

The results of the Rietveld analysis in Fig. 6.38 show a good agreement with the simulation results (Fig. 6.37). The dominant phases at low Mg concentrations ($MgZn_2$, Mg_2Zn_{11}, and CuZn) appear to be consistent with the atomic distributions found in the simulations. The transition of the $MgZn_2$ phase to a rhombohedral MgCuAl mixed phase at Mg concentration between 40 at% and 60 at% matches well with the qualitative observations in Fig. 6.37 c) and d). Moreover, the increase of the pure Mg phase could be observed both experimentally and in the simulations.

Summary:
Investigating the effects of the varied light metal Mg content on an AlCuMgZn system delivered a complex progression of the predominant IM phases. In none of the measured samples,
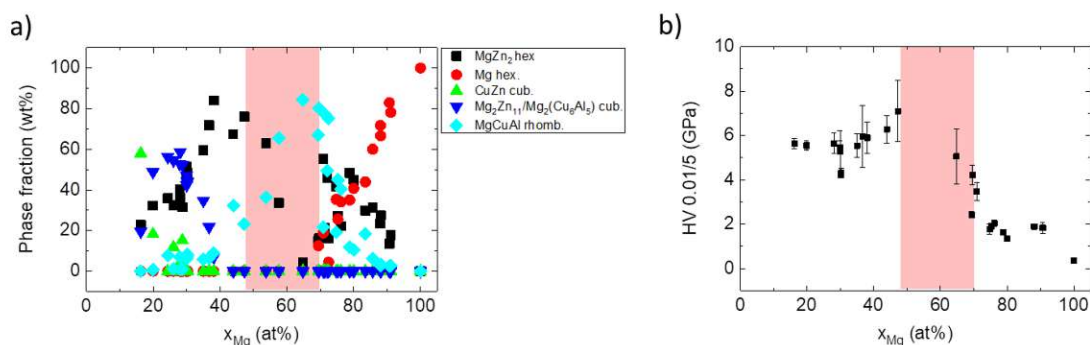
Figure 6.38.: a) Quantification of crystallographic phases identified by XRD for the AlCuMgZn-Mg system. b) Indentation hardness as a function of the Mg concentration. The Mg content was determined from the elemental analysis of the sample's metallographic cross-sections. The region in which segregation of Mg was observed is marked in red.

a single-phase region could be detected. Thermal post-treatment resulted in the separation of Mg, which was indicated by dark areas on the sample surface. Cross-sections showed that Mg accumulated mainly at the layer-substrate interface, which could be explained by the interaction between Mg and oxygen of the SiO_2 glass substrate.

6.1.9. AlMgZn-Cu

In previous studies it was shown that the addition of copper to the magnesium alloy can improve the strength and plasticity [211,212] due to the formation of the $MgCu_2$ phase. Cu has the same atomic radius as Zn, however, there is a significant difference in the electronegativity, which strongly influences binding dynamics. In this section, we examine the quaternary AlMgZnCu system scanning the whole range of Cu content (from 0 at% to 100 at%) to disentangle its influence on the alloy formation. In addition, a combination of DFT and sophisticated cluster expansion calculations were performed to support the experimental findings.

Fig. 6.39 b) shows the compositions of the prepared samples for this series with the Cu content varying from 0 at% (corresponding to the ternary AlMgZn system) to 100 at% (pure Cu). The results of the XRD measurements are depicted in Fig. 6.40.

The analysis identified two single phase regions, which will be discussed further in detail.

Starting at the ternary composition of Al: 48 at%, Mg: 24 at% and Zn: 28 at%, the measured XRD peaks could be assigned to the $MgZn_2$ Laves phase and the pure Al phase. Their presence is in agreement with the results in section 6.1.3. With the addition of small amounts of Cu, these two phases quickly declined in significance and were replaced by a cubic $Mg_2Cu_6Al_5$ intermetallic phase. This crystal phase has already been detected in the AlCuMgZn-Al series in section 6.1.6. The XRD raw data with fitted phases is given in Fig. 6.41. In the Cu concentration range from about 20 at% to about 25 at% (Fig. 6.41 b)), the single phase
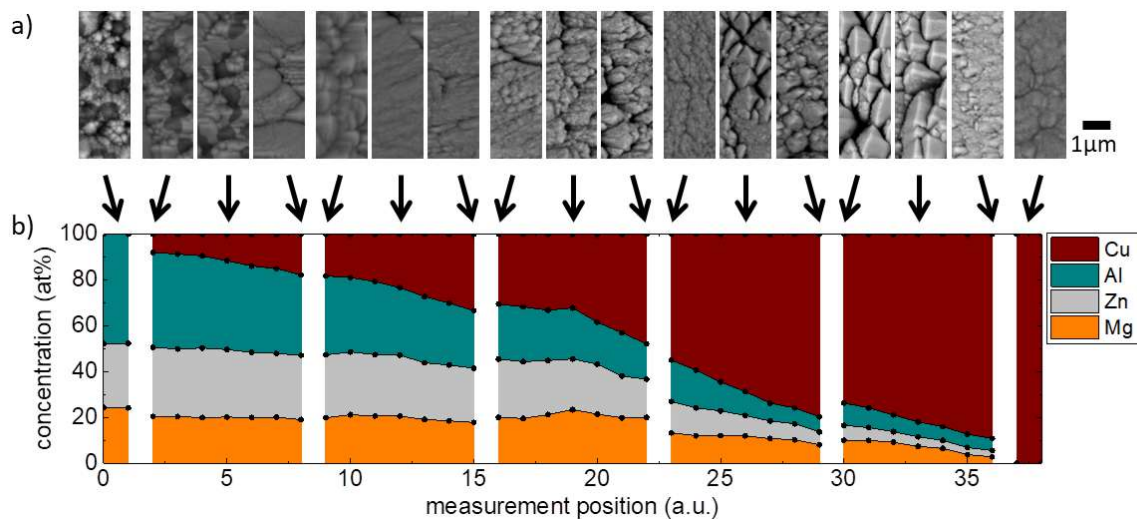
Figure 6.39.: a) Surface structure of AlMgZn-Cu samples detected at selected points.   b) Chemical composition of the prepared samples with varying Cu content.
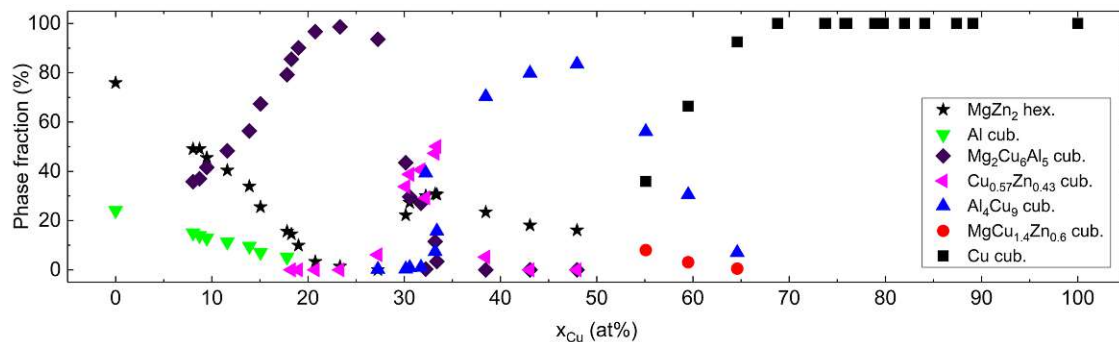
Figure 6.40.: Detected crystal structures and quantitative results of Rietveld analysis for AlMgZnCu samples.

region was detected as all peaks could be fitted with the $Mg_2Cu_6Al_5$ phase (purple areas). Simultaneously, the measured indentation hardness analysis shows a steady growth with an increase of the intermetallic $Mg_2Cu_6Al_5$ phase (compare Fig. 6.42 in the range of 0 at% < x_{Cu} < 30 at%).

The second area of interest was found at higher Cu contents. A detailed discussion was published in our recent paper [213], and a brief summary is given below.

Figure 6.43 a) depicts the variation of the chemical composition in a region with the relative Cu content increasing from 55 at% to 80 at%. The X-ray diffractograms in Figure 6.43 b) indicate the crystallographic order at the respective measuring positions, and reveal rising additional peaks with an increasing amount of alloying materials. A "search and match" approach assigned the newly detected peaks to an Al_4Cu_9 cubic structure (indicated by arrows in Fig. 6.43 b)), in addition to the previously established FCC Cu phase. The performed analysis also identified a $MgCu_{1.4}Zn_{0.5}$ phase; however, due to a small peak height in the segment, it was not further considered. This phase represents a $MgCu_2$ (C15 Laves phase) prototype

a)

b)

c)
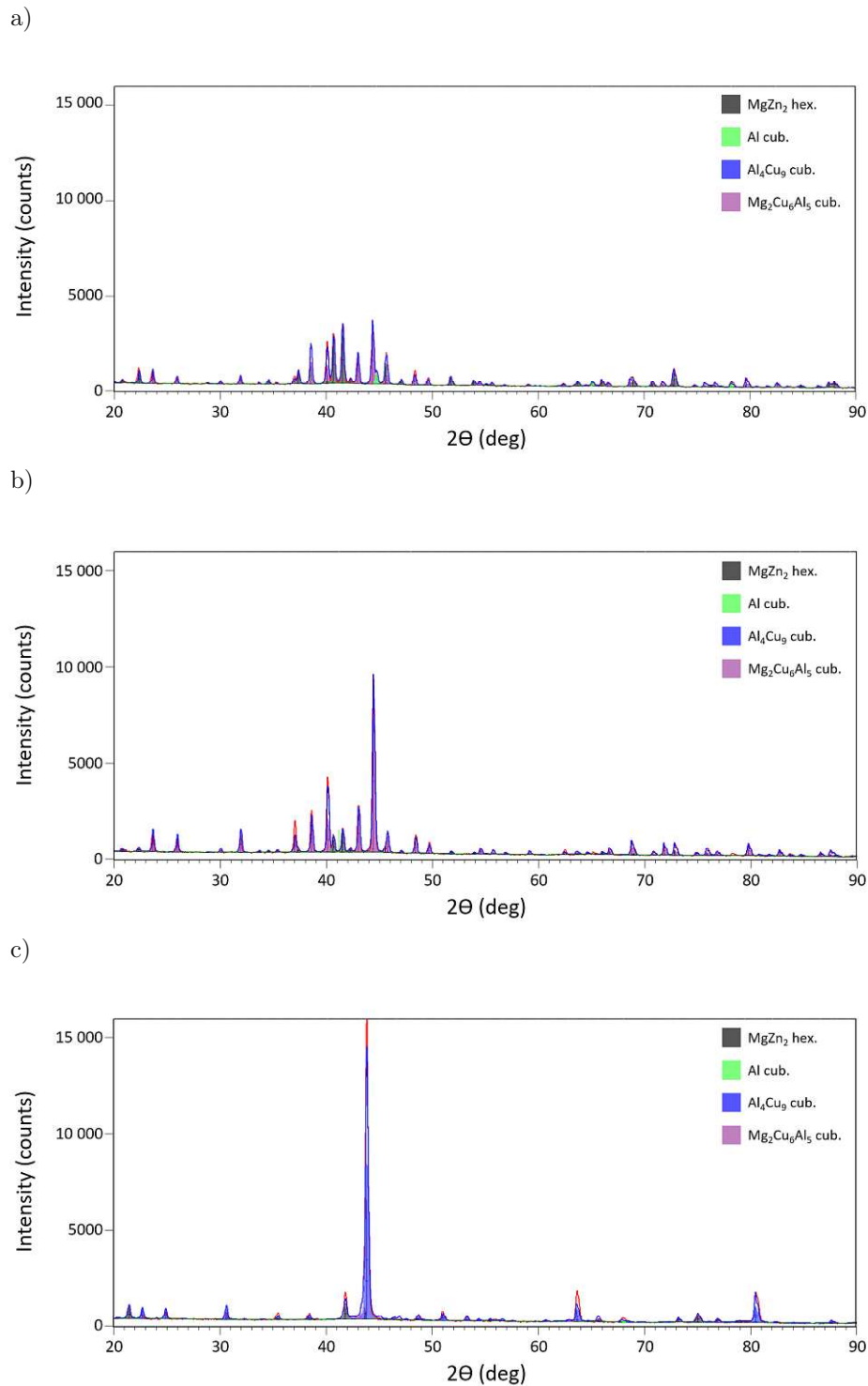
Figure 6.41.: XRD raw data and the identified crystal phases for selected alloy compositions with varying relative Cu content. a) $x_{Cu} \approx 10$ at%, b) $x_{Cu} \approx 20$ at%, and c) $x_{Cu} \approx 50$ at%
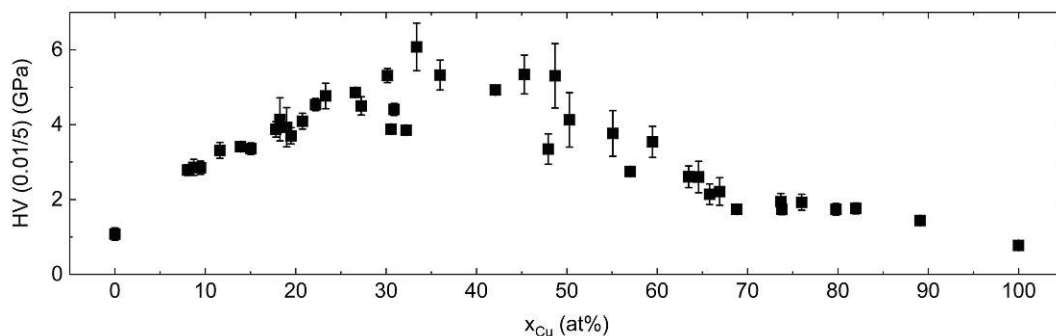
Figure 6.42.: Indentation hardness of AlMgZnCu samples versus the varying Cu content. An initial increase in hardness reaches its maximum at around $x_{Cu} = 35$ at% and afterward gradually decreases, which correlates well with the detected crystallographic phases in Fig. 6.40. The drop in hardness at $x_{Cu} > 50$ at% coincides with the transition of the intermetallic Al_4Cu_9 phase to the pure FCC Cu lattice.

that is distorted due to the occupation of the lattice sites by various alloy atoms (e.g., Zn and Al). Introducing high concentrations of alloying elements into the lattice (Cu: ~64.6 at%, Al: ~12.6 at%, Mg: ~12 at%, Zn: ~10.8 at%) causes the single phase property of the sample to collapse. It is important to note that this single phase behaviour was found at concentrations, at which, according to existing thermodynamic criteria, it should not be occurring. [75, 76]. Figure 6.44 a) shows the quantitative results of the full pattern phase analysis and the indentation hardness measurements for the investigated sample. The crystal structure is dominated by a FCC Cu lattice [214]. Shifts of the Cu peaks towards lower Bragg angles are an indication of a distorted crystal lattice induced by alloying metals occupying Cu sites [215]. With an increase of the Al, Mg, and Zn concentrations, new crystallographic phases, assigned to the cubic Al_4Cu_9 [216] lattice and the cubic $MgCu_{1.4}Zn_{0.6}$ phase (C15 Laves structure), were detected. According to Gaudry *et al.* [197], the cubic Al_4Cu_9 phase can be described by a BCC unit cell. The phase analysis suggests the transition of the Cu FCC to the cubic Al_4Cu_9 crystallographic system. This transition is characterised by an increase of around 100 % in indentation hardness (see Figure 6.44 b)).

Table 6.4.: Chemical composition, calculated valence electron concentration and atomic size difference δr of the individual measurement points throughout the sample (compare Fig. 6.43 a)). In addition, the calculated ΔS_{config}, the ratio of mixing enthalpy and formation enthalpy H_{IM}/H_{mix}, and values according to [6, 75] (right side of eq. (2.8), indicated as 'Senkov' in the Table) of each individual spot are given.

Measurement pos.	Cu (at%)	Al (at%)	Mg (at%)	Zn (at%)	VEC	$\delta r(\%)$	$\Delta S_{config}/R$	$\Delta H_{IM}/\Delta H_{mix}$	Senkov
1	55.1	18.1	13.2	13.6	8.51	6.97	1.176	3.89	1.58
2	59.5	16.5	12	12	8.73	7.58	1.115	3.97	1.59
3	64.6	12.6	12	10.8	9.02	7.73	1.038	3.77	1.56
4	68.8	10.4	11.9	8.9	9.19	8.03	0.961	3.83	1.57
5	73.7	7.8	10.7	7.8	9.48	8.04	0.862	3.67	1.55
6	75.9	6.9	10.2	7	9.61	8.03	0.813	3.68	1.56
7	79.8	6.6	8	5.6	9.81	8.21	0.723	3.91	1.59
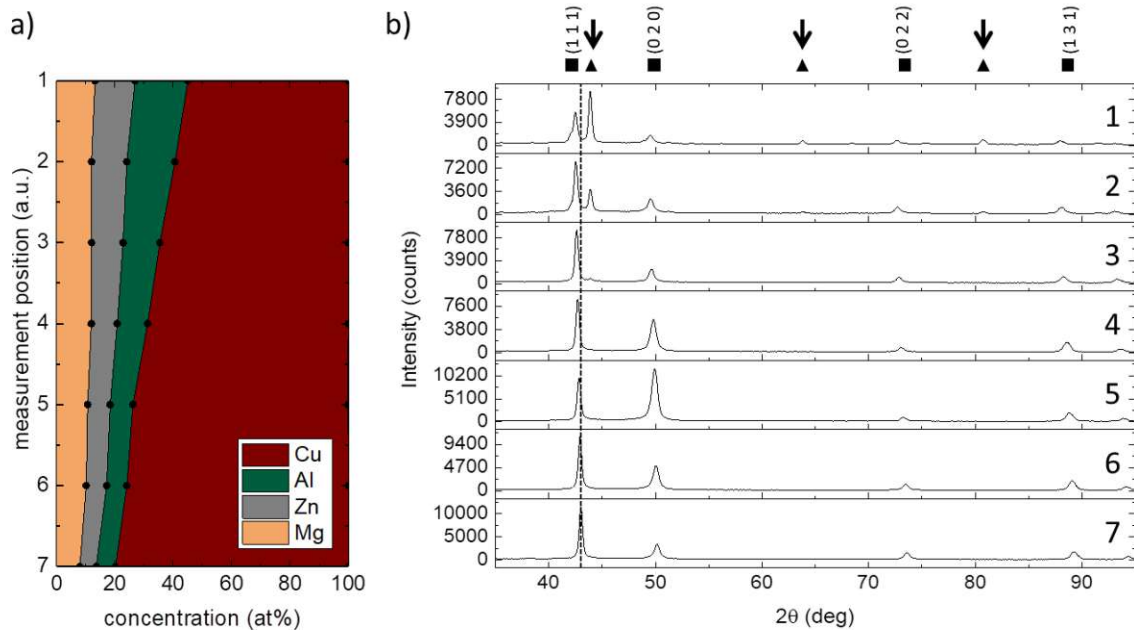
Figure 6.43.: a) Chemical compositions of the Cu-dominated samples. The circles denote the measurement points on the sample b) XRD measurements for the marked spots in a). The arrows indicate the formation of subphases (▲: Al_4Cu_9 cubic, ■: Cu FCC) with increasing concentrations of the alloying materials. A clear shift to smaller Bragg angles can be seen, marked by the horizontal line at the Cu (1 1 1) reflex.
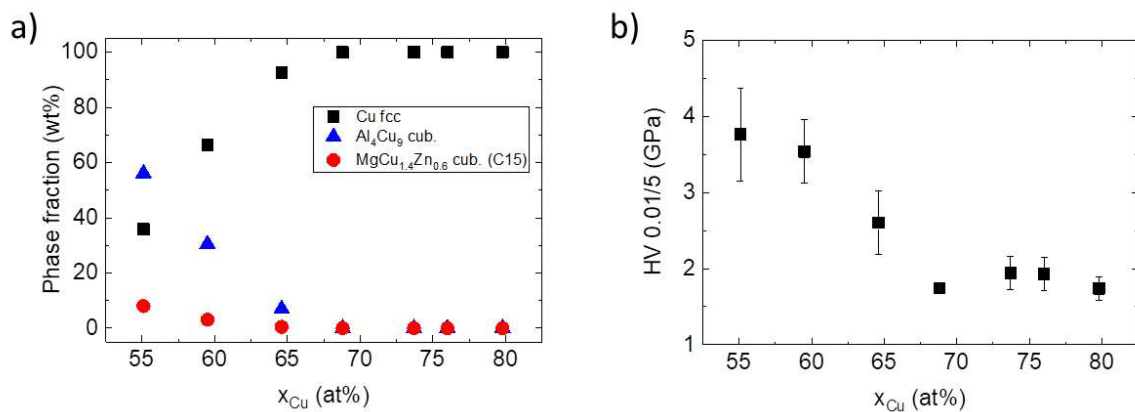
Figure 6.44.: a) Phase fraction of crystallographic phases in the Cu-dominated sample identified by Rietveld fitting. The Cu FCC phase continuously increases, while the Al_4Cu_9 cubic phase gradually decreases. b) Vickers hardness measurements show a decrease in hardness, which is consistent with the formation of the pure Cu phase.
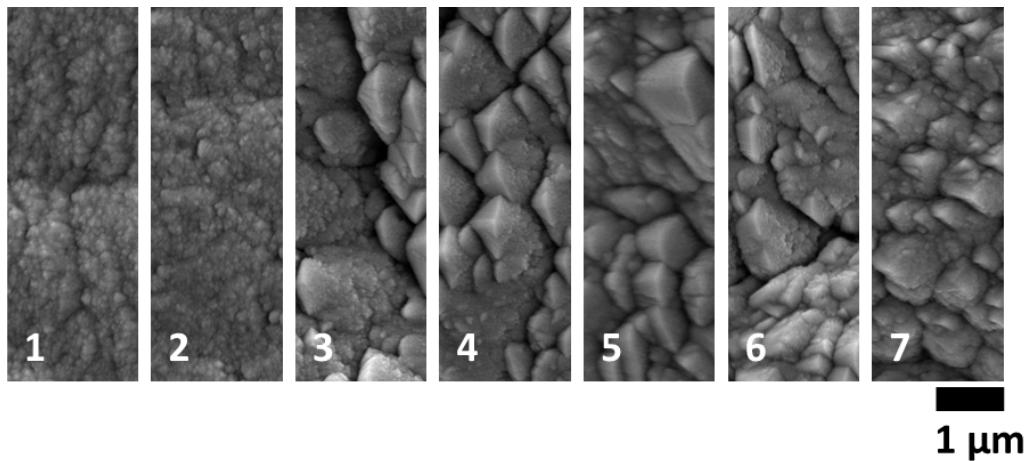
Figure 6.45.: SEM images show a structural change of the surface depending on the different chemical distributions. The numbers indicate the measurement positions on the sample and thus the corresponding compositions (compare Table 6.4).

In addition, the morphology and structure of the surface was investigated as a function of the varying Cu content. The analysis of the SEM images (Figure 6.45) show a transformation of the sample's surface structure.

The initially formed fine-grained structures (measurement positions 1 and 2), with increasing Cu amount, converted into hatched edges and coarse crystalline structures (measurement positions 5 to 7). In the transition region (measurement positions 3 and 4) the degeneration of the crystallographic phases begins and is accompanied by an increase in hardness (see Fig. 6.44). A detailed examination of the microstructure by TEM in diffraction and imaging mode showed a clear decrease in grain size corresponding to the decreasing relative Cu concentration (Fig. 6.46 a) and c)). In Fig. 6.46 b) and d) the diffraction patterns at the selected areas (red circles) are shown. The increased occurrence of diffraction spots indicates the transition to smaller grains and an increase in the polycrystalline character of the sample. For this series, manufactured samples were also reproduced by the simulation (Fig. 6.47). At low Cu concentrations, the separation of AlCu and MgZn domains can be clearly seen. With increasing Cu concentration, progressively more Cu atoms migrate into the MgZn domains (compare Fig. 6.47 b)). In this region, a single-phase intermetallic $Mg_2Cu_6Al_5$ was observed in the XRD measurements. Qualitatively, the increasing diffusion of Cu atoms would result in the formation of this phase, but the extension of the simulation cells is too small to make such a prediction. As the Cu content is further increased, the areas occupied by Cu are expanded, with the Cu atoms showing an overall random arrangement. The experimentally observed transition region, from an intermetallic phase to a terminal solid solution, is shown in Fig. 6.47 c) and d). A conversion from a more structured microstructure (Al-rich and MgZn-rich regions are still clearly separated) to a random arrangement of Cu atoms with incorporated Al, Mg and Zn atoms can be observed. This could indicate the transition to the single phase solid solution region.
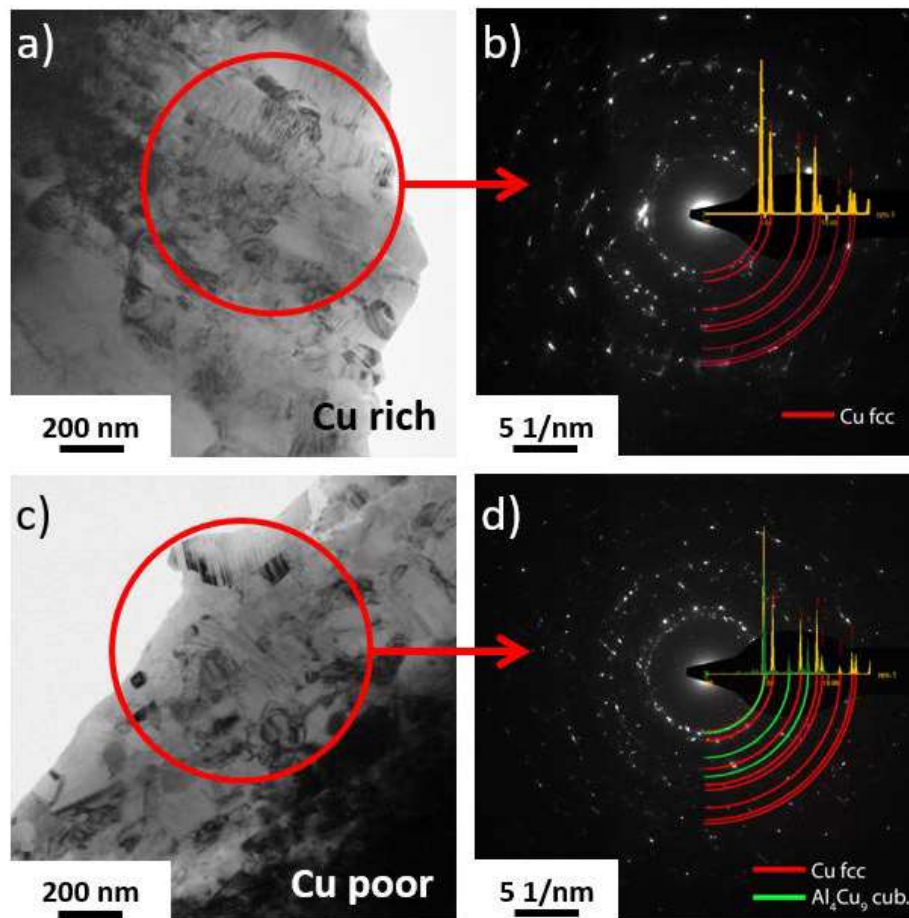
Figure 6.46.: TEM bright field micrographs of regions with a relatively high a) and low c) Cu content. The compositions of these regions are given at pos. 1 and pos. 7 in Table 6.4. The red circles mark the area investigated by electron diffraction (b,d). In the Cu-poor region, the grain size shows refinement, and the diffraction patterns indicate a transition from a single-phase (pure Cu lattice) to a multi-phase system (Cu + Al_4Cu_9 cubic).

Since the investigations of the quaternary system and especially the studies of the Cu trajectory yielded interesting results, DFT based CE calculations were employed to determine the energetic minimum. The experimentally identified crystal systems with variable Al, Mg, Zn, and Cu fractions were modelled, and the occupations of the lattice sites were permuted. The calculated energies of formation for each case were compared to explore the energetically most favourable structure. Different experimentally discovered crystal systems and the minimum formation energies calculated by CE (these correspond to the minimum internal energy) are shown in Fig. 6.48. The grey highlighted region reflects the Cu-dominated part where the transition from FCC Cu to the cubic intermetallic Al_4Cu_9 phase was observed experimentally. This transition was also evident in the convex hull of the CE calculations. A more detailed study on this concentration regime of the AlMgZn-Cu system can be found in [213].
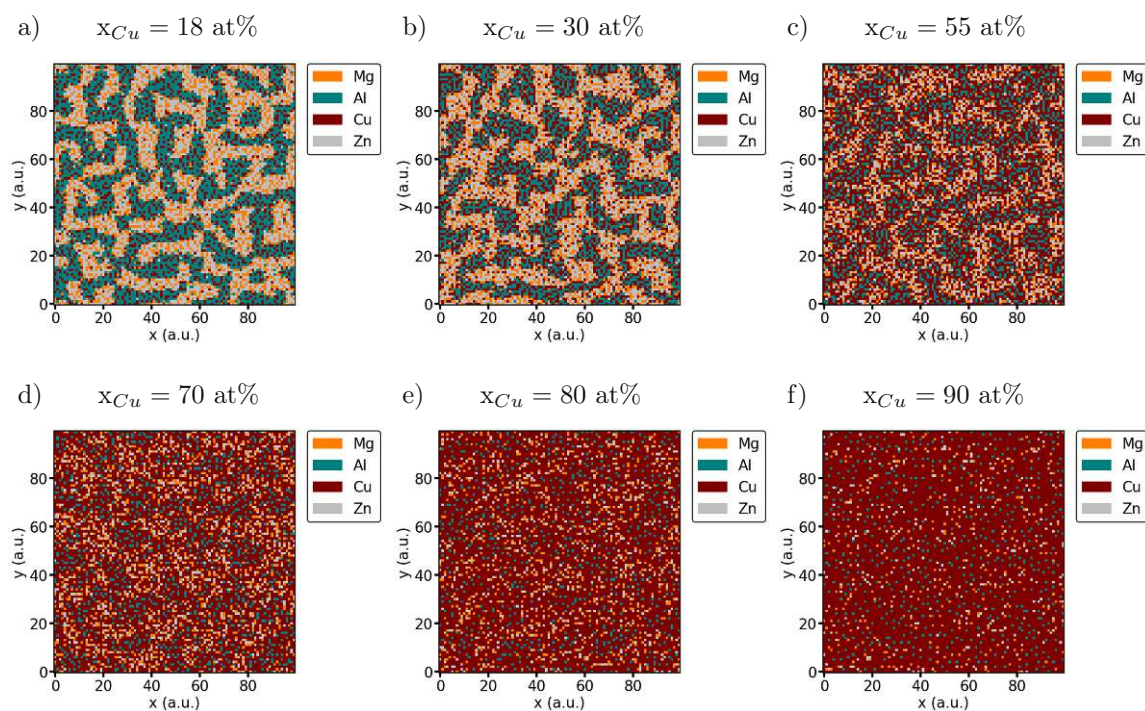
Figure 6.47.: Simulated atomic distributions at different Cu fractions. The transition from clearly separated AlCu and MgZn domains in panel a) to the random arrangement of Cu with incorporation of the remaining alloying materials (in d) -f)) can be seen. Panels b) and c) show the steadily increasing incorporation of Cu within the MgZn rich domains.
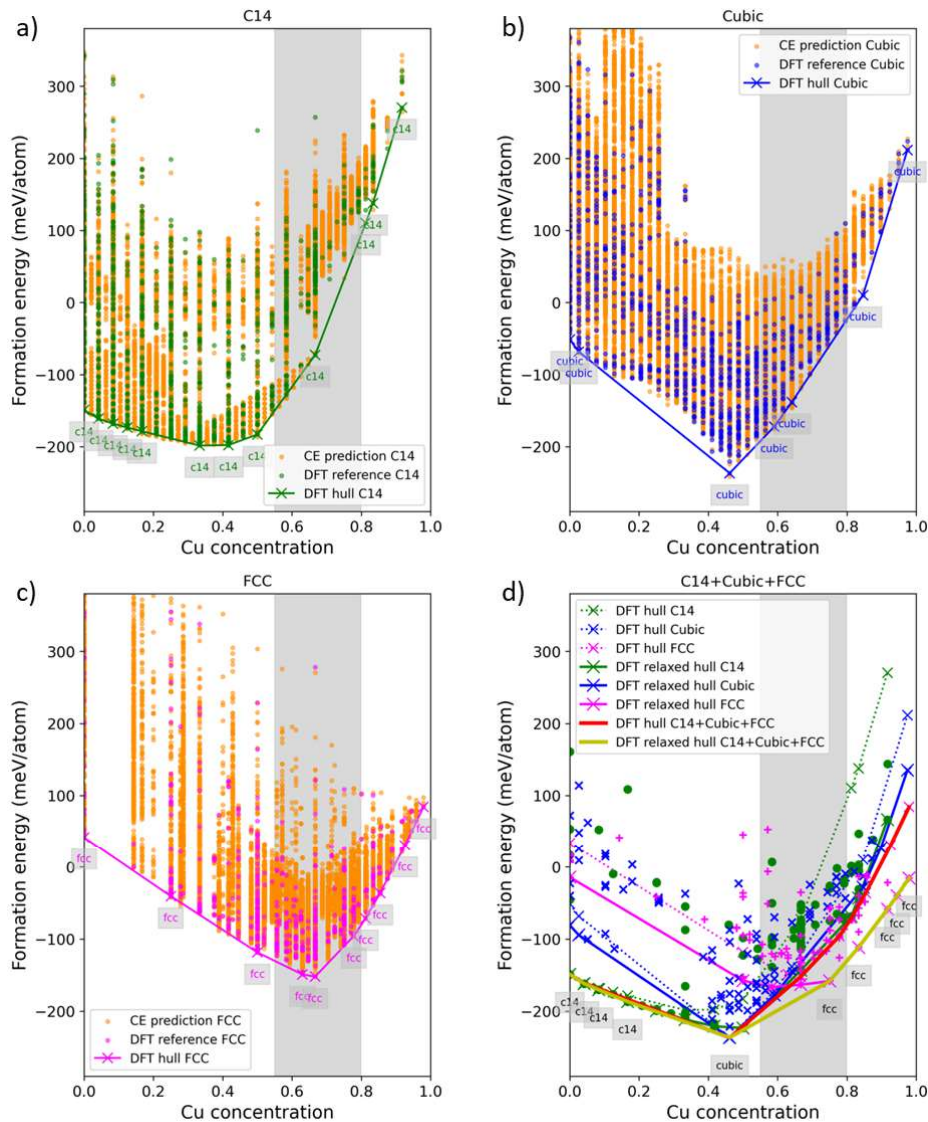
Figure 6.48.: Calculated formation energies using DFT (green and blue) and CE (orange) for a) the C14 Laves phase, b) a cubic, and c) a FCC phase projected onto the Cu concentration axis. The convex hull indicates at which Cu concentration stable structures are predicted. Panel d) includes DFT formation energies for the respective crystal systems calculated at the equilibrium volume of the individual structures. [213]

Summary:

The investigation of the Cu trajectory revealed interesting results concerning the effects of the element Cu on the crystal structure. Two single phase regions have been identified. The first is an extended region of the terminal solid solution at Cu fractions > 65 at%. The second exhibits a cubic $Mg_2Cu_6Al_5$ structure and occurs at relative Cu fractions of 20 at% to 30 at%. The studies confirmed the trend of the previous series that the relative Cu content is the most influential factor for the formation and degeneracy of crystal phases in complex multicompo-

nent alloys. The experimental results were confirmed by DFT combined with CE calculations. The mechanical property in the form of indentation hardness showed a complex progression with significant increase when intermetallic phases were formed.

6.1.10. Summary AlCuMgZn Based Alloys

The investigation of the quaternary AlCuMgZn system, including selected subsystems, provided information about the interactions and interrelations between the individual elements. In order to generate sufficient data to make well-founded statements about the resulting phase behaviour, mechanical properties and structure formation, nine trajectories along the panes and throughout the volume of the spanned compositional tetrahedron have been considered. The most important findings are briefly summarized below:

- **Demixing of Al in AlMgZn:** The weakening of the strong MgZn intermetallic bond was attempted by providing Al to force degeneration of the phase system. It was found that the Mg-Zn bond is too strong, and Al exerts little influence on the predominant crystallographic system. Over the entire concentration space, the coexistence of two structures, the $MgZn_2$ Laves phase and the Al phase, was found, and only in a narrow compositional space, an AlMgZn Bergman phase could be detected. Since this phase was predicted by classical phase diagrams, the applicability to compare sputtered and thermally post-treated samples with classical preparation methods was shown.

- **Influence of Cu:** The variation of the relative compositions showed that Cu has the greatest influence on the formation of crystal phases. Without Cu, strongly separated crystal systems formed. The addition of Cu promoted the degeneration of the crystal phases. This effect can be partially attributed to the increase in entropy resulting from the inclusion of one more element (in this case, Cu). However, the element Cu appears to play a special role in the bond and structure formation dynamics. Comparison with other fabricated quaternary (and partly quinary) systems showed that high entropy could not be responsible for this alone. Alloys with similar entropy values predominantly formed IM phases and showed no single-phase behaviour. Also, each of the newly formed crystal phases contained Cu and was part of a binary Cu-X phase system.

- **Identification of single phase regions:** The analysis of the crystal structures of all the produced samples identified distinct single phase areas. Fig. 6.49 indicates the compositions for which the crystal structure consisted of more than 85 % single phase. In brief, two different cases may be differentiated here:
  - Intermetallic Single Phases: In this case, only one phase is established, showing an intermetallic structure. Such a region was found in the central part of the compositional tetrahedron. Here, the cubic $Mg_2Cu_6Al_5$ phase dominated, which is a complex intermetallic crystal phase with 39 atoms per unit cell [217–219]. This phase was also found to be more stable in the direction of higher Al and Cu

contents. A second region was identified along the boundary surface of the Al-Mg-Zn triangle. In this area, over a wide concentration range, the MgZn$_2$ Laves phase was stable. As shown in section 6.1.3, a separation of this phase and the pure Al phase occured here. The MgZn$_2$ phase dominated the crystal structure up to an Al fraction of x$_{Al}$ = 40 at%.

– Simple Structure Single Phase: In this case, the crystal structure formed a simple lattice structure. This type of single phase was found in a region around the pure elements and exhibited their crystal structure. Two of such phases were identified. The first phase was identified in a small area around pure Al. The maximum "perturbation" by alloying materials up to which the Al phase remains stable was found to be about 10 at%. The second region was located in a zone around pure Cu. Up to a concentration of 35 at% of alloying elements a pure Cu FCC structure could be detected here. This single-phase region occurs in a regime of relatively low entropy. Therefore, the establishment of the single-phase can not (only) be attributed to the entropy effect. Strictly speaking, the alloy has to be regarded as a medium entropy alloy due to the proportion of alloying atoms.

- **Variation of mechanical properties:** The structure and crystalline order naturally influence the mechanical properties of a material. The measured indentation hardness showed a complex progression for most investigated series. An overview of several measured hardness values is shown in Fig. 6.50. The hardness values decreased around the vertices of the tetrahedron, which is plausible since there the pure element properties dominate due to their high proportion in the alloy. The indentation hardness of the elements contained in the system is summarized again in Tab. 6.5. Furthermore, an increase in hardness towards the center of the tetrahedron is evident. This finding is consistent with the experimentally observed establishment of intermetallic crystal systems, which show, in general, a relatively high hardness. The maximum indentation hardness was observed in the center of the tetrahedron. The comparison with Fig. 6.49 reveals the presence of a single-phase intermetallic region (cub. Mg$_2$Cu$_6$Al$_5$). Moreover, according to the definition of configurational entropy, this is the region of maximum entropy. In accordance with the equation, $\Delta G = \Delta H - T\Delta S$, the entropy might dominate and thus lead to the formation of only one phase. Since all alloying elements must be incorporated into this crystal system, significant distortions and defects occur. These act as barriers to the tip when measuring indentation hardness, resulting in an increase of its values.

- **Comparison to computational approaches:** Two computational approaches have been addressed in this work. The comparison of experimental to theoretical results showed excellent agreement for the quaternary Al-Cu-Mg-Zn system:

– Atomic distribution calculation using enthalpy: The presented simplistic approach to calculate bonding preferences and associated atomic distributions delivered
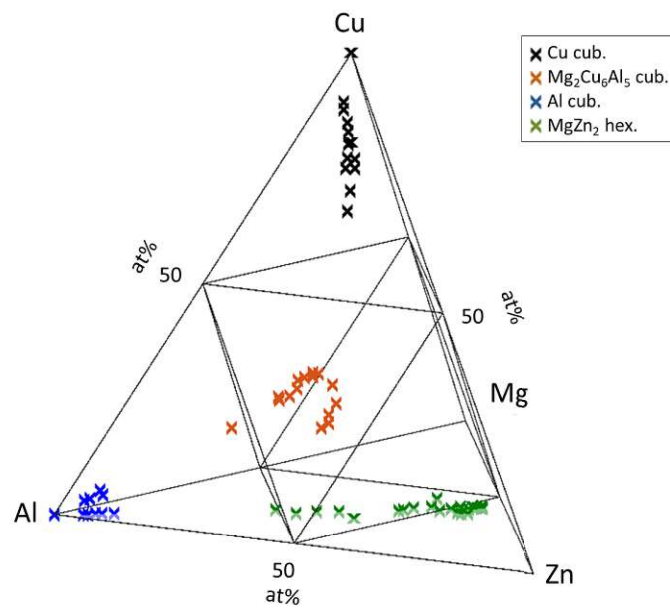
Figure 6.49.: 4-dimensional composition space of an Al-Cu-Mg-Zn system showing measuring points at which predominantly single-phase crystallography was observed.

promising results. Comparison with experimental data sets and literature records demonstrated the plausibility of the calculations for a wide range of compositions. The simulation indicated candidate crystal structures, particularly in regions of multiple coexisting intermetallic phases. In such cases, interpretation of the XRD data is challenging due to the superposition of a large number of peaks along with the ambiguity of the measurement method, and additional information attained from simulations was helpful.

– Cluster Expansion and DFT calculations: the samples prepared and characteristics found during the investigation of the Al-Cu-Mg-Zn system could be reproduced using cluster expansion and DFT methods. The experimentally detected results showed minima of the formation energies in the simulations. In particular, the phase transition of the FCC Cu terminal solid solution to a system of intermetallic phases was demonstrated.

Table 6.5.: Indentation hardness values of 10 μm thick sputtered metallic samples.

	HV 0.01/5 (GPa)
Mg	0.35 ± 0.05
Al	0.55 ± 0.02
Cu	0.77 ± 0.04
Zn	0.57 ± 0.03
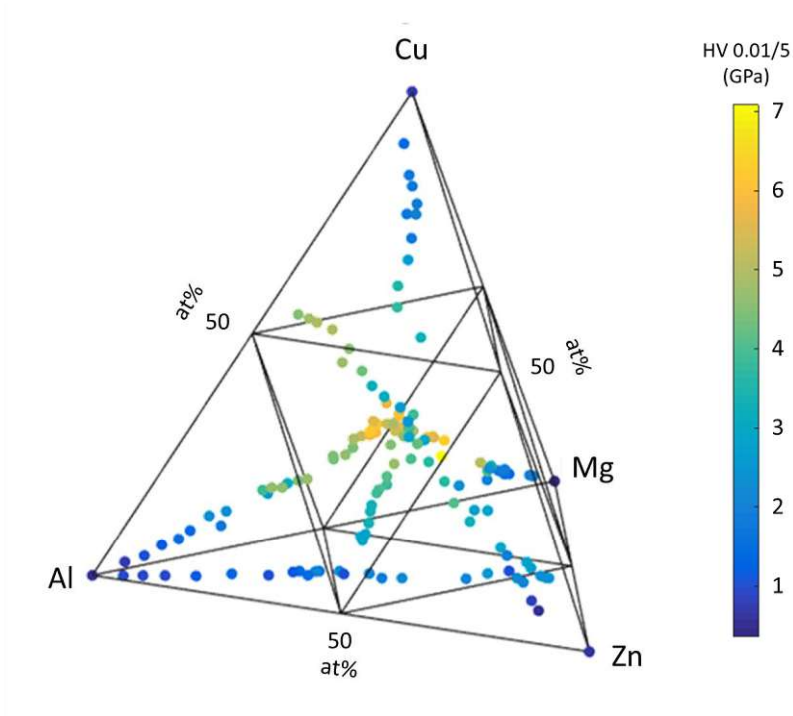
Figure 6.50.: 4-dimensional composition space of an Al-Cu-Mg-Zn system showing indentation hardness values for various compositions.

6.2. Extension to Quinary Systems

Based on the preceding results and taking into account the criteria described in section 2.1.2, a fifth element was chosen, which could be added to the AlCuMgZn system which was already investigated in detail. The most important consideration for the choice was the fulfillment of the criterion described in eq. (2.8), as well as the one in eq. (2.9). The values of the mixing and formation enthalpies needed for the calculations, and all other required quantities, are listed in appendix A.3 and A.4.

The analysis showed that only the addition of the elements Cr and V to the AlMgCuZn system led to the fulfillment of the chosen criteria. For further investigations, Cr was chosen. The analysis of the two criteria identified 6 and 66 compositional combinations, depending on whether eq. (2.8) or eq. (2.9) was used (with step size of 10 at% of each element's concentration (Mg, Al, Cr, Cu, Zn). The possible compositions are shown in Fig. 6.51.
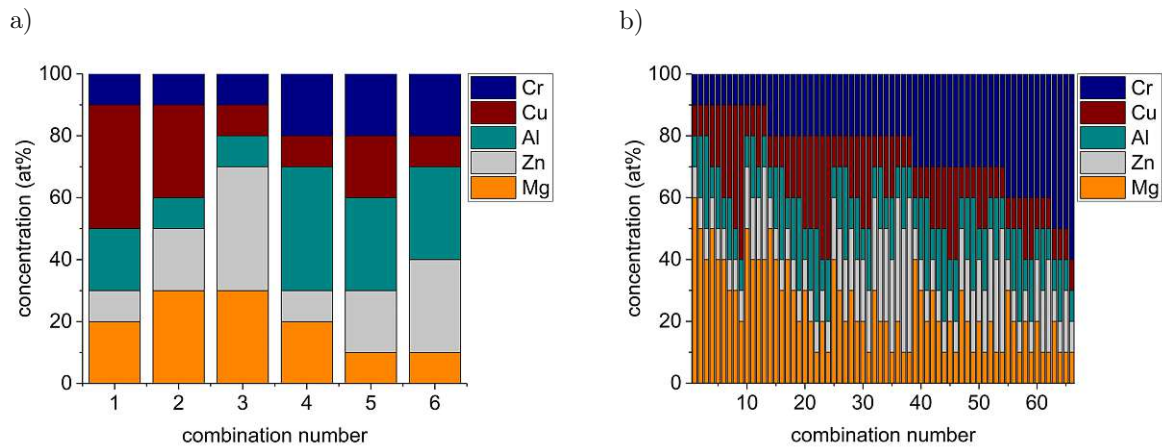
Figure 6.51.: Compositions of alloys fulfilling the criteria according to a) Simson *et al.* [76] and b) Senkov *et al.* [6].

6.2.1. AlMgZn-Cr

The binary phase diagrams of the constituents of the ternary system AlMgZn and of Cu with Cr are shown in Fig. 6.52:

- Al-Cr: Alloying Al with small amounts of Cr is often used to inhibit recrystallization and grain growth [220]. The Al-Cr phase diagram is shown in Fig. 6.52 a). This is based on the work of [221–223] and shows a variety of IM phases in addition to an extended solid solution on the Cr-rich side. The main crystallographic phases are: [220, 224]

  - Al from 0 at% $< x_{Cr} <$ 0.37 at% with a FCC lattice [225–227].

  - $Al_7Cr(Al_{13}Cr_2)$ from 12.4 at% $< x_{Cr} <$ 13.7 at% exhibiting a monoclinic crystal structure (Pearson symbol cF4) [228, 229].

  - $Al_{11}Cr_2(Al_5Cr)$ from 15.2 at% $< x_{Cr} <$ 17 at% having a monoclinic crystal structure (Pearson symbol mC104) [228].

  - Al_4Cr from 18.5 at% $< x_{Cr} <$ 20 at% showing a monoclinic crystal structure as well (Pearson symbol mP180) [228].

  - αAl_9Cr_4 from 30 at% $< x_{Cr} <$ 33.5 at% with a cubic γ-brass like structure (Pearson symbol CI52) [221].

  - αAl_8Cr_5 from 35.5 at% $< x_{Cr} <$ 42 at% exhibiting a trigonal structure (Pearson symbol hR26) [230, 231].

  - $AlCr_2$ from 65.5 at% $< x_{Cr} <$ 71.4 at% showing a tetragonal symmetry (Pearson symbol tI6) [230].

  - Cr from 54 at% $< x_{Cr} <$ 100 at% having a BCC structure (Pearson symbol cI2) [225–227].

- Cr-Mg: In Fig. 6.52 b) the Cr-Mg phase diagram is displayed [141, 232]. The solubility of Cr in Mg, as well as Mg in Cr, is low. The total composition space consists of a mixture of an HCP Mg and a BCC Cr phase.

- Cr-Cu: The phase diagram in Fig. 6.52 c) shows the binary Cr-Cu phase diagram [141, 233]. The solubility of Cu in Cr and Cr in Cu is negligible [234]. The entire concentration range is dominated by a mixture of the FCC Cu phase and the BCC Cr phase.

- Cr-Zn: In Fig. 6.52 d) the Cr-Zn phase diagram is depicted [141, 235]. The following phases are present throughout the composition space: [236–238]

    - The BCC Cr phase does *de facto* not dissolve Zn (0.04 at.% Zn).

    - The $CrZn_{13}$ can be observed at concentrations of 92 at% $< x_{Zn} <$ 93 at%.

    - $CrZn_{17}$: The hexagonal phase occurs at concentrations of 91.2 at% $< x_{Zn} <$ 95.6 at%.

    - the hexagonal Zn phase is predominant in the range 99.98 at% $< x_{Zn} <$ 100 at% (Pearson symbol hP2).

In conclusion, the analysis of the binary Cr-X phase diagrams shows that, except for Al, no strong intermetallic systems are present. Therefore, the addition of Cr to the AlMgZn system is interesting, since the effects of a new binding partner for Al could disturb the dynamics of the alloying elements.

A ternary AlMgZn target served as the basis for the investigation of Cr in a complex metal system, containing the light elements Mg and Al, as well as the transition metal Zn. The composition of the samples using this target was: Al: ≈39 at%, Mg: ≈27 at%, Zn: ≈34 at%. The Cr content was varied from about 10 at% to the pure element. The analysis of the composition of the individual samples for this series is shown in Fig. 6.53 b), in addition to the surface structure at individual measurement points (Fig. 6.53 a)). The initial flake-like textures with round edges become increasingly finer and form the finest structures when the composition of the 4 elements is balanced. With a further increase of the Cr content, the structures become coarser again. Moreover, fissures and cracks appear in the layer. These grow together gradually at Cr concentrations above 50 at%, while the sharp-edged textures remain.

In Fig. 6.54, SEM images of the surface structure and the corresponding cross-sections are shown. These are equivalent to measurement positions 5 (a) and d)), pos. 15 (b) and e)) and pos. 20 (c and f)). Here, the transition from a dense layer to a porous, lamellar structure can be observed. These porous structures subsequently coalesce back into each other, resulting in a decrease of the number of crevices (Fig. 6.54 c)). The formation of sub-micrometer grains and porous structures in PVD produced Cr alloys has already been identified [239].

The simulated atomic distributions in Fig. 6.55 present the calculated behaviour of the system at different compositions. At relatively low Cr concentrations (panel a), two-phases

a)

b)

c)

d)
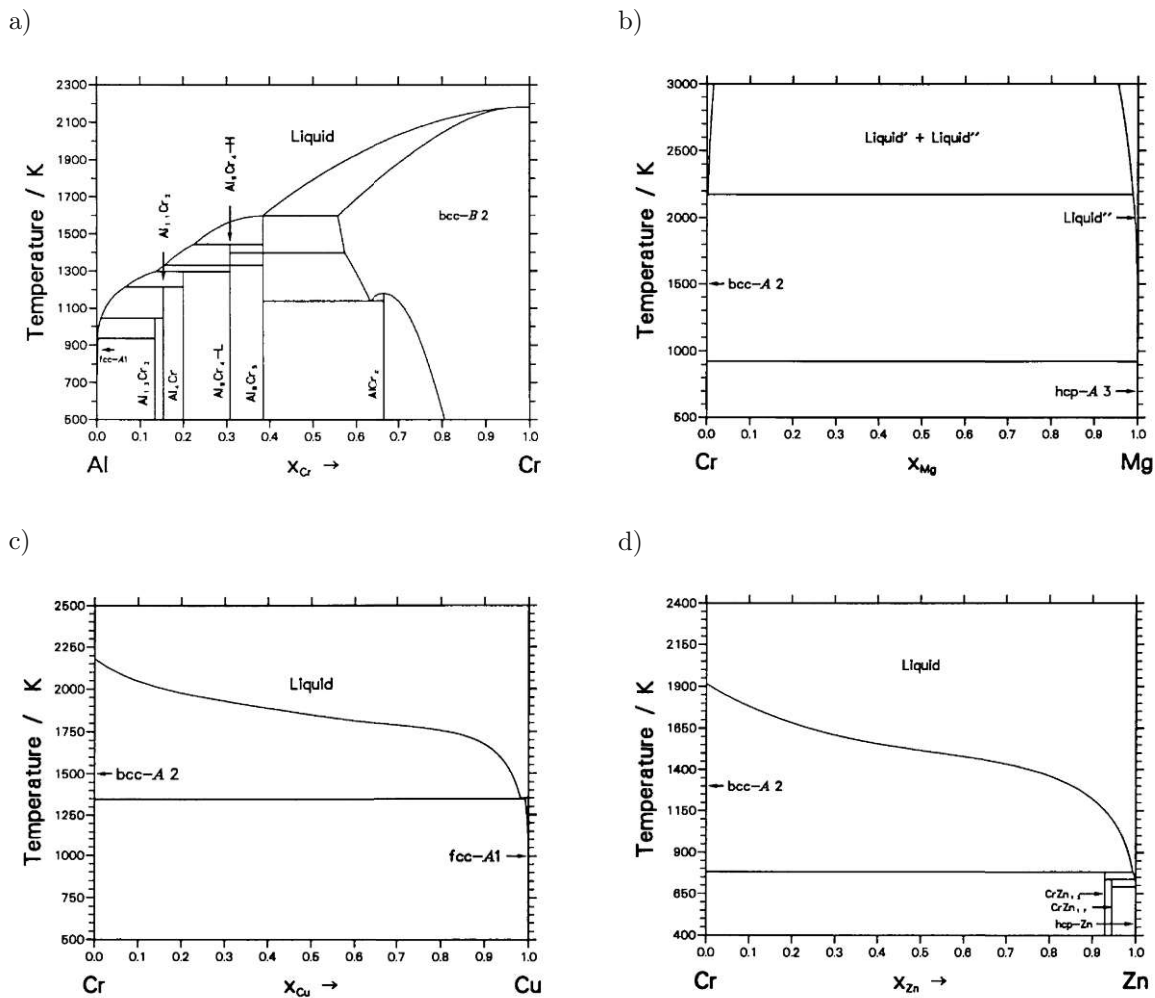
Figure 6.52.: Binary phase diagrams of the a) Al-Cr, b) Cr-Mg, c) Cr-Cu and d) Cr-Zn systems. [141]
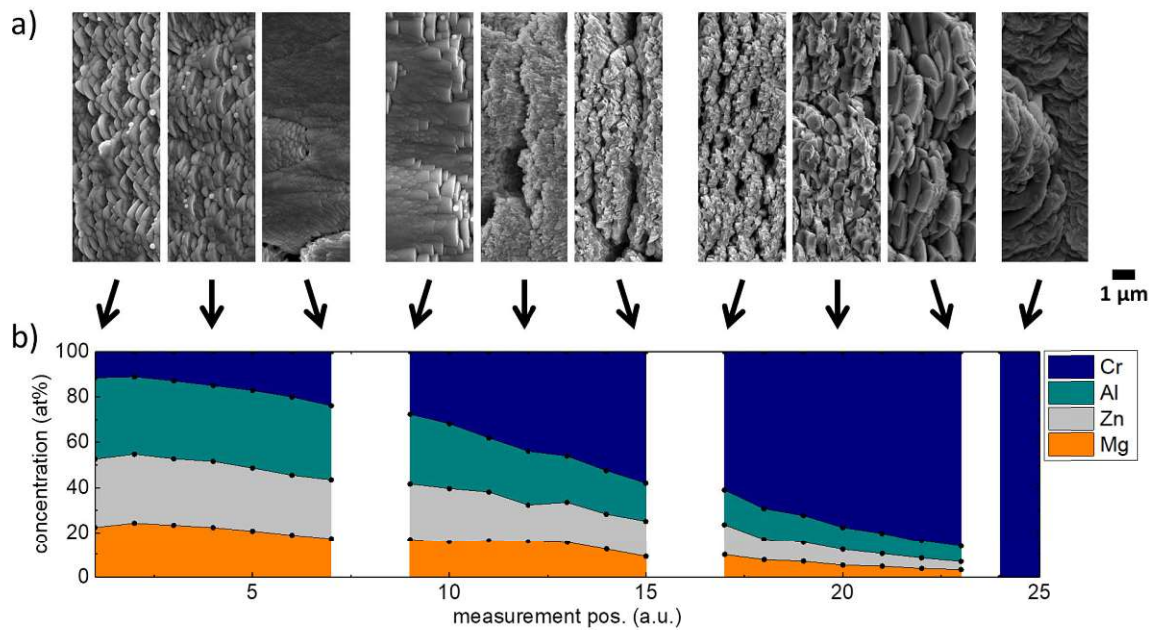
Figure 6.53.: a) The surface structure of the AlMgZn-Cr samples for different compositions. The surface texture exhibits significant variations depending on the relative composition, ranging from coarse, sharp-edged features to dense, smooth structures. b) The chemical composition of this series samples recorded by EDX.

are apparent, a MgZn and an AlCr region, where the latter is dominated by Al. When the Cr content is increased, this separation is initially maintained (Fig. 6.55 b)). However, due to the excess of Cr relative to Al, the dominance in the AlCr domains reverses, and the Cr content increases compared to Al. With an oversupply of Cr (approx. 60 at%), the areas occupied by MgZn decrease progressively, and those occupied by Cr (with Al inclusions) form a continuous matrix, which subsequently contains more pure Cr regions (Fig. 6.55 d)).

The phases found by XRD are shown in Fig. 6.56. At low Cr contents ($x_{Cr} < 20$ at%), two phases dominate: a cubic Cr_5Al_8 phase and the hexagonal $MgZn_2$ Laves phase, which represents the larger proportion. The first phase is based on the BCC Cu_5Zn_8 γ-brass [216,240]. In addition, a small fraction of the tetragonal $AlCr_2$ phase was identified. The two predominant phases were also identified earlier in the calculations based on entropy and enthalpy values. With the increase of the Cr content, the fraction of the $MgZn_2$ phase decreases significantly. In contrast, the proportion of the $AlCr_2$ phase grows continuously and reaches its maximum at a Cr concentration of about 50 at%. This also confirms the trend shown in Fig. 6.55 b) and c). At concentrations of more than 50 at% Cr, a pure BCC Cr phase was identified. This phase grows steadily up to a relative Cr concentration of approx. 80 at% and reaches its maximum at this concentration. Consequently, the previously existing phases decrease and disappear completely. In Fig. 6.56 a) an additional phase, the cubic $Cr_{0.78}Al_{0.22}$ is indicated. This phase exhibits the same prototype as the pure Cr phase; however, the peak positions are shifted which enables the identification of a "new" phase. This is an indication that the
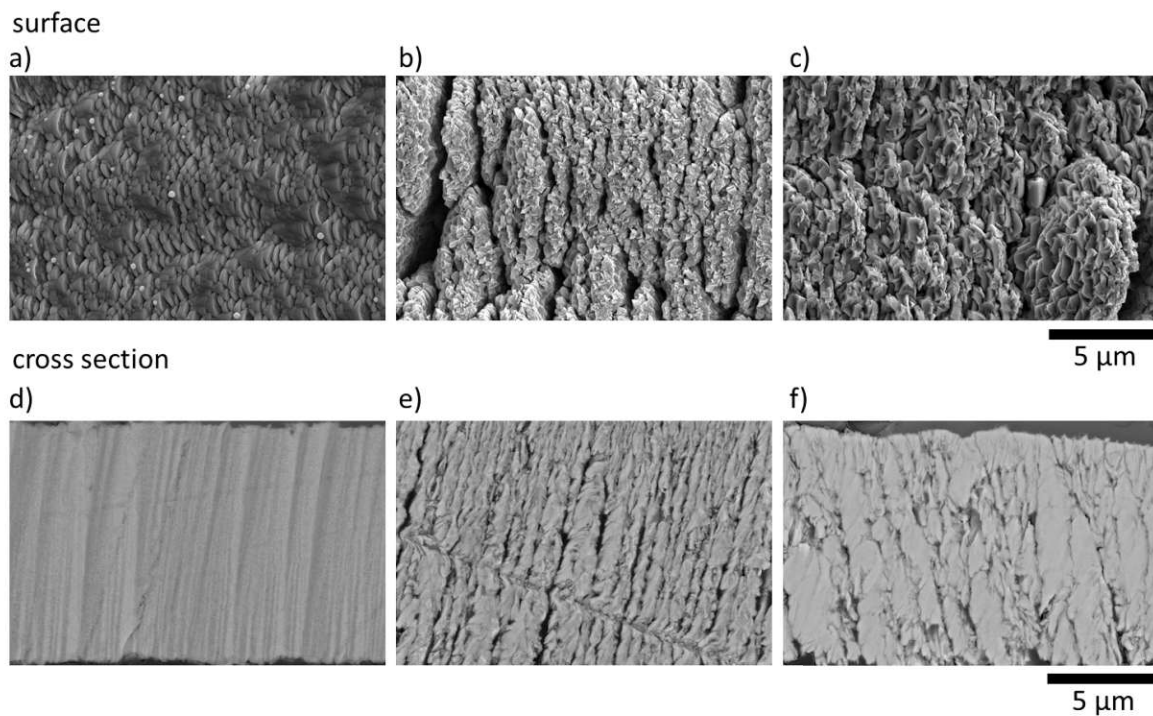
Figure 6.54.: Panels a) to c) show the surface structures of several compositions, while panels d) to f) display the corresponding images of the metallographic cross-sections.
a) & d): x_{Al}: 34 at%, x_{Mg}: 22 at%, x_{Zn}: 29 at%, x_{Cr}: 15 at%
b) & e): x_{Al}: 17 at%, x_{Mg}: 9 at%, x_{Zn}: 16 at%, x_{Cr}: 58 at%
c) & f): x_{Al}: 10 at%, x_{Mg}: 5 at%, x_{Zn}: 7 at%, x_{Cr}: 78 at%

various other alloying elements occupy the sites of the Cr lattice. A more detailed inspection of the relative proportions of the alloying elements, especially Al and Cr, demonstrated that at a critical concentration of $x_{Cr} > 50$ at%, the system follows the diagram of the binary AlCr. The phases described in the introduction of this section occur at the values reported in the literature, i.e., maximum of Al_8Cr_5 phase at ≈ 40 at% and $AlCr_2$ phase at ≈ 68 at%. Also, the appearance of the terminal solid solution at about 80 at% Cr agrees with the expected concentration from the AlCr phase diagram.

The measured mechanical property in the form of the indentation hardness shows a complex progression over the considered concentration range (Fig. 6.56 b)), which can be correlated with the identified phase fractions along with the structural variations. In the $MgZn_2$ and Cr_5Al_8 dominant range, a Vickers hardness of around 5 GPa was measured. In previously studied systems with a predominant $MgZn_2$ content, hardness values in the range of 3 GPa were found. A comparison of these values indicates that the AlCr phase leads to an increase in hardness.

The further evolution of the indentation hardness also confirms a significant influence of the Cr_5Al_8 phase, as it follows the trend of this phase fraction (up to a Cr concentration of about 40 at%). Looking at the surface structure in Fig. 6.53 a) and d), a refinement of the grain sizes
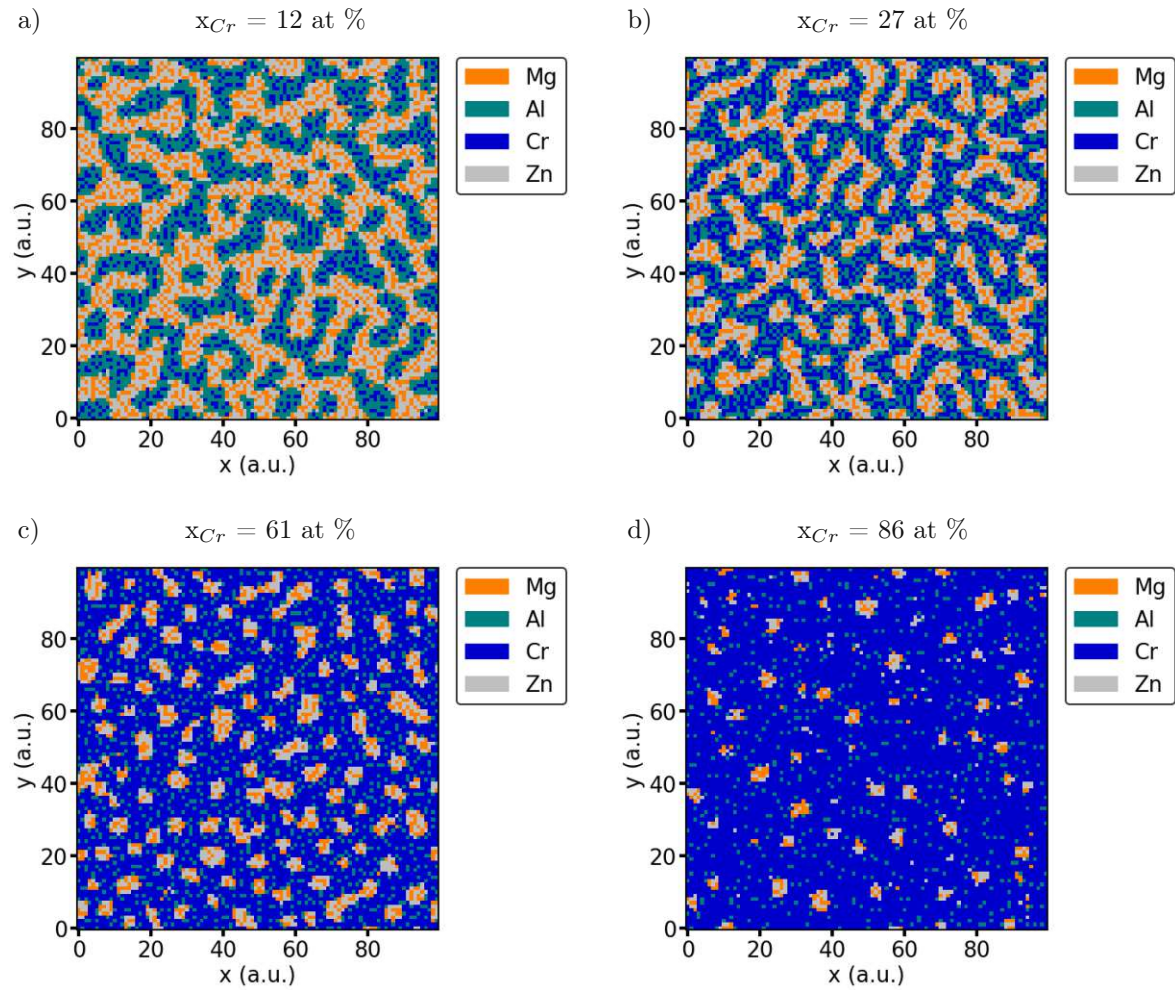
Figure 6.55.: Simulated distributions of different compositions of the AlMgZn-Cr system at varying relative Cr concentrations.

a) 350 °C   b) 350 °C
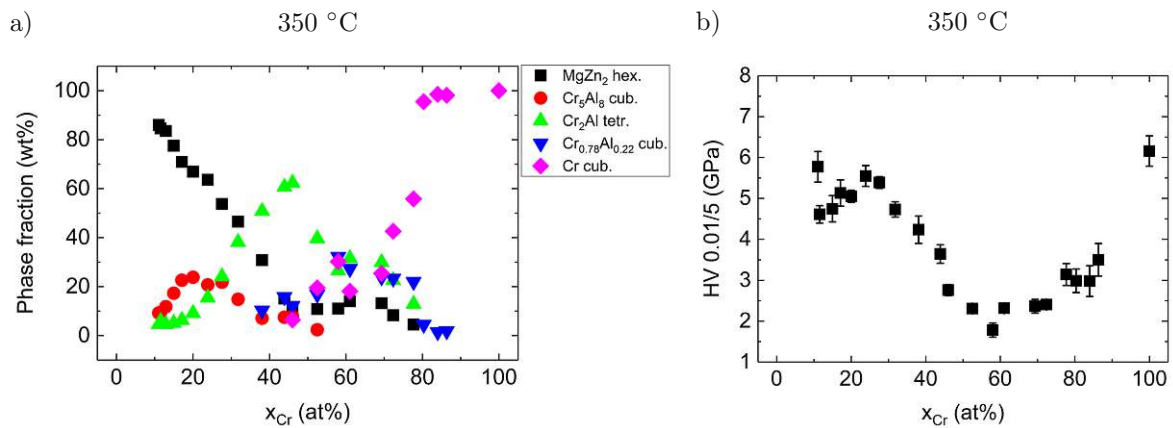
Figure 6.56.: a) Quantifications of the Rietveld fits and b) indentation hardness at various Cr concentrations after heat treatment at 350 °C for 24 h.

and dense structures can be observed, which corresponds to the comparatively hard material and is consistent with the increase in hardness associated with decreasing grain sizes reported in literature [241, 242]. In the range of approx. 60 at% Cr, a substantial drop in indentation hardness to approx. 2 GPa is evident, which occurs due to the establishment of the tetragonal Cr_2Al phase. The surface structure in this region (panels 2 and 3 in Fig. 6.53 a) and Fig. 6.53 b) and e)) reveals the formation of fissures and an overall more porous structure. In addition, the maximum degeneracy of the crystal systems can be found in this region. Four different crystal systems were identified, which occupied a proportion of at least 10 wt%. The terminal hardness increase occurs at a concentration of > 60 at% Cr upon advancement of the pure Cr phase. Although no significant changes were seen in the XRD measurements, there is an evident difference between the pure Cr sample (HV $\approx$ 6 GPa) and those including alloying atoms (HV $\approx$ 3.5 GPa). The structure of the deposits shows densification in this area, the previously pronounced fissures progressively grow together and partially disappear. The investigated samples were exposed to a second heat treatment to test the stability of the detected phases and the robustness of the results. This was carried out at the experimentally maximum accessible temperature of 430 °C for 24 h. The results showed that no significant differences in crystal structure or mechanical properties occurred due to the higher post-treatment temperature and longer annealing time. By comparing Fig. 6.57 a) with Fig. 6.56 a), one can see that higher temperature heat treatment did not change the identified phases, and only their quantity varied. At low Cr concentrations, the fraction of cubic Cr_5Al_8 is significantly higher, while in the regime of larger Cr concentrations, a substantial increase of the cubic $Cr_{0.78}Al_{0.22}$ compared to the 350 °C samples is evident. The indentation hardness measurements replicated the same trend for the longer annealed sample. These results show that at least a metastable state of the system was already reached after heating at 350 °C for 24 hours.
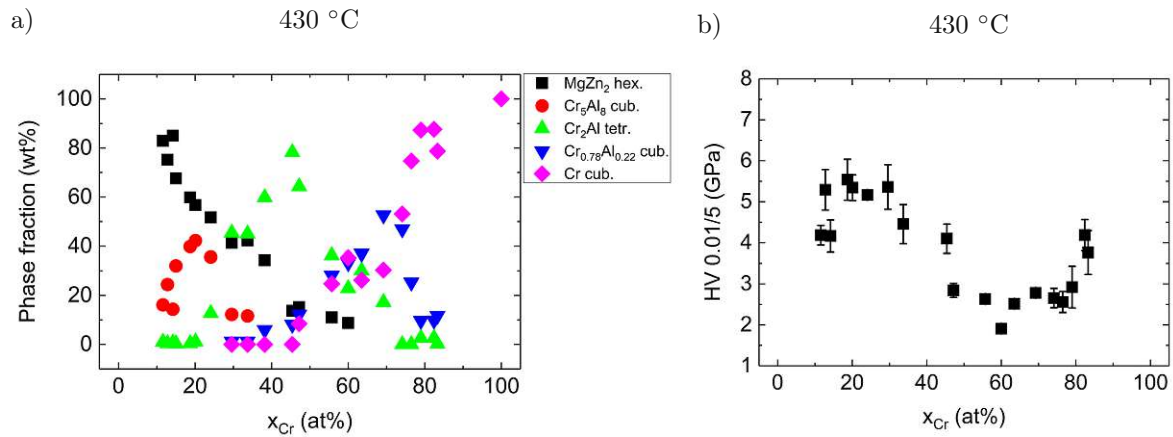
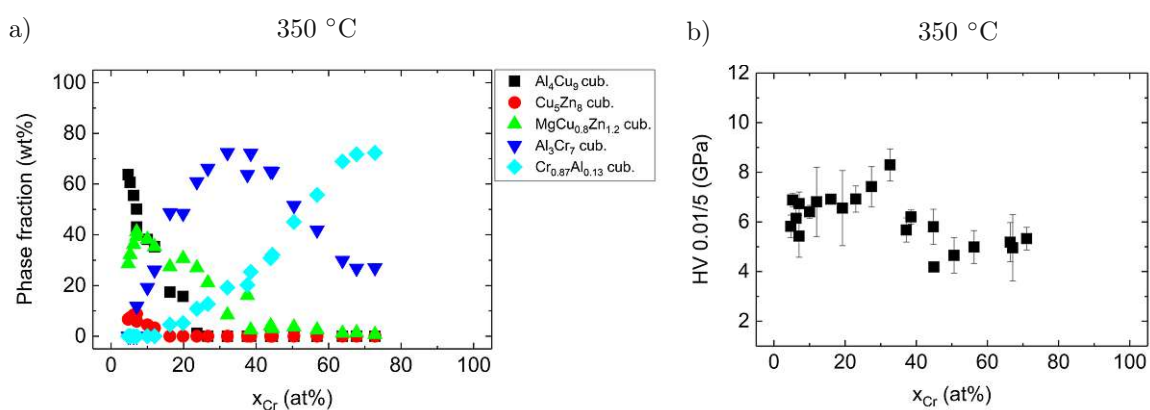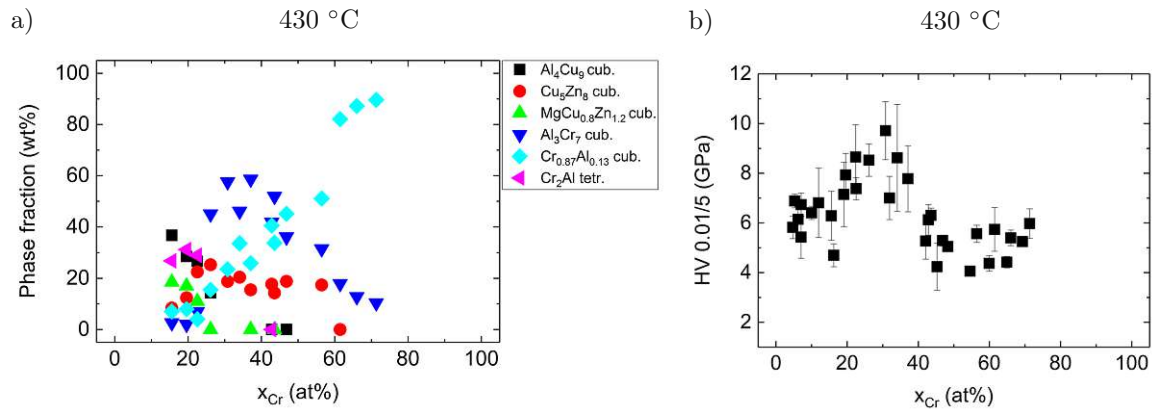Figure 6.57.: a) Quantifications of the Rietveld fits and b) indentation hardness at various Cr concentrations after heat treatment at 430 °C for another 24 h, leading to a total temper time of 48 h.

Summary:

Investigation of the AlMgZn-Cr alloy system was chosen to study the effects of bonding partners with strong binding preferences. As it was already shown in chapter 6.1.3, Mg and Zn preferentially form intermetallic phases along with each other and segregate from Al. Cr forms IM phases only with Al, which is evident from the binary phase diagrams (Fig. 6.52). Both the calculations and the experimental studies showed that the system follows the most plausible path of segregation, the formation of isolated MgZn and AlCr domains. Above a critical concentration of $x_{Cr} > 50$ at%, the system pursues the binary AlCr phase diagram, as it is evident from the XRD measurements. The crystallographic phases occur precisely at the relative Al/Cr ratios predicted in the classical phase diagram. From about 80 at% Cr content (i.e., 20 at% alloying elements), the terminal BCC Cr solid solution is formed. This is also predicted at a Cr content of 80 at% and 20 at% Al in the binary Al-Cr phase diagram (see Fig. 6.52 a)). The indentation hardness shows a minimum in the region of the greatest degeneracy of the crystallographic phases, at a Cr content of about 60 at%. This region is characterized by larger gaps in the surface structure and columnar layer growth. Since there are clear binding preferences and thus large differences in the enthalpies of formation, the approach of calculating atomic intermixing by considering the binary enthalpies of formation provided a good agreement with the experimental results for this system.

6.2.2. AlCuMgZn-Cr

The effect of the addition of Cu has already been shown for the previously studied and presented AlMgZn-Cu systems. In the following section, we investigate whether Cu can weaken the strong presence and dominance of the AlCr structures and thus vary the crystal order found in the earlier presented AlMgZn-Cr alloy system.

This was accomplished by using a quaternary AlCuMgZn and a pure Cr target. By using this

target combination, the compositions shown in Fig. 6.58 b) were prepared. Here, samples of the compositions from measuring point 8 to measuring point 17 should fulfill the criterion according to Senkov.

In Fig. 6.58 a) and Fig. 6.59, the surface textures and the cross-sections are shown for different Cr contents. There is a tendency for the size of surface features with increasing the Cr fraction. The fine surface features transition to rough, flake-like textures, while the finest distribution appears at a balanced ratio of the alloy components. The comparison with the cross-sections in Fig. 6.59 e) to h) confirms these observations. While in panels e), g) and h), laminar structures prevail, which coincide with the flake-like surface structures. In panels b) and f), fine grains and dense structures can be seen again in the cross-section images. Furthermore, a visible contrast difference indicates at least two separate phases.
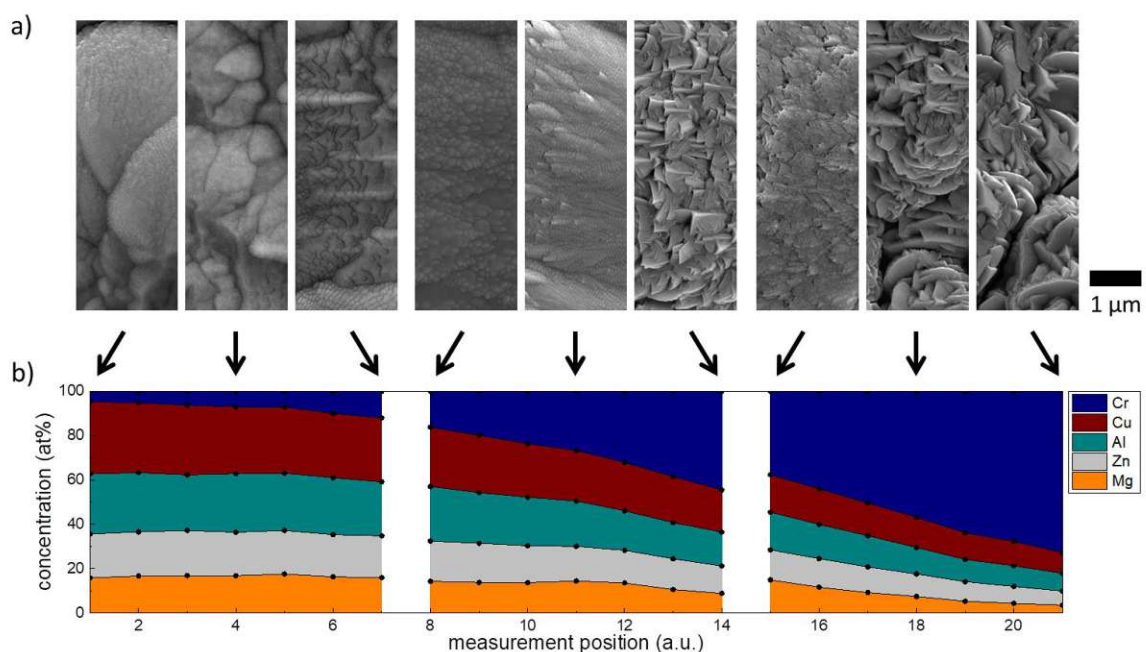
Figure 6.58.: a) The surface structure of the AlCuMgZn-Cr samples for different compositions. Structural changes in the surface texture depending on the relative composition can be observed. b) The chemical composition of the samples for this series recorded by EDX.

The simulations of the atomic distribution for different compositions are shown in Fig. 6.60. At low Cr concentrations (Fig. 6.60 a) and b)), AlCu and MgCuZn domains are predominant with Cu atoms occasionally implemented in the MgZn regions. Similarly, Cr atoms can be detected in the AlCu dominated areas, which suggests that AlCu and MgZnCu phases are distorted by the presence of Cr at low Cr contents. However, with further increase of Cr (Fig. 6.60 c) and d)), AlCr regions progressively separate at the expense of the AlCu areas, while the fraction of MgCuZn phase remains almost the same. At relatively high Cr fractions ($x_{Cr} > 57$ at%, Fig. 6.60 e) and f)), small isolated islands of MgCuZn atoms remain. Simultaneously, the Cr component becomes predominant, with isolated Al atoms
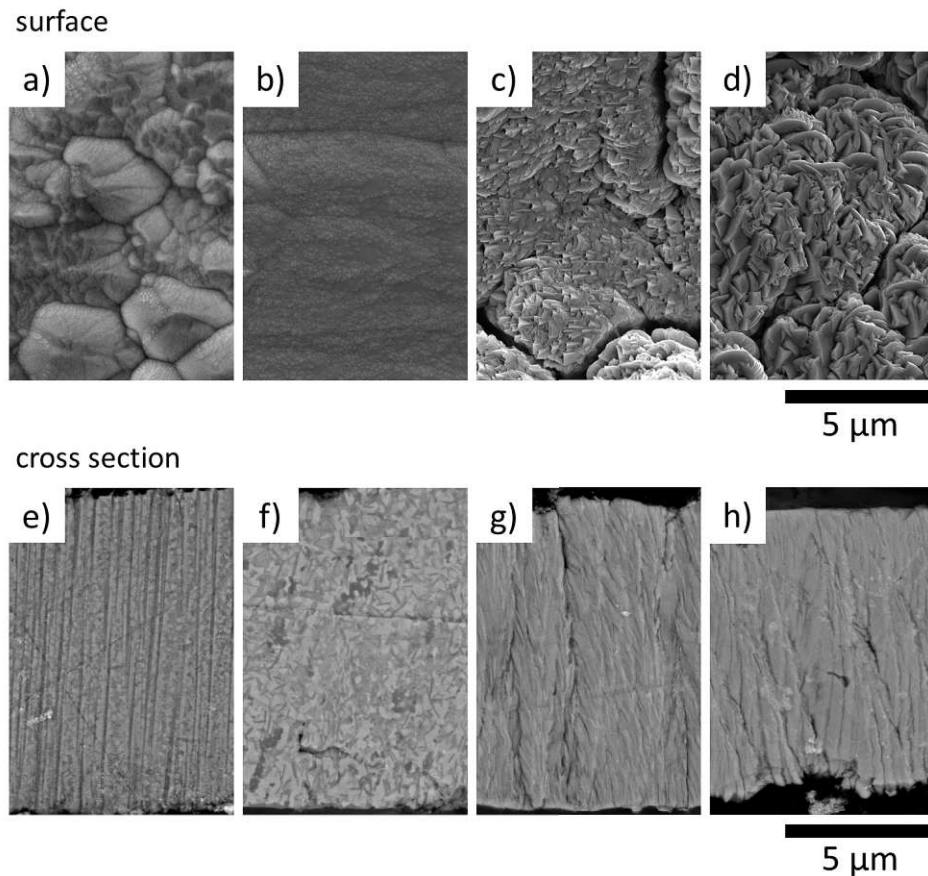
Figure 6.59.: Surface structure and metallographic cross-sections at a) and e) $x_{Cr} = 6$ at%, b) and f) $x_{Cr} = 16$ at%, c) and g) $x_{Cr} = 37$ at%, d) and h) $x_{Cr} = 69$ at%.

enclosed. In the entire concentration space under consideration, no pure single-phase region with significant proportions of the alloying elements could be found.

From the analysis of the XRD measurements after a thermal post-treatment at 350 °C, three distinct regions could be identified (Fig. 6.61):

- At Cr concentrations below 10 at%, the phases already detected in the quaternary systems could be identified: the Al_4Cu_9 cubic intermetallic phase, and the $MgCu_{0.8}Zn_{1.2}$ cubic phase. In addition, a small portion of the Cu_5Zn_8 cubic phase was detected. Also the formation of a cubic Al_3Cr_7 phase is visible. The identified crystallographic structures show a good agreement with the simulated elemental distributions.

- With the increase of the Cr content, the Al_4Cu_9 phase decreases rapidly and also the Cu_5Zn_8 phase disappears. The cubic $MgCu_{0.8}Zn_{1.2}$ structure shows a slight decline but still has a significant proportion. However, the system is dominated by the strongly increasing Al_3Cr_7 phase showing a maximum at a Cr fraction of about 30 at% - 40 at%. By comparing these results to the simulations, we find that the trends perfectly match the simulated distribution patterns.

a) $x_{Cr} = 4$ at%   b) $x_{Cr} = 12$ at%   c) $x_{Cr} = 27$ at%

d) $x_{Cr} = 45$ at%   e) $x_{Cr} = 57$ at%   f) $x_{Cr} = 73$ at%
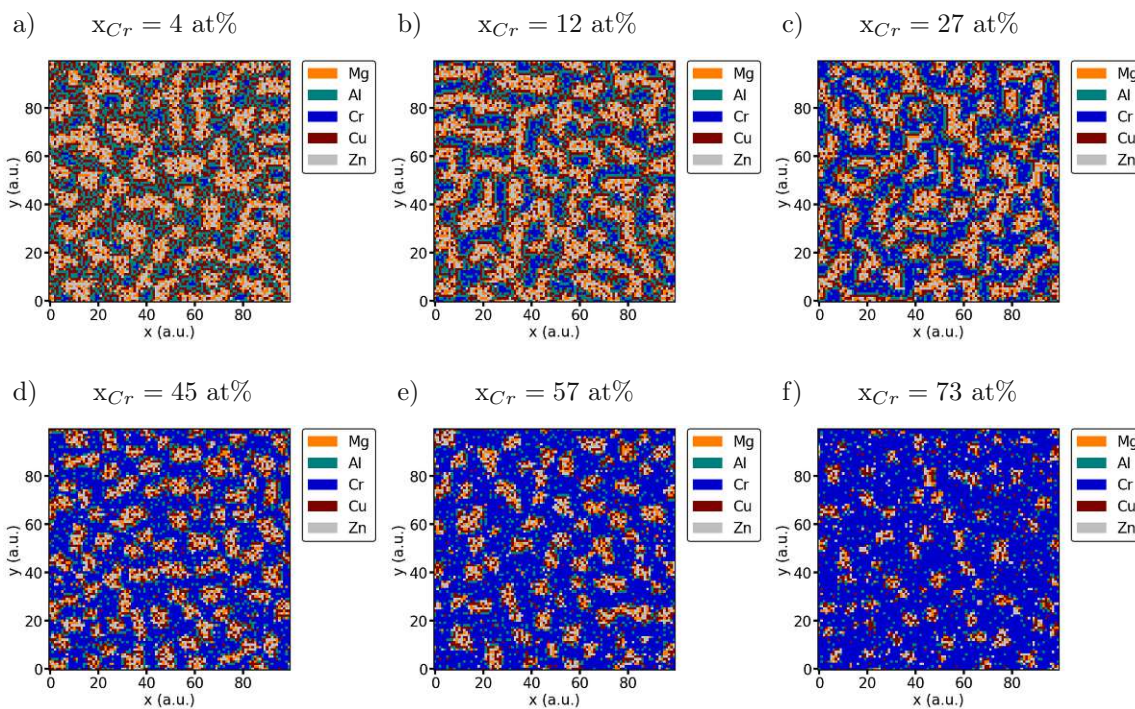
Figure 6.60.: Simulated atomic distributions with variable Cr content. Panels a) - c) show the increase of AlCr regions under depletion of Cu. In panels d) - f) these AlCr regions grow continuously at concentrations of $x_{Cr} > 45$ at%.

a)   350 °C   b)   350 °C

Figure 6.61.: a) Quantifications of the Rietveld fits and b) indentation hardness at various Cr concentrations after heat treatment at 350 °C for 24 h.

127

a) 430 °C b) 430 °C

Figure 6.62.: a) Quantifications of the Rietveld fits and b) indentation hardness at various Cr concentrations after heat treatment at 430 °C for another 24 h (resulting total temper time 48 hours).

- Above a Cr concentration of about 50 at.%, a cubic Cr phase dominates. This lattice prototype shows shifts of the measured reflexes indicating distortions caused by the presence of impurity atoms. The lattice spacing varies from 2.92 Å to 2.89 Å for the pure Cr lattice. The intensity of the cubic Cr phase increases continuously while the previously dominant Al_3Cr_7 phase simultaneously decreases.

The measurements of the indentation hardness are shown in Fig. 6.61 b) and demonstrate a moderate increasing tendency up to Cr fractions of about 30 at% with a maximum hardness value of about 8.5 GPa. The region of these elevated hardness values corresponds to the dense textures detected in the metallographic cross-sections (Fig. 6.59 b) and f)). Thereafter, the material shows softening to a value between 4 and 5 GPa in the range of 30 at% to 40 at% Cr content. The hardness stagnates at this level for the remaining concentrations. This drop in hardness is accompanied by the appearance of columnar textures and the formation of fissures, as visible in Fig. 6.59.

Since the thermal post-treatment temperature of 350 °C was far below the average melting point of the system, the samples were again post-treated a second time at a temperature of approximately 430 °C for 24 h. The quantification of the XRD measurements is shown in Fig. 6.62. The main phases (Al_3Cr_7 and Cr) showed a comparable trend, and only the cub. Cu_5Zn_8 phase gained in intensity. This crystallographic prototype is characterized by a large crystal lattice, which results in numerous reflections in the XRD response. Due to the longer annealing time and the higher final temperatures, additional peaks were detected (assigned to the tetragonal $AlCr_2$ phase). The hardness values show the same qualitative behavior as before (Fig. 6.62 b)). The variation in hardness seems to be slightly more pronounced, and the maximum of hardness reaches around 10 GPa. The decrease of the indentation hardness and the dwell at the low Cr level is comparable to the samples post-treated at 350 °C.

Summary:

Following the investigation of the AlMgZn-Cr system, Cu was added to this system, and the effects on crystallographic, structural, and mechanical properties were studied. The surface structure showed fine grains at low Cr contents, which is consistent with the use of Cr as a grain refiner and recrystallization inhibitor in Al alloys [220]. The analysis of the crystal structures by XRD showed that the addition of Cu, which forms intermetallic phases with Al, Mg, and Zn at low Cr concentration, determines the phase formation. Three phases were identified: The AlCu, the MgCuZn, and the CuZn phase. However, these were rapidly replaced by AlCr phases. This finding can be explained by the fact that no preferred crystal systems prevail due to the presence of Cu, which is reflected in the degeneracy of the crystal systems. As a result, a strongly bound system, in this case, AlCr, can dominate and split the other phases. The calculations of the atomic distribution showed a good agreement with the experimental findings at low Cr fractions. However, for Cr fractions of $x_{Cr} > 35$ at%, the calculations suggested a persistent phase separation of AlCr and MgCuZn. This finding was not confirmed to the full extent experimentally. The indentation hardness showed similarities with the trend of the AlMgZn-Cr system, but the fluctuations of the indentation hardness values were lower. Once more, a decrease in indentation hardness could be observed at a relative Cr concentration of ≈ 40 at%.

6.2.3. AlCuMgZn-Ti

Alloys containing titanium (Ti) are widely used in aerospace applications due to their greater absolute and relative strength compared to other elements such as Al and their lower density than steel. In addition, Ti alloys are characterized by their excellent oxidation and corrosion resistance. [174, p. 178 - p. 179] These aspects led Boeing to be one of the first companies to use Ti alloys for civil purposes, and it gradually replaced other metals in several applications [243, 244]. Moreover, Ti-based alloys are increasingly finding their way into the medical field due to their low elastic modulus and high biocompatibility [174, p. 200] [245]. The development of the Kroll process for obtaining technically pure Ti is regarded as the starting trigger for the extended use of Ti as a metal in other structural applications [174, p. 191]. Due to the high costs of this process, optimization of the expenses while maintaining high performance is the most important aspect in the development of Ti alloys [174, p. 280].

The binary phase diagrams of Ti with the other elements, also present in the studied quinary alloy system, are shown in Fig. 6.63. Ti exists in two distinct phases, α- and β-Ti. The allotropic transformation of the HCP α-Ti phase to the BCC β-Ti phase occurs at about 882 °C. The α phase shows higher mechanical strength but is less ductile due to the lower slip planes. Since the presence of the α phase is desired in many technological applications, phase stabilizers are often added to Ti. Along with oxygen, Al is one of the few α stabilizers used [246].

The binary phase diagrams of Ti-X show both a variety of intermetallic compounds and one immiscible system (Mg-Ti):

- Al-Ti: The Al-Ti phase diagram is dominated by a range of intermetallic phases. The majority of these are based on a tetragonal lattice ($TiAl_3$, Ti_5Al_{11}, $TiAl_2$, Ti_3Al_5, $TiAl$) but also a hexagonal Ti_3Al at approx. 20 at% - 39 at% of Al appears. [247, 248]

- Mg-Ti: The solubility of Ti in Mg and of Mg in Ti is infinitesimal, and no intermetallic phases exist throughout the compositional space [249].

- Cu-Ti: The Cu-Ti binary system is dominated by several intermetallic compounds (see Fig. 6.63). The maximum solubilities of Cu in α-Ti and β-Ti are 1.6 at% and 13.5 at%, respectively. Inversely, the Ti solubility in Cu is 8 at%. Intermetallic phases include Ti_2Cu (bct structure, $MoSi_2$ prototype) [250–252], the equiatomic TiCu phase (B11 structure) in the range of 48 to 52 at% Cu, the tetragonal Ti_3Cu_4,Ti_2Cu_3 and Ti_2Cu, and the orthorhombic $TiCu_4$ phase. [253]

- Ti-Zn: The intermetallic phases present in TiZn include the cubic TiZn and $TiZn_3$, the tetragonal Ti_2Zn, the hexagonal $TiZn_2$ (Laves) phase, or the orthorhombic $TiZn_{16}$ phase. The solubility of Zn in Ti and α-Ti in Zn is negligible. The solubility of Zn in β-Ti is 30 at% at about 1000 °C. [254, 255]

The composition of the prepared samples is given in Fig. 6.64 b). A second quinary system was investigated by adding the pure component Ti to the quaternary AlCuMgZn compound. The Ti content was varied from about 5 at% to over 50 at%.

The simulations of the atomic distributions at different Ti fractions are shown in Fig. 6.65. At low Ti fractions (x_{Ti} = 5 at%), the already identified domains, AlCu and MgZn regions with few Cu inclusions form (Fig. 6.65 a). This finding suggests that AlCu and MgZn phases may predominate at low Ti contents. As the Ti fraction is increased, Ti gets included in the AlCu regions, which can be seen in Fig. 6.65 b) and c). At a Ti fraction of > 50 at% (Fig. 6.65 d)), the vast majority is occupied by AlCuTi, while Mg and Zn occupy random positions. The distribution indicates a preferred AlCuTi crystal structure.

The analysis of the crystal structure by XRD is shown in Fig. 6.66. At small Ti fractions, the system is dominated by a cubic Al_4Cu_9 and a cubic MgCuZn structure. A comparison of the atomic distribution from the simulation results (Fig. 6.65 a)) is consistent with the presence of these two phases. In addition, XRD revealed a presence of a small fraction ($\approx$ 10 wt%) of a cubic $Ti(Al_{2.5}Cu_{0.5})$ intermetallic phase.

At higher Ti contents (x_{Ti} > 5 at%), the latter phase, $Ti(Al_{2.5}Cu_{0.5})$, increases at the expense of the Al_4Cu_9 phase. Moreover, starting from a concentration of x_{Ti} = 14 at%, a further structure is established in the form of the cubic $AlCu_2Ti$ phase. In this case, the atoms occupy the sites of a BCC lattice. This phase remains stable up to a high Ti concentration and coexists with the pure hexagonal Ti phase, which constitutes a significant proportion at a sample composition of x_{Mg} = 11 at%, x_{Al} = 14 at%, x_{Cu} = 14 at%, x_{Zn} = 11 at%, and x_{Ti} = 50 at%. The simulated results in Fig. 6.65 c) and d) reflect the AlCuTi preference, which was confirmed by the experimentally observed formation of the $AlCu_2Ti$ phase. The

a)

b)

c)

d)
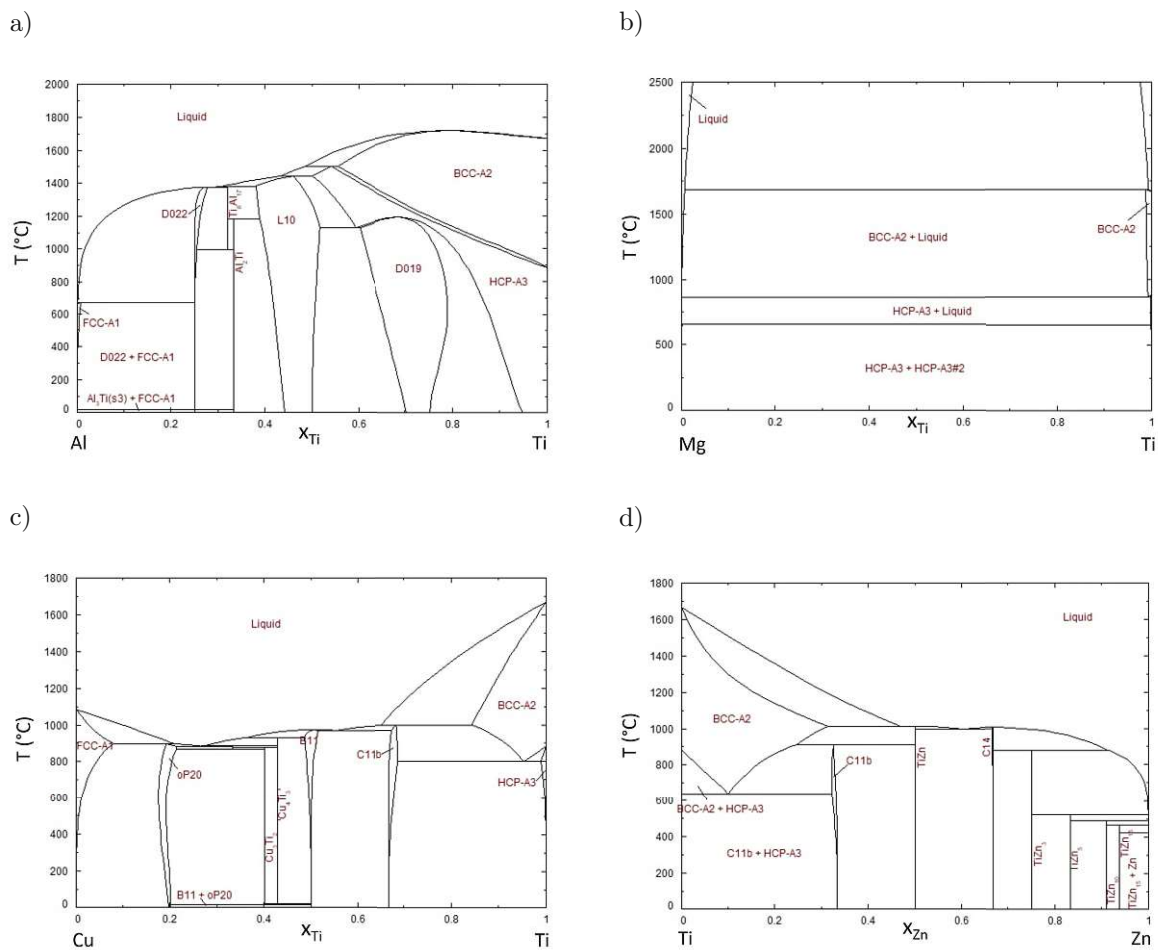
Figure 6.63.: Binary phase diagrams of the a) Al-Ti [256], b) Mg-Ti [257], c) Cu-Ti [258] and d) Ti-Zn [259] systems.
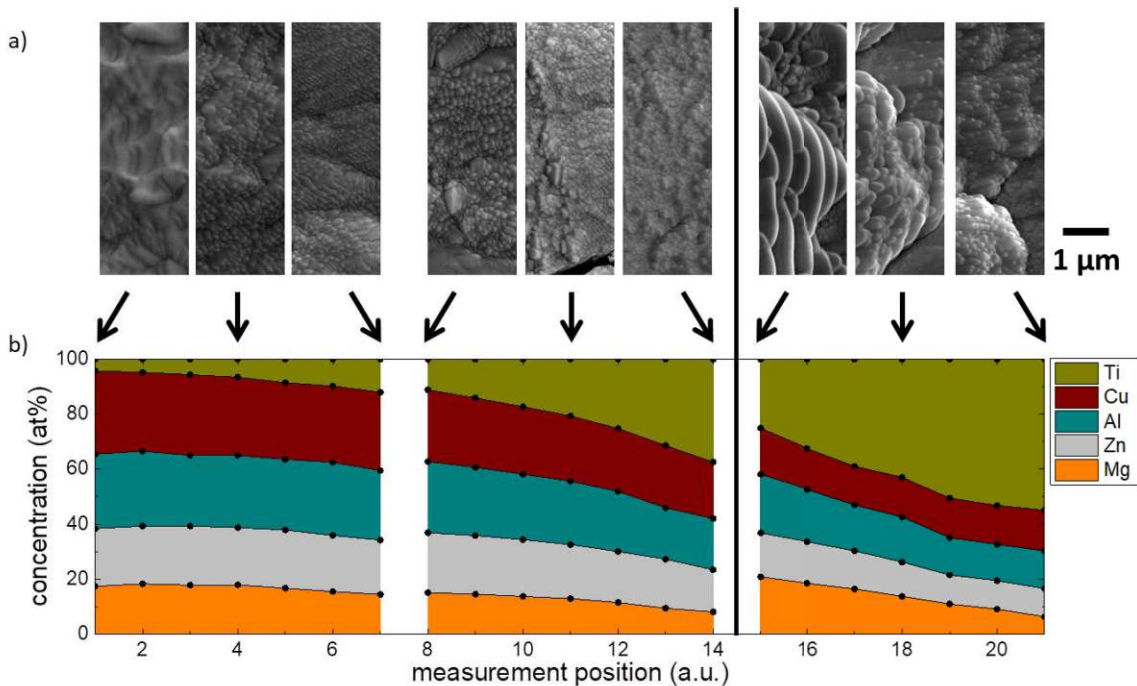
Figure 6.64.: a) The surface structure at selected measurement points. b) The chemical composition of the quinary alloy system with varied Ti content.

comparison between measurement positions with the same amount of Ti but a varying relative composition of the other alloying elements indicates how robust the identified crystallographic phases are. Especially the difference in the relative Cu and Mg content (compare Fig. 6.64 b)) exposed significant effects on the quantitative results. In samples with lower Cu content (indicated as "high Ti" in Fig. 6.66 and Fig. 6.68), the $Al_{2.5}Cu_{0.5}$ phase dominated while the $AlCu_2Ti$ phase declined. However, the qualitative results didn't change within the observed compositional range.

Similar to the quinary samples with Cr, the annealing temperature was increased by about 75 °C, and the already annealed samples were post-treated for an additional 24 h. Examination of the raw data revealed no further changes in the crystal structure in this case either, which confirms the robustness and stability of the phases found in this temperature range. Fig. 6.67 shows representative XRD data of two different compositions after thermal post-treatment at 350 °C and 425 °C.

In Fig. 6.68, the measured indentation hardness is shown as a function of the Ti concentration. In panel a), the rise in hardness of around 40 %, from approximately 4.8 GPa to 6.5 GPa, is evident for a relative increase of the Ti amount of about 30 at%. This finding is in accordance with the formation of the cubic $AlCu_2Ti$ phase (see Fig. 6.66 a). The indentation hardness of the samples with slightly different compositions of the alloying elements shows only minor changes in hardness up to a Ti content of about 50 at% (see panel b)). At Ti concentrations > 50 at%, a significant increment in hardness, up to 7 GPa occurs. A further comparison with the crystallographic phases found in Fig. 6.66 b) suggests that this is driven by the formation

a) $x_{Ti} = 5$ at %   b) $x_{Ti} = 20$ at %

c) $x_{Ti} = 40$ at %   d) $x_{Ti} = 55$ at %
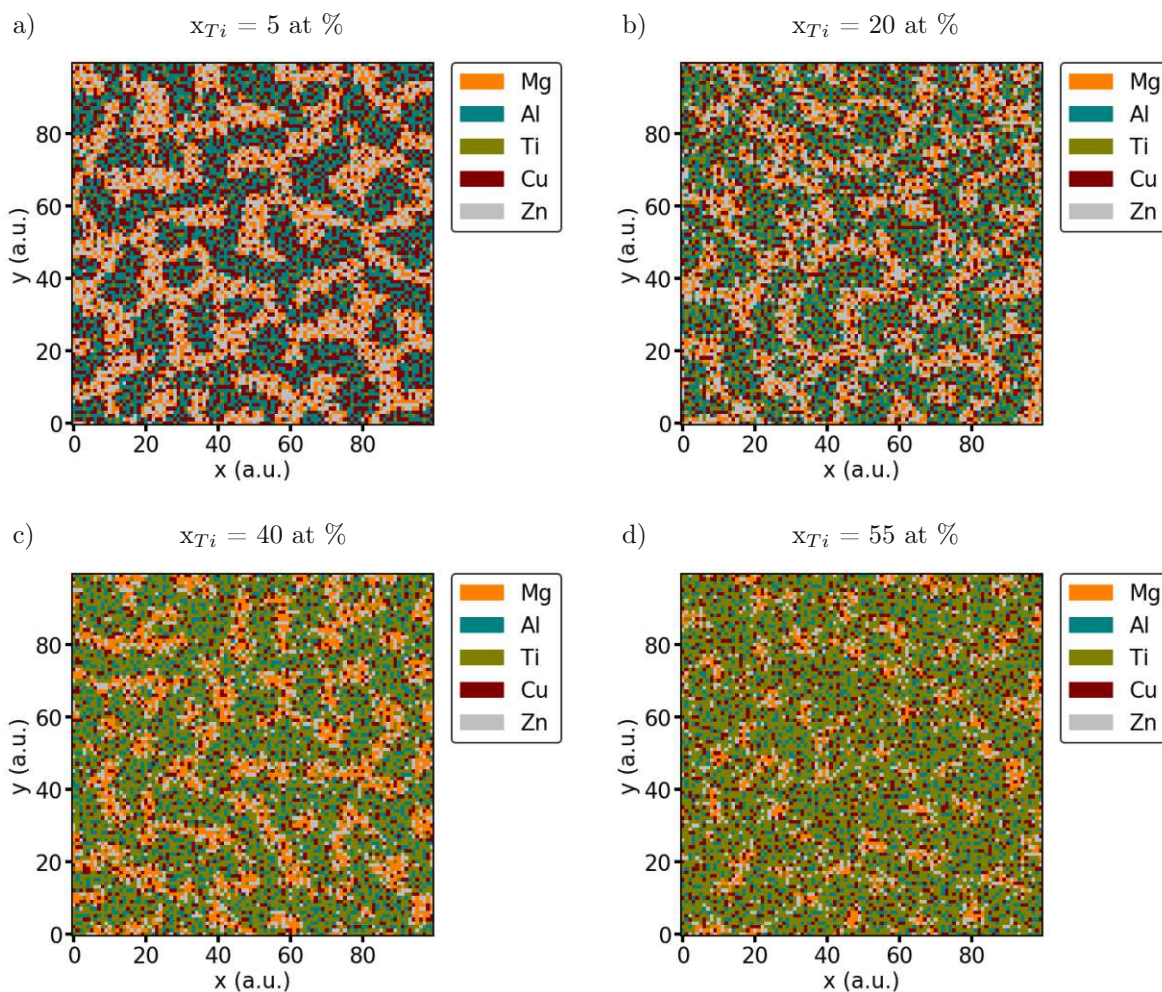
Figure 6.65.: Simulated distribution of different compositions of the AlCuMgZn-Ti system at varying relative Ti concentrations.
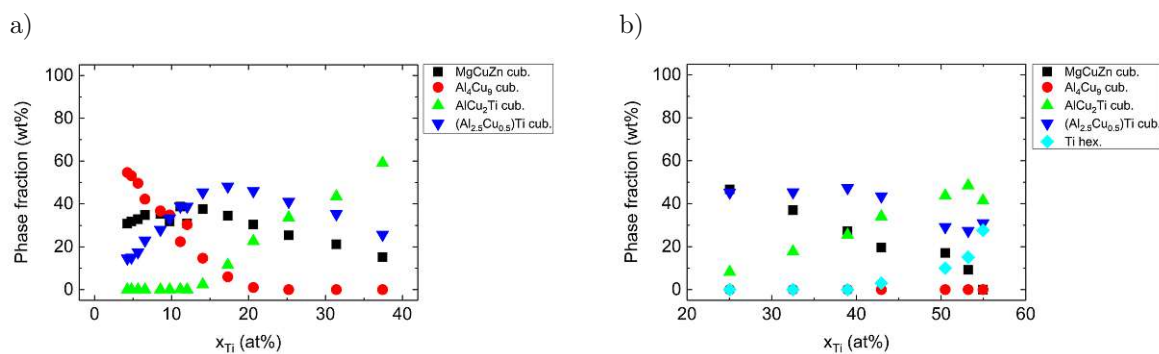
Figure 6.66.: XRD phase quantification for samples with a a) low Ti (left part of Fig. 6.64) and b) a high Ti content (right part) after heat treatment at 350 °C for 24 h.
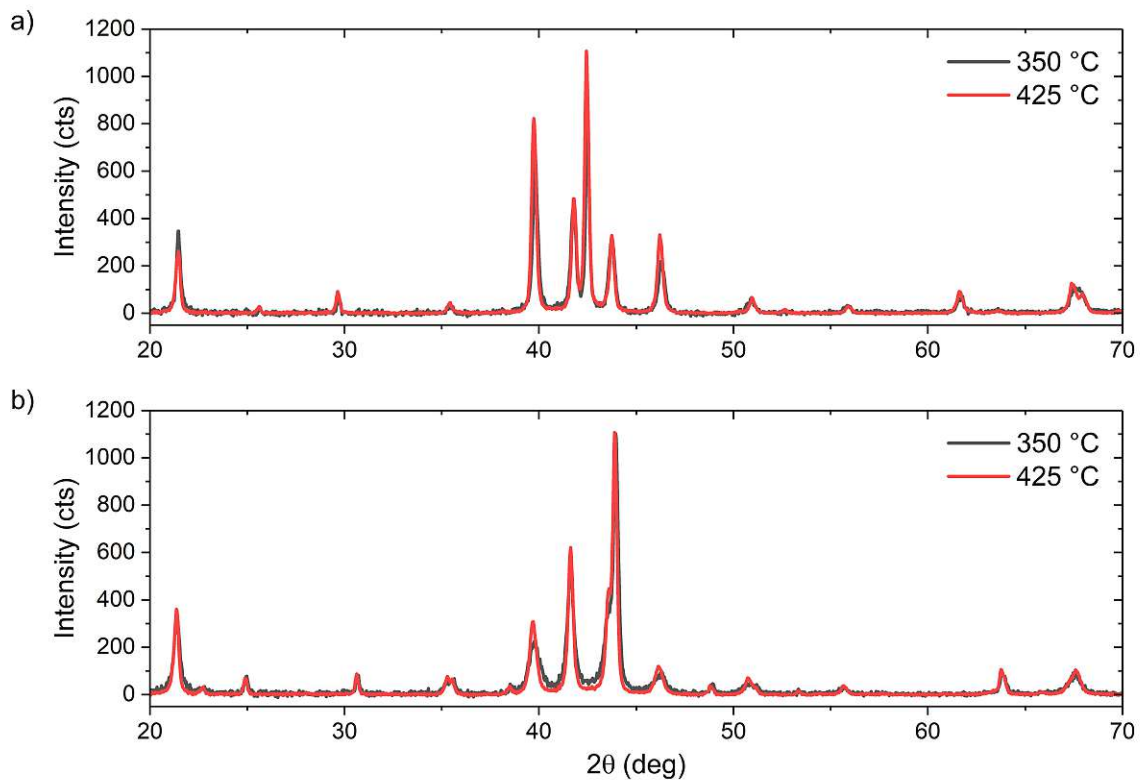
Figure 6.67.: XRD measurements of two compositions post treated at different temperatures. a) x_{Mg} = 13 at%, x_{Al} = 23 at%, x_{Ti} = 21 at%, x_{Cu} = 24 at%, x_{Zn} = 19 at%, and b) x_{Mg} = 18 at%, x_{Al} = 26 at%, x_{Ti} = 7 at%, x_{Cu} = 28 at%, x_{Zn} = 21 at%. No changes could be observed due to the different treatment.

of the HCP Ti phase (α phase). The significant increase of the indentation hardness of an alloy with the addition of Ti has been observed already in other studies [260].

Summary:

The studies of the combination of a quaternary AlCuMgZn alloy with pure Ti demonstrated stabilization of α-Ti at relatively low Ti concentrations compared to the binary phase diagrams. This phase was identified at relative Ti concentrations above 50 at%. Accompanying the establishment of this crystal phase, a significant increase in the hardness of the 5-component alloy was identified. Thermal post-treatments at 350 °C and 420 °C confirmed the stability of the crystal phases found in this temperature range. The comparison of the simulation results with the experimentally obtained data showed good agreement, which demonstrates the validity of the simple calculation principle in this alloy system. In both methods, the concentration-dependent transition from AlCu/CuMgZn to AlCuTi/CuMgZn domains was evident with the formation of the cubic CuMgZn and cubic $AlCu_2Ti$ phases. However, the presence of the pure HCP Ti phase at high Ti concentrations could not be clearly shown in the simulations.

a)

b)
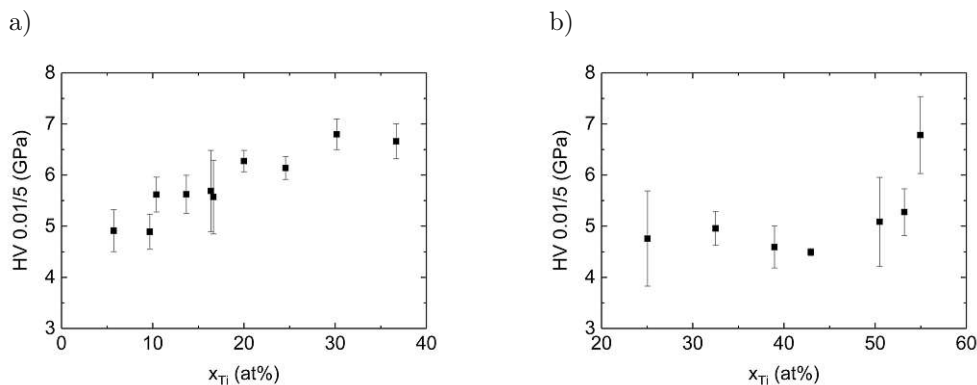
Figure 6.68.: Indentation hardness measurements for samples with a) low Ti (left part of Fig. 6.64) and b) a high Ti content (right part of Fig. 6.64).

6.3. Influence of Semiconductors

Besides light metals and transition metals, semiconductors are among the most essential materials used for industrial applications. The computer chip industry alone, which predominantly uses silicium (Si), has a turnover in the order of hundreds of billions of USD [261]. In addition, Si is finding its way into structural materials which have to sustain high mechanical stress. AlSi alloys are used, for instance, in the development of low weight components in the automotive industry [262].

Due to their unique electronic band structure and conductive behavior, semiconductors notably differ from elements of other groups. Consequently, it is compelling to investigate the effects of semiconductor elements on MPEAs. Si was chosen as the semiconductor element in the present studies.

The effects of the fourth element on a ternary system, consisting of Si, Al and a small amount of Zn, were investigated in the subsequent experiments. In the following, the binary phase diagrams of all possible combinations of the ternary starting target are briefly discussed:

Al-Si: The phase diagram of the binary Al-Si system was previously shown in Fig. 4.8 a). In this eutectic system, two solid solution regions, the FCC Al phase, and the cubic diamond A4 Si phase are present. The solubility range of Si in Al and of Al in Si is low, only 1.5 at% (at 577 °C) and 0.016 at% (at 1190 °C), respectively. AlSi alloys are among the most important commercial alloys, especially with the addition of Cu and Mg to promote age hardening. [263]

Si-Zn: In Fig. 6.69, the eutectic Si-Zn phase diagram is presented. The eutectic transformation occurs at a temperature of 419.58 °C and a relative Si content of 99.955 at%. Si and Zn have negligible mutual solubility. [141, 264]

6.3.1. AlZnSi-Cu

Fig. 6.70 represents the binary CuSi phase diagram. From the analysis of the previously presented phase diagrams, it is evident that both Al and Zn do not form intermetallic phases with Si. These are only formed in combination with and at high concentrations of Cu. The
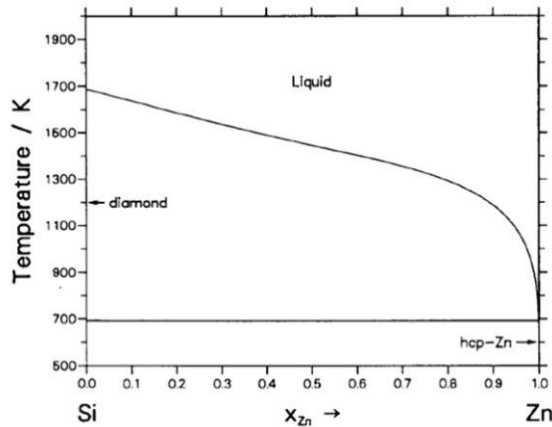
Figure 6.69.: Binary phase diagram of the Si and Zn system [141].

a)

b)
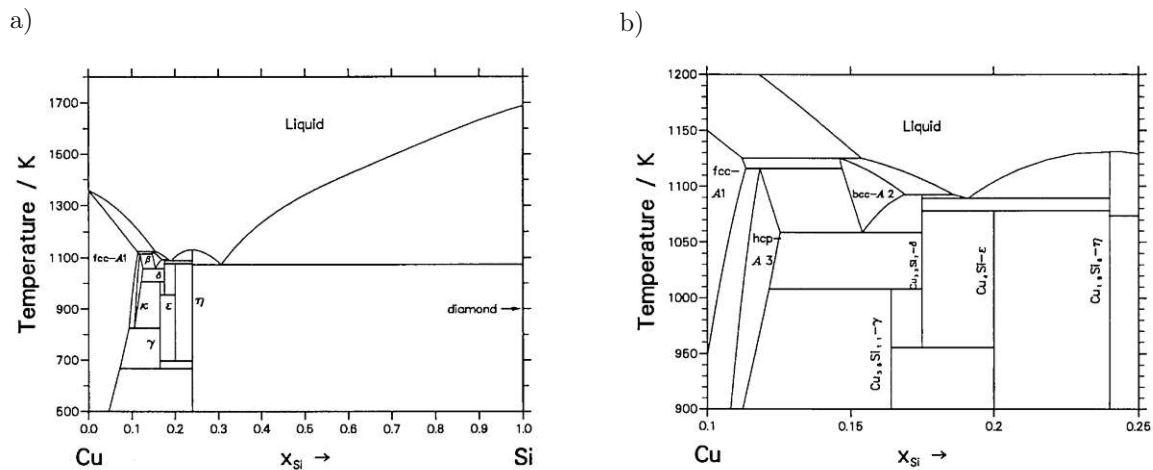
Figure 6.70.: Binary phase diagrams of a) the entire composition range of Cu-Si and b) a detailed depiction of the low Si concentration regime [141].

Cu-Si phase diagram indicates a number of stable structures:

- The terminal Si solid solution with virtually no solubility of Cu. Si exhibits the diamond structure A4 [265].

- The terminal FCC-Cu solid solution. The maximum solubility of Si is 11.25 at% Si at the peritectoid temperature of 842 °C [265, 266].

In the range of 15 at% - 30 at% Si concentration, the following stable intermediate phases exist:

- The high-temperature rhombohedral η phase melts congruently at 859 °C. At lower temperatures, the stable rhobohedral η' and orthorhombic η'' phases form at temperatures of 467 °C - 620 °C and below 570 °C, respectively. [265, 266] These phases have a stoichiometric composition of $Cu_{19}Si_6$ [141, 265].

- In the temperature range of 710 °C - 824 °C, the tetragonal δ phase is stable with a stoichiometric composition of $Cu_{33}Si_7$ [141, 265, 266].

- The cubic ε phase is formed by the peritectic reaction of the δ and η phases at 800 °C [265, 266] and shows a stoichiometric composition of Cu_4Si [141].

- The BCC β phase, which is stable between 785 °C and 852 °C [266].

- The CPH κ phase forms in a temperature range of 785 °C to 852 °C in a Cu range from 85.5 at% to 89 at% [266].

- The cubic γ phase with a stoichiometric composition of $Cu_{56}Si_{11}$ [141, 265] is formed by the peritectic reaction of the δ and κ phase. The γ phase is stable below 729 °C [266].

The chemical composition of the prepared samples is shown in Figure 6.71 b). By using a ternary AlZnSi target, containing mainly Al and Si and a minor amount of Zn, and a pure Cu target, the relative Cu content could be varied. Due to inhomogeneities in the target's composition, the fractions of the ternary elements varied slightly. On average, the atomic ratio of the components Al:Zn:Si was found to be 7.4:1:4.7. The Cu content was altered in a range from $\approx$ 95 at% to $\approx$ 19 at% within this series. Images of the sample surfaces revealed the effects of the different compositions on the surface structure (Fig. 6.71 a)). Dark precipitates formed in the predominantly Al-Si dominated region, which gradually disappeared with the addition of Cu. In these areas, EDX mapping indicated the formation of Si-rich domains. These are shown in detail in Fig. 6.72 a) and b). The surface structure is characterised by a dense microstructure, which exhibits trenches and fissures with increasing Cu content. At a relative Cu content of about 55 at%, the surface structure becomes denser and smoother again. At high Cu concentrations ($x_{Cu} > 80$ at.%), sharp-edged surface features typical for Cu layers form. These become increasingly well-defined and pronounced up to the maximum Cu content.
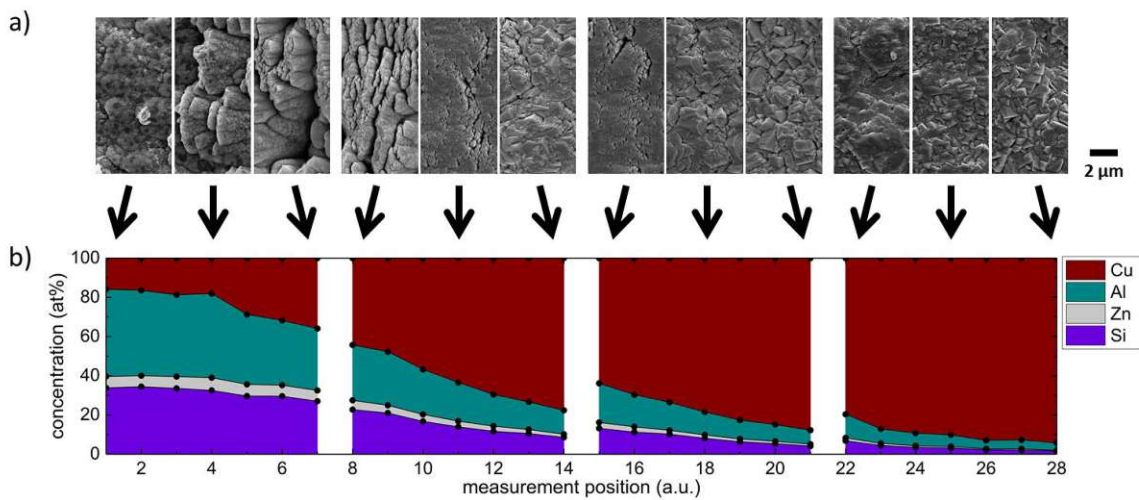
Figure 6.71.: a) The surface structure of the AlZnSi-Cu samples for different compositions. The surface texture exhibits significant variations depending on the relative composition, ranging from coarse, sharp-edged features to dense, smooth structures. b) The chemical composition of the samples in the series as recorded by EDX.
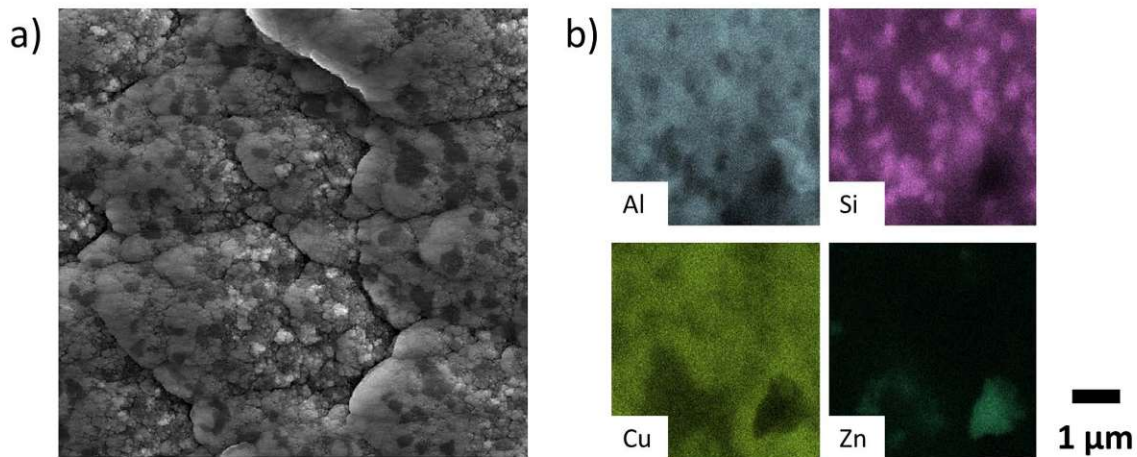
Figure 6.72.: a) A SEM image of the sample's surface structure with the composition of $x_{Cu} = 16$ at%, $x_{Al} = 44$ at%, $x_{Si} = 34$ at%, and $x_{Zn} = 6$ at%, shows dark precipitates. b) EDX mapping identifies these areas as Si-rich domains.

In Fig. 6.73, the results of the simulated atomic distributions are shown. Dark Si precipitates are visible at low Cu fractions (panel a)), while the remaining area is predominantly occupied by AlCu, in which Zn inclusions are present. The comparison with the SEM images and the EDX mappings in Fig. 6.72 reinforces these findings. As the Cu fraction is increased, the pattern depicted in Fig. 6.73 b) was calculated. Cu penetrates into the Si regions, and also its content rises in the remaining portions of the simulation array. However, the presence of two clearly separated phases is still evident. Finally, in panel c) ($x_{Cu} = 80$ at%), a pure Cu matrix predominates with the elements Al, Zn and Si incorporated in it. This result is an

indication of the formation of a Cu crystal system.
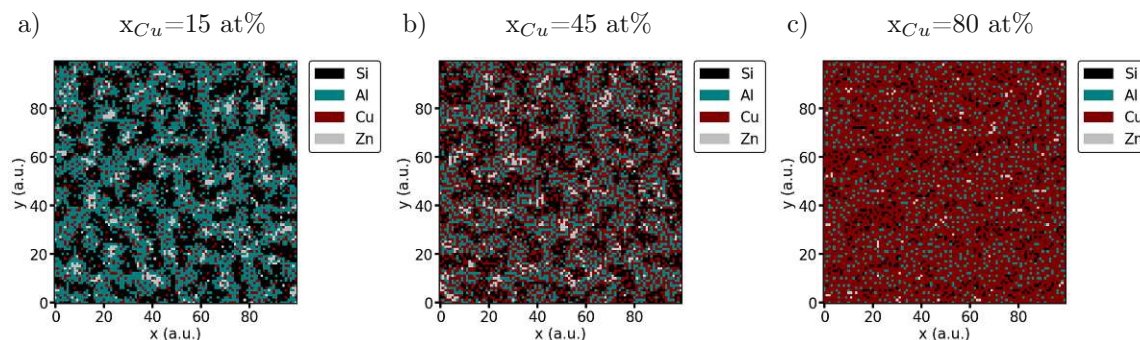
Figure 6.73.: Simulated elemental distribution of different experimentally produced samples. a) shows clearly separated Si domains. b) shows the increasing intermixing of Cu with the other alloying elements until in c) a Cu matrix with incorporated impurity atoms forms.

The results of the phase analysis by XRD are shown in Fig. 6.74. A variety of crystal phases is visible over the entire compositional space. AlCu structures dominate at Cu concentrations below 60 at%. The identified phases include a small fraction of the tetragonal Al_2Cu phase and dominant parts of the cubic Si and cubic Al_4Cu_9 phases. The cubic AlCu phase shows increased distortions at Cu fractions below 40 at%, so the patterns of rhombic and orthorhombic prototypes led to better fitting results. This is shown in detail in Fig. 6.74. At first, a CuSi intermetallic phase appears at high Cu contents of > 60 at% in the form of a hexagonal Cu_7Si_2 phase. At a Cu content of 70 at%, the first pure Cu FCC prototypes emerged. The "search and match" approach initially yielded structures with impurity atoms ($Cu_{0.67}Zn_{0.33}$ and $Cu_{0.83}Si_{0.17}$), which could be attributed to the occupation of Cu lattice sites with alloying elements. However, with increasing Cu content, the "pure" Cu FCC structure crystallizes and dominates at $x_{Cu} > 80$ at%.
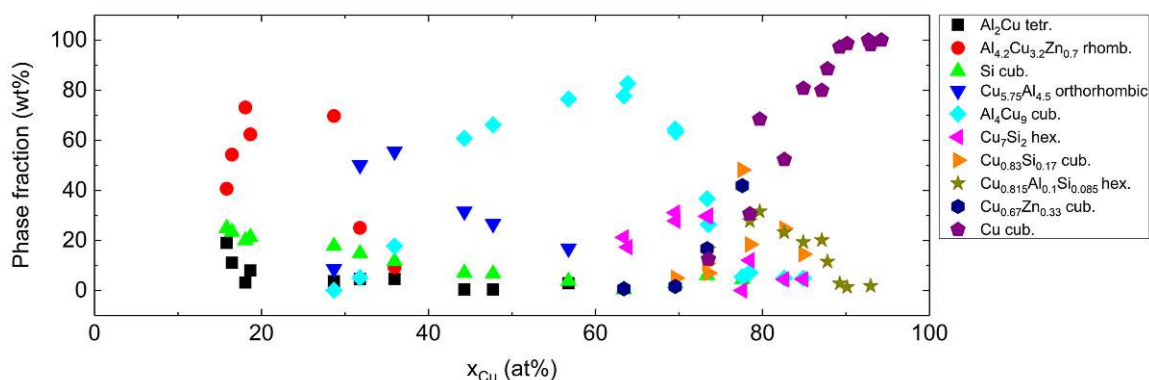
Figure 6.74.: The phase analysis of the AlZnSi-Cu series shows the complex sequence of the crystallographic phases with varying Cu content.

The measurements of the mechanical property of indentation hardness are given in Figure 6.75 b). Since the morphological structure of the samples is closely related to the hardness

properties, SEM surface images at certain points in the hardness profile are shown in panel a). At low Cu contents ($x_{Cu} < 20$ at%), the Vickers hardness exhibits a value of about 5 GPa. Such a relatively high hardness value for the system can be attributed to the existence of the tetragonal Al_2Cu and the rhombic $Al_{4.2}Cu_{3.2}Zn_{0.7}$ phase. A similar hardness value has been observed in other systems with the dominant Al_2Cu phase studied in this work. The sample structure in this region is characterized by fine-grained textures and a dense microstructure. With increasing Cu content, the indentation hardness initially decreases and reaches its minimum of about 1.6 GPa at a Cu concentration of approximately 35 at%. A transition of the surface structure to more porous textures with deep trenches and a phase transition from a rhombic to an orthorhombic prototype (corresponding to a distortion of the unit cell) accompany this decrease. An increase in hardness up to a new maximum of about 5 GPa at a Cu concentration between 60 at% and 70 at% follows this decline. Analogous to the low Cu contents, the surface structure is denser and the cracks and fissures disappear. Crystallographically, the cubic Al_4Cu_9 phase forms in this region and dominates to a large extent. This finding is similar to the hardness increase with the establishment of the same phase shown in the AlMgZn-Cu system in section 6.1.9 in the region of high Cu contents. The subsequent drop was also observed there as well as in this system. The drop coincides with the disappearance of the intermetallic phase and the progressive formation of the pure Cu FCC prototype. The surface structure is dominated by edgy textures. These were also observed in the studies of the AlMgZn-Cu quaternary alloy system at high Cu fractions (> 70 at%) and dominant Cu FCC phase. This consistency represents an important result since the samples were prepared under different process parameters (deposition rate, composition of the ternary target, deposition time) and underlines again the applicability of the presented process to achieve materials in thermodynamic equilibrium.

Summary:

In summary, the study of the AlZnSi-Cu system showed that the crystal structure is dominated by phases of the binary AlCu system and pure Si at low Cu fractions. This finding was shown in the electron micrographs by segregation behavior, as well as by the measured crystallography. At high Cu contents, both the binary AlCu and AlSi phases dominate until finally, at above 85 at%, the pure Cu solid solution phase is established. The amount of alloy elements, until which the single-phase region is stable, is substantially smaller than the one observed in section 6.1.9. In this system again, the simple simulation method led to an excellent agreement with the experimental results. The calculated distribution showed initially two separated regions, which the XRD results assigned to AlCu in coexistence with CuSi intermetallic phases. Also, the transition into a single phase Cu system was shown by the calculations and the XRD results. The indentation hardness showed a complex trend following the course and quantities of the various crystal systems.
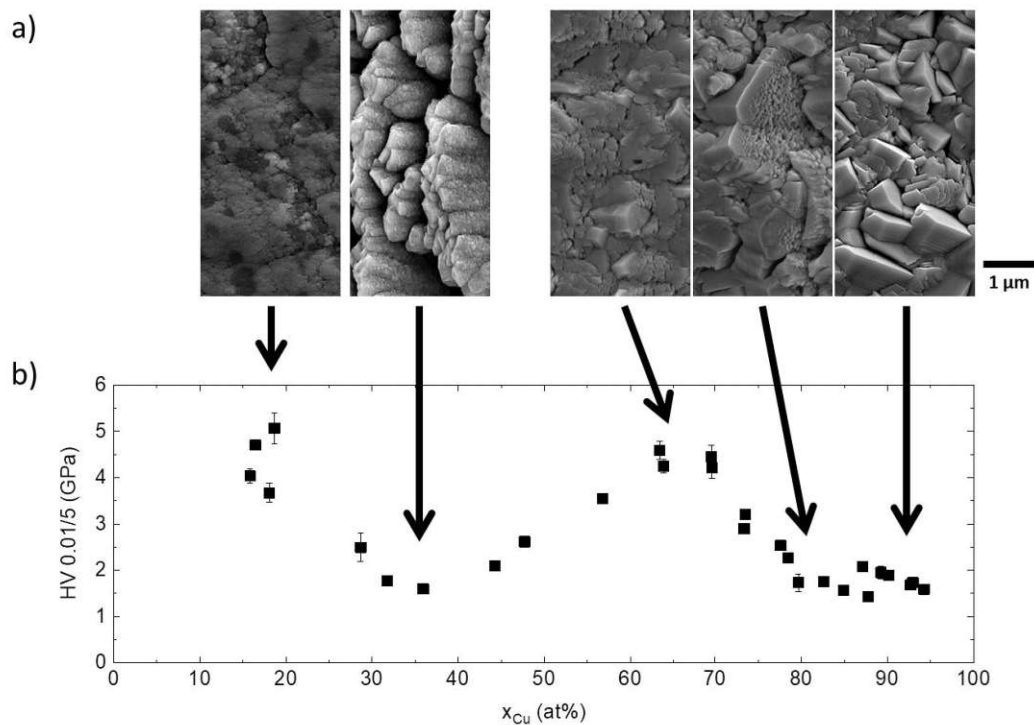
Figure 6.75.: a) The surface structure at different Cu contents. The transition from dense, fine structures to coarse textures can be observed. b) Indentation hardness as a function of the Cu content. Arrows indicate the respective surface texture at the different hardness regimes.

6.3.2. AlZnSi-Cr

The addition of Cr to the ternary AlZnSi system resulted in the elemental combination of Cr and Si, not yet presented in this thesis. This binary system is briefly described below.

Cr-Si: The intermediate phases of the Cr-Si system possess technically relevant properties, e.g., thermoelectricity [267]. The binary Cr-Si phase diagram is shown in Fig. 6.76.

- Terminal solid solution of Cr: The maximum solubility of Si in Cr is 9.5 at% at the eutectic temperature of 1705 °C [267–270].

- The solubility of Cr in the Si solid solution is negligible and lies at $8 \cdot 10^{-6}$ at% Cr at the eutectic temperature of 1305 °C [268–271].

In addition, a variety of intermetallic phases are present:

- A cubic Cr_3Si phase congruently melts at a temperature of 1770 °C [267, 270].

- A tetragonal Cr_5Si_3 phase, which congruently melts at a temperature of 1680 °C, and undergoes a polymorphic transformation at a temperature of 1505 °C [267, 269].

- A cubic CrSi phase that decomposes peritectally at 1413 °C [267, 269].
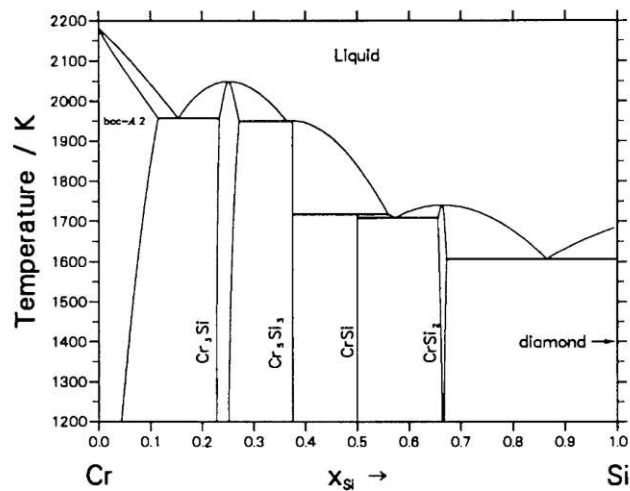
Figure 6.76.: Phase diagram of the binary Cr-Si system. [141]

a)

b)
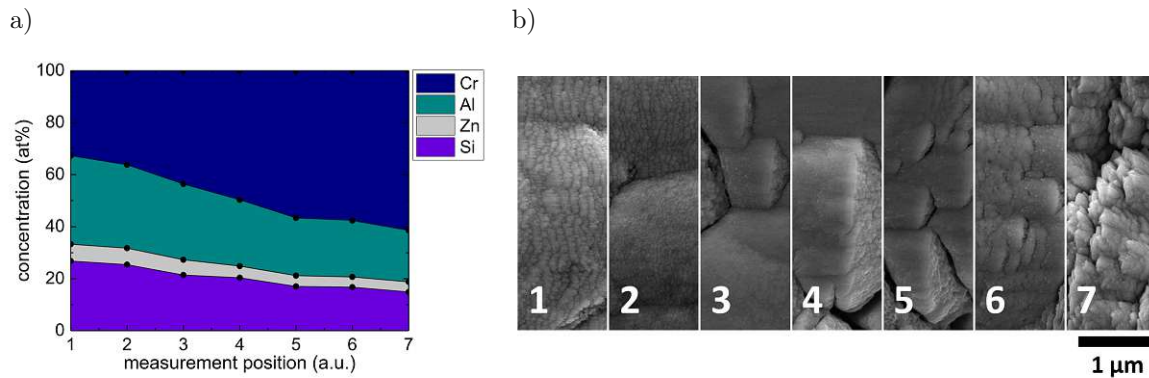
Figure 6.77.: a) EDX analysis of an AlZnSi-Cr sample b) Electron microscope images of the surface structure at the measurement points from a).

- The CrSi$_2$ as the Si richest phase shows a hexagonal structure that melts congruently at a temperature of 1490 °C [267, 269, 270].

The effects of Cr on the ternary AlZnSi system were obtained by combining the target used in chapter 6.3.1 and a pure Cr target. The produced compositions are shown in Fig. 6.77 a). The Cr content varied from 33 at% to 61 at% on a single substrate. In Fig. 6.77 b), the surface texture at different chemical compositions is shown. Fine structures in the submicrometer range can be seen for all of them. While at relatively low Cr contents ($x_{Cr} < 57$ at%), these fine structures predominate, they become increasingly coarse and sharp (pos. 7) with rising Cr concentration.

To obtain a more detailed impression of the sample properties, electron microscope images of its cross-sections were captured and are shown in Fig. 6.78. The analysis of the textures shows more pronounced columnar structures with increasing Cr content. At Cr concentrations below 50 at%, contrast differences in the backscattered images show primary elemental separation.
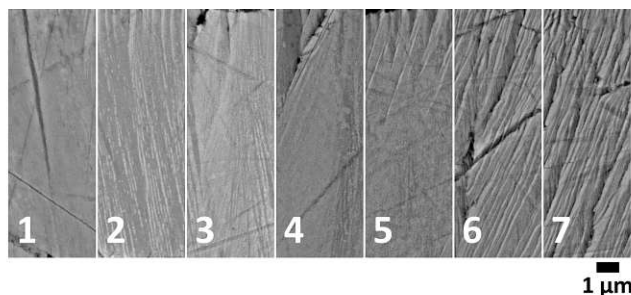
Figure 6.78.: Backscattered electron images of the metallographic cross-sections of the AlZnSi-Cr alloy system. Columnar features becoming more pronounced at higher Cr content (pos. 6 and 7) can be seen.
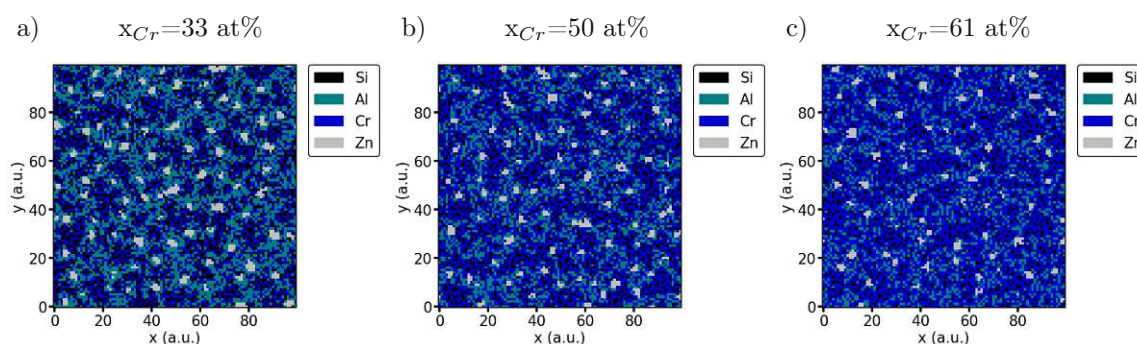
Figure 6.79.: Simulated atomic distribution after relaxation. The Cr content increases from a) 33 at% to b) 50 at% and c) 61 at%. Zn-rich precipitates are visible over the entire concentration range. At lower Cr contents (a), ternary AlCrSi regions are visible, while at higher Cr contents (c), more random arrangements of Al and Si embedded in the Cr matrix are observed (except for the Zn islands). This indicates the dominance of a Cr phase with embedded impurity atoms.

At a Cr content of about 50 at%, this columnar growth seems to reach a minimum, while at higher Cr contents, columnar features are again appearing in the structure. Comparison with the images of the sample surfaces reflects this behavior. The images which were taken at positions 6 and 7 in Fig. 6.77 b) show cracks that coincide with these columnar lamellas. Atomic distribution simulations were carried out for all the produced compositions. The results for three compositions are shown in Fig. 6.79. In the calculated distributions exhibiting a relatively low Cr concentration of 33 at%, CrSi and CrAl mixtures can be found in addition to the gray Zn-rich domains. As the Cr content increases, the area of the CrAlSi mixtures grows. The Zn domains remain stable over the entire considered composition range.

The XRD measurements revealed the phases depicted in Fig. 6.80 a). At a Cr concentration of about 30 at%, the hexagonal $CrSi_2$ phase dominated. The "search and match" approach also indicated that an increased phase fraction could be fit by the $Cr(Al_{0.422}Si_{1.578})$ structure. This corresponds to a hexagonal $CrSi_2$ phase in the binary CrSi system, which is distorted by the alloying elements. The peak positions do not correspond to the latter, as the lattice is distorted by the other elements, mainly Al. Some peaks in the diffractogram were assigned

a)

b)
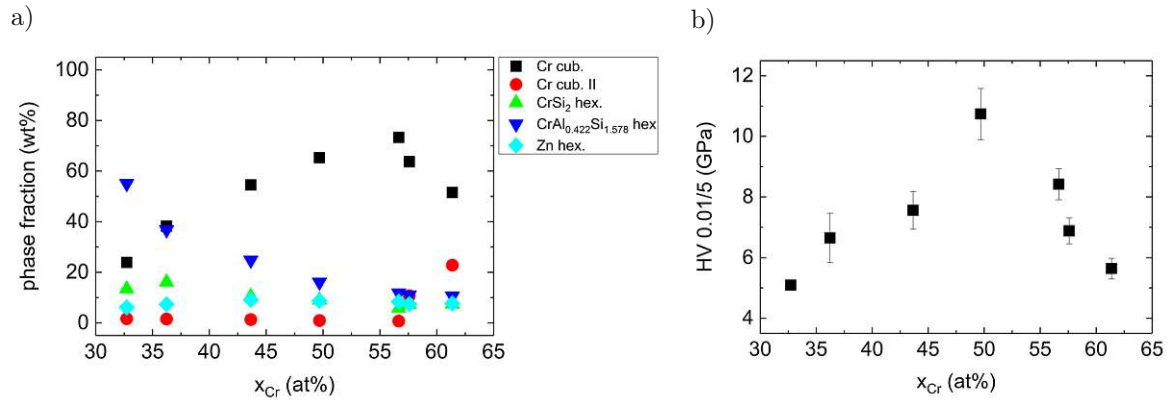
Figure 6.80.: a) Quantification of the phase analysis and b) measured indentation hardness versus Cr concentration.
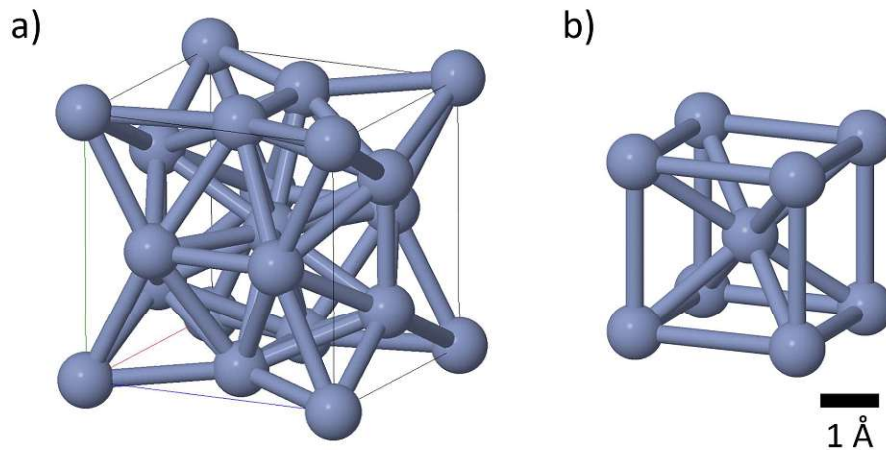
Figure 6.81.: Crystal structures of the Cr phases detected in the series. Panel a) shows the distorted Cr structure, which was found with high proportions of the alloying elements ($x > 45$ at%) and panel b) the relaxed pure cubic Cr structure (cub. Cr II).

to Zn patterns and could be quantified to a small fraction (< 10 %) in the Rietveld fits. The second most dominant crystal phase is the cubic Cr phase. The Cr phase is separated in two parts. The black squares in Fig. 6.80 a) correspond to a distorted cubic Cr crystal phase with a lattice parameter of a = 4.582 Å while the red circles quantify the the "normal" cubic Cr phase (a = 2.89 Å). In Fig. 6.81 the two different Cr phases are shown next to each other.

The indentation hardness values of the different alloy concentrations are given in Fig. 6.80 b). The trend shows a complex progression with variable Cr content. At a Cr concentration of about 33 at%, the indentation hardness equals 5 GPa. This value increases to a maximum of 11 GPa at $x_{Cr} = 50$ at% before a further significant drop. The comparison with the electron microscopy images confirms the measured behavior. Already in the previous section, a minimum of columnar structures was observed in the electron micrographs in the region

where the hardness increase of over 120 % was detected. In Fig. 6.80 the hardness curve can be directly compared to the identified crystallographic phases. A loose correlation between the evolution of the cubic Cr phase and the indentation hardness can be observed. The maximum is slightly shifted (max. of cub. Cr at $x_{Cr} \approx 55 \ at\%$ Cr versus max. indentation hardness at $x_{Cr} \approx 50 \ at\%$ Cr). Similarly, the consistencies in the morphological and structural changes are apparent. The cubic Cr II phase leads to the sharp-edged and lamellar structures previously found in the electron microscope images.

Summary:

The variation of the Cr content in AlZnSi-Cr alloys revealed an extensive dominance of Cr structures. A strong distortion of the crystal lattices was observed. The indentation hardness showed a maximum value of about 11 GPa in the range of the maximum proportion of the distorted pure Cr phase, which was followed by a rapid decline with the increase of the "relaxed" cubic Cr structure. The comparison of the atomic distribution simulations and the XRD phase analysis demonstrated an excellent agreement in this system. The Zn phases consistently detected in the XRD measurements also appeared in the simulations. The mixtures of Cr, Si, and Al atoms represent the identified intermetallic crystal phases. In addition, the increasing Cr dominance is consistent with the random arrangement of the Al and Si atoms in the Cr matrix, which is evident in the calculations.

6.3.3. AlZnSi-Mg

To investigate the influence of light metals on the AlZnSi system, Mg was chosen as the pure component. The binary phase diagram of the Mg-Si system is given in Fig. 6.82. The general characteristics of the equilibrium phase diagram, which were first reported by Vogel, are well established and accepted [272]. The solid phases of the eutectic phase diagram consist of three regions:

- Mg solid solution: The terminal Mg solid solution region exhibits a hexagonal Mg phase. The solubility of Si in Mg is negligible at temperatures < 450 °C and has a maximum value at about 0.003 at% Si [273].

- Si solid solution: The terminal Si solid solution region is characterised by an FCC crystal system. The solubility of Mg in Si is also negligible [273].

- Mg_2Si: The Mg_2Si phase represents the only stable phase in the MgSi system. It melts congruently at about 1082 °C and forms a semiconductor (n-type) [273].

The influence of Mg on the ternary Al-Zn-Si system was studied in a range of about 46 at% < x_{Mg} < 80 at% Mg concentration. The chemical composition measured by EDX is shown in Fig. 6.83 a). In addition, the surface structure at the different measurement points is depicted in panel b). Here, a transition from porous structures with submicrometer-sized grains to a continuous layer (pos. 3 and 4) can be observed. The surface appears most dense
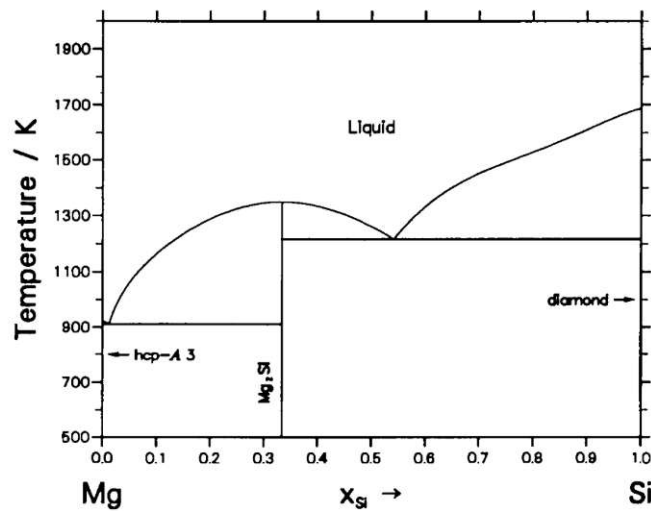
Figure 6.82.: Phase diagram of the Mg-Si system [141].

a)

b)
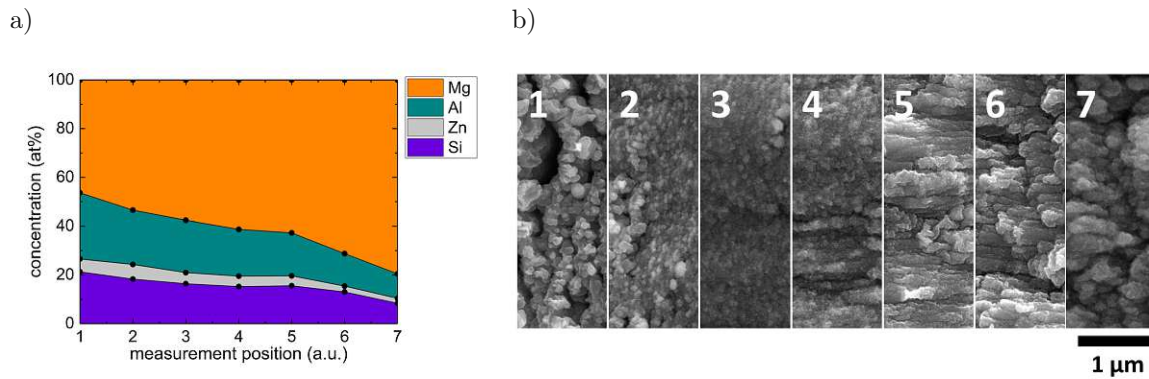
Figure 6.83.: a) Composition of the AlZnSi-Mg sample. b) The surface structure, measured at points of different chemical compositions.

at measuring position 3, at which a Mg content is approx. 58 at%. Subsequently, at higher concentrations, more porous and coarser structures emerge.

The images of the cross-sections show contrast differences indicating the separation of the alloying elements. Local EDX measurements and mappings revealed segregation of Al and Si. In particular, at high Mg contents, a homogeneous Mg distribution can be observed with sustained separation of Al and Si atoms (see Fig 6.84 c)). The separation of Al and Si has already been discussed in section 4.2.1.

The experimentally produced compositions were reconstructed by means of simulation. Selected compositions are shown in Fig. 6.85. The modeled distributions show a relatively clear separation of Mg-Si dominated domains and Al enriched regions at relatively low Mg content (panel a). Zn plays a minor role due to its low concentration and shows a generally random distribution. However, as the Mg content significantly advances, the pure Al domains split and increasingly mix with Mg atoms (panel b). The calculated distribution suggests the

a)

b)   pos. 1

c)   pos. 7
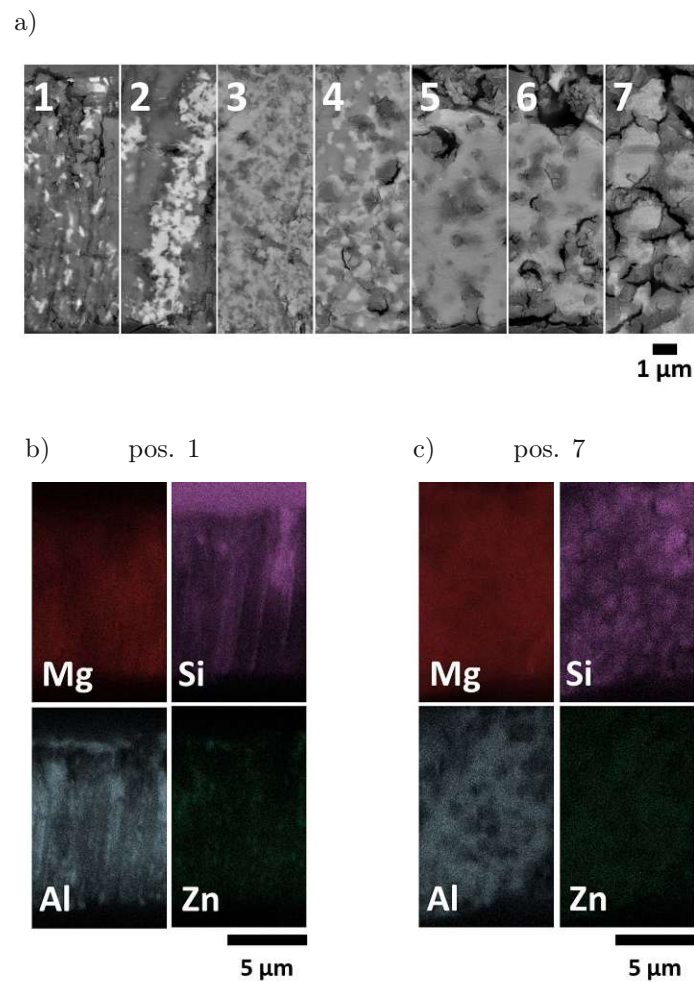
Figure 6.84.: a) Backscattered electron micrographs of the metallographic cross-sections at various compositions. An elemental separation, as well as changes in the structure, depending on the composition can be seen. Panels b) and c) show the elemental distribution along the sample's cross-section retrieved from the EDX mapping.
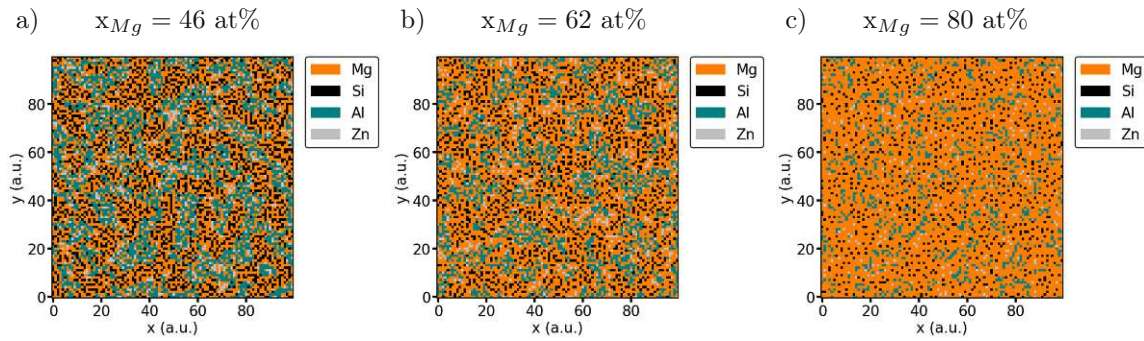
Figure 6.85.: Simulated atomic distribution of the produced samples after relaxation. The Mg content increases from a) 46 at% to b) 61 at% and c) 80 at%. Initially, Al-rich domains are visible (a), which disappear with increasing Mg concentration. Furthermore, MgSi structures are visible. Zn plays a subordinate role due to its low concentration and mixes primarily with Mg.

presence of 2 intermetallic crystal phases, a MgSi and a MgAl phase. Fig. 6.85 c) depicts the atomic distribution when the Mg concentration is in extensive excess relative to the other elements. Due to the dominance of Mg, large pure Mg regions form, which are interrupted by Al and Si clusters. A homogeneous mixture of Si and Al in these clusters is not apparent at this composition either, which corresponds to the maintenance of the IM systems in addition to the formation of larger Mg phases. The results seem plausible, especially after taking into consideration the EDX mappings, in which a homogeneous Mg distribution and separated Al and Si domains are detected.

The crystallography was analyzed by XRD, and the results are presented in Fig. 6.86 a). For a more clear overview, only phases with a content of more than 10 wt% were taken into account. From the Rietveld quantifications, a binary phase constellation results in the Mg poor composition. One of the formed phases follows the cubic Mg_2Si prototype, which was also identified as the only stable IM phase in the binary Mg-Si phase diagram. Furthermore, a pure Al phase was detected. A comparison with the simulated distributions in Fig. 6.85 a) shows a good agreement with the measured X-ray crystallographic investigations. At Mg concentrations around $x_{Mg} = 60$ at%, a transition from the Al phase to a cubic $Mg_{17}Al_{12}$ phase is observed. In this region, a narrow area of a Mg_4AlSi_4 tetragonal phase is also visible, which quickly disappears afterwards. This transition was already observed and discussed in the calculated distributions and was confirmed experimentally here. The strong Mg_2Si phase remains and shows only a slight loss in intensity. At high Mg contents of about 80 at%, a pure Mg hexagonal system forms, in addition to the two phases already mentioned, which is consistent with the calculated profiles and the theoretically formed Mg Matrix.

The phase investigation revealed that in the quaternary AlZnSi-Mg, the binary AlMg and SiMg systems are dominant. The examination of the binary phase diagrams confirms these results. Al-Mg and Si-Mg form intermetallic phases, while Al-Si does not form strong compounds over a wide concentration range.
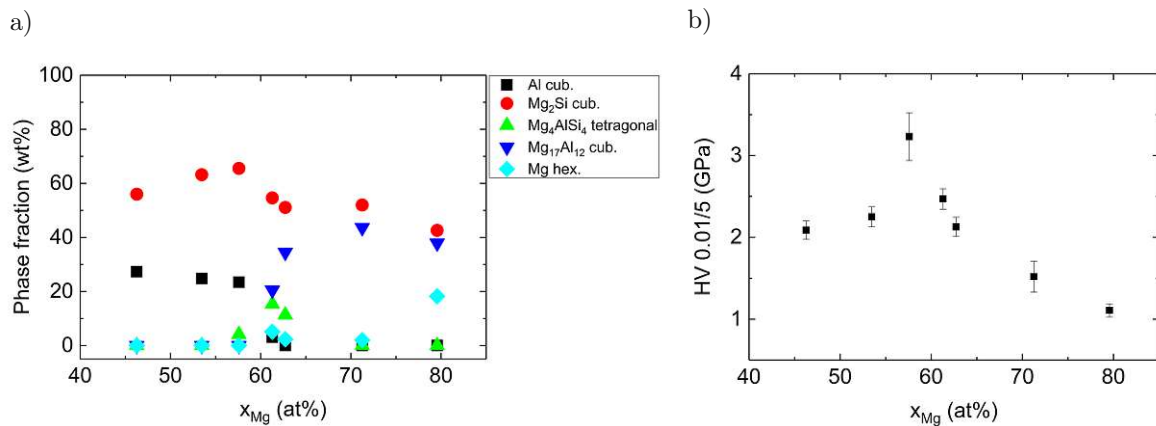
Figure 6.86.: a) Quantification of Rietveld fits and b) indentation hardness for different Mg concentrations.

The analysis of the indentation hardness at the measuring points showed the progression shown in Fig. 6.86 b). The hardness value amounts to 2 GPa at a Mg content of about 46 at% and is relatively constant up to a content of just over 50 at%. At $x_{Mg} \approx 55$ at%, a significant increase in indentation hardness (> 3 GPa) is evident. Comparison with the surface structure in Fig. 6.83 b) (measurement position 3) shows the densest structure at this measurement point. In the XRD analyses, a transition of the crystal phases can be seen in this area. This degeneracy and the resulting confusion of the system could explain the observed results in this area. Further increase of the Mg content again results in a decrease of the indentation hardness, which is around 1 GPa at the maximum Mg concentration of 80 at%. This is consistent with the increase in Mg dominated phases and an associated expectable reduction in hardness.

Summary:
The investigation of AlZnSi-Mg alloys showed a segregation behaviour of SiMg domains, which could be verified by atomic distribution simulations as well as EDX mappings and XRD measurements. No areas with single-phase behaviour could be detected. The indentation hardness showed a significant increase in the range of $x_{Mg} \approx 55$ at%, which was consistent with the densest structure in the SEM images.

6.4. Summary AlZnSi-X Alloys

Si was combined with the previously screened elements Al, Zn and (Mg, Cu, Cr) in order to extend the developed screening procedure to the material class of semiconductors. For this purpose, one trajectory each in the system AlZnSi + Cu, Cr, Mg was scanned exemplarily. The obtained experimental results were compared with classical binary phase diagrams of the constituents to visualize trends and to find the dominating subsystems.
This comparison showed that, in addition to phases already dominant in the other systems

(e.g., cubic Al_4Cu_9), significant proportions of Si+X phases were detected in the complex alloys. However, no distinct single phase areas could be detected in the samples examined. These were not expected, as none of the postulated criteria were fulfilled based on the material combinations.

The computational calculations incorporating the binary enthalpies of formation and the local configurational entropy showed excellent agreement with the experimental findings in all three systems considered. Both, segregation dynamics, for example, in the case of the low Cu content region in the AlZnSi-Cu system and the formation of intermetallic phases in all three alloy systems were reproduced. The indentation hardness measurements showed a complex progression with changing compositions in all alloy groups. The evolution could be correlated with structural and crystallographic variations of the samples. Compact and dense as well as dentric, porous layer structures were observed.

The investigations provided important evidence that the presented methods of sample preparation, analysis and characterization are applicable to alloys containing semiconductor materials. The selective sampling of chosen trajectories in the quaternary compositional space also provided potentially interesting starting points for future dedicated investigations in the respective subsystems.

7. Conclusion

In the present work, complex multi-component alloys were investigated. These included elements used in previous studies of High Entropy Alloys (HEAs) as well as elements which, due to their more complex properties, have not been considered in this alloying concept so far. Mainly light metals or semiconductors, which are relevant for industrial applications, were examined in this study. Despite being not well understood in the context of high entropy alloys, they are especially relevant for applications in which a reduction in weight, while maintaining the same high mechanical strength, is essential. These are, for example, applications in automotive and aerospace industries.

Since the definition of HEAs results in an immense number of possible compositional combinations, effective screening methods are essential to identify potential compositions of interest. An approach that employs sample synthesis through magnetron sputtering from multiple sources to quickly and easily scan larger compositional arrays has been developed and presented. By using two separate targets, controlled trajectories in an n-dimensional space (n = number of components) could be systematically scanned and characterized. The application of the PVD process enabled the simple combination of metallic systems, which would have been difficult or almost impossible to be achieved by conventional melt synthesis for some elemental combinations.

To select the process parameters to be adjusted, a simulation method was developed to calculate the content of several elements condensing on the substrate. By applying geometric considerations, this method can be used to predict the composition of the samples, taking the emission characteristics of sputtered particles and the material and energy dependencies of the sputtering yield into account. This allowed a theoretical tuning of the applied voltage, the relative distance to and the tilting of the substrate, which led to an a priori estimate of best suited process parameters. This information is essential for conducting high throughput material screening experiments. The developed algorithm was verified by comparison to samples prepared under different process parameters and was applied to prepare alloys with defined compositions in an efficient manner.

However, even with relatively effective experimental screening approaches, problems arise in the systematic selection of prepared samples due to a large number of possible elements and relative compositions. In addition to criteria established in literature for predicting potential HEAs and considering the technological relevance of element groups, a simple approach was

developed in this work to make predictions about promising element combinations and their relative proportions for the formation of potential single phase HEAs.

For this purpose, experimentally produced compositions were randomly distributed on a 100 x 100 pixel array, reflecting the elemental distribution initially assumed due to the fast cooling rate during sputtering. A Monte Carlo algorithm was used to calculate the minimum Gibbs free energy considering both, the enthalpy of formation of the binary partners and the configurational entropy. The values for the formation enthalpies were retrieved by data mining of databases based on experimental and theoretical studies.

The simple calculation method for complex multicomponent systems proved to be extremely informative. Despite the fact that only the enthalpy of formation was used to find a final state based on a minimal Gibbs free energy and important factors such as atom-dependent diffusion behavior were not taken into account, the computational results agreed well with those observed experimentally after the thermal post-treatment. This was confirmed by XRD studies and locally resolved EDX mappings of produced samples. Simple model systems have been studied, and the degree of complexity was stepwise increased. The starting point consisted of miscible and immiscible binary systems. After the calculations were able to reproduce the behaviour of these easy-to-control systems, they were extended to ternary compositions. Experimentally produced and characterized samples were compared to data retrieved from literature. Fig. 7.1 shows a comparison of the simulated atomic distribution along with results from SEM and XRD measurements.

It has not yet been possible to use this method of computation to effectively predict potential single phase solutions in systems with > 3 elements, but the results suggest that it can be employed to analyze systems with a large number of IM phases for support. In particular, ambiguous XRD results may cause difficulties in the determination of the exact crystal structure, and so an approximate knowledge of the atomic distribution can lead to a simpler and more accurate determination of the predominant phases. Since the simulations were developed during this work, they were not used here for prediction, though they were included for subsequent comparison. The similarities between the experiment and simulation described in each chapter were used to motivate the validity of the simulation for various systems.

The core of the experimental part of the work was the development of a methodology to scan a large compositional space of metallic alloy systems. The strategy presented in this thesis is schematically shown in Fig. 7.2.

Magnetron sputtering was chosen as a universal and easily applicable technique for combining a wide range of metals in order to produce material libraries. In addition, a method was developed to thermally treat the produced samples under protective atmosphere. This was necessary to overcome the non-equilibrium nature of sputter deposition. To separate the results from possible manufacturing dependencies, efforts were made to investigate the effects of different process parameters on the sample properties. By the investigation of the properties of samples produced under different conditions it could be shown that there were no significant
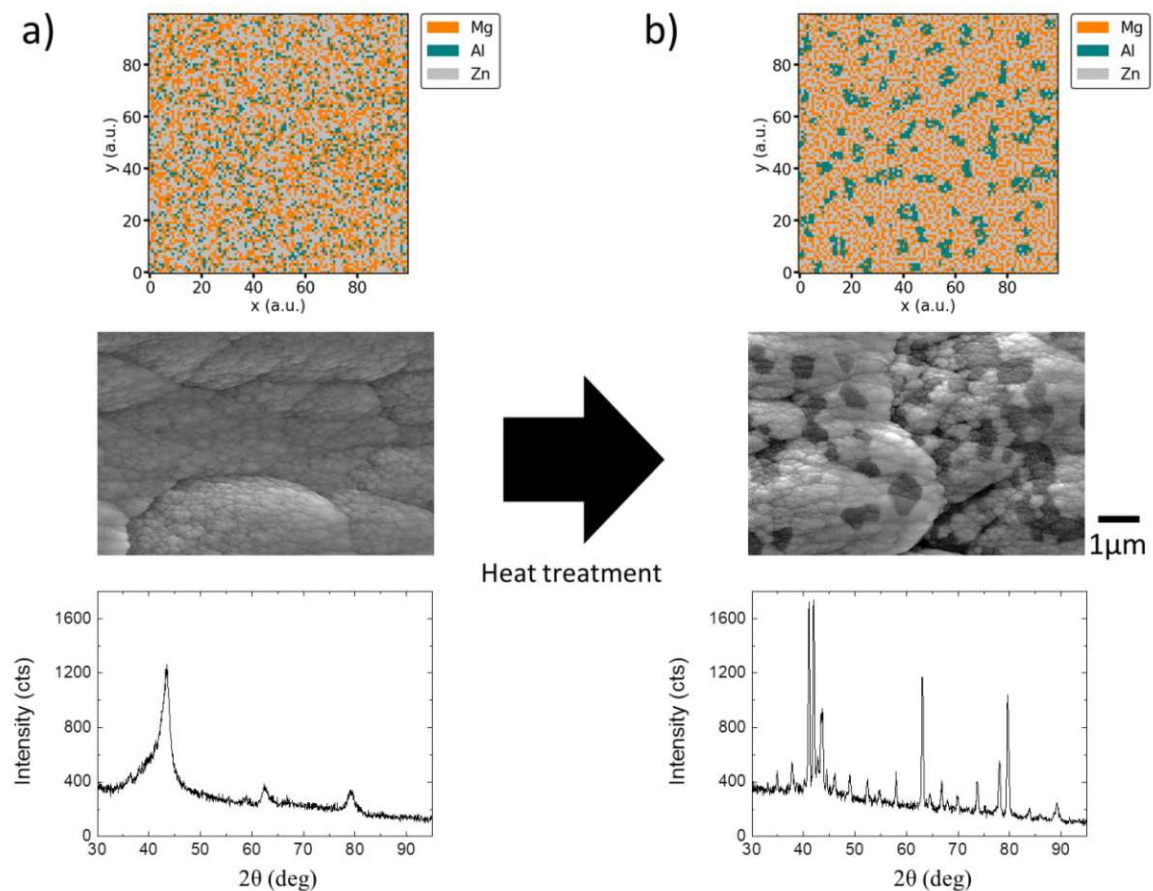
Figure 7.1.: Comparison of the conditions of prepared samples a) before and b) after thermal treatment. XRD measurements of untempered samples motivated the approach of a random initial distribution of atoms in the simulations described in the text.

differences in sample properties due to varying coating rates, slightly different post-treatment temperatures or deposition angles. The selection of roughened substrates did lead to a different surface structure, but on different size scales, which made it possible to separate the effect of the substrate roughness.

The methods used to investigate the sample properties included electron microscopy-based methods (SEM, TEM, locally resolved EDX measurements) as well as X-ray-based studies to determine the underlying crystal structure and Vickers hardness tests to characterize the mechanical properties.

The systems under investigation included elements from the group of light and transition metals (Mg, Al, Ti, Cr, Zn, Cu), and also semiconductors (Si). Special focus was directed to the quaternary AlCuMgZn system. In this system, some close-to single phase regions were found, which are shown graphically in Fig. 6.49. Besides the IM phase dominated region found in the central region of the 4 dimensional phase space, which seems plausible by referring to the entropy reasoning, a large single phase region with a simple FCC lattice was found close
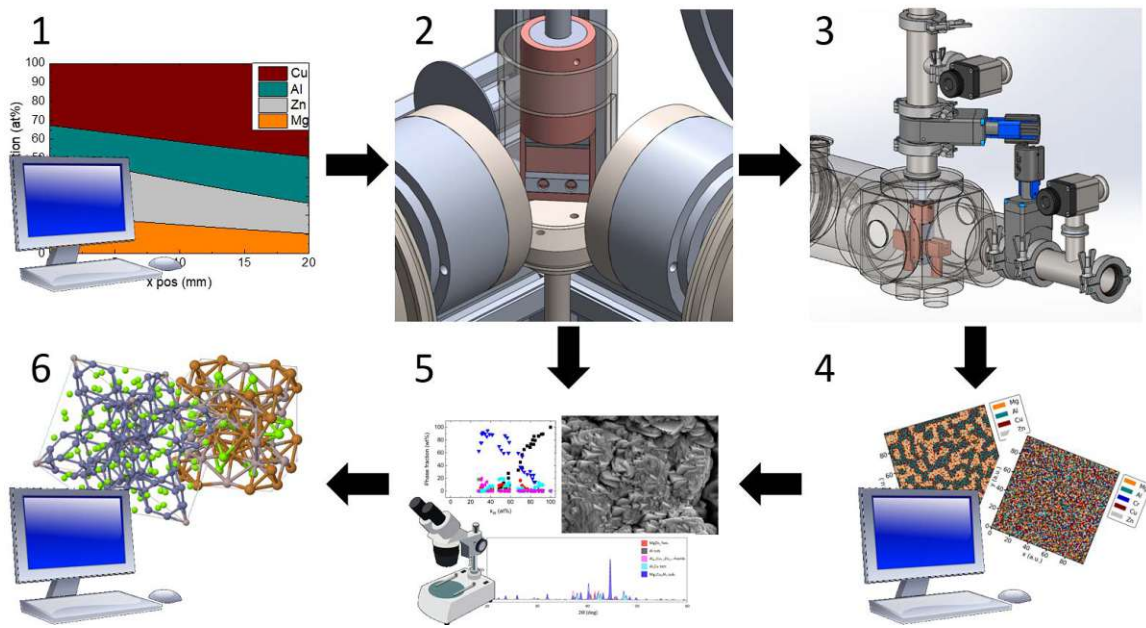
Figure 7.2.: Illustration of the screening approach presented in this thesis: 1) Calculation of the composition on the substrate provided by two separated sputter sources. 2) Experimental production of multicomponent samples. 3) One set of samples was thermally post-treated under a protective Ar atmosphere. 4) Simulations of the atomic distribution for the produced compositions by considering the enthalpy of formation and entropy. 5) Characterization using multiple analysis methods. 6) CE and DFT simulations of produced samples.

to pure Cu.

The large terminal solid solution range and the associated replacements of Cu atoms on the lattice sites with the elements Al and Mg led to a significant decrease in density while maintaining a simple crystal structure. The lowest density exhibiting a pure FCC Cu was around $\rho = 6.5$ g/cm^3. In addition, the indentation hardness showed a complex progression within the alloy system.

The investigations of trajectories to the vertices of the compositional tetrahedron (i.e. pure elements) showed the preferences of the individual elements with regard to binding. This determined the range in which the binary phase diagrams were valid and which subsystems were dominant. Here, both MgZn, CuZn and AlCu were identified as strong phases in accordance with the formation enthalpy values found in databases. Cu was identified as the preferred bonding partner of Al and Zn and could retard the observed segregation behaviour in the AlMgZn system.

The extension of the considered alloy systems with elements of other main groups such as technologically relevant transition metals (Cr and Ti) and semiconductors (Si) could demonstrate the universal applicability of the experimental screening approach. In all the systems investigated, new phases were successively formed in addition to those already found in the Al(Cu)MgZn alloys: AlCr dominates the crystal systems both with and without Cu in

the alloys with variable Cr content. The hardness profile showed significant concentration-dependent variations, with a maximum and a minimum of HV ≈ 10 GPa and ≈ 4 GPa, respectively. Besides the common complex hardness profile in the AlMgZn-Cr and AlCuMgZn-Cr systems, the textures also showed similar trends, with flake-like structures at high Cr contents. The heat treatments performed at two different annealing temperatures (350 °C and 430 °C) showed no differences in the resulting phase distributions. Analogously, the established AlMgCuZn phases were also split by the addition of Ti and primarily AlCuTi crystal phases were formed.

The comparison of the ternary AlZnSi system with addition of Mg, Cr and Cu could directly show the differences of the various additive elements in the presence of a semiconductor. While the addition of Mg resulted in strong binary MgSi and MgAl subsystems, the presence of Si in the AlZnSi-Cu alloys did not show a major influence on the predominant AlCu structures. The addition of Cr led to a preferred Cr structure which was distorted by the other alloying elements. The indentation hardness varied significantly depending on the elemental composition of the alloy constituents and was assigned to either the observed layer structure or the crystallography of the alloy.

For all the systems investigated in this work, the crystallographic order, the surface structure and the texture of the sample influenced the resulting physical properties. Several phenomena discussed in the context of MPEAs and HEAs like solute hardening or lattice distortion have been observed. However, the systems under consideration generally behaved according to the trends expected from the classical binary phase diagrams and no unexpected phases were observed. In the majority of the investigations, the observed trends could be explained by structural and crystallographic considerations.

The results showed in particular that the criteria and postulates developed and used to date, intended to predict the formation of high entropy alloys and which already provided promising results for many systems, are not valid for alloys based on light metals. One reason for this is that they were developed mainly for transition metals, which are characterized by simpler bonding structures and smaller differences among them. The anisotropic bonding behavior of light metals leads to the failure of most criteria, which means that new, more sophisticated methods for predicting possible HEAs are necessary.

Through the collaboration with the Institute of Advanced Ceramics of the Hamburg University of Technology, the energy of formation of experimentally prepared samples was recalculated and the preferred crystal structure was compared. CE models were developed to fit previously generated DFT training datasets. This allowed the efficient calculation of a large number of different stoichiometric mixtures without performing a comparable time-consuming DFT calculation for each configuration. Based on the experimental results, the C14 and C15 Laves phase and a cubic crystal lattice were used as basic symmetries. The numerical methods were applied to the single phase regions found experimentally in this study and were able to provide consistent data. In particular, the phase transition from the FCC Cu terminal solid solution

to the cubic intermetallic phase and the C14 Laves phase reproduced in the simulations is remarkable. [213] These results demonstrate the applicability of the experimental approach as well as the computational methods developed by the TU Hamburg. While to date, in the DFT and CE simulations the experimental outcomes served as input variables and were "only" confirmed by the theoretical studies, it is an important step towards an a priori model to search for specific structures within multi component alloys.

Outlook

The results of this work have already provided important insights regarding the interaction of the single constituents in complex metallic multicomponent systems. In particular, the comparison with theoretical models and the verification of the experimental results represent an important base for the future exploitation of HEAs in the light metal sector. To date, the theoretical methods presented in this thesis have been used to confirm the experimental data and have required input from the experimental data. The goal would be to reverse this process so that structures and phases can be predicted theoretically and subsequently confirmed experimentally. This would allow an effective computational screening of a multitude of different elemental combinations and relative concentrations. Cluster expansion methods and DFT calculations are promising candidates to achieve this. However, training data, which can be collected through studies such as the one conducted here, are necessary.

The experimental methods proved to be very practical and optimal for the desired application. Due to the geometric arrangement, gradients of the composition could be exploited to scan larger compositional areas. This conceptual advantage can become a drawback when a region of interest is found, as it is not possible to produce larger samples exhibiting a homogeneous composition. A solution might be the incorporation of a substrate holder that allows rotation of the sample during coating. This could result in a homogenization of the layer composition. In addition, the limitation to 2 separate targets is problematic for the systematic investigation of systems with more than 2 components. Due to the limited number of sources, compound targets have to be used, which do not allow an individual adjustment of the individual components.

Another issue is the controlled production of compounds. The simulation used in this work to determine the process parameters for the experiments delivered good results. Thus, it was possible to ensure the production of the samples in a targeted manner within certain limits. However, for more precise predictions and increased homogeneity, the proposed calculation method might be too inaccurate. A simulation method that theoretically predicts the composition in real time and adjusts the process parameters (e.g. in the form of the applied power) if necessary would be helpful. Such an approach is pursued at the Institute of Solid State Physics in the form of a "virtual machine". Once provided with material-specific parameters, the virtual machine can calculate the composition of the material deposited on the substrate. In addition, the ageing effects of the target and thus emission characteristics deviating from the ideal must be taken into account for an accurate prediction of the sample composition.

By using a variety of element combinations, the universal applicability of the proposed screening approach was demonstrated. In addition to the main system MgAlCuZn, more exotic elements such as Si were introduced into the alloys. First results within the scope of this work could give indications about the investigated properties, however, for a deeper understanding of the dynamics of phase formation further trajectories in the composition space have to be investigated.

A. Appendix

A.1. Sputter Yield

The sputter yield is one of the determining parameters of the sputtering process and describes the mean number of emitted target atoms per impacting working gas ions. It indicates how easily atoms can be ejected from the target. Several factors such as atomic mass of the target material as well as the working gas or the activation energy to name a few have an influence on the magnitude of the sputter yield. The sputter yield values used in the applied simulations are based on the empirical work of Matsunami and Noriaki [94]:

$$Y(E) = 0.42 \frac{\alpha' \, Q \, K \, s_{el}(\epsilon)}{U_S(1 + 0.35 \, U_S \, s_{in}(\epsilon))}(1 - (E_{th}/E)^{1/2})^{2.8} \; . \tag{A.1}$$

Here, E is the energy of the impacting ions, $s_{el}(\epsilon)$ and $s_{in}(\epsilon)$ are approximations for the elastic and inelastic stopping function according to the Lindhard model, U_S the sublimation energy and α' as well as Q empirical parameters. E_{th} is the value for the threshold energy. The reduced energy ϵ is given by

$$\epsilon = \frac{0.03255}{Z_{ion} \, Z_{target} \, (Z_{ion}^{2/3} + Z_{target}^{2/3})^{1/2}} \, \frac{M_{target}}{M_{target} + M_{ion}} \, E[eV] \; . \tag{A.2}$$

The conversion factor from the elastic stopping function to the stopping power is called K and is calculated according to the formula:

$$K = 8.478 \frac{Z_{ion} \, Z_{target}}{(Z_{ion}^{2/3} + Z_{target}^{2/3})^{1/2}} \, \frac{M_{ion}}{M_{target} + M_{ion}} \; . \tag{A.3}$$

The remaining parameters in eq. (A.1) are calculated according to the following equations:

$$\alpha' = 0.08 + 0.164 \, (M_{target}/M_{ion})^{0.4} + 0.0145 \, (M_{target}/M_{ion})^{1.29} \tag{A.4}$$

$$E_{th} = U_S \, (1.9 + 3.8 \, (M_{target}/M_{ion})^{-1} + 0.134 \, (M_{target}/M_{ion})^{1.24}) \tag{A.5}$$

$$s_{el}(\epsilon) = \frac{3.441 \, \sqrt{\epsilon} \, \ln(\epsilon + 2.718)}{1 + 6.355 \, \sqrt{\epsilon} + \epsilon \, (-1.708 + 6.882 \, \sqrt{\epsilon})} \tag{A.6}$$

$$s_{in}(\epsilon) = 0.079 \sqrt{\epsilon} \; \frac{(M_{target} + M_{ion})^{3/2}}{M_{target}^{1/2} \, M_{ion}^{3/2}} \; \frac{Z_{ion}^{2/3} \, Z_{target}^{1/2}}{(Z_{ion}^{2/3} + Z_{target}^{2/3})^{3/4}} \qquad \text{(A.7)}$$

The values for Q and E_0, which depend on the type of the atom, were taken from [94] and [274] and are given in Table A.1. For elements for which the required values could not be found, experimentally measured sputteryields were fitted, and thus the values for Q and E_0 were estimated. These are marked with an asterisk in Table A.1 Mg.

As in the experiments, Ar with an atomic number of $Z = 18$ and the mass $M_{ion} = 39.948$ atomic units was selected as the working gas.

Table A.1.: Material-specific parameters for the calculation of the sputter yield [94, 274]

Target	Z	Sublimation Energy [eV]	Q
Mg*	12	1.54	0.49
Al	13	3.39	1.09 ± 0.14
Si	14	4.63	0.78 ± 0.17
Ti	22	4.85	0.58 ± 0.10
Cr	24	4.10	1.23 ± 0.21
Cu	29	3.49	1.30 ± 0.22
Zn*	30	1.35	1.00

A.2. Calculation of Sputtering Cooling Rate

The method of sputtering is associated with high cooling rates. These are estimated in the subsequent section. The temperature of the particles reaching the substrate can be estimated by means of the average particle energy of the sputtered atoms. This is of the order of a few eV [275, 276]. From

$$E = k_B T \tag{A.8}$$

follows (for simpler calculation an energy of 1 eV was assumed):

$$T = \frac{E}{k_B} = \frac{1 \; [eV]}{1.38 \cdot 10^{-23} \; [J/K]} = \frac{1.6021 \cdot 10^{-19} \; [J]}{1.38 \cdot 10^{-23} \; [J/K]} = 11609 \; [K]. \tag{A.9}$$

Assuming that particles arriving at the substrate have time to reach a thermodynamic minimum until the formation of the next full monolayer is completed, it follows that the cooling rate becomes

$$R_{cool} = \frac{\Delta E \; [J] \cdot R \; [nm/s]}{k_B [J/K] \cdot d_{ML} \; [nm]}, \tag{A.10}$$

where ΔE is the energy difference between the substrate and the incoming coating particles, R denotes the deposition rate in the order of a few nm/s, and d_{ML} the thickness of a monolayer (in the range of a few Å $= 10^{-1}$ nm). This results in cooling rates R_{cool} of around 10^2 K/s - 10^7 K/s depending on the substrate's temperature and the choice of the deposition rate.

A.3. Binary Enthalpies

Table A.2.: Binary formation enthalpies and mixing enthalpies in [meV/atom] taken from [77, 149].

ΔH_{mix} \ ΔH_{form}	Mg	Li	Ca	Na	Sn	Si	Ga	Ge	Al	Sc	Ti	V	Cr	Mn	Fe	Co	Ni	Cu	Zn	Y	Zr
Mg	Mg	-64	-126	-227,2	-191	-182,3	-148,4	-308,1	-37,5	-46,5	18,7	129,3	158,1	90	75	-33,8	-725,6	-148,8	-139	-110,47	-31,7
Li	-31,1	Li	-18,8	19,5	-410,5	-315,1	-336,5	-351,9	-189,8	84,1	99,2	172,1	276,4	148,3	193,2	66,1	-43,6	-72,1	-218,0	49,2	81,6
Ca	-62,2	-10,4	Ca	24,6	-659,8	-541,8	-511,4	-667,6	-329,7	86,3	233,0	325,5	351,0	169,7	215,2	102,9	-189,1	-149,4	-302,3	42,4	119,3
Na	103,6	41,5	10,4	Na	-191,1	-17,6	-163,8	-123,9	34,8	133,6	238,1	336,1	232,0	232,8	422,3	298,3	239,9	78,9	-61,7	96,4	176,5
Sn	-93,3	-186,6	-466,4	-82,9	Sn	134,0	13,7	64,8	63,2	-686,7	-418,7	-78,7	116,0	-18,2	-27,5	-134,6	-283,1	-44,9	39,6	-776,2	-601,0
Si	-269,5	-310,9	-528,6	-114,0	-114,0	Si	101,4	25,5	44,7	-835,4	-793,2	-587,0	-376,8	-440,5	-514,3	-615,7	-550,2	-71,7	95,4	-853,8	-935,6
Ga	-41,5	-93,3	-290,2	51,8	10,4	-176,2	Ga	38,8	3,0	-615,3	-481,3	-241,9	-82,9	-192,2	-348,2	-290,3	-419,6	-115,0	9,8	680,1	641,9
Ge	-274,7	-357,6	-616,7	-222,8	-129,6	-150,3	-160,6	Ge	39,9	-845,1	-699,8	-334,0	-124,7	-122,4	120,2	-212,4	307,0	-3,6	60,2	-898,9	819,8
Al	-37,3	-41,5	-207,3	134,7	41,5	-196,9	10,4	-150,3	Al	-484,4	-433,1	-289,4	-142,7	-278,5	-359,0	-629,0	-658,8	-212,5	9,4	-534,3	-540,5
Sc	-31,1	124,4	176,2	352,4	-466,4	-767,0	-393,8	-720,3	-393,8	Sc	38,0	83,0	119,0	-142,0	-281,0	-359,0	-525,0	-284,0	-380,0	18,0	-29,0
Ti	165,8	352,4	445,7	704,8	-217,6	-684,0	-238,4	-533,8	-310,9	82,9	Ti	37,0	-372,0	-277,0	-418,0	-386,0	-435,0	-147,0	-198,0	111,0	24,0
V	238,4	383,5	456,0	756,6	-10,4	-497,5	-82,9	-326,5	-165,8	72,5	-20,7	V	-88,0	-286,0	-176,0	-199,0	-250,0	13,0	-51,0	143,0	26,0
Cr	248,7	362,7	393,8	735,9	103,6	-383,5	-10,4	-191,7	-103,6	10,4	-72,5	-20,7	Cr	-110,0	-8,0	5,0	-30,0	108,0	44,0	150,0	-150,0
Mn	103,6	196,9	196,9	507,8	-72,5	-466,4	-134,7	-326,5	-196,9	-82,9	-82,9	-10,4	20,7	Mn	9,0	-19,0	-115,0	29,0	-25,0	40,0	-192,0
Fe	186,6	269,5	259,1	642,6	-114,0	-104,7	-20,7	-160,6	-114,0	-114,0	-176,2	-72,5	-10,4	0,0	Fe	-60,0	-97,0	65,0	-23,0	-290,0	
Co	31,1	82,9	20,7	424,9	0,0	-393,8	-114,0	-222,8	-196,9	-310,9	-290,2	-145,1	-41,5	-51,8	-10,4	Co	-21,0	54,0	-58,0	-198,0	-324,0
Ni	-41,5	10,4	-72,5	331,7	-41,5	-414,6	-155,5	-243,6	-228,0	-404,2	-362,7	-186,6	-72,5	-82,9	-20,7	0,0	Ni	-6,0	-256,0	-437,0	-463,0
Cu	-31,1	-51,8	-134,7	165,8	72,5	-196,9	10,4	-119,2	-10,4	-248,7	-93,3	51,8	124,4	41,5	134,7	62,2	41,5	Cu	-92,0	-258,0	-169,0
Zn	-41,5	-72,5	-228,0	62,2	10,4	-186,6	0,0	-160,6	10,4	-300,6	-155,5	-20,7	51,8	-62,2	41,5	-51,8	-93,3	-82,0	Zn	-405,0	-301,0
Y	-62,2	82,9	114,0	290,2	-528,6	-756,6	-414,6	-751,4	-393,8	10,4	155,5	176,2	114,0	-10,4	-10,4	-228,0	-321,3	-228,0	-321,3	Y	40,0
Zr	62,2	279,8	383,5	611,5	-445,7	-870,6	-414,6	-751,4	-456,0	41,5	0,0	-41,5	-124,4	-155,5	-259,1	-424,9	-507,8	-238,4	-300,6	93,3	Zr

A.4. Element Properties

A brief overview of some properties of various elements is given below:

Table A.3.: Properties of a selection of elements considered to be part of studied systems [20, 172, 173]

Element	Mass [u]	Density [g/cm^3]	Radius [Å]	VEC	T_{melt} [°C]
Li	6.94	0.53	1.52	1	180
Na	22.99	0.97	1.54	1	98
Mg	24.31	1.74	1.60	2	639
Al	26.98	2.70	1.43	3	660
Si	28.05	2.36	1.17	4	1410
Ca	40.08	1.55	1.97	2	839
Sc	44.96	3.00	1.61	3	1539
Ti	47.87	4.54	1.45	4	1660
V	50.94	6.11	1.35	5	1890
Cr	51.99	7.14	1.40	6	1857
Mn	54.94	7.43	1.37	7	1245
Fe	55.85	7.87	1.24	8	1535
Ni	58.69	8.90	1.25	10	1455
Co	58.93	8.90	1.25	9	1495
Cu	63.55	8.96	1.28	11	1083
Zn	65.39	7.13	1.33	12	420
Ga	69.72	5.90	1.30	3	30
Ge	72.63	5.32	1.25	4	938
Y	88.90	4.47	1.80	3	1523
Zr	91.22	6.51	1.59	4	1852
Sn	118.71	7.31	1.51	4	232

A.5. Calculation of Excess Entropy

The excess entropy has been used as an extension for the description of the entropy in a system. To get an estimation of the magnitude of the excess entropy the apporach presented in [18, 72] was followed.

According to the Carnahan and Starling theory it is possible to express the compressibility Z using the following expressions:

$$\Delta_{i,j} = \left[(\xi_i\xi_j)^{1/2}/\xi\right]\left[(d_i - d_j)^2/d_id_j\right](c_ic_j)^{1/2} \tag{A.11}$$

$$y_1 = \sum_{j>i=1}^{m} \Delta_{i,j}(d_i + d_j)/(d_id_j)^{-1/2} \tag{A.12}$$

$$y_2 = \sum_{j>i=1}^{m} \Delta_{i,j} \sum_{k=1}^{m} \left(\frac{\xi_k}{\xi}\right)\frac{(d_id_j)^{1/2}}{d_k} \tag{A.13}$$

$$y_3 = \left[\sum_{k=1}^{m} \left(\frac{\xi_k}{\xi}\right)^{2/3} c_i^{1/3}\right]^3 \tag{A.14}$$

$$\xi_i = \frac{1}{6}\pi\rho_N d_i^3 c_i \tag{A.15}$$

$$\xi = \sum_{i=1}^{m} \xi_i \tag{A.16}$$

as

$$Z = \left[(1 + \xi + \xi^2) - 3\xi(y_1 + y_2\xi) - y_3\xi^3\right](1 - \xi)^{-3}. \tag{A.17}$$

In the previous equations, d_i is the diameter and c_i the atomic fraction of the ith element, ρ_N the number density and ξ the overall packing fraction. The number density is the number of atoms in a defined volume, and for a given material can be calculated using the density of the pure material ρ, the molar mass M and the Avogadro constant N_A by

$$\rho_N = \frac{\rho}{M}N_A. \tag{A.18}$$

The excess entropy of mixing S_E can then be calculated using

$$\frac{F - F^{id}}{k_bT} = -\frac{3}{2}(1 - y_1 + y_2 + y_3) + (3y_2 + 2y_3)(1 - \xi)^{-1}$$
$$+ \frac{3}{2}(1 - y_1 - y_2 - \frac{1}{3}y_3)(1 - \xi)^{-2} + (y_3 - 1)\ln(1 - \xi) \tag{A.19}$$

in the equation

$$\frac{S_E}{k_B} = \frac{F - F^{id}}{k_b T} - \ln(Z) - (3 - 2\xi)(1 - \xi)^{-2} + 3$$
$$+ \ln\left[(1 + \xi + \xi^2 - \xi^{-3})(1 - \xi)^{-3}\right]. \tag{A.20}$$

A.6. Data of Experimental Results

The data of the analysis of the various samples series are given below:

A.6.1. AlZn

Table A.4.: Results of the analysis of the AlZn series. The phase fractions are given in wt%.

pdf Code:	Zn (at%)	Al (at%)	Zn hex. 04-008-6027	Al cub. 04-013-9777
	92.51	7.49		
	94.6	5.4		
	94.46	5.54		
	92.99	7.01		
	92.24	7.76		
	89.66	10.34		
	86.89	13.11		
	87.3	12.7	99.4	0.6
	84.9	15.1	97.8	2.2
	81.3	18.7	96.6	3.4
	75.2	24.8	94.7	5.3
	69.1	30.9	88.7	11.3
	64.1	35.9	85	15
	56.8	43.2	80.8	19.2
	59.8	40.2	85	15
	54.5	45.5	80.2	19.8
	49.1	50.9	76.1	23.9
	45.9	54.1	71.7	28.3
	42	58	66.9	33.1
	38.4	61.6	62.9	37.1
	33.7	66.3	59.4	40.6
	44.6	55.4	75.3	24.7
	40	60	69.4	30.6
	34.5	65.5	63.2	36.8
	26.8	73.2	56.9	43.1
	25.2	74.8	50.4	49.6
	22.8	77.2	43.9	56.1
	20	80	38.2	61.8

A.6.2. AlCu

Table A.5.: Results of the analysis of the AlCu series. The phase fractions are given in wt%.

pdf Code:	Al (at%)	Cu(at%)	Cu cub. 04-003-2430	Al$_4$Cu$_9$ cub. 03-065-3347	AlCu monoclinic 00-026-0016	Al$_{35.472}$Cu$_{47.792}$ orthorhombic 01-072-3506
	17.05	82.95	89.2	10.8	0	0
	20.53	79.47	72.3	27.3	0	0
	26.48	73.52	44	56	0	0
	32.86	67.14	11.2	88.8	0	0
	41.1	58.9	0	73.9	26.1	0
	46.72	53.28	0	46.1	53.6	0.2
	51.4	48.6	0	0	65.9	34.1

A.6.3. Al-MgZn

Table A.6.: Results of the analysis of the Al-MgZn series. The phase fractions are given in wt%.

pdf Code:	Mg (at%)	Zn (at%)	Al (at%)	HV 0.01/5 (GPa)	σ(HV)	Al cub 04-012-7848	MgZn$_2$ hex. 04-003-2083	AlMg$_2$Zn$_2$ cub. 04-007-2215
	40.6	53.5	6	2.34	0.17	0	100	0
	41.9	53.1	4.9			0	99.9	0.1
	40.8	54.4	4.9			0	100	0
	40.6	54.1	5.3	2.45	0.05	0	100	0
	39.6	53.9	6.6			0	99.9	0.1
	35.7	55.5	8.8			0	98.2	1.8
	35.6	53.6	10.8	2.11	0.11	1.5	96.3	2.1
	41.1	52	6.9	2.27	0.08	0.9	98.5	0.6
	39.1	52.9	8			0.6	98.3	1
	39.8	50.6	9.6			3.4	94.5	2.1
	37.6	50.5	11.9	2.29	0.11	5	92.6	2.3
	36.9	47	16.1			5.5	92.3	2.2
	34.6	45.3	20.1			6.5	91.2	2.3
	32.5	44.9	22.5	2.06	0.05	5.9	92.3	1.7
	37.7	44.4	17.8	2.54	0.16	5.7	91.6	2.7
	31.9	42	26.2			5.7	92.1	2.1
	28.5	39.4	32.1			8.4	90.6	1
	27	37.2	35.8	2.17	0.08	11.7	87.4	1
	26.7	37	36.3			12	87.3	0.7
	25.4	35.3	39.3			11.8	87.4	0.8
	25.1	34.9	40	1.92	0.01	12.5	86.5	1
	26.7	30.9	42.4	2.07	0.08	16.1	49.6	32.9
	25.4	26.1	48.5	2.17	0.17	23.9	62.8	13.3
	23	23.5	53.5	2.14	0.10	27.3	69.9	2.8
	23.5	23.8	52.7	1.69	0.08	30.3	67.9	1.8
	21.7	21.5	56.8	1.46	0.08	33.1	65.2	1.7
	20.6	21.2	58.2	1.13	0.06	34.6	64.2	1.2
	16.4	20.2	63.4	0.99	0.04	37.3	61	1.8
	20	24.8	55.2	1.44	0.01	33	65.7	1.2
	18.2	21.8	60			37.9	60.8	1.3
	15.9	17.6	66.5			43.5	55.5	1
	13.8	15.2	70.9	1.36	0.11	48.5	49.8	1.3
	11.7	12.7	75.6			53.7	44.1	2.1
	8.2	10.4	81.4			57.7	40.5	1.8
	6.6	8.5	84.9	0.98	0.06	62.6	36.6	0.8
	9.2	12.3	78.5	1.11	0.03	64.9	33	2.1
	6.7	8.9	84.5			72.3	24.9	2.7
	5.7	7.5	86.8			79.8	17.4	2.8
	4.6	5.9	89.5	0.95	0.02	86	14	0
	3.9	5.3	90.7			90.1	9.9	0
	2.9	4.5	92.5			90.3	7.9	1.8
	2.6	3.8	93.6	0.93	0.01	92.7	7.1	0

A.6.4. Al₂Cu-MgZn₂

Table A.7.: Results of the analysis of the Al₂Cu-MgZn₂ series. The phase fractions are given in wt%.

pdf Code:	Mg (at%)	Zn (at%)	Al (at%)	Cu (at%)	MgZn₂ hex. 04-003-2083	Mg₂Zn₁₁ cub. 04-007-1412	Al cub. (wt%) 00-004-0787	Al₂Cu tetr. 04-007-0566	Al₄Cu₉ cub. 03-065-3347	AlCu monoclinic 04-007-1323
	44.2	55.8	0	0						
	46.1	53.9	0	0	89.1	10.6	0	0	0	0
	37.4	53.5	7.4	1.7	87.2	11.2	1.2	0	0	0
	37.9	50.3	10.5	1.2	87.5	9.4	2.8	0	0	0
	34.4	52.9	10.9	1.9	87.8	9.3	2.5	0	0	0
	33.5	50.5	14	2	87.7	8.1	3.9	0	0	0
	34.3	50.2	13.4	2	87.7	9.2	2.8	0	0	0
	33.2	49.4	14.9	2.5	86.6	8.9	4.2	0	0	0
	31	50.6	15.7	2.8	86.1	9.8	3.8	0	0	0
	32.9	49.5	14.1	3.6	83.4	14.2	2.1	0	0	0
	32.5	46.7	17.2	3.6	82.7	14.4	2.7	0	0	0
	30.7	46.2	19.1	4	80.9	14.2	4.7	0	0	0
	28.7	42.4	24.7	4.2	79.6	15.4	4.8	0	0	0
	27.3	41.6	26.1	5	74.9	19.2	5.7	0	0	0
	26.8	42	25.1	6.1	70.7	22.3	6.9	0	0	0
	25.2	41.4	26.3	7.1	64.6	26.4	8.9	0	0	0
	26.3	36.5	30.7	6.5	71.1	22.9	6	0	0	0
	22.8	34.7	35	7.4	63.8	28	8.2	0	0	0
	20.8	32.2	38.7	8.2	52.7	34.6	11	1.7	0	0
	19.4	30.8	39.3	10.6	43.8	40.4	13.1	2.7	0	0
	17	27.3	44.2	11.5	34	43.9	13.9	8.2	0	0
	14.7	24.3	47.1	13.8	29.6	37.5	12.7	20.1	0	0
	12.9	21.1	49.7	16.3	26.5	30.6	9.9	32.9	0	0
	17.2	23.5	44	15.3	44.1	3.7	3.8	47.3	1	0
	14.9	21.4	46.3	17.4	37.1	3.6	2.8	55.4	1	0
	13.2	18.4	49.9	18.5	32.7	4.6	2.8	58.8	1.1	0
	11.9	16.9	52.5	18.7	28.7	4.7	2.7	63	0.9	0
	10	14	55.8	20.2	25.5	4.1	3	66.6	0.8	0
	8.7	12.6	58	20.7	24.1	3.6	2.8	69.1	0.4	0
	7.4	11.6	59.1	21.8	22.2	3.7	3	70.7	0.4	0
	11.7	14.2	51.9	22.1	28.7	4.7	0.6	65.7	0.3	0
	10.9	12.8	52.4	23.9	25	4.9	1.7	67.6	0.8	0
	10.1	11.4	55.3	23.2	23.4	0.2	0	74.7	1.7	0
	8.7	10.3	57.2	23.8	19.7	0.2	0	78.5	1.6	0
	8.2	9.8	57.5	24.6	17.3	0.2	0	81.1	1.4	0
	6.4	8.4	59.9	25.3	12.8	0	0	83.0	0	4.2
	6.1	8.1	59.4	26.4	8.6	0	0	85.2	0	6.2
	0.1	0.1	67.6	32.2	0	0	0	80.9	0	19.1

A.6.5. AlCu$_2$-MgZn$_2$

Table A.8.: Results of the analysis of the AlCu$_2$-MgZn$_2$ series. The phase fractions are given in wt%.

Mg (at%)	Zn (at%)	Al (at%)	Cu (at%)	HV 0.01/5 (GPa)	σ(HV)	MgZn$_2$ hex. 04-008-7744	MgZn$_{11}$ cub. 04-007-1412	Al$_{0.25}$Cu$_{0.75}$ cub. 04-002-8292	Cu$_{0.2}$Zn$_{0.8}$ hex. 03-065-6066	MgCu$_{0.54}$Zn$_{1.46}$ hex. 04-001-5866	Mg$_2$Cu$_6$Al$_5$ cub. 04-009-9448	Al$_{0.8}$Cu$_{0.92}$ cub. 04-007-2997	AlCu$_{1.7}$ hex. 04-001-0976	Cu$_3$Zn$_8$ cub. 01-071-5803
41.53	55.77	2.6	0.1			49.7	50.3	0	0	0	0	0	0	0
42.31	54.83	2.82	0.05											
28.1	58.8	7.9	5.3	2.69	0.07	28.5	71.5	0	0	0	0	0	0	0
27.8	59	7.8	5.4											
27.3	58.8	8.1	5.9	2.80	0.06	28	72	0	0	0	0	0	0	0
27.2	57.9	8.4	6.5											
26.4	57.4	8.9	7.2			23	77	0	0	0	0	0	0	0
24.7	57.7	9.1	8.5											
24.3	53.5	12.8	9.4	2.91	0.07	15.2	84.8	0	0	0	0	0	0	0
26.1	45.3	13.1	15.5	2.81	0.30	0	64.1	0	13.2	22.4	0	0	0	0
24.1	44.7	13.7	17.5			0	64.1	0	14.3	10.1	0	0	0	0
22.8	42.5	15.9	18.8			0	64.8	0	15.1	19.7	0	0	0	0
21.6	40.4	17.3	20.8	2.29	0.38	0	63.5	0	20.3	16	0	0	0	0
20.5	37.4	19	23.1			0	61.3	0	26.3	12.1	0	0	0	0
19.1	33.4	21.4	26.1	2.90	0.36	0	52.7	17.7	22.8	6.9	0	0	0	0
16.6	29	24.4	30			0	45.8	29.5	18.9	5.9	0	0	0	0
19	30.4	21.5	29.1	2.91	0.13	0	3.6	45.7	15.1	35.6	0	0	0	0
16.9	26.7	23.6	32.8	2.47	0.29	0	3.9	51.3	6.7	38.1	0	0	0	0
14.7	25.2	24.2	35.9	2.65	0.20	0	8.9	51.1	2	38	0	0	0	0
13	22.2	26.8	38	3.16	0.09	0	3.2	70.7	1.5	24.7	0	0	0	0
11.2	20	28.6	40.2	3.28	0.04	0	0	77.4	0	0	7.7	1.3	2.6	7.5
10.6	16.8	29.7	42.9	4.27	0.14	0	0	66.3	0	0	12.1	3.6	9.9	6.2
8.1	14	33.2	44.7	4.75	0.21	0	0	56.8	0	0	13.4	4.7	18.9	3.7
9.9	12.3	30.9	46.9	4.59	0.18	0	0	31.4	0	0	12.7	11.7	33.7	10.3
8.6	11.3	31.7	48.4			0	0	25.3	0	0	12.4	28.7	28.1	5.3
8.6	10.5	31.8	49.1			0	0	19.7	0	0	13	33.8	29.6	3.8
7.7	8.5	33.1	50.7	4.89	0.27	0	0	12.4	0	0	10.4	47.1	27	3
7.6	7.8	33.6	51			0	0	4.5	0	0	9.6	48.5	34.3	3.1
7	6.6	34.5	51.9	4.96	0.20	0	0	2.2	0	0	11.2	46.9	38.2	1.5
6.4	5.8	35.8	52			0	0	0	0	0	8.4	29.7	58.9	1.7
4.97	8.91	35.17	50.95			0	0	0	0	0	11.6	36.8	51.6	0
3.54	7.36	35.59	53.51			0	0	0	0	0	9.4	18.8	71.7	0
3.28	7.49	37.2	52.03	4.82	0.14	0	0	0	0	0	8.8	13.5	77.6	0
3.3	6.14	37.09	53.46			0	0	0	0	0	6.9	13.1	80	0
2.97	5.33	37.63	54.07											
2.77	4.69	38.68	53.87	4.47	0.29									
2.66	4.11	39.1	54.13											
0	0	41.3	58.7			0	0	0	0	0	0	42.3	57.7	0
0	0	43.5	56.5											

A. Appendix

A.6.6. AlCuMgZn-Al

Table A.9.: Results of the analysis of the AlCuMgZn-Al series. The phase fractions are given in wt%.

pdf Code:	Mg (at%)	Zn (at%)	Al (at%)	Cu (at%)	HV 0.01/5 (GPa)	σ(HV)	Al cub. 04-016-2981	MgZn$_2$ hex. 01-074-5966	CuZn cub. 04-001-3151	Mg$_2$Cu$_6$Al$_5$ cub. 04-009-9448	CuAl$_2$ tetr. 04-007-0566	Al$_{4.2}$Cu$_{3.2}$Zn$_{0.7}$ rhomb. 01-073-8801
	18.1	22.6	28.9	30.5								
	17.4	22.8	28.2	31.6	5.27	0.34	0	18.1	18	62.5	0	0
	15.62	21.22	30.89	32.27	5.60	0.42	0	3.8	0.9	75.7	0	19.6
	16.84	21.4	30.3	31.45	6.25	0.35	0	5.2	0.4	75.6	1.1	17.6
	17.68	21.58	31.15	29.59	5.94	0.31	0	0.4	0.4	89.4	0	9.8
	17.18	21.2	32.54	29.08	5.90	0.25	0.4	0.2	0.3	90.5	0.3	8.3
	16.26	21.39	32.21	30.14	6.32	0.72	0.4	0.1	0	92	0.1	7.4
	16.64	20.11	34.47	28.78	5.24	0.29	0.2	0.1	0	89.5	0.3	9.9
	15.56	19.81	36.24	28.39	4.96	0.18	0.1	0	0	85.4	0.2	14.2
	16.9	19.8	37	26.3	4.44	0.62	0.4	0.7	0.3	94.7	3.9	0
	16.8	19.4	39.1	24.8	4.59	0.69	0.7	2.4	0.2	88.9	7.9	0
	15.5	18.2	41.7	24.6	4.49	0.71	1.4	2.4	0.3	87.9	8.1	0
	14.8	19.2	41.8	24.2	4.44	0.24	3.2	1.1	0.3	88.4	7	0
	11.7	15.5	54.5	18.4	4.58	0.57	3.7	1	0.3	86.9	8	0
	10.7	14.3	56.6	18.4	4.65	0.40	5.7	1.4	0.2	83.6	9	0
	10	13.4	58.7	17.9	3.87	0.32	8.5	2.7	0.1	76.3	12.5	0
	14.9	16.7	48.6	19.7	4.72	0.58	3.2	8.5	0.3	69.9	18.1	0
	14	15.9	50.6	19.4	4.46	0.41	6.3	9.7	0.3	64.3	19.4	0
	13.4	14.7	53.1	18.8	3.18	0.07	12.7	9.5	0	59.2	18.6	0
	11.8	13.5	57.9	16.8	2.93	0.06	20.2	7.4	0.4	59.4	12.6	0
	11.1	13.9	57.8	17.2	2.48	0.09	27.6	4.3	0.8	59.8	7.5	0
	8.6	10.4	67.7	13.3	2.32	0.20	32.7	3.2	1.3	59.3	3.6	0
	7.3	8.8	71.6	12.3	2.28	0.13	36.7	3	1.4	54.1	4.8	0
	10.5	9.8	69.8	9.8	1.78	0.20	45.1	16.5	0.9	37.6	0	0
	9.5	8.6	71.5	10.4			57	8.5	0.4	34	0	0
	8.6	7.7	73.5	10.1			64.9	5.2	0.2	29.8	0	0
	7.7	6.8	76.6	8.9	1.40	0.08	70.6	3.2	0	26.2	0	0
	6.5	6.1	80.3	7.1			73.6	1.6	0	24.8	0	0
	5.8	5.6	82	6.6			79.8	0.7	0	19.4	0	0
	5.6	4.9	83.5	6	1.10	0.06	85.6	0.1	0	14.3	0	0
	6.64	6.52	79.56	7.27	1.47	0.10	68.5	0.6	0	30.8	0	0
	5	5.53	83.1	6.37			73.2	0	0	25.1	1.6	0
	4.51	5.29	84.59	5.61			79.3	0.3	0	14.4	6.1	0
	3.86	4.28	87.86	4	1.08	0.05	85.9	0.4	0.1	6	7.5	0
	3.6	3.31	88.15	4.94			86.3	0.5	0.1	0	13	0
	2.98	2.97	90.96	3.09			88.8	1	0	0.2	9.9	0
	2.51	2.47	92.32	2.71	0.68	0.03	89.3	0.7	0	0.5	9.5	0
	0	0	100	0	0.55	0.02	100	0	0	0	0	0

A.6.7. **AlCuMgZn-Zn**

Table A.10.: Results of the analysis of the AlCuMgZn-Zn series. The phase fractions are given in wt%.

pdf Code:	Mg (at%)	Zn (at%)	Al (at%)	Cu (at%)	HV 0.01/5 (GPa)	σ(HV)	$Cu_{0.2}Zn_{0.8}$ hex. 03-065-6066	$Mg_2Zn_{11}/Mg_2Cu_6Al_5$ cub. 04-007-1412/04-009-9448	$MgZn_2$ hex. 01-074-7051	CuZn cub. 04-003-4270	Zn hex. 01-080-4436	ZnO hex. 01-070-2551
	17.11	23.94	27.7	31.25								
	17.12	24.02	26.95	31.91	4.96	0.43	3.3	38	25.1	30.2	0	0
	16.67	27.92	25.46	29.95	4.64	0.19	4.2	11.3	34.4	44.8	0	0
	17.26	29.2	23.55	29.99			5.1	17.9	31.8	40.7	0	0
	17.57	29.19	23.77	29.47			5.4	29.6	27.5	34.2	0	0
	16.98	31.06	23.13	28.83	4.22	0.08	4.8	38.9	23.1	28.5	0	0
	17.59	31.46	23.94	27.01			8.3	44.2	18.2	25.8	0	0
	17.01	33.43	22.71	26.85			16.3	44.7	15.2	21.7	0	0
	16.35	35.75	21.93	25.97	3.69	0.11	20.1	44.8	13	21.1	0	0
	18.76	30.4	25.56	25.28	3.99	0.15	5.2	58.5	14.6	20.9	0	0
	17.84	34.85	22.8	24.51			12.7	64	12.4	10.3	0	0
	17.89	36.83	21.86	23.42			23.5	66.4	5.9	3.8	0	0
	18	39.81	19.96	22.23	3.72	0.21	31	64.9	3.4	0.5	0	0
	17.44	42	19.63	20.93			34.4	62.4	1.9	0	0	0
	17.08	45.21	18.11	19.6			42.1	54.7	2.9	0	0	0
	16.43	49.87	15.48	18.22	2.74	0.14	45.8	50.9	3.1	0	0	0
	17.52	44.46	19.39	18.63	4.04	0.10	34.9	62.9	1.8	0	0	0
	17.66	47.14	17.88	17.32			34.1	62.4	3.2	0	0	0
	19.12	49.46	16.9	14.52			34.8	62.5	2.4	0	0	0
	16.99	50.03	17.24	15.74	3.38	0.18	48	49.1	2.6	0	0	0
	18.3	60.03	9.51	12.16			78.7	20.6	0.7	0	0	0
	22.01	58.55	9.1	10.35			83.9	13.4	2.7	0	0	0
	20.05	58.78	11.79	9.39	2.02	0.29	87.4	9.6	3	0	0	0
	18.91	61.8	12.39	6.91	1.09	0.12	70.6	3.7	4.3	0	21.4	0
	17.15	63.74	10.46	8.65			73.2	3.8	4	0	19	0
	12.1	72.79	8.8	6.31			69.8	2.7	4.6	0	22.9	0
	11.21	75.1	9.29	4.4	0.79	0.05	44.6	3.2	4.8	0	47.4	0
	8.53	78.61	8.92	3.95			36.2	2.9	4.9	0	56	0
	9.3	77.8	9.06	3.85			30.7	4.2	4.4	0	60.7	0
	8.7	79.43	8.36	3.51	0.48	0.02	27.6	4.4	6.1	0	61.9	0
	0	100	0	0	0.57	0.03	0	0	0	0	82	18

A.6.8. **AlCuMgZn-Mg**

Table A.11.: Results of the analysis of the AlCuMgZn-Mg series. The phase fractions are given in wt%.

pdf Code:	Mg (at%)	Zn (at%)	Al (at%)	Cu (at%)	HV 0.01/5 (GPa)	σ(HV)	MgZn$_2$ hex 01-074-5966	Mg hex. 04-015-0486	CuZn cub. 04-001-3151	Mg$_2$Zn$_{11}$/Mg$_2$Cu$_6$Al$_5$ cub. 04-007-1412/04-009-9448	MgCuAl rhomb. 04-007-2226
	16.29	21	26.91	35.8	5.62444	0.23455	22.7	0	57.9	19.5	0
	19.94	21.9	25.1	33.06	5.54528	0.21674	32.2	0	18.2	48.8	0.7
	28.73	17.43	26.09	27.75			31.5	0	15.2	52.3	1
	26.06	18.7	25.87	29.37			32.4	0	11.8	54.5	1.3
	28.1	17.51	26.32	28.07	5.64233	0.4607	36.2	0	4.4	58.6	0.8
	24.36	18.64	26.54	30.46			35.9	0	0	56.2	7.8
	27.93	19.07	24.64	28.36			40.3	0	0	52.8	6.9
	29.99	18.12	24.21	27.68	5.46839	0.28826	46.3	0	0	47	6.7
	30.31	17.39	25.46	26.84	4.31399	0.19268	48.4	0	0	43.8	7.8
	30.16	19.08	23.71	27.05	4.22327	0.12079	47.6	0	0	44.2	8.2
	30.01	18.96	24	27.03	5.26664	0.94745	51.4	0	0	42.3	6.3
	35.03	20.07	20.02	24.87	5.53592	0.53434	59.5	0	0	34.7	5.9
	36.71	17.66	21.36	24.26	5.94755	1.38927	71.8	0	0	21.8	6.4
	38.13	17.55	20.21	24.11	5.89765	0.70366	84	0	0	7	8.9
	43.96	15.88	18.29	21.86	6.28245	0.62624	67.4	0	0	0	32.3
	47.3	14.8	20.1	17.8	7.09603	1.37925	76	0.1	0	0	23.2
	53.8	13.5	16.4	16.3			62.9	0.1	0	0	36.3
	57.6	12.5	14.8	15.1			33.6	0.1	0	0	65.5
	64.8	9.9	13	12.3	5.05199	1.25014	4.2	0.1	0	0	84.4
	71.4	8	10.6	10			21.3	0.1	0	0	77.4
	72.1	7.6	10.7	9.6			45.7	1.4	0	0	49.6
	70.9	7.8	11.2	10.1	3.47777	0.42127	55.2	18.8	0	0	21.6
	69.63	8.65	12.27	9.45	4.22078	0.45184	16.2	0.4	0	0	80.3
	72.49	7.78	11.17	8.57			16.3	4.4	0	0	75.1
	69.46	8.91	11.67	9.96	2.4272	0.14654	14.8	12.5	0	0	67.1
	75.27	7.56	8.71	8.46	1.90213	0.15435	27.2	25.6	0	0	44.9
	74.8	6.94	10.08	8.16	1.77569	0.24403	41.7	35.3	0	0	19.2
	78.81	5.45	9.25	6.49	1.61652	0.05555	48.4	35.1	0	0	11.8
	80	5.42	8.32	6.26	1.35866	0.11364	44.9	40.8	0	0	10.4
	76.2	4.9	13.2	5.7	2.04006	0.01409	22.3	34.1	0	0	40.4
	83.5	4.2	7	5.3			29.8	43.9	0	0	18.5
	85.7	4	5.3	5			31.2	60	0	0	6.1
	88.1	3.4	4.4	4.1	1.89239	0.09303	27.4	66.6	0	0	3.3
	88	3.2	4.6	4.3			23.5	71.7	0	0	2.7
	91.1	2.3	3.6	3			17.8	78.1	0	0	2.8
	90.7	2.3	3.8	3.2	1.83772	0.24007	13.6	82.9	0	0	2.6
	100	0	0	0	0.35717	0.04722	0	100	0	0	0

A.6.9. AlMgZn-Cu

Table A.12.: Results of the analysis of the AlMgZn-Cu series. The phase fractions are given in wt%.

Mg (at%)	Zn (at%)	Al (at%)	Cu (at%)	HV 0.01/5 (GPa)	σ(HV)	Cu cub. 04-003-2430	MgCu$_{1.4}$Zn$_{0.6}$ cub. 04-020-8570	Al$_4$Cu$_9$ cub. 04-007-2997	Cu$_{0.57}$Zn$_{0.43}$ cub. 04-021-2017	Mg$_2$Cu$_6$Al$_5$ cub. 04-009-9448	Al cub. 01-071-4624	MgZn$_2$ hex. 00-034-0457
24.3	27.9	47.8	0									
24.1	28.2	47.7	0	1.08	0.17	0	0	0	0	0	24.1	75.9
20.37	30.23	41.35	8.05	2.78	0.14	0	0	0	0	35.8	15	49.1
20.29	29.52	41.48	8.72	2.86	0.22	0	0	0	0	37	13.9	49.1
19.9	30.34	40.28	9.48	2.85	0.18	0	0	0	0	41.6	12.9	45.5
20.1	29.46	38.83	11.61	3.31	0.21	0	0	0	0	48.3	11.3	40.4
19.87	28.54	37.7	13.9	3.41	0.11	0	0	0	0	56.4	9.6	33.9
20.01	27.88	37.04	15.06	3.36	0.15	0	0	0	0	67.4	7.1	25.5
19	28.08	35.11	17.82	3.87	0.21	0	0	0	0	79.2	5.2	15.6
19.8	27.45	34.48	18.27	4.14	0.58	0	0	0	0	85.5	0	14.5
21.14	27.37	32.48	19.01	3.93	0.53	0	0	0	0	90.1	0	9.9
20.54	26.81	31.9	20.75	4.09	0.21	0	0	0	0	96.7	0	3.3
20.52	26.64	29.52	23.32	4.76	0.34	0	0	0	0	98.6	0	1.4
19.04	24.78	28.92	27.26	4.50	0.24	0	0	0.2	6.1	93.6	0	0
18.46	24.39	27	30.16	5.31	0.19	0	0	0.3	33.8	43.5	0	22.2
17.75	23.67	25.19	33.39	6.08	0.64	0	0	15.7	50.1	3.4	0	30.6
19.96	25.47	24	30.57	3.88	0.10	0	0	0.9	38.8	29.6	0	27.3
19.53	24.79	23.93	31.74			0	0	1	40.6	27	0	28.1
21.15	23.65	21.98	33.21			0	0	7.4	47.3	11.5	0	30.8
23.34	22.15	22.28	32.23	3.85	0.13	0	0	39.3	29.2	0.3	0	30
21.4	21.79	18.34	38.47			0	0	70.3	5.2	0	0	23.4
19.78	18.23	18.92	43.07			0	0	79.8	0	0	0	18.1
19.97	16.67	15.41	47.95	3.34	0.41	0	0	83.5	0	0	0	16.1
13.2	13.7	18.1	55.1	3.76	0.61	35.9	8	56.1	0	0	0	0
12	12.1	16.5	59.5	3.54	0.42	66.4	3.1	30.5	0	0	0	0
12	10.8	12.6	64.6	2.60	0.42	92.5	0.5	7	0	0	0	0
11.9	8.9	10.4	68.8	1.74	0.05	100	0	0	0	0	0	0
10.7	7.7	7.8	73.7	1.94	0.22	100	0	0	0	0	0	0
10.2	7	6.9	76	1.93	0.21	100	0	0	0	0	0	0
8	5.6	6.6	79.8	1.74	0.15	100	0	0	0	0	0	0
10	6.5	9.7	73.8	1.74	0.14	100	0	0	0	0	0	0
9.9	5.6	8.6	75.8			100	0	0	0	0	0	0
9.1	4.6	7.3	78.9			100	0	0	0	0	0	0
7.3	4.2	6.5	82	1.76	0.15	100	0	0	0	0	0	0
6.4	3.5	6	84.1			100	0	0	0	0	0	0
3.7	3.1	5.8	87.4			100	0	0	0	0	0	0
2.7	2.8	5.3	89.1	1.44	0.09	100	0	0	0	0	0	0
0	0	0	100	0.77	0.04	100	0	0	0	0		

A.6.10. AlMgZn-Cr (350 °C)

Table A.13.: Results of the analysis of the AlMgZn-Cr series (heat treated at 350 °C). The phase fractions are given in wt%.

Mg (at%)	Zn (at%)	Al (at%)	Cr (at%)	HV 0.01/5 (GPa)	σ(HV)	MgZn$_2$ hex. 04-008-7744	Cr$_{0.78}$Al$_{0.22}$ cub. 04-020-3028	Cr$_2$Al tetr. 04-004-8635	Cr cub. 04-004-2650	Al cub. 04-022-7228	Cr$_5$Al$_8$ cub. 04-003-1320
22.42	30.19	35.84	11.55	4.61	0.21	84.6	0	5.8	0	0	9.4
24.28	30.48	34.15	11.09	5.77	0.37	86	0	4.6	0	0	9.2
23.34	29.39	34.36	12.91			83.5	0	4.6	0	0	11.8
22.34	29.24	33.45	14.97	4.74	0.32	77.5	0	5.1	0	0	17.3
20.74	27.9	34.25	17.11	5.13	0.32	70.9	0	6.3	0	0	22.6
18.95	26.5	34.52	20.03	5.05	0.15	66.9	0	9.1	0	0	23.8
17.34	26.07	32.72	23.87	5.55	0.25	63.6	0	15.4	0	0	20.7
16.94	24.73	30.76	27.57	5.39	0.14	53.7	0	24.1	0	0	21.8
15.69	23.91	28.6	31.8	4.73	0.19	46.5	0	38.1	0	0	14.8
16.42	21.64	23.87	38.07	4.23	0.34	30.8	10.3	50.8	0	0	7.1
15.96	16.34	23.79	43.9	3.64	0.22	15.1	15.8	60.7	0	0	7.5
15.33	18.15	20.5	46.02	2.76	0.13	11.3	12.2	62.3	6.4	0	7.9
12.34	15.93	19.25	52.48	2.31	0.11	10.8	16.8	39.6	19.5	0	2.4
9.13	15.97	16.91	57.99	1.78	0.17	11	32.2	26.5	30.2	0	
9.91	13.65	15.41	61.03	2.32	0.05	14	27.3	31.5	18.1	9.1	0
7.7	9.32	13.66	69.32	2.36	0.17	13.2	23.9	29.9	25.4	7.6	0
6.99	8.35	12.3	72.36	2.41	0.10	8.3	23.3	22.6	42.6	3.1	0
5.28	6.92	10.11	77.69	3.14	0.27	4.5	22	12.9	55.8	4.8	0
4.81	5.53	9.33	80.33	2.99	0.29	0	4.5	0	95.5	0	0
3.81	4.61	7.57	84	2.98	0.38	0	1.5	0	98.5	0	0
3.3	3.57	6.78	86.35	3.50	0.40	0	1.9	0	98.1	0	0
0	0	0	100	6.16	0.37	0	0	0	100	0	0

A.6.11. AlMgZn-Cr (430 °C)

Table A.14.: Results of the analysis of the AlMgZn-Cr series (heat treated at 430 °C). The phase fractions are given in wt%.

Mg (at%)	Zn (at%)	Al (at%)	Cr (at%)	HV 0.01/5 (GPa)	σ(HV)	MgZn$_2$ hex. 04-008-7744	Cr$_{0.78}$Al$_{0.22}$ cub. 04-020-3028	Cr$_2$Al tetr. 04-004-8635	Cr cub. 04-004-2650	Al cub. 04-022-7228	Cr$_5$Al$_8$ cub. 04-003-1320	Zn hex. 01-078-7026
22.4	31.2	34.9	11.6	4.18	0.24	82.9	0	1	0	0	16.1	0
21.8	31.9	32	14.2	4.17	0.39	85	0	0.7	0	0	14.3	0
23.2	29	35	12.8	5.29	0.49	75.2	0	0.4	0	0	24.4	0
22	27.3	35.7	15			67.6	0	0.3	0	0	32	0
19	25.3	37	18.7	5.54	0.50	59.8	0	0.4	0	0	39.8	0
19	26.7	34.1	20.1	5.34	0.31	56.7	0	1.1	0	0	42.2	0
18.2	27.2	30.6	24.1	5.17	0.08	51.7	0	12.7	0	0	35.6	0
17.5	24.6	28.3	29.6	5.36	0.54	41.3	1.2	45.4	0	0	12.2	0
17	23.9	25.4	33.7	4.45	0.48	42.3	1.2	45	0	0	11.6	0
18.1	21	22.6	38.2			34.3	5.9	59.8	0	0	0	0
18.2	12.8	23.6	45.4	4.10	0.36	13.7	8.1	78.2	0	0	0	0
15	17.9	19.9	47.2	2.84	0.17	15.2	12.2	64.3	8.4	0	0	0
10.4	15.3	18.6	55.7	2.63	0.08	11	28.1	36.2	24.7	0	0	0
9	15.2	15.7	60	1.91	0.10	8.7	33.2	22.8	35.3	0	0	0
10.4	8.6	17.4	63.5	2.52	0.03	0	37	30.1	26.2	6.7	0	0
8.8	7.3	14.7	69.2	2.78	0.08	0	52.6	17.2	30.3	0	0	0
7.2	6	12.7	74.1	2.65	0.24	0	46.9	0	53.1	0	0	0
6	6.5	11.1	76.5	2.56	0.25	0	25.3	0	74.7	0	0	0
5	6.4	9.7	79	2.92	0.51	0	9.7	2.6	87.3	0	0	0.4
4	5.9	7.8	82.4	4.19	0.38	0	9.8	2.6	87.6	0	0	0
3.1	6.9	6.7	83.3	3.76	0.53	0	11.7	0.2	78.7	0	0	9.4
0	0	0	100			0	0	0	100	0	0	0

A.6.12. AlCuMgZn-Cr (350 °C)

Table A.15.: Results of the analysis of the AlCuMgZn-Cr series (heat treated at 350 °C). The phase fractions are given in wt%.

Mg (at%)	Zn (at%)	Al (at%)	Cu (at%)	Cr (at%)	HV 0.01/5 (GPa)	σ(HV)	MgCu$_{0.8}$Zn$_{1.2}$ cub. 04-005-5214	Al$_3$Cr$_7$ cub. 03-065-6108	Al$_4$Cu$_9$ cub. 04-007-2997	(Al$_{37}$Mg$_3$)$_{0.1}$ cub. 01-077-6796	Cr$_{0.87}$Al$_{0.13}$ cub. 04-001-8491	Cu$_5$Zn$_8$ cub. 04-007-1117
15.86	19.76	27.12	32.52	4.73	5.82	0.45	28.6	0	63.7	0	0	6.7
16.73	19.88	26.75	31.39	5.26	6.88	0.27	32.2	0	60.6	0	0	7.3
16.88	20.36	25.07	31.45	6.24	6.15	0.51	36.2	0	55.5	0	0	8.4
16.82	19.63	26.39	30.12	7.05	5.43	0.85	41.1	0	50.1	0	0	8.8
17.61	19.64	25.81	29.87	7.08	6.74	0.47	39.3	11.8	43	0	0	5.9
16.32	19.05	25.66	28.94	10.03	6.40	0.26	38.2	19.2	38.1	0	0	4.5
15.96	18.84	24.37	28.85	11.99	6.81	1.40	35.3	26.1	35.3	0	0	3.3
14.29	18.15	24.59	26.74	16.23			27.4	48.7	17.4	1.9	4.6	0
13.81	17.68	22.81	25.82	19.87			30.7	48.4	15.7	0	5.2	0
13.73	16.61	21.88	24.13	23.65			27	60.9	1.2	0	10.8	0
14.46	15.6	20.44	22.82	26.69			21.1	66.2	0	0	12.7	0
13.57	14.73	17.78	21.83	32.09			8.4	72.4	0	0	19.2	0
10.62	13.87	16.31	19.01	38.52			2.5	72.1	0	0	25.4	0
8.87	12.35	15.27	19.01	44.49			3	65	0	0	32.1	0
14.91	13.55	16.98	16.95	37.61			16.1	63.7	0	0	20.2	0
11.64	12.89	15.42	16.06	44			4.1	65.1	0	0	30.8	0
9.22	11.61	14.05	14.68	50.44			3.6	51.5	0	0	45	0
7.46	10.16	11.92	13.66	56.81			2.5	41.8	0	0	55.7	0
5.31	8.83	10.02	12.02	63.82			1.2	29.9	0	0	68.9	0
4.38	7.61	9.33	10.96	67.71			1.4	26.8	0	0	71.8	0
3.58	6.31	8.01	9.31	72.78			0.7	27	0	0	72.3	0
17.92	17.25	22.9	25.92	16	6.92	0.21						
14.52	17.39	23.17	25.68	19.24	6.56	1.51						
14.37	16.54	21.44	24.64	23	6.92	0.53						
14.58	15.41	19.78	22.8	27.42	7.42	0.81						
13.22	14.77	17.95	21.44	32.63	8.30	0.65						
11.24	13.71	15.85	20.7	38.51	6.20	0.28						
8.56	12.58	14.81	19.23	44.82	5.80	0.71						
15.68	12.93	17.21	17	37.19	5.68	0.49						
12.43	12.21	14.63	15.77	44.96	4.18	0.05						
9.71	11.28	13.47	14.91	50.63	4.65	0.71						
7.68	9.99	12.32	13.76	56.25	4.99	0.66						
5.75	7.98	9.15	10.7	66.42	5.18	0.79						
4.03	7.88	9.37	11.62	67.1	4.96	1.34						
3.94	6.46	8.64	9.95	71.01	5.33	0.46						

A.6.13. **AlCuMgZn-Ti**

Table A.16.: Results of the analysis of the AlCuMgZn-Ti series. The phase fractions are given in wt%.

pdf Code:	Mg (at%)	Zn (at%)	Al (at%)	Cu (at%)	Ti (at%)	HV 0.01/5 (GPa)	σ(HV)	MgCuZn cub. 04-002-1278	Al$_4$Cu$_9$ cub. 04-007-2997	AlCu$_2$Ti cub. 03-065-0485	(Al$_{2.5}$Cu$_{0.5}$))Ti cub. 01-077-8150	Ti hex. 00-001-1198
	17.42	20.96	27.1	30.27	4.26	4.91	0.41	30.8	54.6	0	14.6	0
	18.29	21.04	27.22	28.67	4.79	5.61	0.43	31.9	53.1	0	15	0
	17.82	21.52	25.67	29.35	5.64	5.60	0.44	32.9	49.6	0	17.5	0
	17.93	20.85	26.23	28.43	6.55	4.89	0.34	34.8	42.2	0	23	0
	16.74	21.15	25.7	27.85	8.56	6.12	1.17	35.3	36.7	0	28	0
	15.53	20.36	26.58	27.77	9.77	4.95	0.69	31.9	34.8	0	33.3	0
	14.42	19.8	25.29	28.46	12.03	5.69	0.79	30.9	30.4	0	38.7	0
	15.1	21.8	25.86	26.1	11.15	5.62	0.34	38.7	22.4	0.1	38.8	0
	14.54	21.28	24.83	25.28	14.07	5.62	0.37	37.5	14.7	2.4	45.4	0
	13.74	20.65	23.76	24.53	17.32	5.57	0.72	34.5	6	11.5	48.1	0
	12.91	19.64	23.04	23.77	20.64	6.27	0.21	30.4	1	22.6	46	0
	11.52	18.54	21.84	22.87	25.23	6.14	0.22	25.4	0	33.6	41	0
	9.41	17.86	18.65	22.67	31.42	6.80	0.30	21.2	0	43.4	35.3	0
	8.12	15.35	18.56	20.55	37.42	6.66	0.34	15.2	0	59.1	25.7	0
	20.85	15.95	21.33	16.81	25.05	4.76	0.93	46.6	0	8.2	45.2	0
	18.51	15.13	19	14.85	32.51	4.96	0.33	37	0	17.7	45.3	0
	16.45	13.83	16.7	14.06	38.96	4.59	0.41	27.2	0	25.5	47.3	0
	13.77	12.47	16.38	14.43	42.95	4.49	0.07	19.6	0	34	43.4	3
	10.99	10.55	13.58	14.4	50.49	5.08	0.87	17.1	0	43.7	29.2	10
	9.14	10.34	13.2	14.12	53.2	5.27	0.46	9.2	0	48.4	27.4	15.1
	6.35	10.24	13.69	14.77	54.95	6.78	0.75	0	0	41.4	31	27.6

A.6.14. AlZnSi-Cu

Table A.17.: Results of the analysis of the AlZnSi-Cu series. The phase fractions are given in wt%.

pdf Code:	Si (at%)	Zn (at%)	Al (at%)	Cu (at%)	HV 0.01/5 (GPa)	σ(HV)	Cu cub. 01-070-3039	$Cu_{0.83}Au$ Sloss. hex. 04-017-5016	Al_xCu_9 cub. 03-065-3347	Si cub. 04-014-8844	Cu_7Si_3 hex. 04-014-4306	$Cu_{60}Zn_{40.35}$ cub. 04-001-3150	$Cu_{0.83}Si_{0.17}$ cub. 04-014-4308	Al_2Cu tetr. 01-074-7042	Al cub. 04-001-8743	Zn hex. 01-078-7028	$Al_{1.2}Cu_{0.8}Zn_{0.7}$ rhomb. 04-009-7047	Cu_xZn_8 cub. 04-005-1988	$Cu_{3.75}Al_{15}$ orthorhomb. 04-012-4340
	33.82	5.81	44.55	15.83	4.04	0.16	0	0	0	24.9	0	0	0	19	10.1	5.3	40.7	0	0
	34.46	5.59	43.49	16.46	4.70	0.10	0	0	0	23.4	0	0	0	11.1	6.1	5.2	54.3	0	0
	33.59	6	41.74	18.67	5.07	0.33	0	0	0	21.3	0	0	0	8	3.4	4.9	62.4	0	0
	32.53	6.48	42.92	18.07	3.67	0.21	0	0	0.1	20	0	0	0	3.2	1.4	2.4	73.1	0	0
	29.65	6	35.67	28.68	2.49	0.31	0	0	5.1	17.8	0	0	0	3.7	0	0	69.7	0	8.6
	29.58	5.64	32.99	31.79	1.77	0.10	0	0	17.7	14.8	0	0	0	4.6	0	0	25	0	50.1
	27.02	5.47	31.57	35.94	1.60	0.05	0	0	0	11.7	0	0	0	4.6	0	0	9.3	0	55.6
	22.71	4.77	28.23	44.3	2.09	0.05	0	0	60.8	7	0	0	0	0.4	0	0	0	0	31.6
	21.02	3.93	27.3	47.73	2.61	0.07	0	0	66.2	6.7	0	0	0	0.4	0	0	0	0	26.6
	16.73	3.55	22.96	56.77	3.55	0.08	0	0	76.5	3.8	0	0	0	2.9	0	0	0	0	16.8
	13.96	2.9	19.73	63.4	4.59	0.20	0	0	77.7	0.4	21.2	0.7	0	0	0	0	0	0	0
	11.68	2.65	16.12	69.55	4.46	0.24	0	0	64.5	2.8	31.1	1.6	0	0	0	0	0	0	0
	10.53	2.1	14.02	73.36	2.90	0.11	0	0	36.7	6.1	29.6	16.7	10.8	0	0	0	0	0	0
	8.61	1.57	12.22	77.59	2.53	0.06	0	0	5.5	4.4	0	41.9	48.2	0	0	0	0	0	0
	13.19	3.03	19.91	63.87	4.24	0.15	0	0	82.7	0	17.3	0	0	0	0	0	0	0	0
	11.29	2.69	16.39	69.62	4.21	0.22	0	0	63.3	0	27.8	0	5	0	0	0	0	3.9	0
	10.22	1.98	14.28	73.52	3.21	0.07	12.5	16.5	26.4	0	30	0	7	0	0	0	0	7.7	0
	8.11	1.73	11.67	78.48	2.26	0.08	30.6	27.7	7.2	0	12.1	0	18.4	0	0	0	0	4.1	0
	6.35	1.43	9.61	82.61	1.76	0.07	52.3	23.2	5	0	4.4	0	24.7	0	0	0	0	8.1	0
	5.37	1.26	8.48	84.89	1.57	0.07	80.7	19.3	4.9	0	4.5	0	14.5	0	0	0	0	0.5	0
	4.12	0.99	7.12	87.78	1.42	0.09	88.5	11.5	0	0	0	0	0	0	0	0	0	0	0
	6.87	1.46	12.01	79.67	1.73	0.19	68.4	31.6	0	0	0	0	0	0	0	0	0	0	0
	4.49	1.04	7.36	87.1	2.08	0.09	79.9	20.1	0	0	0	0	0	0	0	0	0	0	0
	3.5	0.82	6.43	89.25	1.95	0.14	97.2	2.8	0	0	0	0	0	0	0	0	0	0	0
	3.18	0.75	5.93	90.14	1.88	0.10	98.6	1.4	0	0	0	0	0	0	0	0	0	0	0
	2.26	0.47	4.31	92.95	1.73	0.07	98.2	1.8	0	0	0	0	0	0	0	0	0	0	0
	2.15	0.59	4.58	92.68	1.68	0.08	100	0	0	0	0	0	0	0	0	0	0	0	0
	1.58	0.38	3.8	94.24	1.59	0.05	100	0	0	0	0	0	0	0	0	0	0	0	0

A.6.15. AlZnSi-Cr

Table A.18.: Results of the analysis of the AlZnSi-Cr series. The phase fractions are given in wt%.

pdf Code:	Si (at%)	Zn (at%)	Al (at%)	Cr (at%)	HV 0.01/5 (GPa)	σ(HV)	Cr cub. 04-002-9097	Cr cub. II 04-004-8467	CrSi_2 hex. 01-073-6046	CrAl_0.422Si_1.578 hex. 04-007-8574	Zn hex. 04-005-9306
	26.8	6.5	33.97	32.73	5.09	0.14	23.9	1.6	13.4	55.1	6.1
	25.44	6.31	32.03	36.23	6.65	0.81	38.2	1.5	16.1	36.8	7.3
	21.44	5.87	29.05	43.65	7.56	0.62	54.5	1.3	10.4	24.8	9.1
	20.38	4.51	25.43	49.69	10.74	0.84	65.3	0.9	9	16.1	8.7
	17.06	4.14	22.14	56.66	8.42	0.51	73.3	0.7	5.8	11.8	8.4
	16.76	3.94	21.71	57.59	6.88	0.43	63.7	10.7	7.3	11	7.4
	14.92	3.86	19.85	61.37	5.64	0.34	51.5	22.8	7.4	10.6	7.7

A.6.16. AlZnSi-Mg

Table A.19.: Results of the analysis of the AlZnSi-Mg series. The phase fractions are given in wt%.

pdf Code:	Si (at%)	Zn (at%)	Al (at%)	Mg (at%)	HV 0.01/5 (GPa)	σ(HV)	Al cub. 01-078-5052	Zn hex. 01-078-7031	Si cub. 04-006-2527	Mg$_2$Si cub. 00-035-0773	MgZn$_2$ hex. 04-003-2083	Mg$_4$AlSi$_4$ tetr. 04-020-3392	Mg$_{17}$Al$_{12}$ cub. 04-014-7592	Mg hex. 04-017-4914
	21.27	5.27	27.09	46.27	2.09	0.11	27.3	6.7	7.2	56	2.7	0	0	0
	18.31	5.97	22.26	53.47	2.25	0.12	24.8	5.2	2.1	63.2	4.7	0	0	0
	16.38	4.57	21.46	57.59	3.23	0.29	23.4	2.3	0.9	65.5	3.9	4.1	0	0
	15.22	4.29	19.2	61.29	2.47	0.13	3.1	0.3	0.1	54.6	1	15.3	20.5	5.1
	15.57	4.06	17.64	62.73	2.13	0.12	0	0.2	0.1	51.1	0.4	11.3	34.5	2.3
	13.01	2.4	13.33	71.26	1.52	0.19	0	0.6	0.1	52	1.7	0	43.6	2
	8.35	2	10.1	79.56	1.11	0.08	0	0.2	0.1	42.6	0.9	0	37.9	18.2

A.7. Temperature Calibrations

Thermal factors during the production and post-treatment of alloys are largely responsible for their properties. Therefore, the exact determination and control of the temperature are essential. The geometry of the experimental setup and the design as well as the positioning of the temperature sensors and the heating cartridge, required calibration in order to accurately estimate the sample temperature. The heating cartridges/temperature sensors employed were obtained from the company *Heinz Stegmeier*. Cartridges of the type *HS 10 315 W* were used. For the exact measurement of the surface temperature, a temperature sensor (type k) was clamped on a glass substrate and fixed in the substrate holder. Subsequently, different temperatures were set using the *Eurotherm 3216* temperature controller and compared to the actual temperatures measured on the substrate. The results of these comparisons for the substrate holder used for sample preparation and the one used for thermal post-treatment are shown in Fig. A.1.

Linear fitting of the data points was performed to know the desired temperatures for the whole range. The correlations between the controller temperature $T_{controller}$ and the substrate surface temperature are:

$$T_{substrate} = 0.7096 \cdot T_{controller} + 18.096 \tag{A.21}$$

a)

b)
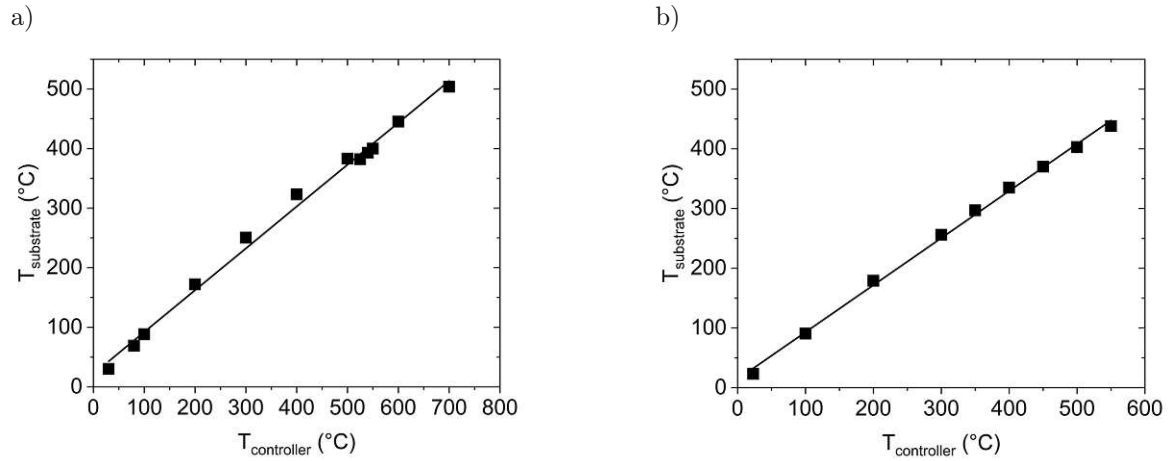
Figure A.1.: Comparison of the set temperature at the controller and the measured value at the sample surface for a) the substrate holder used for the deposition experiments and b) the substrate holder used for the thermal post-treatment. The lines represent the linear fits of the data points (compare eq. (A.21) and eq. (A.22)).

for the substrateholder in the sputtering setup and

$$T_{substrate} = 0.7879 \cdot T_{controller} + 14.21 \tag{A.22}$$

for the substrate holder used for the thermal post-treatment. The temperatures have the units of °C.

Bibliography

[1] N. K. Kumar, C. Li, K. Leonard, H. Bei, and S. Zinkle, "Microstructural stability and mechanical behavior of FeNiMnCr high entropy alloy under ion irradiation," *Acta Mater.*, vol. 113, pp. 230–244, 2016.

[2] E. Schubert, M. Klassen, I. Zerner, C. Walz, and G. Sepold, "Light-weight structures produced by laser beam joining for future applications in automobile and aerospace industry," *Journal of Materials Processing Technology*, vol. 115, no. 1, pp. 2–8, 2001.

[3] L. Cheah, "Cars on a diet: The material and energy impacts of passenger vehicle weight reduction in the US," Ph.D. dissertation, Massachusetts Institute of Technology, 2010.

[4] C. E. Scott, "Aluminium sheet for autobody construction," *Matériaux & Techniques*, vol. 83, no. 10-11, pp. 21–27, 1995.

[5] W. S. Miller, L. Zhuang, J. Bottema, A. J. Wittebrood, P. De Smet, A. Haszler, and A. Vieregge, "Recent development in aluminium alloys for the automotive industry," *Materials Science and Engineering A*, vol. 280, no. 1, pp. 37–49, 2000.

[6] D. B. Miracle and O. N. Senkov, "A critical review of high entropy alloys and related concepts," *Acta Materialia*, vol. 122, pp. 448–511, 2017.

[7] J. W. Yeh, S. K. Chen, S. J. Lin, J. Y. Gan, T. S. Chin, T. T. Shun, C. H. Tsau, and S. Y. Chang, "Nanostructured high-entropy alloys with multiple principal elements: Novel alloy design concepts and outcomes," *Advanced Engineering Materials*, vol. 6, no. 5, pp. 299–303, 2004.

[8] J. W. Yeh, "Recent progress in high-entropy alloys," *Annales de Chimie: Science des Materiaux*, vol. 31, no. 6, pp. 633–648, 2006.

[9] J. W. Yeh, Y. L. Chen, S. J. Lin, and S. K. Chen, "High-entropy alloys – a new era of exploitation," *Advanced Structural Materials III*, vol. 560, pp. 1–9, 2007.

[10] A. Mehta and Y. Sohn, "High Entropy and Sluggish Diffusion "core" Effects in Senary FCC Al-Co-Cr-Fe-Ni-Mn Alloys," *ACS Combinatorial Science*, vol. 22, no. 12, pp. 757–767, 2020.

[11] S. Guo and C. T. Liu, "Phase stability in high entropy alloys: Formation of solid-solution phase or amorphous phase," *Progress in Natural Science: Materials International*, vol. 21, no. 6, pp. 433–446, 2011.

[12] O. N. Senkov, J. M. Scott, S. V. Senkova, D. B. Miracle, and C. F. Woodward, "Microstructure and room temperature properties of a high-entropy TaNbHfZrTi alloy," *Journal of Alloys and Compounds*, vol. 509, no. 20, pp. 6043–6048, 2011.

[13] X. Yang, Y. Zhang, and P. K. Liaw, "Microstructure and compressive properties of NbTiVTaAlx high entropy alloys," *Procedia Engineering*, vol. 36, pp. 292–298, 2012.

[14] L. Lilensten, J. P. Couzinié, L. Perrière, J. Bourgon, N. Emery, and I. Guillot, "New structure in refractory high-entropy alloys," *Materials Letters*, vol. 132, pp. 123–125, 2014.

[15] B. Gludovatz, A. Hohenwarter, D. Catoor, E. H. Chang, E. P. George, and R. O. Ritchie, "A fracture-resistant high-entropy alloy for cryogenic applications," *Science*, vol. 345, no. 6201, pp. 1153–1158, 2014.

[16] "Scopus - Web of Science," 2021. [Online]. Available: https://www.scopus.com/ (Accessed 2022-02-13).

[17] X. Yang and Y. Zhang, "Prediction of high-entropy stabilized solid-solution in multi-component alloys," *Materials Chemistry and Physics*, vol. 132, no. 2-3, pp. 233–238, 2012.

[18] Y. F. Ye, Q. Wang, J. Lu, C. T. Liu, and Y. Yang, "Design of high entropy alloys: A single-parameter thermodynamic rule," *Scripta Materialia*, vol. 104, pp. 53–55, 2015.

[19] ——, "The generalized thermodynamic rule for phase selection in multicomponent alloys," *Intermetallics*, vol. 59, pp. 75–80, 2015.

[20] S. Guo, C. Ng, J. Lu, and C. T. Liu, "Effect of valence electron concentration on stability of fcc or bcc phase in high entropy alloys," *Journal of Applied Physics*, vol. 109, no. 10, 2011.

[21] A. Takeuchi, K. Amiya, T. Wada, K. Yubuta, W. Zhang, and A. Makino, "Entropies in alloy design for high-entropy and bulk glassy alloys," *Entropy*, vol. 15, no. 9, pp. 3810–3821, 2013.

[22] S. Guo, Q. Hu, C. Ng, and C. T. Liu, "More than entropy in high-entropy alloys: Forming solid solutions or amorphous phase," *Intermetallics*, vol. 41, pp. 96–103, 2013.

[23] D. B. Miracle, J. D. Miller, O. N. Senkov, C. Woodward, M. D. Uchic, and J. Tiley, "Exploration and development of high entropy alloys for structural applications," *Entropy*, vol. 16, no. 1, pp. 494–525, 2014.

[24] C. Zhang and M. C. Gao, "CALPHAD modeling of high-entropy alloys," in *High-Entropy Alloys: Fundamentals and Applications.* Springer, Cham, 2016, pp. 399–444.

[25] W. Kohn and L. J. Sham, "Self-consistent equations including exchange and correlation effects," *Physical Review*, vol. 140, no. 4A, p. A1133, 1965.

[26] M. Gao and D. Alman, "Searching for Next Single-Phase High-Entropy Alloy Compositions," *Entropy*, vol. 15, no. 12, pp. 4504–4519, 2013.

[27] R. Hummel, *Understanding Materials Science: History, Properties, Applications*, 2nd ed. Springer, 2004.

[28] S. Ranganathan, "Alloyed pleasures: Multimetallic cocktails," *Current Science*, vol. 85, no. 10, pp. 1404–1406, 2003.

[29] B. S. Murty, J. W. Yeh, and S. Ranganathan, *High-Entropy Alloys.* Elsevier Science, 2014.

[30] W. Hume-Rothery and G. V. Raynor, *The structure of metals and alloys*, 3rd ed., ser. Monograph and report series / Institute of Metals. London: Inst. of Metals, 1954.

[31] W. Hume-Rothery, *Atomic theory for students of metallurgy*, 4th ed., ser. Monograph and report series / Institute of Metals. London: Institute of Metals, 1962.

[32] W. Hume-Rothery, G. W. Mabbott, and K. M. Channel Evans, "The freezing points, melting points, and solid solubility limits of the alloys of sliver and copper with the elements of the B sub-groups," *Philosophical Transactions of the Royal Society of London. Series A*, vol. 233, no. 721, pp. 1–97, 1934.

[33] J. W. Yeh, "Physical metallurgy," in *High-Entropy Alloys: Fundamentals and Applications.* Springer, Cham, 2016, pp. 51–113.

[34] W. Smith and J. Hashemi, *Foundations of Materials Science and Engineering*, ser. McGraw-Hill series in materials science and engineering. McGraw-Hill, 2006.

[35] D. A. Goodman, L. H. Bennett, and R. E. Watson, "Valency effects and relative solubilities in transition metal alloys," *Scripta Metallurgica*, vol. 17, no. 1, pp. 91–96, 1983.

[36] M. A. White, *Physical properties of materials*, 2nd ed. Boca Raton, Fla. [u.a.]: CRC Press, 2012.

[37] B. Cantor, K. Kim, and P. J. Warren, "Novel Multicomponent Amorphous Alloys," *Journal of Metastable and Nanocrystalline Materials*, vol. 13, pp. 27–32, 2002.

[38] B. Cantor, I. T. Chang, P. Knight, and A. J. Vincent, "Microstructural development in equiatomic multicomponent alloys," *Materials Science and Engineering A*, vol. 375-377, pp. 213–218, 2004.

[39] T. K. Chen, M. S. Wong, T. T. Shun, and J. W. Yeh, "Nanostructured nitride films of multi-element high-entropy alloys by reactive DC sputtering," *Surface and Coatings Technology*, vol. 200, no. 5-6, pp. 1361–1365, 2005.

[40] C. Y. Hsu, J. W. Yeh, S. K. Chen, and T. T. Shun, "Wear resistance and high-temperature compression strength of Fcc CuCoNiCrAl0.5Fe alloy with boron addition," *Metallurgical and Materials Transactions A: Physical Metallurgy and Materials Science*, vol. 35 A, no. 5, pp. 1465–1469, 2004.

[41] P. K. Huang, J. W. Yeh, T. T. Shun, and S. K. Chen, "Multi-principal-element alloys with improved oxidation and wear resistance for thermal spray coating," *Advanced Engineering Materials*, vol. 6, no. 1-2, pp. 74–78, 2004.

[42] J. W. Yeh, S. K. Chen, J. Y. Gan, S. J. Lin, T. S. Chin, T. T. Shun, C. H. Tsau, and S. Y. Chang, "Formation of simple crystal structures in Cu-Co-Ni-Cr-Al-Fe-Ti-V alloys with multiprincipal metallic elements," *Metallurgical and Materials Transactions A: Physical Metallurgy and Materials Science*, vol. 35 A, no. 8, pp. 2533–2536, 2004.

[43] R. Swalin, *Thermodynamics of Solids.* John Wiley & Sons, 1972.

[44] I. A. Tomilin and S. D. Kaloshkin, "High entropy alloys - semi-impossible regular solid solutions?" *Materials Science and Technology*, vol. 31, no. 10, pp. 1231–1234, 2015.

[45] B. Fultz, "Vibrational thermodynamics of materials," *Progress in Materials Science*, vol. 55, no. 4, pp. 247–352, 2010.

[46] F. Otto, Y. Yang, H. Bei, and E. P. George, "Relative effects of enthalpy and entropy on the phase stability of equiatomic high-entropy alloys," *Acta Materialia*, vol. 61, no. 7, pp. 2628–2638, 2013.

[47] Y. F. Ye, Q. Wang, J. Lu, C. T. Liu, and Y. Yang, "High-entropy alloy: challenges and prospects," *Materials Today*, vol. 19, no. 6, pp. 349–362, 2016.

[48] S. M. Liang and R. Schmid-Fetzer, "Evaluation of Calphad Approach and Empirical Rules on the Phase Stability of Multi-principal Element Alloys," *Journal of Phase Equilibria and Diffusion*, vol. 38, no. 4, pp. 369–381, 2017.

[49] K. Zhang and Z. Fu, "Effects of annealing treatment on phase composition and microstructure of CoCrFeNiTiAlx high-entropy alloys," *Intermetallics*, vol. 22, pp. 24–32, 2012.

[50] Y. Zhang, T. T. Zuo, Z. Tang, M. C. Gao, K. A. Dahmen, P. K. Liaw, and Z. P. Lu, "Microstructures and properties of high-entropy alloys," *Progress in Materials Science*, vol. 61, no. October 2013, pp. 1–93, 2014.

[51] D. A. Porter, K. E. Easterling, and M. Y. Sherif, *Phase transformations in metals and alloys*, 3rd ed. Boca Raton, Fla. [u.a.]: CRC Press, 2009.

[52] T. B. Massalski, "Phase diagrams in materials science," *Metallurgical Transactions A*, vol. 20, no. 8, pp. 1295–1323, 1989.

[53] D. G. Pettifor, "Phenomenology and theory in structural prediction," *Journal of Phase Equilibria*, vol. 17, no. 5, pp. 384–395, 1996.

[54] M. De Graef and M. E. McHenry, *Structure of materials : an introduction to crystallography, diffraction, and symmetry*, 2nd ed. Cambridge [u.a.]: Cambridge Univ. Press, 2012.

[55] J. W. Yeh, S. Y. Chang, Y. D. Hong, S. K. Chen, and S. J. Lin, "Anomalous decrease in X-ray diffraction intensities of Cu-Ni-Al-Co-Cr-Fe-Si alloy systems with multi-principal elements," *Materials Chemistry and Physics*, vol. 103, no. 1, pp. 41–46, 2007.

[56] K. Y. Tsai, M. H. Tsai, and J. W. Yeh, "Sluggish diffusion in Co-Cr-Fe-Mn-Ni high-entropy alloys," *Acta Materialia*, vol. 61, no. 13, pp. 4887–4897, 2013.

[57] Y. Zhang, Y. J. Zhou, J. P. Lin, G. L. Chen, and P. K. Liaw, "Solid-solution phase formation rules for multi-component alloys," *Advanced Engineering Materials*, vol. 10, no. 6, pp. 534–538, 2008.

[58] Y. F. Kao, S. K. Chen, T. J. Chen, P. C. Chu, J. W. Yeh, and S. J. Lin, "Electrical, magnetic, and Hall properties of AlxCoCrFeNi high-entropy alloys," *Journal of Alloys and Compounds*, vol. 509, no. 5, pp. 1607–1614, 2011.

[59] O. N. Senkov, G. B. Wilks, D. B. Miracle, C. P. Chuang, and P. K. Liaw, "Refractory high-entropy alloys," *Intermetallics*, vol. 18, no. 9, pp. 1758–1765, 2010.

[60] C.-J. Tong, Y.-L. Chen, J.-W. Yeh, S.-J. Lin, S.-K. Chen, T.-T. Shun, C.-H. Tsau, and S.-Y. Chang, "Microstructure characterization of Al_xCoCrCuFeNi high-entropy alloy system with multiprincipal elements," *Metallurgical and Materials Transactions A*, vol. 36, no. 4, pp. 881–893, 2005.

[61] C. W. Tsai, Y. L. Chen, M. H. Tsai, J. W. Yeh, T. T. Shun, and S. K. Chen, "Deformation and annealing behaviors of high-entropy alloy Al0.5CoCrCuFeNi," *Journal of Alloys and Compounds*, vol. 486, no. 1-2, pp. 427–435, 2009.

[62] C. Y. Hsu, C. C. Juan, W. R. Wang, T. S. Sheu, J. W. Yeh, and S. K. Chen, "On the superior hot hardness and softening resistance of AlCoCrxFeMo0.5Ni high-entropy alloys," *Materials Science and Engineering A*, vol. 528, no. 10-11, pp. 3581–3588, 2011.

[63] O. N. Senkov, G. B. Wilks, J. M. Scott, and D. B. Miracle, "Mechanical properties of Nb25Mo25Ta 25W25 and V20Nb20Mo 20Ta20W20 refractory high entropy alloys," *Intermetallics*, vol. 19, no. 5, pp. 698–706, 2011.

[64] M.-H. Tsai, C.-W. Wang, C.-W. Tsai, W.-J. Shen, J.-W. Yeh, J.-Y. Gan, and W.-W. Wu, "Thermal Stability and Performance of NbSiTaTiZr High-Entropy Alloy Barrier for Copper Metallization," *Journal of The Electrochemical Society*, vol. 158, no. 11, p. H1161, 2011.

[65] M. H. Tsai, J. W. Yeh, and J. Y. Gan, "Diffusion barrier properties of AlMoNbSiTa-TiVZr high-entropy alloy layer between copper and silicon," *Thin Solid Films*, vol. 516, no. 16, pp. 5527–5530, 2008.

[66] T. T. Shun, C. H. Hung, and C. F. Lee, "Formation of ordered/disordered nanoparticles in FCC high entropy alloys," *Journal of Alloys and Compounds*, vol. 493, no. 1-2, pp. 105–109, 2010.

[67] W. H. Liu, Y. Wu, J. Y. He, T. G. Nieh, and Z. P. Lu, "Grain growth and the Hall-Petch relationship in a high-entropy FeCrNiCoMn alloy," *Scripta Materialia*, vol. 68, no. 7, pp. 526–529, 2013.

[68] C. C. Juan, C. Y. Hsu, C. W. Tsai, W. R. Wang, T. S. Sheu, J. W. Yeh, and S. K. Chen, "On microstructure and mechanical performance of AlCoCrFeMo 0.5Nix high-entropy alloys," *Intermetallics*, vol. 32, pp. 401–407, 2013.

[69] E. J. Pickering and N. G. Jones, "High-entropy alloys: a critical assessment of their founding principles and future prospects," *International Materials Reviews*, vol. 61, no. 3, pp. 183–202, 2016.

[70] T. Saito, T. Furuta, J. H. Hwang, S. Kuramoto, K. Nishino, N. Suzuki, R. Chen, A. Yamada, K. Ito, Y. Seno, T. Nonaka, H. Ikehata, N. Nagasako, C. Iwamoto, Y. Ikuhara, and T. Sakuma, "Multifunctional alloys obtained via a dislocation-free plastic deformation mechanism," *Science*, vol. 300, no. 5618, pp. 464–467, 2003.

[71] J. W. Yeh, "Alloy design strategies and future trends in high-entropy alloys," *JOM*, vol. 65, no. 12, pp. 1759–1771, 2013.

[72] G. A. Mansoori, N. F. Carnahan, K. E. Starling, and T. W. Leland, "Equilibrium thermodynamic properties of the mixture of hard spheres," *The Journal of Chemical Physics*, vol. 54, no. 4, pp. 1523–1526, 1971.

[73] T. B. Massalski, "Comments concerning some features of phase diagrams and phase transformations," *Materials Transactions*, vol. 51, no. 4, pp. 583–596, 2010.

[74] M. G. Poletti and L. Battezzati, "Electronic and thermodynamic criteria for the occurrence of high entropy alloys in metallic systems," *Acta Materialia*, vol. 75, pp. 297–306, 2014.

[75] O. N. Senkov and D. B. Miracle, "A new thermodynamic parameter to predict formation of solid solution or intermetallic phases in high entropy alloys," *Journal of Alloys and Compounds*, vol. 658, pp. 603–607, 2016.

[76] C. Simson, "Compositionally Complex Alloys im Bereich niedriger Dichten – experimentelle und thermodynamische Betrachtungen," *9. Ranshofener Leichtmetalltage*, p. 7, 2016.

[77] M. C. Troparevsky, J. R. Morris, P. R. Kent, A. R. Lupini, and G. M. Stocks, "Criteria for predicting the formation of single-phase high-entropy alloys," *Physical Review X*, vol. 5, no. 1, p. 011041, 2015.

[78] Y. Zhang, C. C. Koch, S. G. Ma, H. Zhang, and Y. Pan, "Fabrication routes," in *High-Entropy Alloys: Fundamentals and Applications*. Springer International Publishing, 2016, pp. 151–179.

[79] A. Kumar and M. Gupta, "An Insight into Evolution of Light Weight High Entropy Alloys: A Review," *Metals*, vol. 6, no. 9, p. 199, 2016.

[80] L. J. Santodonato and P. K. Liaw, "Advanced characterization techniques," in *High-Entropy Alloys: Fundamentals and Applications*. Springer International Publishing, 2016, pp. 115–150.

[81] G. Kienel and K. Röll, *Vakuumbeschichtung: Band 2: Verfahren Und Anlagen*, ser. VDI-Buch. Springer, 1997.

[82] H. Frey, *Dünnschichttechnologie*. Düsseldorf: VDI-Verl., 1987.

[83] R. A. Haefer, *Oberflächen- und Dünnschicht-Technologie : 1. Beschichtungen von Oberflächen*, ser. Werkstoff-Forschung und -Technik. Berlin: Springer, 1987.

[84] W. R. Grove, "VII. On the electro-chemical polarity of gases," *Philosophical Transactions of the Royal Society of London*, vol. 142, pp. 87–101, 1852.

[85] J. E. Greene, "Review Article: Tracing the recorded history of thin-film sputter deposition: From the 1800s to 2017," *Journal of Vacuum Science & Technology A: Vacuum, Surfaces, and Films*, vol. 35, no. 5, p. 05C204, 2017.

[86] J. T. Gudmundsson and D. Lundin, "Introduction to magnetron sputtering," in *High Power Impulse Magnetron Sputtering: Fundamentals, Technologies, Challenges and Applications*, 2019, pp. 1–48.

[87] I. V. Tudose, F. Comanescu, P. Pascariu, S. Bucur, L. Rusen, F. Iacomi, E. Koudoumas, and M. P. Suchea, "Chemical and physical methods for multifunctional nanostructured interface fabrication," in *Functional Nanostructured Interfaces for Environmental and Biomedical Applications*. Elsevier, 2019, pp. 15–26.

[88] R. A. Powell, S. M. Rossnagel, and A. Ulman, "Chapter 2: Physics of sputtering," in *PVD for Microelectronics*, ser. Thin Films, R. A. Powell and S. M. Rossnagel, Eds. Elsevier, 1999, vol. 26, pp. 23–49. [Online]. Available: https://www.sciencedirect.com/science/article/pii/S1079405099800052

[89] Y. M. Liu, R. Q. Han, F. Liu, Z. L. Pei, and C. Sun, "Sputtering gas pressure and target power dependence on the microstructure and properties of DC-magnetron sputtered AlB2-type WB2 films," *Journal of Alloys and Compounds*, vol. 703, pp. 188–197, 2017.

[90] A. A. Komlev, E. A. Minzhulina, V. V. Smirnov, and V. I. Shapovalov, "Influence of argon pressure and current density on substrate temperature during magnetron sputtering of hot titanium target," *Applied Physics A: Materials Science and Processing*, vol. 124, no. 1, pp. 1–5, 2018.

[91] M. Chinmulgund, R. B. Inturi, and J. A. Barnard, "Effect of Ar gas pressure on growth, structure, and mechanical properties of sputtered Ti, Al, TiAl, and Ti3Al films," *Thin Solid Films*, vol. 270, no. 1-2, pp. 260–263, 1995.

[92] M. A. Lieberman and A. J. Lichtenberg, *Principles of Plasma Discharges and Materials Processing*, 2nd ed. Hoboken: Wiley-Interscience, 2005.

[93] K. Wasa, I. Kanno, and H. Kotera, *Handbook of Sputter Deposition Technology: Fundamentals and Applications for Functional Thin Films, Nano-Materials and MEMS*. Elsevier Science, 2012.

[94] N. Matsunami, Y. Yamamura, Y. Itikawa, N. Itoh, Y. Kazumata, S. Miyagawa, K. Morita, R. Shimizu, and H. Tawara, *Energy dependence of the yields of ion-induced sputtering of monatomic solids*. Nagoya: Institute of Plasma Physics, Nagoya Univ., 1983.

[95] M. Wutz, H. Adam, W. Walcher, and K. Jousten, *Handbuch Vakuumtechnik*. Vieweg+Teubner Verlag, 2018.

[96] A. Roth, *Vacuum Technology*. North-Holland, 1982.

[97] "Vacuum technology — Vocabulary — Part 1: General terms." [Online]. Available: https://www.iso.org/obp/ui/#iso:std:iso:3529:-1:ed-2:v1:en (Accessed 2021-07-15).

[98] W. Demtröder, *Experimentalphysik 1 : Mechanik und Wärme*, 4th ed., ser. Springer-Lehrbuch. Berlin, Heidelberg: Springer-Verlag Berlin Heidelberg, 2006.

[99] I. A. T. Airco, *Physical Vapor Deposition*. Airco Temescal, 1976.

[100] "Types of flow." [Online]. Available: https://www.pfeiffer-vacuum.com/en/know-how/introduction-to-vacuum-technology/fundamentals/types-of-flow/ (Accessed 2021-12-28).

[101] B. Sundén and J. Fu, "Low-Density Heat Transfer," in *Heat Transfer in Aerospace Applications.* Elsevier, 2017, pp. 45–70. [Online]. Available: http://dx.doi.org/10.1016/B978-0-12-809760-1.00004-1

[102] W. Demtröder, *Experimentalphysik 1 : Mechanik und Wärme*, 9th ed., ser. Springer-Lehrbuch. Berlin Heidelberg: Springer Berlin Heidelberg Imprint: Springer Spektrum, 2021.

[103] J. F. O'Hanlon, *A user's guide to vacuum technology*, 3rd ed. Hoboken, NJ: Wiley-Interscience, 2003.

[104] M. v. Pirani, "Selbstzeigendes vakuum-messinstrument," *Verhandl. deut. Physik Ges*, vol. 8, no. 686, p. 104, 1906.

[105] M. Knoll, "Eichung eines Wärmeleitungsmanometers," in *Anleitungen zum Arbeiten im Röhrenlaboratorium.* Springer, Berlin, Heidelberg, 1937, pp. 15–21. [Online]. Available: https://link.springer.com/chapter/10.1007/978-3-642-91814-8{_}3

[106] G. Weissler and R. Carlson, *Vacuum Physics and Technology*, ser. ISSN. Elsevier Science, 1980.

[107] C. Mehofer, "Hochtemperaturbenetzung von Aluminiumoxid auf Refraktärmetallen unter Variation des Sauerstoffdrucks," Master's thesis, Vienna Technical University, 2018.

[108] L. Reimer, *Scanning Electron Microscopy*, ser. Springer Series in Optical Sciences. Berlin, Heidelberg: Springer Berlin Heidelberg, 1998, vol. 45.

[109] H. Alexander, *Physikalische Grundlagen der Elektronenmikroskopie*, ser. Teubner-Studienbücher : Angewandte Physik. Stuttgart: Teubner, 1997.

[110] S. Amelinckx, D. Van Dyck, J. Van Landuyt, and G. Van Tendeloo, *Electron Microscopy: Principles and Fundamentals.* Weinheim [Germany]: VCH, a Wiley Co., 2007.

[111] N. Gleichmann, "SEM vs TEM - Technology Networks," 2020. [Online]. Available: https://www.technologynetworks.com/analysis/articles/sem-vs-tem-331262 (Accessed 2021-10-06).

[112] A. Linnemann, S. Kühl, B. Ilsinger, S. Lenz, and M. Thaler, *Grundlagen der Licht- und Elektronenmikroskopie*, ser. utb Band-Nr. 4864 Biologie, Medizin, Molekularbiologie, Ernährungs-, Lebensmittelwissenschaften. Stuttgart: Verlag Eugen Ulmer, 2018.

[113] J. Goldstein, D. E. Newbury, D. C. Joy, C. E. Lyman, P. Echlin, E. Lifshin, L. Sawyer, and J. Michael, *Scanning Electron Microscopy and X-Ray Microanalysis*, 3rd ed. Springer US, 2003.

[114] D. B. Williams and C. B. Carter, "The Transmission Electron Microscope," in *Transmission Electron Microscopy*. Springer, Boston, MA, 1996, pp. 3–17. [Online]. Available: https://link.springer.com/chapter/10.1007/978-1-4757-2519-3{_}1

[115] "TECNAI F20 | TU Wien." [Online]. Available: https://www.tuwien.at/ustem/geraeteausstattung/tecnai-f20 (Accessed 2022-01-02).

[116] G. H. Michler, "Transmission Electron Microscopy: Fundamentals of Methods and Instrumentation," in *Electron Microscopy of Polymers*. Springer, Berlin, Heidelberg, 2008, pp. 15–51. [Online]. Available: https://link.springer.com/chapter/10.1007/978-3-540-36352-1{_}3

[117] N. D. Klein, K. R. Hurley, Z. V. Feng, and C. L. Haynes, "Dark field transmission electron microscopy as a tool for identifying inorganic nanoparticles in biological matrices," *Analytical Chemistry*, vol. 87, no. 8, pp. 4356–4362, 2015.

[118] M. Ermrich and D. Opper, *XRD for the analyst: getting acquainted with the principles*. PANalytical, 2013.

[119] D. Tabor, *The hardness of metals*, ser. Monographs on the physics and chemistry of materials. Oxford: Clarendon Press, 1951.

[120] ——, "Indentation Hardness and its Measurements: Some Cautionary Comments," in *ASTM Special Technical Publication*. ASTM, 1985, pp. 129–159.

[121] V. Lysaght, *Indentation Hardness Testing*. Reinhold Publishing Corporation, 1949.

[122] R. E. Reed-Hill, *Physical metallurgy principles*, ser. University series in basic engineering. Princeton, NJ [u.a.]: Van Nostrand, 1964.

[123] S. Müller, C. Wolverton, L. W. Wang, and A. Zunger, "Coherent phase stability in Al-Zn and Al-Cu fcc alloys: the role of the instability of fcc Zn," *Physical Review B - Condensed Matter and Materials Physics*, vol. 60, no. 24, pp. 16 448–16 462, 1999.

[124] E. O. Hall, "The deformation and ageing of mild steel: III Discussion of results," *Proceedings of the Physical Society. Section B*, vol. 64, no. 9, pp. 747–753, 1951.

[125] J. I. Gersten and F. W. Smith, *The physics and chemistry of materials*, ser. A Wiley-Interscience publication. New York, NY [u.a.]: Wiley, 2001.

[126] L. Bragg, "A theory of the strength of metals," *Nature*, vol. 149, no. 3784, pp. 511–513, 1942.

[127] U. F. Kocks, "The relation between polycrystal deformation and single-crystal deformation," *Metallurgical and Materials Transactions*, vol. 1, no. 5, pp. 1121–1143, 1970.

[128] G. Saada, "Hall-Petch revisited," *Materials Science and Engineering A*, vol. 400-401, pp. 146–149, 2005.

[129] E. Arzt, "Size effects in materials due to microstructural and dimensional constraints: A comparative review," *Acta Materialia*, vol. 46, no. 16, pp. 5611–5626, 1998.

[130] C. Varvenne and W. A. Curtin, "Strengthening of high entropy alloys by dilute solute additions: CoCrFeNiAlx and CoCrFeNiMnAlx alloys," *Scripta Materialia*, vol. 138, pp. 92–95, 2017.

[131] L. E. Samuels, "Microindentations in Metals," in *ASTM Special Technical Publication*. ASTM, 1985, pp. 5–24.

[132] F. Fröhlich, P. Grau, and W. Grellmann, "Performance and analysis of recording microhardness tests," *physica status solidi (a)*, vol. 42, no. 1, pp. 79–89, 1977.

[133] H. Bückle, *Mikrohärteprüfung und ihre Anwendung.* Stuttgart: Berliner Union, 1965.

[134] M. Arvinth Davinci, N. L. Parthasarathi, U. Borah, and S. K. Albert, "Effect of the tracing speed and span on roughness parameters determined by stylus type equipment," *Measurement: Journal of the International Measurement Confederation*, vol. 48, no. 1, pp. 368–377, 2014.

[135] A. V. Rogov and Y. V. Kapustin, "Angular Distributions during Magnetron Sputtering of Polycrystalline Mg, Al, Si, Ti, Cr, Cu, Zn, Ge, Zr, Nb, Mo, Ag, In, Sn, W, Pt, Au, and Bi Targets," *Instruments and Experimental Techniques*, vol. 63, no. 5, pp. 776–781, 2020.

[136] P. Sigmund, "Sputtering of single and multiple component materials," *Journal of Vacuum Science and Technology*, vol. 17, no. 1, pp. 396–399, 1980.

[137] J. W. Coburn, "The influence of ion sputtering on the elemental analysis of solid surfaces," *Thin Solid Films*, vol. 64, no. 3, pp. 371–382, 1979.

[138] W. Eckstein and H. M. Urbassek, "Computer simulation of the sputtering process," *Topics in Applied Physics*, vol. 110, pp. 21–31, 2007.

[139] E. Gillam, "The penetration of positive ions of low energy into alloys and composition changes produced in them by sputtering," *Journal of Physics and Chemistry of Solids*, vol. 11, no. 1-2, pp. 55–67, 1959.

[140] J. W. Coburn, "Sputtering in the Surface Analysis of Solids: A Discussion of some Problems," *J Vac Sci Technol*, vol. 13, no. 5, pp. 1037–1044, 1976.

[141] I. Ansara, A. T. Dinsdale, and M. H. Rand, *COST 507 Definition of thermochemical and Thermochemical database for light metal alloys.* European Commission EUR 18499 EN, 1998, vol. 2.

[142] P. Liang, T. Tarfa, J. A. Robinson, S. Wagner, P. Ochin, M. G. Harmelin, H. J. Seifert, H. L. Lukas, and F. Aldinger, "Experimental investigation and thermodynamic calculation of the Al-Mg-Zn system," *Thermochimica Acta*, vol. 314, no. 1-2, pp. 87–110, 1998.

[143] M. Nageswararao, V. Gerold, and G. Kralik, "Factors leading to grain-boundary fatigue crack propagation in Al-Zn-Mg alloys," *Journal of Materials Science*, vol. 10, no. 3, pp. 515–524, 1975.

[144] M. Voith, A. I. Mardare, and A. W. Hassel, "Synthesis and characterization of Al-Mg-Zn thin film alloys co-deposited from vapour phase," *Physica Status Solidi (A) Applications and Materials Science*, vol. 210, no. 5, pp. 1000–1005, 2013.

[145] S. Li, L. J. Zhang, J. Ning, X. Wang, G. F. Zhang, J. X. Zhang, and S. J. Na, "Microstructures and mechanical properties of Al-Zn-Mg aluminium alloy samples produced by wire + arc additive manufacturing," *Journal of Materials Research and Technology*, vol. 9, no. 6, pp. 13 770–13 780, 2020.

[146] J. Kirschner, C. Eisenmenger-Sittner, J. Bernardi, A. Großalber, S. Frank, and C. Simson, "Structural Changes in Multi Principal Element Alloys in Dependence on the Aluminium Content," *Materials Science Forum*, vol. 1016, no. 1, pp. 691–696, 2021.

[147] Z. Balogh and G. Schmitz, "Diffusion in Metals and Alloys," in *Physical Metallurgy: Fifth Edition.* Elsevier, 2014, vol. 1, pp. 387–559.

[148] N. L. Peterson, "Diffusion in Metals," *Solid State Physics - Advances in Research and Applications*, vol. 22, no. C, pp. 409–512, 1969.

[149] S. Curtarolo, W. Setyawan, S. Wang, J. Xue, K. Yang, R. H. Taylor, L. J. Nelson, G. L. Hart, S. Sanvito, M. Buongiorno-Nardelli, N. Mingo, and O. Levy, "AFLOWLIB.ORG: A distributed materials properties repository from high-throughput ab initio calculations," *Computational Materials Science*, vol. 58, pp. 227–235, 2012.

[150] S. Kirklin, J. E. Saal, B. Meredig, A. Thompson, J. W. Doak, M. Aykol, S. Rühl, and C. Wolverton, "The Open Quantum Materials Database (OQMD): Assessing the accuracy of DFT formation energies," *npj Computational Materials*, vol. 1, no. 1, pp. 1–15, 2015.

[151] J. E. Saal, S. Kirklin, M. Aykol, B. Meredig, and C. Wolverton, "Materials design and discovery with high-throughput density functional theory: The open quantum materials database (OQMD)," *JOM*, vol. 65, no. 11, pp. 1501–1509, 2013.

[152] C. Wolverton, "Open Quantum Materials Database." [Online]. Available: http://oqmd.org/ (Accessed 2021-10-13).

[153] M. Widom, "Alloy Database," 2012. [Online]. Available: http://alloy.phys.cmu.edu/ (Accessed 2021-10-13).

[154] A. Jain, S. P. Ong, G. Hautier, W. Chen, W. D. Richards, S. Dacek, S. Cholia, D. Gunter, D. Skinner, G. Ceder, and K. A. Persson, "Commentary: The materials project: A materials genome approach to accelerating materials innovation," p. 011002, 2013. [Online]. Available: https://aip.scitation.org/doi/abs/10.1063/1.4812323

[155] W. Steurer, "Single-phase high-entropy alloys – a critical update," *Materials Characterization*, vol. 162, p. 110179, 2020.

[156] R. Kozak, A. Sologubenko, and W. Steurer, "Single-phase high-entropy alloys - An overview," *Zeitschrift fur Kristallographie*, vol. 230, no. 1, pp. 55–68, 2015.

[157] D. C. Jiles, *Introduction to the principles of materials evaluation.* Boca Raton, Fla. [u.a.]: CRC Press, 2008.

[158] R. Thomas, S. Mochizuki, T. Mihara, and T. Ishida, "Influence of sputtering and annealing conditions on the structure and ferroelectric properties of Pb(Zr,Ti)O3 thin films prepared by RF magnetron sputtering," *Japanese Journal of Applied Physics, Part 1: Regular Papers and Short Notes and Review Papers*, vol. 40, no. 9 B, pp. 5511–5517, 2001.

[159] H. Wu and G. Fan, "An overview of tailoring strain delocalization for strength-ductility synergy," p. 100675, 2020.

[160] J. Sarkar, "Sputtering Target Manufacturing," in *Sputtering Materials for VLSI and Thin Film Devices.* William Andrew Publishing, 2014, pp. 197–289.

[161] R. Saha and W. D. Nix, "Effects of the substrate on the determination of thin film mechanical properties by nanoindentation," *Acta Materialia*, vol. 50, no. 1, pp. 23–38, 2002.

[162] S. K. Vanimisetti and R. Narasimhan, "A numerical analysis of spherical indentation response of thin hard films on soft substrates," *International Journal of Solids and Structures*, vol. 43, no. 20, pp. 6180–6193, 2006.

[163] B. Jönsson and S. Hogmark, "Hardness measurements of thin films," *Thin Solid Films*, vol. 114, no. 3, pp. 257–269, 1984.

[164] J. Westbrook, H. Conrad, and A. S. for Metals, *The Science of Hardness Testing and Its Research Applications.* American Society for Metals, 1973.

[165] Z. S. Ma, Y. C. Zhou, S. G. Long, and C. Lu, "On the intrinsic hardness of a metallic film/substrate system: Indentation size and substrate effects," *International Journal of Plasticity*, vol. 34, pp. 1–11, 2012.

[166] J. A. Thornton, "Influence of substrate temperature and deposition rate on structure of thick sputtered cu coatings," *Journal of Vacuum Science and Technology*, vol. 12, no. 4, pp. 830–835, 1975.

[167] B. Movchan and A. Demchishin, "Investigations of the structure and properties of thick Ni, Ti, W, Al2O3 and ZrO2 vacuum condensates," *Fiz. Met. Metalloved*, vol. 28, pp. 653–660, 1969.

[168] C. Wei and J. Y. Yen, "Effect of film thickness and interlayer on the adhesion strength of diamond like carbon films on different substrates," *Diamond and Related Materials*, vol. 16, no. 4-7, pp. 1325–1330, 2007.

[169] G. Abadias, E. Chason, J. Keckes, M. Sebastiani, G. B. Thompson, E. Barthel, G. L. Doll, C. E. Murray, C. H. Stoessel, and L. Martinu, "Review Article: Stress in thin films and coatings: Current status, challenges, and prospects," *Journal of Vacuum Science & Technology A: Vacuum, Surfaces, and Films*, vol. 36, no. 2, p. 020801, 2018.

[170] D. Sheeja, B. K. Tay, K. W. Leong, and C. H. Lee, "Effect of film thickness on the stress and adhesion of diamond-like carbon coatings," *Diamond and Related Materials*, vol. 11, no. 9, pp. 1643–1647, 2002.

[171] O. Heavens, "Some factors influencing the adhesion of films produced by vacuum evaporation," *Journal de Physique et le Radium*, vol. 11, no. 7, pp. 355–360, 1950.

[172] P. Villars and L. D. Calvert, *Pearson's handbook of crystallographic data for intermetallic phases*, 2nd ed. Materials Park, OH : ASM International, 1991.

[173] M. Winter, "The periodic table of the elements." [Online]. Available: https://www.webelements.com/ (Accessed 2020-06-02).

[174] K. K. Sankaran and R. S. Mishra, *Metallurgy and Design of Alloys with Hierarchical Microstructures*. Saint Louis: Elsevier, 2017.

[175] K. S. Tun, A. Kumar, and M. Gupta, "Introducing a High Performance Mg-Based Multicomponent Alloy as an Alternative to Al-Alloys," *Frontiers in Materials*, vol. 6, p. 215, 2019.

[176] M. R. Raza, F. Ahmad, N. Ikram, R. Ahmad, and A. Salam, "Development and strengthening of 2219 aluminium alloy by mechanical working and heat treatment," *Journal of Applied Sciences*, vol. 11, no. 10, pp. 1857–1861, 2011.

[177] H. Löffler, "Structure and Structure Development in Al-Zn Alloys," *Akademie Verlag, Berlin*, p. 487, 1995.

[178] W. K. Krajewski, J. Buraś, P. K. Krajewski, A. L. Greer, K. Faerber, and P. Schumacher, "New Developments of Al-Zn Cast Alloys," in *Materials Today: Proceedings*, vol. 2, no. 10. Elsevier, 2015, pp. 4978–4983.

[179] A. E. Ares and C. E. Schvezov, "Influence of solidification thermal parameters on the columnar-to-equiaxed transition of aluminum-zinc and zinc-aluminum alloys," in *Metallurgical and Materials Transactions A: Physical Metallurgy and Materials Science*, vol. 38 A, no. 7. Springer, 2007, pp. 1485–1499.

[180] Z. Boumerzoug and M. Fatmi, "Effect of heat treatments on discontinuous precipitation kinetics in Al-30 wt.% Zn alloy," *Materials Characterization*, vol. 60, no. 8, pp. 768–774, 2009.

[181] Y. Alemdağ and T. Savaşkan, "Mechanical and tribological properties of Al-40Zn-Cu alloys," *Tribology International*, vol. 42, no. 1, pp. 176–182, 2009.

[182] T. Savaşkan and Y. Alemdağ, "Effect of nickel additions on the mechanical and sliding wear properties of Al-40Zn-3Cu alloy," *Wear*, vol. 268, no. 3-4, pp. 565–570, 2010.

[183] W. R. Osório, J. E. Spinelli, N. Cheung, and A. Garcia, "Secondary dendrite arm spacing and solute redistribution effects on the corrosion resistance of Al-10 wt% Sn and Al-20 wt% Zn alloys," *Materials Science and Engineering A*, vol. 420, no. 1-2, pp. 179–186, 2006.

[184] S. Popović and B. Gržeta, "Precipitation and Dissolution Phenomena in Al-Zn Alloys," *Croatica Chemica Acta*, vol. 72, no. 2-3, pp. 621–643, 1999.

[185] D. Lamrous, M. Y. Debili, and E. Boehm-Courjault, "Microstructure and phase composition of Al-Zn alloys," *Journal of Advanced Microscopy Research*, vol. 8, no. 4, pp. 266–269, 2013.

[186] H. Xu, L. D. Xu, S. J. Zhang, and Q. Han, "Effect of the alloy composition on the grain refinement of aluminum alloys," *Scripta Materialia*, vol. 54, no. 12, pp. 2191–2196, 2006.

[187] F. Gonzales and M. Rappaz, "Dendrite growth directions in aluminum-zinc alloys," *Metallurgical and Materials Transactions A: Physical Metallurgy and Materials Science*, vol. 37, no. 9, pp. 2797–2806, 2006.

[188] W. R. Osório, P. R. Goulart, G. A. Santos, C. M. Neto, and A. Garcia, "Effect of dendritic arm spacing on mechanical properties and corrosion resistance of Al 9 wt pct Si and Zn 27 wt pct Al alloys," *Metallurgical and Materials Transactions A: Physical Metallurgy and Materials Science*, vol. 37, no. 8, pp. 2525–2538, 2006.

[189] J. L. Murray, "The Al-Zn (Aluminum-Zinc) system," *Bulletin of Alloy Phase Diagrams*, vol. 4, no. 1, pp. 55–73, 1983.

[190] J. B. Friauf, "The crystal structures of two intermetallic compounds," *Journal of the American Chemical Society*, vol. 49, no. 12, pp. 3107–3114, 1927.

[191] T. B. Massalski, "The Al-Cu (Aluminum-Copper) system," *Bulletin of Alloy Phase Diagrams 1980 1:1*, vol. 1, no. 1, pp. 27–33, 1980.

[192] "Collection of Phase Diagrams: Al-Cu," p. 2008, 2008. [Online]. Available: https://www.crct.polymtl.ca/fact/phase_diagram.php?file=Al-Cu.jpg&dir=FTlite (Accessed 2021-11-26).

[193] G. Rasinger, "Synthetisierung und Charakterisierung von metallischen Mehrkomponentenschichten mit Schichtdicken von bis zu 10 Mikrometern," Master's thesis, Vienna Technical University, 2020.

[194] H. Liang and Y. A. Chang, "A thermodynamic description for the Al-Cu-Zn system," *Journal of Phase Equilibria*, vol. 19, no. 1, pp. 25–37, 1998.

[195] P. Liang, H. J. Seifert, H. L. Lukas, G. Ghosh, G. Effenberg, and F. Aldinger, "Thermodynamic modelling of the Cu-Mg-Zn ternary system," *Calphad: Computer Coupling of Phase Diagrams and Thermochemistry*, vol. 22, no. 4, pp. 527–544, 1998.

[196] "Collection of Phase Diagrams: Mg-Zn," p. 2008, 2008. [Online]. Available: https://www.crct.polymtl.ca/fact/phase_diagram.php?file=Mg-Zn.jpg&dir=FTlite (Accessed 2021-11-26).

[197] É. Gaudry, A. K. Shukla, T. Duguet, J. Ledieu, M. C. Deweerd, J. M. Dubois, and V. Fournée, "Structural investigation of the (110) surface of γ-Al 4Cu9," *Physical Review B - Condensed Matter and Materials Physics*, vol. 82, no. 8, 2010.

[198] M. Snajdar-Musa and Z. Schauperl, "ECAP - new consolidation method for production of aluminium matrix composites with ceramic reinforcement," *Processing and Application of Ceramics*, vol. 7, no. 2, pp. 63–68, 2013.

[199] Q. Liu and L. Cheng, "Structural evolution and electronic properties of Cu-Zn alloy clusters," *Journal of Alloys and Compounds*, vol. 771, pp. 762–768, 2019.

[200] V. J. Keast, J. Ewald, K. S. De Silva, M. B. Cortie, B. Monnier, D. Cuskelly, and E. H. Kisi, "Optical properties and electronic structure of the Cu-Zn brasses," *Journal of Alloys and Compounds*, vol. 647, pp. 129–135, 2015.

[201] M. Natesan, S. Selvaraj, T. Manickam, and G. Venkatachari, "Corrosion behavior of metals and alloys in marine-industrial environment," *Science and Technology of Advanced Materials*, vol. 9, no. 4, p. 045002, 2008.

[202] R. Li, J. C. Gao, and K. Fan, "Microstructure and mechanical properties of MgMnAlZnCu high entropy alloy cooling in three conditions," *Materials Science Forum*, vol. 686, pp. 235–241, 2011.

[203] D. Lide, *CRC Handbook of Chemistry and Physics. (Special Student Edition): A Ready-Reference Book of Chemical and Physical Data*, 74th ed. CRC-Press, 1993.

[204] K. M. Youssef, A. J. Zaddach, C. Niu, D. L. Irving, and C. C. Koch, "A novel low-density, high-hardness, high-entropy alloy with close-packed single-phase nanocrystalline structures," *Materials Research Letters*, vol. 3, no. 2, pp. 95–99, 2014.

[205] K. Kanaya and S. Okayama, "Penetration and energy-loss theory of electrons in solid targets," *Journal of Physics D: Applied Physics*, vol. 5, no. 1, pp. 43–58, 1972.

[206] T. E. Everhart and P. H. Hoff, "Determination of kilovolt electron energy dissipation vs penetration distance in solid materials," *Journal of Applied Physics*, vol. 42, no. 13, pp. 5837–5846, 1971.

[207] P. J. Potts, *A Handbook of Silicate Rock Analysis.* Dordrecht: Springer Netherlands, 1987.

[208] S. K. Sahoo, R. K. Sabat, S. Panda, S. C. Mishra, and S. Suwas, "Mechanical Property of Pure Magnesium: From Orientation Perspective Pertaining to Deviation from Basal Orientation," *Journal of Materials Engineering and Performance*, vol. 24, no. 6, pp. 2346–2353, 2015.

[209] Y. Ouyang, K. Liu, C. Peng, H. Chen, X. Tao, and Y. Du, "Investigation of diffusion behavior and mechanical properties of Mg-Zn system," *Calphad: Computer Coupling of Phase Diagrams and Thermochemistry*, vol. 65, pp. 204–211, 2019.

[210] R. Li, J. C. Gao, and K. Fan, "Study to Microstructure and Mechanical Properties of Mg Containing High Entropy Alloys," *Materials Science Forum*, vol. 650, pp. 265–271, 2010.

[211] A. Luo and M. O. Pekguleryuz, "Cast magnesium alloys for elevated temperature applications," *Journal of Materials Science*, vol. 29, no. 20, pp. 5259–5271, 1994.

[212] P. L. Mao, B. Yu, Z. Liu, F. Wang, and Y. Ju, "Mechanical properties and electronic structures of MgCu2, Mg2Ca and MgZn2 Laves phases by first principles calculations," *Transactions of Nonferrous Metals Society of China (English Edition)*, vol. 24, no. 9, pp. 2920–2929, 2014.

[213] J. Kirschner, W. Mayr-Schmölzer, J. Bernardi, R. Gaschl, S. Schwarz, C. Simson, G. B. Vonbun-Feldbauer, and C. Eisenmenger-Sittner, "Characterization of an Al-Cu-Mg-Zn Multi Principal Element Alloy by Experimental and Computational Screening Methods," *Acta Materialia*, vol. 224, p. 117510, 2022.

[214] M. De, "Thermal expansion of some Cu- and Ag-base alloys at high temperatures," *Indian J. Phys.*, vol. 43, pp. 367–376, 1969.

[215] S. Ng, B. N. Brockhouse, and E. Hallman, "Characterization of large alloy single crystals by neutron diffraction," *Mat. Res. Bull.*, vol. 2, pp. 69–73, 1967.

[216] E. H. Kisi and J. D. Browne, "Ordering and structural vacancies in non-stoichiometric Cu–Al γ brasses," *Acta Crystallographica Section B*, vol. 47, no. 6, pp. 835–843, 1991.

[217] M. Klanjšek, S. Jazbec, M. Feuerbacher, and J. Dolinšek, "Physical properties of the V-Al5Cu6Mg2 complex intermetallic phase," *Intermetallics*, vol. 39, pp. 50–57, 2013.

[218] S. Samson, "Die Kristallstruktur von Mg2Zn11. Isomorphie zwischen Mg2Zn11 und Mg2Cu6Al5." *Acta Chemica Scandinavica*, vol. 3, pp. 835–843, 1949.

[219] ——, "Die Kristallstruktur von Mg2Cu6Al5." *Acta Chemica Scandinavica*, vol. 3, pp. 809–834, 1949.

[220] J. L. Murray, "The Al-Cr (aluminum-chromium) system," *Journal of Phase Equilibria*, vol. 19, no. 4, pp. 367–375, 1998.

[221] W. Köster, E. Wachtel, and K. Grube, "Aufbau und magnetische eigenschaften der aluminium-chrom-legierungen," *International Journal of Materials Research*, vol. 54, no. 7, pp. 393–401, 1963.

[222] F. J. den Broeder, G. van Tendeloo, S. Amelinckx, J. Hornstra, R. de Ridder, J. van Landuyt, and H. J. van Daal, "Microstructure of $Cr_{100-x}Al_x$ alloys (10 at% $\leq$ x $\leq$ 33 at%) studied by means of transmission electron microscopy and diffraction. I. Microstructure and diffraction. II. Discovery of a new phase," *physica status solidi (a)*, vol. 67, no. 1, pp. 233–248, 1981.

[223] G. van Tendeloo, F. J. den Broeder, S. Amelinckx, R. de Ridder, J. van Landuyt, and H. J. van Daal, "Microstructure of $Cr_{100-x}Al_x$ alloys (10 at% $\leq$ x $\leq$ 33 at%) studied by means of transmission electron microscopy and diffraction. I. Microstructure of the β-phase," *physica status solidi (a)*, vol. 67, no. 1, pp. 217–232, 1981.

[224] "Collection of Phase Diagrams: Al-Cr," p. 2008, 2008. [Online]. Available: https://www.crct.polymtl.ca/fact/phase_diagram.php?file=Al-Cr.jpg&dir=FTlite (Accessed 2021-11-04).

[225] P. Villars and L. D. Calvert, *Pearson's handbook of crystallographic data for intermetallic phases : 1 (1985)*, 1st ed. Metals Park, Ohio: ASM International, 1985.

[226] ——, *Pearson's handbook of crystallographic data for intermetallic phases : 2 (1985)*, 1st ed. Metals Park, Ohio: ASM International, 1985.

[227] ——, *Pearson's handbook of crystallographic data for intermetallic phases : 3 (1985)*, 1st ed. Metals Park, Ohio: ASM International, 1985.

[228] T. Onishi, Y. Nakatani, and K. Obayashi, "Crystal structures of intermetallic θ, η and ε phases in al-cr system," *Bulletin of University of Osaka Prefecture. Series A, Engineering and natural sciences*, vol. 24, no. 2, pp. 183–191, 1975.

[229] M. Cooper, "The structure of the intermetallic phase θ (cr-al)," *Acta Crystallographica*, vol. 13, no. 3, pp. 257–263, 1960.

[230] A. Bradley, S. Lu, and X. An, "An x-ray study of the chromium-aluminium equilibrium diagram," *J. Inst. Met*, vol. 60, pp. 319–337, 1937.

[231] J. Visser, "On the structure of (cr5al8) 26r. a correction," *Acta Crystallographica Section B: Structural Crystallography and Crystal Chemistry*, vol. 33, no. 1, p. 316, 1977.

[232] "Collection of Phase Diagrams: Cr-Mg," p. 2008, 2008. [Online]. Available: https://www.crct.polymtl.ca/fact/phase_diagram.php?file=Cr-Mg.jpg&dir=FTlite (Accessed 2021-11-04).

[233] "Collection of Phase Diagrams: Cr-Cu," p. 2008, 2008. [Online]. Available: https://www.crct.polymtl.ca/fact/phase_diagram.php?file=Cr-Cu.jpg&dir=FTlite (Accessed 2021-11-04).

[234] D. J. Chakrabarti and D. E. Laughlin, "The Cr-Cu (Chromium-Copper) system," *Bulletin of Alloy Phase Diagrams*, vol. 5, no. 1, pp. 59–68, 1984.

[235] "Collection of Phase Diagrams: Cr-Zn," p. 2008, 2008. [Online]. Available: https://www.crct.polymtl.ca/fact/phase_diagram.php?file=Cr-Zn.jpg&dir=FTlite (Accessed 2021-11-04).

[236] G. Reumont and P. Perrot, "Thermodynamic assessment of the zinc-rich part of the Cr-Zn system," *Journal of Phase Equilibria*, vol. 24, no. 1, pp. 50–54, 2003.

[237] Z. Moser and L. Heldt, "The Cr-Zn (Chromium-Zinc) System," *Journal of Phase Equilibria*, vol. 13, no. 2, pp. 172–176, 1992.

[238] H. Okamoto, "Cr-Zn (Chromium-Zinc)," *Journal of Phase Equilibria and Diffusion*, vol. 33, no. 3, pp. 246–247, 2012.

[239] T. C. Reiley and W. D. Nix, "The structure and mechanical properties of physically vapor deposited chromium," *Metallurgical Transactions A*, vol. 7, no. 11, pp. 1695–1701, 1976.

[240] J. K. Brandon, W. B. Pearson, P. W. Riley, C. Chieh, and R. Stokhuyzen, "γ-Brasses with R cells," *Acta Crystallographica Section B Structural Crystallography and Crystal Chemistry*, vol. 33, no. 4, pp. 1088–1095, 1977.

[241] B. B. Jung, H. K. Lee, and H. C. Park, "Effect of grain size on the indentation hardness for polycrystalline materials by the modified strain gradient theory," *International Journal of Solids and Structures*, vol. 50, no. 18, pp. 2719–2724, 2013.

[242] H. Conrad and J. Narayan, "Mechanisms for grain size hardening and softening in Zn," *Acta Materialia*, vol. 50, no. 20, pp. 5067–5078, 2002.

[243] Justin Hale, "Boeing 787 - From the ground up," *Aero Quarterly*, pp. 17–23, 2006.

[244] V. Venkatesh and R. Boyer, "Conference Highlights: Advancements in titanium technology," *Advanced Materials and Processes*, vol. 176, no. 5, pp. 37–39, 2016.

[245] P. Nasker and A. Sinha, "Titanium based bulk metallic glasses for biomedical applications," in *Fundamental Biomaterials: Metals*. Woodhead Publishing, 2018, pp. 269–283.

[246] J. Mantione, M. Garcia-Avila, M. Arnold, D. Bryan, and J. Foltz, "Properties of Novel High Temperature Titanium Alloys for Aerospace Applications," *MATEC Web of Conferences*, vol. 321, p. 04006, 2020.

[247] V. Raghavan, "Al-Ti (Aluminum-Titanium)," *Journal of Phase Equilibria and Diffusion*, vol. 26, no. 2, pp. 171–172, 2005.

[248] F. Zhang, S. L. Chen, Y. A. Chang, and U. R. Kattner, "A thermodynamic description of the Ti-Al system," *Intermetallics*, vol. 5, no. 6, pp. 471–482, 1997.

[249] J. L. Murray, "The Mg-Ti (Magnesium-Titanium) system," *Bulletin of Alloy Phase Diagrams*, vol. 7, no. 3, pp. 245–248, 1986.

[250] X. L. Meng, M. Sato, and A. Ishida, "Influence of Ti2Cu precipitates on B19 martensite structure in a Ti-rich Ti-Ni-Cu thin film," *Philosophical Magazine Letters*, vol. 88, no. 8, pp. 575–582, 2008.

[251] L. C. Tsao, "Effect of heat treatment conditions on the mechanical properties and machinability of Ti15SnxCu alloys," *Materials Research*, vol. 23, no. 3, pp. 1–9, 2020.

[252] C. Ohkubo, I. Shimura, T. Aoki, S. Hanatani, T. Hosoi, M. Hattori, Y. Oda, and T. Okabe, "Wear resistance of experimental Ti-Cu alloys," *Biomaterials*, vol. 24, no. 20, pp. 3377–3381, 2003.

[253] J. L. Murray, "The Cu-Ti (Copper-Titanium) system," *Bulletin of Alloy Phase Diagrams*, vol. 4, no. 1, pp. 81–95, 1983.

[254] H. Okamoto, "Ti-Zn (Titanium-Zinc)," *Journal of Phase Equilibria and Diffusion*, vol. 29, no. 2, pp. 211–212, 2008.

[255] J. L. Murray, "The Ti-Zn (Titanium-Zinc) system," *Bulletin of Alloy Phase Diagrams*, vol. 5, no. 1, pp. 52–56, 1984.

[256] "Collection of Phase Diagrams: Al-Ti," p. 2008, 2008. [Online]. Available: https://www.crct.polymtl.ca/fact/phase_diagram.php?file=Al-Ti.jpg&dir=FTlite (Accessed 2021-11-04).

[257] "Collection of Phase Diagrams: Mg-Ti," p. 2008, 2008. [Online]. Available: https://www.crct.polymtl.ca/fact/phase_diagram.php?file=Mg-Ti.jpg&dir=FTlite (Accessed 2021-11-04).

[258] "Collection of Phase Diagrams: Cu-Ti," p. 2008, 2008. [Online]. Available: https://www.crct.polymtl.ca/fact/phase_diagram.php?file=Cu-Ti.jpg&dir=FTlite (Accessed 2021-11-04).

[259] "Collection of Phase Diagrams: Ti-Zn," 2008. [Online]. Available: https://www.crct.polymtl.ca/fact/phase_diagram.php?file=Ti-Zn.jpg&dir=FTlite (Accessed 2021-11-04).

[260] B. He, N. Zhang, D. Lin, Y. Zhang, F. Dong, and D. Li, "The phase evolution and property of fecocrnialtix high-entropy alloying coatings on q253 via laser cladding," *Coatings*, vol. 7, no. 10, 2017.

[261] K. A. Jackson, *Silicon devices : structures and processing*. Weinheim, Germany: Wiley VCH, 1998.

[262] A. K. Dahle, K. Nogita, S. D. McDonald, C. Dinnis, and L. Lu, "Eutectic modification and microstructure development in Al-Si Alloys," *Materials Science and Engineering A*, vol. 413-414, pp. 243–248, 2005.

[263] J. L. Murray and A. J. McAlister, "The Al-Si (Aluminum-Silicon) system," *Bulletin of Alloy Phase Diagrams*, vol. 5, no. 1, pp. 74–84, 1984.

[264] S. Zn, R. W. Olesinski, and G. J. Abbaschian, "The Si-Zn (Silicon-Zinc) System," *Bulletin of Alloy Phase Diagrams*, vol. 6, no. 6, pp. 545–548, 1985.

[265] Y. C. X. Yan, "A Thermodynamic Analysis of the Cu-Si System," *J. Alloys Compd.*, vol. 308, no. 1-2, pp. 221–229, 2000.

[266] R. W. Olesinski and G. J. Abbaschian, "The Cu-Si (Copper-Silicon) system," *Bulletin of Alloy Phase Diagrams*, vol. 7, no. 2, pp. 170–178, 1986.

[267] A. B. Gokhale and G. J. Abbaschian, "The Cr-Si (Chromium-Silicon) system," *Journal of Phase Equilibria*, vol. 8, no. 5, pp. 474–484, 1987.

[268] H. J. Goldschmidt and J. A. Brand, "The constitution of the chromium-niobium-silicon system," *Journal of the Less Common Metals*, vol. 3, no. 1, pp. 34–43, 1961.

[269] Y. Chang, "Phase relationships in the system chromium- silicon(phase relationships of cr-si binary system based on melting point and x ray, metallographic and differential thermal analysis studies)," *AIME, TRANSACTIONS*, vol. 242, pp. 1509–1515, 1968.

[270] J. A. Kocherzhinsky, "Differential Thermocouple up to 2450°C and Thermographic Investigation of Refractory Silicides," *Advances in Instrumentation*, pp. 549–559, 1972.

[271] R. Kieffer, F. Benesovsky, and H. Schroth, "Contribution to the system chromium-silicon and silicide mixtures," *Z. Metallkd.*, vol. 44, pp. 437–442, 1953.

[272] R. Vogel, "Metallographische Mitteilungen aus dem Institut für physikalische Chemie der Universität Göttingen. LXX. Über Magnesium-Siliciumlegierungen," *Zeitschrift für anorganische Chemie*, vol. 61, no. 1, pp. 46–53, 1909.

[273] A. A. Nayeb-Hashemi and J. B. Clark, "The Mg-Si (Magnesium-Silicon) system," *Bulletin of Alloy Phase Diagrams*, vol. 5, no. 6, pp. 584–592, 1984.

[274] Y. Kudriavtsev, A. Villegas, A. Godines, and R. Asomoza, "Calculation of the surface binding energy for ion sputtered particles," *Applied Surface Science*, vol. 239, no. 3-4, pp. 273–278, 2005.

[275] J. Lu and C. G. Lee, "Numerical estimates for energy of sputtered target atoms and reflected Ar neutrals in sputter processes," *Vacuum*, vol. 86, no. 8, pp. 1134–1140, 2012.

[276] R. V. Stuart and G. K. Wehner, "Energy distribution of sputtered Cu atoms," *Journal of Applied Physics*, vol. 35, no. 6, pp. 1819–1824, 1964.

List of Figures

List of Tables

Curriculum vitae

Persönliche Information

Name	**Dipl. Ing. KIRSCHNER, Johannes, BSc**
E-Mail	johannes.kirschner@tuwien.ac.at
Nationalität	Österreich
Geburtsdatum	30.12.1990
Status	ledig

seit Jänner 2022	Angestellter in der Optikentwicklung für EUV Lithographie-Systeme Carl Zeiss SMT GmbH Rudolf-Ebert-Straße 2 D-73447 Oberkochen
seit April 2018	Doktorand der Technischen Physik ‚Entwicklung von Leichtmetall Hochentropie-Legierungen' Technische Universität Wien Karlsplatz 13 A-1040 Wien
März 2016 – April 2018	Wissenschaftlicher Mitarbeiter ‚Untersuchung der Oberfläche von Flüssigkeiten' AMOLF Science Park 104 NL-1098 XG Amsterdam
Oktober 2013 – März 2016	Master Studium der Technischen Physik Technische Universität Wien Karlsplatz 13 A-1040 Wien
Oktober 2010 – August 2013	Bachelor Studium der Technischen Physik Technische Universität Wien Karlsplatz 13 A-1040 Wien
September 2001 - Juni 2009	Matura Akademisches Gymnasium Salzburg Sinnhubstraße 15 A-5020 Salzburg

Oktober 2014 – März 2016	Diplomarbeit an der Technischen Universität Wien in Kollaboration mit der 'Miba Gleitlager GmbH' zum Thema Dünnschichtphysik

	Technische Universität Wien	Miba Gleitlager GmbH
	Karlsplatz 13	Dr.-Mitterbauer-Straße 3
	A-1040 Wien	A- 4663 Laakirchen

August 2014 – September 2014	Praktikum in der Abteilung 'Neuroradiologie' der Christian Doppler Klinik in Salzburg

Christian Doppler Klinik Salzburg
Ignaz-Harrer-Straße 79
A-5020 Salzburg

Persönliche Fähigkeiten und Kompetenzen

Muttersprache	**Deutsch**

weitere Sprachen	Englisch (fließend), Französisch (gute Kenntnisse), Spanisch (gute Kenntnisse), Niederländisch (Grundkenntnisse), Latein

Technische Fähigkeiten	Guter Umgang mit geometrischen und mathematischen Computerprogrammen (GeoGebra, Mathematica, Matlab)

Sehr gute Kenntnisse von Microsoft Office (Word, Excel, PowerPoint)
Programmierkenntnisse (C, C++, Fortran, Python, LabView)
Erfahrung im Umgang mit CAD Software (SolidWorks)
Bereits Berufserfahrung in den Bereichen Supraleitung, Röntgenanalyse, Atomphysik und Laserphysik
Diplomarbeit zum Thema Dünnschichtphysik
    Entwurf und Aufbau einer Beschichtungsanlage um Effekte von Verunreinigungen auf das Schichtwachstum zu untersuchen
Publikation von mehreren Fachartikeln in Peer Review Journalen
3D Druck und Prototypentwicklung